

UNIVERSITÉ DE STRASBOURG

ÉCOLE DOCTORALE DE PHYSIQUE ET CHIMIE-PHYSIQUE

INSTITUT DE PHYSIQUE ET DE CHIMIE DES MATÉRIAUX DE STRASBOURG

Tunneling spectroscopy of mono- and di-nuclear organometallic molecules on surfaces

Thèse présentée par:

Anis AMOKRANE

POUR OBTENIR LE GRADE DE:

Docteur de l'Université de Strasbourg

Discipline: *Physique*

Thèse dirigée par:

Pr. Jean-Pierre Bucher

Rapporteurs:

Pr. Talal Mallah

Dr. Florian Klappenberger

Examineurs:

Pr. Mario Ruben

Dr. Guillaume Rogez

Thèse soutenue le 22 février 2016

ACKNOWLEDGMENTS / REMERCIEMENTS

Je profite de la possibilité de citer quelques noms dans cette thèse pour remercier les personnes qui ont contribué (consciemment ou non) au bon déroulement de mon parcours doctoral à Strasbourg. Tout d'abord, aller jusqu'au bout n'aurait jamais été possible sans le soutien moral de tous les membres de ma famille, à mes parents : Naïma et Abderrezak, mon frère et ma sœur Billel et Sarah ainsi que les autres membres (particulièrement Soraya et Yasmine). Je n'oublie pas mes grands-parents Kheira Ouaguennouni et Ali Amrouche qui ont porté une attention très particulière à toutes les étapes de mon séjour en Alsace (et au Pays-Bas).

Un nouveau monde s'est ouvert à moi à Strasbourg où j'y ai rencontré mes amis qui ont su faire de mon expérience doctorale une expérience bizarrement unique et particulièrement agréable. Un grand merci va à mes amis de l'association des doctorants et docteurs d'Alsace qui m'ont aidé, soutenu, conseillé et guidé durant mon parcours, mais pas que... A Pilar, Elena et Yuliya pour les AfterWorks et les soirées inoubliables qu'on a passés à Strasbourg. Orphée, Kenneth, Simon, Nicoals, Cécilia et plein d'autres pour des réunions de bureau plus ou moins agitées.

Mon passage à l'IPCMS m'a permis de rencontrer des gens aussi agréables qu'amicaux. Je remercie Mathilde pour son humeur indescriptible qui m'a permis de passer des moments inoubliables au bureau. A Georges pour les délires au labos et les pré-AfterWork@Work. Je n'en oublie pas Selvi, Marco, Melania, Catalina, Antonio, PO, Vincent, Delephine T., Julien, Assil, Saber, Manu qui ont fait de mes journées à l'institut et au DMO une ambiance de travail dans la joie et la bonne humeur. Merci également à Andreina pour son soutien moral et sa personnalité émettrice d'ondes positives.

Je tiens à remercier profondément Jonathan Kaiser pour sa présence et son accompagnement à toute épreuve durant ces années, qui m'ont permis de connaître une personne dévouée et prête à tout pour aider ses proches. A Jérémy Moultier, Vanessa, Jennifer & Ruud, Max & Elo, Marie-Claude et Jacky, Mamie Lucienne et Finel... Merci beaucoup. Un remerciement particulier va également à mes amis de longue date Lamis, Razine, Amine,

Kamel et bien d'autres...

Je remercie de manière très particulière Nicolas Beyer, Benoît Heinrich et Emilie Couzigné pour leur aide technique et matérielle qui était plus que nécessaire pour l'accomplissement de cette recherche. Je tiens à remercier également Shawulienu pour son assistance et son aide avec le microscope. Je remercie profondément le Professeur Jean-Pierre Bucher pour m'avoir permis d'effectuer ce doctorat, ainsi que le Professeur Mario Ruben et que le Docteur Mauro Boero pour leur encadrement supplémentaire dans ce projet.

TABLE OF CONTENTS

Table of contents	iii
Résumé étendu	1
Introduction	9
1 Short theoretical overview	13
1.1 Single molecular magnets	13
1.2 Ligand field theory	17
1.3 The Kondo effect	20
1.3.1 Liquid Fermi theory	20
1.3.2 Kondo approach	23
1.3.3 Anderson model	24
1.3.4 Fano resonance	27
1.3.5 π -Kondo resonance	29
1.4 Summary	30
References	33
2 Scanning tunneling microscope	39
2.1 Tunnelling microscopy	40
2.2 Scanning tunneling spectroscopy (STS)	46
2.3 Instrument and experimental approach	48
2.3.1 STM instrument	48
2.3.2 Ultra high vacuum	51
2.3.3 Tip and sample preparation	51
2.3.4 Deposition techniques	52

2.4	Experimental approach	52
2.5	Summary	56
References		57
3	Isolated TbPc₂ molecules on surfaces	61
3.1	A brief overview	61
3.2	Addressing terbium double-decker molecules on surfaces	64
3.3	Height analysis	68
3.4	Adsorption sites and orientations	69
3.4.1	Gold (111) substrate	70
3.4.2	Copper (111) substrate	72
3.4.3	Copper (100) substrate	76
3.5	Tunneling spectroscopy above single molecules	76
3.6	Kondo resonance appearance on Au (111) surface	82
3.7	Summary and conclusions	88
References		91
4	Terbium double-decker domains on surfaces	101
4.1	Structural and electronic properties of double-deckers	102
4.1.1	Domain growth on Cu (111) substrate	102
4.1.2	Domain growth on Ag (111) substrate	104
4.1.3	Domain growth on Au (111) substrate and Kondo peak appearance .	107
4.2	Domain construction from isolated molecules	112
4.3	Molecular densities	118
4.4	Second layer molecule	120
4.5	Summary and conclusions	121
References		123
5	Capping a terbium double-decker with a cerium atom	127
5.1	CePcTbPc complexes	128
5.2	Site and substrate dependent STS	130
5.2.1	Ce/TbPc ₂ /Cu (111)	131
5.2.2	Ce/TbPc ₂ /Ag (111)	133
5.2.3	Ce/TbPc ₂ /Au (111)	134
5.2.4	General discussion	137

5.3	Magnetic investigation and spin density analysis	139
5.4	Kondo resonance (Magnetic CDD)	142
5.5	Atomic manipulation	144
5.5.1	Uncapping the CePcTbPc	144
5.5.2	Hiding cerium (a new way to store information)	145
5.6	Summary and conclusions	147
References		149
6 Genesis of metal-phthalocyanine on surfaces		153
6.1	DFT calculation	153
6.2	From TCNB to Fe-4(TCNB)	154
6.2.1	1,2,4,5-Tetracyanobenzene	154
6.2.2	Dosing TCNB layer with Fe	155
6.3	Thermally activated Fe(TCNB) ₄	158
6.3.1	Valence and charge properties	158
6.3.2	Density of states	161
6.4	On-surface synthesis of FePc by covalent self-assembly	161
6.5	Specific calculation parameters	165
6.6	Summary and conclusion	167
References		169
General conclusion		175
Appendices		179

RÉSUMÉ ÉTENDU

Traditionnellement, les matériaux métalliques sont tout à fait adaptés à l'utilisation en nanotechnologies. Néanmoins, leur usage et leur versatilité restent, à ce jour, extrêmement limités. Pendant les dernières décennies, plusieurs composants électroniques composés de matériaux organiques ont progressivement été incorporés dans les nano-composants grâce au développement de modèles structurels adaptés. Dans ce but, l'habilité des éléments π -conjugués à s'auto-assembler est une caractéristique majeure contribuant à l'amélioration des performances de ces composants comme les transistors par exemple.

La formation de réseaux moléculaires étendus sur des surfaces à température ambiante, constitue une avancée majeure dans ce domaine ouvrant ainsi la porte à des améliorations conséquentes dans le domaine du photovoltaïque et du stockage de l'information.

La formation de réseaux moléculaires périodiques sur des surfaces nécessite la synthèse de nanostructures hybrides avec une fonctionnalité appropriée, et cela tout en ayant une précision atomique afin de satisfaire une reproductibilité stable. Ces réseaux sont généralement basés sur des interactions non-covalentes (de type Van der Waals), interactions hydrogène ou des interactions métal-ligand. Il devient alors nécessaire d'avoir une géométrie spécifique pour satisfaire au système désiré avec les interactions appropriées permettant la construction de blocs moléculaires.

Le processus d'auto-assemblage est aujourd'hui une technique répandue pour la formation de nouveaux composants organiques ou organométalliques. De façon particulière, l'auto-assemblage sous ultravide montre des résultats probants pour des études par microscopie. La synthèse de molécules sur des surfaces avec des orbitales délocalisées permet quant-à-elle d'amplifier le transport électronique comme c'est le cas pour les molécules π -conjuguées.

La compétition pour la découverte du meilleur composant SMM (pour Single Molecular Magnet) capable de stocker l'information pour un temps de relaxation relativement long, a

suscité l'intérêt de beaucoup de scientifiques de par le monde. A travers des techniques d'approche différentes et variées, il a été possible de produire un nombre, aujourd'hui incalculable de complexes magnétiques. La plupart de ces recherches sont orientées vers l'étude des propriétés électroniques des matériaux organométalliques dont les propriétés sont dépendantes, non seulement de leur composition atomique, mais également de leurs structures.

Une des meilleures techniques d'investigation est la microscopie à effet tunnel. Cette approche offre des possibilités variées comme l'imagerie au niveau atomique, la spectroscopie tunnel, l'excitation moléculaire, l'investigation de propriétés magnétiques ainsi que la manipulation atomique/moléculaire.

La thèse présentée dans ce document rapporte les résultats obtenus et théories développées sur un travail réalisé par microscopie à effet tunnel de complexes organométalliques et ce, sur différentes surfaces. La sélection de complexes s'est tournée sur une molécule à base d'un centre métallique de terbium et de ligands de phthalocyanine (notée $TbPc_2$) comme rapporté dans la Figure 3.3, le choix de cette structure est motivé par la présence d'un centre magnétique (terbium) et d'une géométrie offrant un axe d'anisotropie normal aux plans des ligands.

A travers plusieurs chapitres, il a été démontré que même si les molécules initiales ont les mêmes propriétés électroniques, magnétiques et géométriques, leur dépôt sur une surface modifie significativement ces propriétés en fonction de la nature de la surface. De ce fait le choix de la nature atomique et la cristallographie de la surface a été cruciale dans cette étude.

Le premier chapitre de cette thèse donne une introduction générale à l'électronique et le magnétisme moléculaire où sont développés les principes théoriques et fondamentaux. L'origine de l'anisotropie dans les SMMs ainsi que leur réponse à un champ magnétique y sont introduits de manière généraliste. La théorie du champ cristallin y est également présentée afin de démontrer l'importance des ligands dans ce type de complexes moléculaires où leur nature et leur symétrie jouent un rôle déterminant dans les propriétés intrinsèques comme la distribution des orbitales moléculaires. L'application de cette théorie aux lanthanides laisse apparaître une contribution non négligeable de l'effet Zeeman et de l'interaction hyperfine expliquant ainsi la singularité d'une molécule de $TbPc_2$.

Ce chapitre revient également sur la physique de la résonance Kondo qui y est présentée au travers de deux approches complémentaires afin de caractériser sa nature. L'effet Kondo naît de la diffusion des électrons de conduction par un moment magnétique lo-

calisé au niveau d'une « impureté ». Cette interaction entre les spins est d'un type anti-ferromagnétique et se traduit par une résonance (caractérisée entre autres par sa largeur à mi-hauteur) apparaissant sur la courbe de conductance au voisinage de l'énergie de Fermi. Ainsi un minimum de résistance est observé à une température du système supérieure au zéro absolu. Cette température, appelée température Kondo (T_K) est directement liée à la largeur à mi-hauteur du pic de résonance (Γ).

Afin d'approcher le Problème Kondo, la théorie du liquide fermionique a été introduite en lien avec le Modèle d'Anderson qui décrit un système similaire. Ainsi, il a été possible de compléter l'approche de Kondo appliquant la théorie de perturbation développée au second ordre sur la diffusion des électrons par un centre magnétique. Il existe plusieurs techniques pour détecter et mesurer la résonance Kondo, néanmoins, la spectroscopie tunnel reste à ce jour le meilleur moyen pour caractériser ce pic de manière sensible. La spectroscopie tunnel permet également de détecter les orbitales singulièrement occupées, condition pour l'obtention d'une telle résonance.

Le second chapitre de cette thèse développe une approche théorique étendue de la transmission électronique par effet tunnel menant au courant tunnel réellement mesurable. Les dérivées de ce développement tel que la spectroscopie tunnel et la topographie y sont également présentées de manière à apporter au lecteur une vision claire des résultats exposés.

Le troisième chapitre de la thèse rapporte les résultats obtenus sur une molécule unique déposée sur différents substrats tel que Cu (111), Cu (100), Ag (111), Au (111) et îlots de cobalt. La molécule isolée apparaît en topographie comme une structure à huit lobes (voir Figure 3.4(a)) qui correspondent à la distribution électronique du ligand supérieur, signifiant ainsi un découplage important entre cette phthalocyanine et le substrat.

Une analyse topographique de la molécule sur les différentes surfaces démontre que la molécule de TbPc₂ se positionne différemment en fonction de la nature et la symétrie du substrat. Ainsi, il a été vu que au-dessus de l'Au (111), par exemple, la molécule adopte une position « top » (voir Figure 3.5) alors qu'au-dessus d'un substrat de Cu (111) elle a été déterminée avec une position « bridge » (voir Figure 3.6(c)). Ce positionnement s'accompagne d'une orientation spécifique aux directions cristallographiques de la surface. De même, la hauteur apparente de la molécule montre une variation en fonction de la nature du substrat tel que 3.2 Å sont mesurés au-dessus de l'or alors que 1.8 Å sont mesurés au dessus d'un îlot de cobalt.

D'un autre côté, la conductance relevée au-dessus du centre métallique (terbium) varie

selon le substrat utilisé. Ainsi, même si la forme globale du spectre de conductance reste similaire entre -1 V et +1 V, le fait de modifier la réactivité du substrat (en changeant sa nature) déplace énergétiquement les orbitales moléculaires par rapport au niveau de Fermi. Ce déplacement est conduit par l'ajustement du potentiel chimique à l'interface molécule-substrat pour atteindre l'équilibre. De plus, seules les surfaces de Au (111) et Ag (111) ont permis l'observation des états vides du complexe au-dessus du lanthanide indiquant que ces états sont fortement modifiés par la nature atomique du substrat.

De même, la diffusion moléculaire est augmentée de façon importante quand la réactivité de la surface augmente. A cet effet, le gap séparant la première orbitale occupée (HOMO) de la première orbitale non occupée (LUMO) est mesuré respectivement à 800 meV, 950 meV, 2.4 eV et 2.6 eV pour l'Au (111), Ag (111), Cu (111) et îlots de cobalt.

De manière étonnante, lorsque la molécule est adsorbée sur une surface d'Au (111), l'investigation de la spectroscopie tunnel au voisinage du niveau de Fermi laisse apparaître un pic attribué à la résonance Kondo tel qu'introduite dans le premier chapitre. Cette résonance est ajustée avec une équation Fano suivant les paramètres: $q = 3.93$ et $\Gamma = 9.56$ meV (où q représente le paramètre d'asymétrie de l'équation de Fano).

Ce pic est localisé au-dessus des huit lobes de la molécule et tend à disparaître lorsque la pointe du STM est déplacée ailleurs. D'un autre côté, lorsque la molécule est déposée sur une première couche de TbPc₂ la découplant ainsi fortement du substrat, aucune résonance au voisinage de l'énergie de Fermi n'est mesurée. De ce fait, il devient clair que la nature du substrat ainsi que la présence des électrons de surfaces sont responsables de l'apparition de cette diffusion magnétique.

Il devient ainsi évident, après analyse, que la source de ce pic Kondo (l'impureté magnétique) n'est autre que le spin 1/2 délocalisé sur les deux ligands et naturellement présent sur une molécule de TbPc₂. Ce spin joue le rôle du centre magnétique qui diffuse les électrons de surface présents sur le substrat d'Au (111). Ceci expliquerait donc l'absence d'une résonance sur une deuxième couche car les deux spins 1/2 des molécules empilées s'apparient, annihilant ainsi le magnétisme local qui donne lieu à la résonance Kondo. Ce pic est défini par sa largeur à mi-hauteur qui donne accès à une température caractéristique évaluée à 37K. La Figure 3.14 résume la situation de présence de la résonance Kondo sur un substrat d'Au (111).

Le quatrième chapitre de la thèse complète les résultats précédents par une investigation sur des îlots de molécules et des domaines plus étendus. Une croissance de film a été réalisée

en évaporant une plus grande quantité de molécules sur les différents substrats précédemment étudiés afin de les analyser. Différentes configurations sont alors observées en fonction de la nature de la surface. En effet, au-dessus du Cu (111), les molécules s'assemblent de manière parallèle formant ainsi une cellule unitaire carrée contenant une seule molécule de TbPc_2 . Par ailleurs, sur un substrat de Ag (111), un angle de 15° est mesuré entre deux molécules voisines dans un domaine.

Une monocouche obtenue sur un substrat d' Au (111) montre quant-à-elle une nouvelle structure où la géométrie de la TbPc_2 se trouve modifiée. Une topographie STM réalisée à très faible courant et basse tension laisse apparaître la distribution électronique interne du cycle de la phthalocyanine supérieure tel qu'obtenu par des calculs théoriques. Cette distribution correspond également à ce qui est attendu pour une molécule de phthalocyanine unique fortement découplée d'une surface.

A partir de ces images topographiques, il a été possible d'identifier deux types de structures au-dessus de l'or : une structure semblable à celle observée jusque-là et où les ligands forment un angle de 45° entre eux, appelée structure de *Type-A* et une autre structure où l'angle séparant les deux phthalocyanines est réduit à 30° définie comme une structure de *Type-B*. Au-dessus de l' Au (111), ces deux structures s'alternent dans la croissance du domaine comme le montre la Figure 4.4.

De la même manière que la molécule isolée, l'investigation de la conductance au voisinage du niveau de Fermi laisse apparaître un pic Kondo avec une température caractéristique de 22 K, significativement plus basse en comparaison à la molécule isolée. De plus, ce pic est exclusivement localisé au niveau des intersections intermoléculaires dans un domaine (région commune à 4 molécules). Afin de comprendre l'origine de ce pic et de chercher un lien entre la résonance Kondo obtenue dans un domaine et celle obtenue sur une molécule isolée, une croissance manuelle et graduelle d'un domaine à 4 molécules a été effectuée (voir Figure 4.7). Grâce à une manipulation moléculaire, il a été possible de construire à travers plusieurs étapes un dimère, un trimère et un tétramère. Une investigation au voisinage de l'énergie de Fermi a été effectuée au-dessus de chaque îlot. Ainsi, sur un dimère, aucune résonance n'a été observée alors que sur un trimère, un pic Kondo avec une température caractéristique de 34 K a été mesuré au niveau de l'intersection des molécules. Sur l'îlot de 4 molécules, ce pic est observé avec une température caractéristique plus basse à 31 K.

Ce qu'il ressort de ces manipulations c'est que la température Kondo décroît en fonction de la taille de l'îlot comme résumé dans le tableau 1.

Il a été démontré dans le 1^{er} chapitre que la température caractéristique de la réson-

Table 1 Résumé de la présence et de l'absence de la résonance Kondo sur les différents systèmes (du monomère au film). La température caractéristique T_K ainsi que la largeur à mi-hauteur Γ y sont également présentées.

	Monomère	Dimère	Trimère	Tetramère	Film
Présence Kondo	Oui (Lobes)	Non	Oui (intersection)	Oui (intersection)	Oui (Intersection)
T_K	37 K	/	34 K	31 K	22 K
Γ	9.56 meV	/	9 meV	8 meV	6 meV

nance Kondo est dépendante de la densité électronique des électrons de conduction et de l'interaction d'échange entre le centre magnétique et ces électrons. Dans le cas présent, un réseau de spin est formé au niveau des ligands supérieurs de molécules formant le réseau. Ces électrons constituent ainsi les particules diffusées par un spin électronique localisé sur le même réseau. La construction manuelle des îlots moléculaires mène à une possible adaptation des propriétés électroniques et magnétiques intrinsèques à la molécule menant à une présence de résonance Kondo pour un nombre pair d'électrons excédentaires. Plus l'îlot moléculaire est grand, et plus la densité des électrons de conduction s'affaiblit réduisant ainsi la température Kondo.

Le cinquième chapitre de cette thèse introduit un nouveau complexe à base de deux centres magnétiques où un atome de cérium a été déposé au-dessus de la molécule précédente (TbPc_2). Au-dessus du substrat de cuivre, deux études ont été menées, une sur la molécule isolée (voir Figure 5.3(a)) et l'autre sur une molécule à deux centres magnétiques dans un domaine (Figure 5.3(c)). Sur l'or, il a été impossible d'obtenir une molécule isolée de CeTbPc_2 dû à la faible réactivité de la surface qui empêche l'obtention de monomères sans manipulation. Ainsi, au-dessus de Au (111) seuls les domaines ont été étudiés comme présenté dans la Figure 5.5.

D'importantes modifications sont observées à travers l'investigation des configurations électroniques et structurales de ce nouveau complexe. Plus particulièrement, au-dessus de l'or, la variation dans les niveaux énergétiques des orbitales HOMO et LUMO est induite par la configuration géométrique du voisinage.

Lorsqu'une CeTbPc_2 est adsorbée sur un substrat d'Or (111), le niveau de la LUMO est transféré vers les énergies supérieures comparé au cas du Cu (111) et Ag (111). Ceci indique que le nouveau complexe a moins d'électrons excédentaires quand il est adsorbé sur un substrat à faible réactivité. Une possible explication serait que la première orbitale vide soit fournie par la molécule de TbPc_2 qui accueille l'atome de cérium.

Après l'adsorption du Ce, l'électron excédentaire présent dans une molécule de TbPc₂ a de fortes probabilités d'interagir, voire d'être transféré vers le cérium, en accord avec les précédentes mesures de conductance.

Sur Au (111), une spectroscopie à haute résolution enregistrée sur l'atome de cérium au-dessus d'une molécule de type A révèle une résonance Kondo avec une température caractéristique de $T_k = 30$ K (voir Figure 5.8), cette résonance trouve son origine d'un couplage entre le magnétisme local du cérium et les électrons de la monocouche de TbPc₂ formée sur le substrat. Contrairement aux cas précédents de présence de résonance Kondo, ce pic n'est plus exclusivement localisé sur une région mais est délocalisé sur le ligand supérieur de la molécule. Ainsi, une résonance similaire (même largeur et amplitude) est observée sur les huit lobes observables par topographie d'une molécule CeTbPc₂ de *Type-A*.

L'impureté magnétique de cette interaction trouve son origine soit de l'électron non apparié provenant du ligand supérieur de la molécule, soit de l'électron f de la dernière couche remplie du cérium. Néanmoins, il semble plus probable que la seconde supposition soit la plus adaptée dans le cas présent considérant le fait que la température Kondo soit différente en comparaison au cas d'un domaine. L'information du spin pourrait dans ce cas être transférée au voisinage laissant apparaître une résonance Kondo sur les huit lobes.

De manière surprenante, cette résonance disparaît lorsque le cérium est déposé sur une molécule de *Type-B*. La raison d'un tel comportement reste à clarifier, toutefois, cet effet pourrait être causé par le fait que la distribution électronique de la molécule de *Type-B* a des zones de chevauchement avec les molécules voisines de *Type-A* (ce qui n'est pas le cas dans l'autre sens voir Figure 5.8). De plus, une spectroscopie tunnel effectuée au-dessus du cérium dans les deux cas montre un pic HOMO observable uniquement sur une molécule de *Type-A* confirmant cette théorie.

Le sixième chapitre de cette thèse présente un travail supplémentaire réalisé dans l'optique de comprendre la formation de molécules de FePc à partir d'une simple molécule de TCNB (1,2,4,5-Tetracyanobenzène) sur une surface de Au (111). Les premières expériences menées se sont focalisées sur la formation de monomères de Fe-4(TCNB) à travers un dépôt initial de TCNB suivi de l'évaporation d'atomes de Fe avec un ratio de 4:1. La spectroscopie dI/dV du film ainsi formé montre deux spectres distincts quand elle est enregistrée sur le Fe et sur la TCNB, les deux éléments montrent une réponse STS similaire à leur cas respectifs isolés sur le même substrat. Ceci indique qu'il n'y a pas, ou très peu, de changement au niveau électronique du Fe et de la TCNB.

Après un léger recuit (activation thermique), la topographie montre que l'atome de Fer crée une coordination avec ses 4 molécules de TCNB voisines pour former un monomère comme le montre la Figure 6.5. La spectroscopie tunnel sur ce nouveau complexe montre, contrairement au cas précédent, une localisation des états d_{z^2} au-dessus de l'atome de fer. Les calculs DFT confirment ces résultats où un transfert de charge de $-0.28|e^-|$ donné par le métal aux molécules de TCNB a été obtenu.

Lorsque le ratio du dépôt de fer est doublé et qu'il est suivi d'une activation thermique à 450K, un réseau uniforme de $\text{Fe}-(\text{TCNB})_2$ est obtenu comme montré dans la Figure 6.9. L'investigation STS sur ce nouveau système ressemble particulièrement au spectre observé sur une molécule de FePc au-dessus du même substrat. Ceci indique qu'un environnement électronique similaire est présent dans les deux cas. Néanmoins, le pic Kondo attendu sur la FePc n'apparaît pas sur la nouvelle structure de $\text{Fe}-(\text{TCNB})_2$ à cause d'un remplissage de l'orbitale d_{z^2} différent. En effet, les calculs DFT montrent que cette orbitale se trouve au-dessus de l'énergie de Fermi dans le réseau contrairement au cas de la FePc où elle est singulièrement occupée permettant ainsi la diffusion des électrons de conduction.

Un recuit supplémentaire à 550K du réseau de $\text{Fe}-(\text{TCNB})_2$ fait apparaître une formation de molécules d'Octacyano-FePc (voir Figure 6.11(b)) qui représente ainsi une étape de pré-polymérisation. L'énergie de liaison intermoléculaire est réduite, et les complexes montrent une monocouche de ce qui semble être des monomères isolés.

La spectroscopie STS enregistrée dans ce cas au-dessus du Fe révèle une résonance Kondo sur les Octaphthalo-FePc similaire à celle obtenue sur une FePc, indiquant la présence d'un moment magnétique et d'un état de spin similaire dans les deux structures. De ce fait, il a été possible via les expérimentations effectuées ici et de révéler la formation des molécules de FePc par un auto-assemblage d'atomes de fer et de molécules de TCNB sur une surface de Au (111). Cette procédure offre une méthode prometteuse pour l'interprétation des données spectroscopiques de molécules auto-assemblées similaires.

INTRODUCTION

In the last decades, electronic devices based on organic materials were progressively integrated into nanotechnologies thanks to the successful development with specific structural configuration of new materials. In this topic, the ability of π -conjugated elements to auto-assemble contribute to increase the performance of transistors. Formation of extended molecular networks on surfaces which work at room temperature constitutes a major breakthrough in the nanotechnology domain. Thus improving some properties such as energy conversion in solar cells or information storage.

Extended periodical molecular networks on surfaces necessitate the synthesis of hybrid nanostructure that depict appropriate functions with an atomic precision in order to satisfy a stable and easily reproducible systems. These networks are generally based on non-covalent bonding such as Van der Waals, hydrogen bond or metal-ligand coordination. Specific geometries and bond forces are necessary to allow the hierarchy of molecular bulks.

Auto-assembling on surface process is nowadays the most investigated procedure to the creation of novel organic or organo-metallic nanostructures. Particularly the auto-assembling obtained under ultra-high vacuum which depict very satisfying results when studied with microscopy techniques. On-surface synthesis of molecules with delocalized orbitals may allow the enhancement of the electronic transport such as for π -conjugated molecules.

The present Thesis is dedicated on the investigations on such derivative molecules based on metal-coordinated atom to an organic ligand. The document is separated in seven chapter as follows:

Chapter one gives a general introduction to the molecular magnetism. First principles and theoretical investigations are developed. The origin of anisotropy in single molecular magnets as well as their response to a magnetic field. The ligand field theory is also introduced because of its major role in the molecular magnetism in the studied structures. The

Kondo physics, which is a main quantum behavior observed in this research is introduced in this chapter and explained with a strong theoretical background. Its related liquid Fermi theory and Anderson model are presented. The Fano resonance leading to a description of the Kondo resonance at low temperatures is also introduced.

Chapter two introduces the scanning tunneling microscopy which is the main technique used in the experimental investigations. First, a theoretical background on the tunneling effect and its application to microscopy are given with explicit equations, the related spectroscopic investigations are also presented. Then, the experimental device is briefly presented, the ultra-high vacuum and various techniques used by the scanning tunneling microscope are briefly presented.

Chapter three concerns the main molecule a terbium double-decker (TbPc_2) used in the experiments, a general overview of the intrinsic characteristics and already communicated results are presented first. The structural and electronic properties of the complex are described and discussed in a second time. As the molecule was deposited on various substrates, the crystal effect on electronic and magnetic properties are investigated. At last, a Kondo resonance, which to our knowledge, has been poorly communicated in literature is presented and widely discussed, its origin is demonstrated by means of comparison of both, communicated and obtained results.

Chapter four is dedicated to the molecular domain construction. Similar to single molecule, various substrates were used for the molecular growth. Crystal nature is found to influence both, the molecular electronic properties and structural conformation. Interestingly, the lowest reactive substrate induces an internal geometrical modification thus, altering the electronic properties of initially similar structures these results are deeply discussed in this chapter. Similarly to isolated molecule, a Kondo resonance is observed on specific locations of the terbium double-decker monolayer. In order to understand its origin and link it to the Kondo observed in the previous chapter, a step-by-step four-molecule island construction is presented where the magnetic behavior is followed at each step. Further investigations related to the monolayer formation of molecule such as a second layer adsorption or the molecular density variation on different surfaces are presented and discussed.

Chapter five introduces a new complex where a cerium atom is deposited on top of a terbium double decker molecule. The geometry and electronic properties are widely investigated on Au (111), Ag (111) and Cu (111) substrates. A Kondo resonance which is

believed to be intrinsic to the new complex is observed on various locations of the structure. In order to understand the magnetism of this complex, theoretical calculations were performed accounting the substrate nature. The results analysis gives a good indications about the electronic properties and the molecular orbital distribution. An anti-ferromagnetic coupling between the two lanthanides is observed and discussed.

Specific manipulations on these molecules were performed where a removal of the added lanthanide is made possible when adsorbed on Cu (111). On Au (111) the manipulation process led to hide the lanthanide under the TbPc₂ monolayer, this is found reversible under specific conditions discussed in the dedicated section.

Chapter six is dedicated to a supplementary work which led to the publication of two papers in international scientific reviews. The work focused on the genesis of FePc molecule starting from a co-deposition of iron atoms and 1,2,4,5-Tetracyanobenzene molecules on metallic surface. The different steps of this formation are presented and discussed. In particular, theoretical investigations were performed which led to understand the genesis process that led the transformation of two isolated entities to form a unique molecule with coordination bonding.

SHORT THEORETICAL OVERVIEW

Traditionally metallic materials are suitable for the nano scale magnetism study. However their usage and versatility remain extremely limited. It is in the main research topics to find the best candidates that lead to the formation of extended self-assembled networks free of contamination and able to work at room temperature window. Therefore, a bottom-up approach is necessary to investigate on various elements whose usage is possible at larger scales. Hybrid single molecular magnets (SMMs) satisfy these conditions as they couple the magnetic properties of the metal with the low relaxation process thus, enhancing the molecular spin-orbit coupling.[1–3]

1.1 Single molecular magnets

Although pure organic SMM based only on s - and p -electrons have been reported[4–7], typical SMMs consist of a magnetic center formed by one or more metallic atoms which are surrounded by organo-based ligands. The magnetic elements might be either transition metals (such as Fe, Mn, Co...) or lanthanides (like Nd, Tb, Dy...).[8–11] By changing the geometry and nature of the ligand, the magnetic behavior of the SMM can be tuned and which shows controlled response to an external excitation such as a magnetic field. Furthermore, the network formation of these molecules on surfaces can be controlled in order to observe a desired 2D or 3D arrangement. By creating interacting SMM monolayers, it would be possible to investigate the inter-molecular interactions (exchange energy, magnetic coupling...etc).

Usually, molecular magnetism is sensitive to thermal excitation but below a certain tem-

perature, it can be possible to find its magnetism invariant. In this case, the system is said *blocked* below a *blockade temperature* T_B . These materials have a large high-spin ground state as well as a large easy-axis magnetic anisotropy, it creates an energy barrier Δ which is dominant when $T < T_B$. [12]

Since the first discovered SMM in 1980 [13], the investigations made in order to explain the magnetic behavior of this system are still intriguing. One of the most prominent result in these investigations is the study by Sessoli et al. where an exponential variation of the magnetic relaxation with respect to the temperature was found below T_B . [14] It is found to follow the equation below:

$$M(t) = M_0 \cdot (1 - e^{-\frac{t}{\tau}}), \quad (1.1)$$

where $M(t)$ is the magnetic variation with respect to the time, M_0 represents the initial magnetization and τ , the system relaxation time. τ depend on the anisotropy constant described by Néel-Arrhenius equation as below: [15, 16]

$$\tau = \tau_0 \cdot e^{\frac{\Delta}{k_B T}}, \quad (1.2)$$

where τ_0 represents a pre-exponential factor providing a quantitative measure of the time relaxation from the thermal phonon bath of the system, and Δ (the energy barrier) depend on the system composition and geometry, it holds for the magnetization reversal below T_B .

The energy barrier is calculated from the energy difference between the lowest lying level and the highest lying level as presented in Figure 1.1(a). The energy barrier has the following form:

$$\Delta = \hat{D} \cdot S_z^2, \quad (1.3)$$

\hat{D} is the axial anisotropy following the easy axis along S_z . [1]

Therefore, it is understood that the higher the energy barrier, the stronger the magnetization of the SMM. Designing the best molecule must then consider the largest high-spin ground state and the largest easy-axis magnetic anisotropy for the complex.

To this end, two possibilities emerge:

- Increasing the spin: by use of a larger amount of magnetic centers.
- Increasing the axial anisotropy: by selecting the suitable metals or finding a specific molecular geometry leading to enhance the easy axis anisotropy.

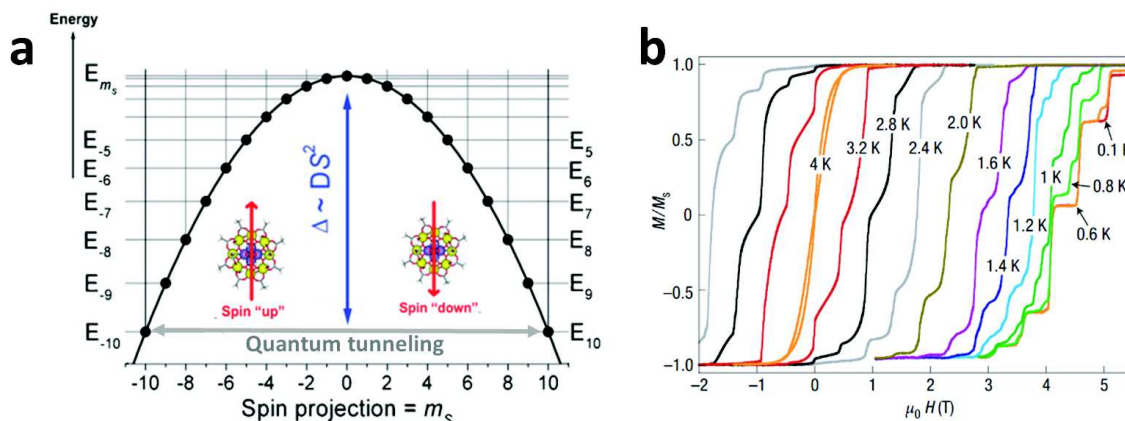


Fig. 1.1 a) [Mn-OAc] potential energy versus the projected magnetic spin on the sub-states of $S = 10$. Image was reproduced from [17] by permission from John Wiley & Sons Ltd. b) Temperature dependent hysteresis loops of single [Mn₁₂-*t*BuAc] crystals at constant field sweep rate of 2 mT/s. A series of steps are visible, they denote a resonant quantum tunnelling between energy levels. Below 0.6 K, the hysteresis becomes temperature independent. From [18]. Mn-OAc \equiv Mn₁₂O₁₂(CH₃CO₂)₁₆(H₂O)₄. Mn₁₂-*t*BuAc \equiv Mn₁₂O₁₂(O₂CCH₂C(CH₃)₃)₁₆(CH₃OH)₄

In both processes, care should be taken to keep the gap between the SMM's ground state and its first excited state as large as possible. Although recent reports show that these two parameters are correlated [19, 20], increasing the cluster/SMM anisotropy seem to be the most promising and easiest to investigate method.

Therefore, atoms containing a large spin-orbit coupling are preferred (lanthanides and transition metals have this kind of ability). An atom with a ground state S finds its orbitals degenerated through the spin-orbit coupling. Therefore the S components split in zero-field leading to a preferable orientation with a proportional amplitude of the total magnetization with respect to the anisotropic axis.

Magnetic switching between $|m_S\rangle = -S$ and $|m_S\rangle = +S$ is usually thermal dependent. However, as explained earlier, below T_B this reversal does not depend on the temperature. At these low temperatures, SMMs can relax through a supplementary process which is the quantum tunneling where the two states can be switched as presented in Figure 1.1(a). The quantum tunneling is made possible because of the existence of dipolar forces, hyperfine fields or a transverse anisotropy.

In the latter case, the presence of anisotropy does not allow the quantum tunneling to happen except if there is a perturbation field leading to a shift from one to another.

Therefore, magnetic behavior of the SMM can be expressed by its time dependent Hamilto-

nian:

$$H = \hat{D}.S_z^2 + \frac{\hat{E}}{2}(S_+^2 + S_-^2) + V, \quad (1.4)$$

where \hat{D} and \hat{E} are the axial and rhombic anisotropy tensors respectively, usually these tensors are diagonalized and the principle axis of the molecule would correspond to their eigenvalues. S_z and S_{\pm} are the spin operators of the system with units such as $\hbar = 1$ and $S_{\pm} = S_x \pm iS_y$. $V(t)$ represent a coupling with the magnetization moment of any external contribution to the Hamiltonian of the system. In the presence of an external magnetic field, V will describe the Zeeman effect generated by the magnetic field as $V \equiv \mu.S.B(t)$, where $B(t)$ represent the time dependent magnetic field and μ , the magnetic moment.[21, 22]

In order to obtain a non-zero magnetization of an SMM, the ground state of the molecule should correspond to the highest magnetization state of the molecule, and this can be possible only if \hat{D} is negative.[1] $\hat{D}.S_z^2$ represent the barrier height Δ . The presence of the second term in the right side of equation 1.4 allows the transition between the sub-states with a spin S in the sequence $| -S \rangle, | -S + 2 \rangle, | -S + 4 \rangle, \dots, | S - 2 \rangle, | S \rangle$. A magnetization reversal in a SMM would correspond to the climbing of $2S + 1$ energy levels as indicated in Figure 1.1(a).

If the anisotropy was neglected with the absence of a magnetic field B , the ground state system would be doubly degenerated. The magnetic moments will correspond to the two states where $m_S = +S$ and $m_S = -S$ as they are projected on the quantization axis. A small coupling will remain between $| +S \rangle$ and $| -S \rangle$ which is generated by the rhombic anisotropy \hat{E} . For a very large axial anisotropy $\frac{\hat{D}}{\hat{E}} \gg 1$ the two orientations will be separated by the energy barrier Δ which would then be responsible for the slow magnetic relaxation. Keep in mind, however, that at low temperature (below T_B) a soft relaxation remain due to the quantum tunneling through the barrier.

However, the particularity of SMMs is the presence of an anisotropy essentially due to the ligands. Therefore it leads to an internal state mixing where the parameters \hat{D} and \hat{E} govern the quantum tunneling properties of the SMM.

In the presence of an external magnetic field, the energy levels will be shifted with respect to each other lead to an alignment of levels at certain resonance fields. Therefore the spin can flip its orientation by direct quantum tunneling between the two states.

The quantum tunneling effect can be directly observed when varying the external field, while collecting the magnetization amplitude and direction of the SMM below T_B as presented in Figure 1.1(b). Where a hysteresis loop is observed for a Mn_{12} -*t*BuAc molecule. Interestingly, step-like features are observed on the molecular magnetic response, these steps

correspond to the resonant quantum tunneling between two states for certain magnetic field values. A decrease in temperature lead to the broadening of the hysteresis loop because of the lack in the thermal magnetization reversal, favouring the quantum tunneling which appears in this case with a well-defined and larger steps.

1.2 Ligand field theory

On coordination with other elements, the magnetic ion finds its orbitals modified due to the presence of an electric field. This effect is known as the Stark effect.[23, 24] In order to explain the magnetism of a SMM in an organo-metallic based complex, one needs to understand the role and the effect of the surrounding ligands on the unpaired spin carrier.

The ligand-field is a formalism distinguishing between the different interactions and couplings that contribute to the global cohesion of the elements in a given complex.[25, 26] It results in analytical identification of energies and molecular states. The ligand-field is strongly affected by the geometry as well as symmetry of the complex. Thus, the corresponding Hamiltonian H_{LF} can be formally written in the function of the electrostatic potential V in the near space of the complex as:

$$H_{LF}(r) = \sum_i V(r - R_i), \quad (1.5)$$

where R_i represents the position of the ion i of the complex. The electrostatic potential can be rather complicated when the system geometry is uncommon. Considering the cases of molecular magnets where the studied complex has a known symmetry, the Hamiltonian can be written using the Stevens formalism with the Abragam and Bleaney notations as:[27–29]

$$H_{LF} = \sum_{l=2,4,6} \sum_{m=-l}^{+l} B_l^m \cdot O_l^m = \sum_{l=2,4,6} a_l \sum_{m=-l}^{+l} A_l^m \cdot \langle r^k \rangle \cdot O_l^m, \quad (1.6)$$

where l and m are the operator orders, the first one must be an even integer because of the symmetry inversion of the crystal field potential and the second varies between $-l$ and $+l$. Here, $a_{2,4,6}$ are the Stevens equivalent operators for α , β and γ respectively. B_l^m and A_l^m are called ligand field parameters to be determined experimentally. O_l^m represents the Stevens main operators which are combination of the components of the J operator. O_l^m is proportional to the sub-space spherical harmonics of the field potential as following:[30]

$$\langle Jm_j | O_l^m | Jm'_j \rangle \propto \langle Jm_j | Y_l^m(\theta, \phi) | Jm'_j \rangle, \quad (1.7)$$

where $Y_l^m(\theta, \phi)$ represent the spherical harmonics obtained from the electrostatic potential V such as:

$$V(r) = \sum_{l=0}^{\infty} \sum_{m=-l}^{+l} a_l^m r^l Y_l^m(\theta, \phi). \quad (1.8)$$

The proportionality between O_l^m and Y_l^m is made possible through the Wigner-Eckart theorem[31, 32] which allows to write the spherical harmonics in a linear combination of the Stevens operators.

The complex symmetry allows to reduce the number of terms of 1.6 to a more simplified form. As an example, a C_4 symmetry leads to write H_{LF} as:

$$H_{LF}^{C_4} = \alpha A_2^0 \langle r^2 \rangle O_2^0 + \beta (A_4^0 \langle r^4 \rangle O_4^0 + A_4^4 \langle r^4 \rangle O_4^4) + \gamma (A_6^0 \langle r^6 \rangle O_6^0 + A_6^4 \langle r^6 \rangle O_6^4), \quad (1.9)$$

while a D_{4d} symmetry keeps only the terms with factor $m = 0$.

Application to lanthanide based complexes

For sake of simplicity and link to the main subject in this Thesis, a lanthanide Ln(III) is considered as the central ion in the magnetic complex and the system must be described by its global Hamiltonian which will be separated in four parts:

$$H = H_{LF} + H_{Ln} + H_{Zeeman} + H_{hyp} \quad (1.10)$$

The first term of the right hand side of 1.10 represents the Hamiltonian of the free lanthanide ion, the second term is the Ligand Field Hamiltonian of the complex as described above. The third term refers to the Zeeman effect which is a result of the ligand field on the orbitals of the lanthanide while the last term contains the hyperfine interaction.

The Hamiltonian of the free lanthanide is well described by both its internal kinetic energy, electron-electron repulsion and the spin-orbit coupling as follows:

$$H_{Ln} = \sum_i \left(\frac{\vec{P}_i^2}{2m} - \frac{Ze^2}{r_i} \right) + \sum_{i < j} \frac{e^2}{|r_i - r_j|} + \sum_i \delta_i \hat{l}_i \cdot \hat{s}_i, \quad (1.11)$$

where \vec{P}_i refers to the linear momentum of electron i , m the electron mass, Z the atomic number (number of electrons of the lanthanide), $r_{i,j}$ is the position of i^{th} (j^{th}) electron. \hat{l}_i, \hat{s}_i are the orbital and spin angular momentum operators of electron i and δ refer to the strength of the spin-orbit coupling.

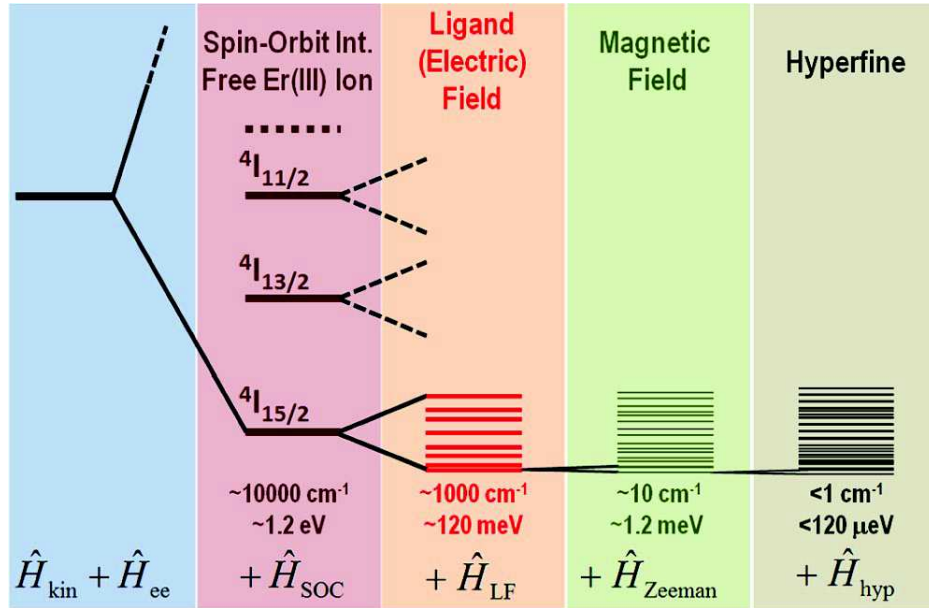


Fig. 1.2 Energy levels of the lowest-lying multiplets of a free Er(III). Each column depicts the effect of the specified term in 1.10. From [33]

Under the magnetic field created by the ligand-field, a Zeeman effect splits the $|m_j\rangle$ doublets and is described as:

$$H_{Zeeman} = g_j \cdot \mu_B \cdot \mu_0 \cdot J \cdot H, \quad (1.12)$$

where g_j is the Landé factor defined as: $g_j = (3/2) + (S(S+1) - L(L+1))/(2J(J+1))$.

The ground state multiplets of Er(III) is presented in Figure 1.2 where every effect in the terms of the Hamiltonian in 1.10 is depicted. Presence of f -electrons which are screened by the "internal" electrons leads to a high localization of these electrons.[33, 34]

The hyperfine term H_{hyp} is found to be mandatory on rare earth metals as it strongly couples the angular momentum \mathbf{J} of the lanthanide to its nuclear momentum \mathbf{I} . This interaction is of dipolar form and must be expressed as:

$$H_{hyp} = A_{hyp} \cdot \mathbf{J} \cdot \mathbf{I}, \quad (1.13)$$

with

$$\mathbf{J} \cdot \mathbf{I} = J_z I_z + \frac{1}{2}(J_+ I_- + J_- I_+), \quad (1.14)$$

where \mathbf{J} and \mathbf{I} describe the total angular momentum and the nuclear momentum of the lanthanide respectively. A_{hyp} represents the hyperfine constant. The term $J_z I_z$ thus splits the electronic states from the ground state doublet to nuclear spin states.

The hyperfine interaction may induce a off-diagonal terms of the total momentum and thus promote the quantum tunneling magnet of an SMM. If the magnetic element is a *Kramer ion* (has an odd number of electrons) a double-degeneracy of the electronic states occurs for half-integer spins because of Kramers theorem which would exclude any magnetization at $\mu_0 H = 0 T$. However for some complexes such as LnPc_2 the hyperfine interaction is, in contrary, promoting the magnetization.[33, 35, 36]

1.3 The Kondo effect

In order to introduce the Kondo effect, some basics of the quantum physics related to the Kondo effect will be briefly presented. The liquid Fermi theory which is a theory developed to understand the behavior of liquid ^3He will be first presented, followed by Jun Kondo's approach to explain the electron scattering by a magnetic impurity at the Fermi energy and its related Anderson model which completes this approach. Finally the Fano resonance which is a theoretical approach to a scattering resonance which is applied to a Kondo effect will be briefly presented.

1.3.1 Liquid Fermi theory

The understanding of electric characteristics of a metal is simplified when considering the electrons as a non-interacting bodies (free electron model). Sommerfeld development led to the formulation of the free-electron model where the particles are treated as quantum particles governed by the Schrödinger equation.[37] In a metal the ground state of the system is filled with N -particles (fermions) up to the Fermi energy which is defined as the energy of the highest occupied state in the metal. In another words, it is the maximal kinetic energy of the occupied state of the metal. At this level, are defined \vec{k}_F : the Fermi wave vector and \vec{P}_F : its corresponding Fermi vector such as:

$$\vec{P}_F = \hbar \vec{k}_F \implies \varepsilon_F = \frac{P_F^2}{2m} = \frac{\hbar^2 k_F^2}{2m}, \quad (1.15)$$

ε_F defines the Fermi-energy where all states below its related \vec{P}_F are occupied.

In a 3D expansion, the particle density in a Fermi volume V_F which is defined as the space

containing all particles with energy lower than ε_F takes the following form:

$$\frac{N}{V_F} = \frac{P_F^3}{3\pi^2\hbar^3}. \quad (1.16)$$

Since the problem deals with fermions, the average occupation of the states with respect to the temperature is given by the Fermi-Dirac distribution [38, 39]

$$n(\varepsilon) = \frac{1}{e^{\beta(\varepsilon-\mu)} + 1}, \quad (1.17)$$

where $\beta = 1/(k_B \cdot T)$ and k_B is the Boltzmann constant, μ represents the chemical potential of the system.

Therefore, the density of states $g(\varepsilon)$ is of the form:

$$\frac{N}{V} = \int_0^\infty g(\varepsilon)n(\varepsilon)d\varepsilon \quad \Longrightarrow \quad g(\varepsilon) = \frac{dN/V}{d\varepsilon} = \frac{1}{2\pi^2} \cdot \left(\frac{2m}{\hbar^2}\right)^{3/2} \cdot \sqrt{\varepsilon}. \quad (1.18)$$

However, the approach above has serious limitations when a more realistic model is considered. In fact, the particles in such a system interact between each others creating the well-known and unsolved many-body problem.[40] Hopefully, Landau dressed a simple phenomenological *Fermi liquid theory* to the problem when the system is considered at low temperatures and low excitation energies.[41, 42] Indeed, during the collision process, a momentum transfer occurs between the particles. By considering the ideal gas where all states with $|\vec{P}| < |\vec{P}_F|$ are filled and adding a supplementary single state at $|\vec{P}| \gg |\vec{P}_F|$, the total system becomes excited with the following energy:

$$\varepsilon_P - \varepsilon_F = \frac{P^2}{2m} - \varepsilon_F \approx \frac{\vec{P}_F}{m}(\vec{P} - \vec{P}_F), \quad (1.19)$$

This approximation is valid if $|\vec{P}| - |\vec{P}_F| \ll |\vec{P}_F|$ ($|\vec{P}|$ close to $|\vec{P}_F|$). At weaker interactions, 1.19 remains almost valid in a way that the excitation energy is proportional to $|\vec{P}| - |\vec{P}_F|$.

In his Fermi-liquid theory, Landau posed three conditions:

- The particle's excitation spectrum remains similar as for the free-electron gas theory.
- A new particles have to be assumed and defined as *quasi-particles*
- These quasi-particles have a long life-time at low energy ($\tau \propto \frac{1}{\varepsilon - \varepsilon_F}$), which is valid at low temperatures and energies close to ε_F

Therefore it becomes necessary in order to satisfy 1.19 to define an effective mass m^* for the quasi-particles such as:

$$\varepsilon_P - \varepsilon_F = \frac{P_F}{m^*}(P - P_F). \quad (1.20)$$

As discussed earlier, the interactions are represented by hidden variable(s) in m^* . Formally, in Landau's formalism, the effective mass has the following form when it is re-normalized:¹

$$\frac{m^*}{m} = 1 + \frac{F_1^s}{3}, \quad (1.21)$$

where F_1^s is symmetric Landau parameter.[44]

The Fermi-liquid theory is applied to calculate several measurable properties of a Fermi-like liquid system such as specific heat of the metal C , the magnetic susceptibility χ or the metal resistivity R : [45]

$$C = \frac{\pi^2}{3} \cdot g(\varepsilon_F) k_B^2 T + O(T^2), \quad \chi = \mu_B \mu^2 \frac{g(\varepsilon_F)}{1 + F_0^a}, \quad R = R_0 + A \cdot T^2, \quad (1.22)$$

where $O(T^2)$ indicates a negligible Taylor development at the second order. μ_B and μ are the Bohr magneton and the particle's magnetic moment respectively. F_0^a is an anti-symmetric Landau parameter. R_0 is the residual resistivity of the system and A a factor satisfying the relation $A \propto \frac{C}{T} \equiv \gamma^2$.

Since all these parameters are proportional to the density of states $g(\varepsilon_F)$, a relations containing such parameters hold such as the Sommerfeld-Wilson ratio Γ : [46]

$$\Gamma = \frac{\pi^2 k_B^2}{3 \mu_b \mu_m^2} \cdot \frac{\chi}{\gamma} = \frac{1}{1 + F_0^a}. \quad (1.23)$$

The Fermi-liquid theory is the basic model to describe the non-superfluid Fermi liquid. It can however be generalized to systems other than ^3He for which it was originally made. Moreover it holds for both normal- and super-conducting materials even for extreme cases such as heavy fermions systems.

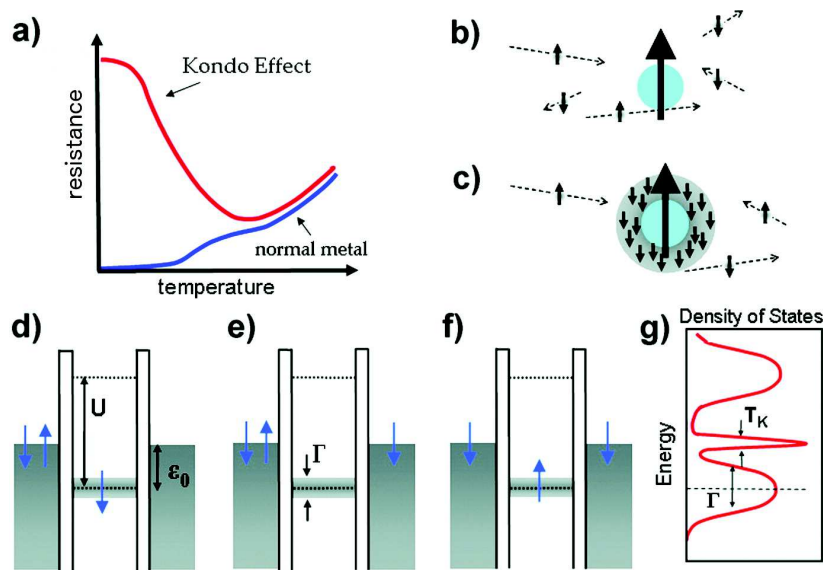


Fig. 1.3 a) Resistance versus temperature for both "classic" metals (blue) and those depicting a minimum resistance at a non-zero temperature (red). b) and c) Magnetic impurity surrounded by conduction electrons above and below the minimum resistance temperature. d-f) Initial, virtual and final state at the tunneling process where a Kondo resonance appears. g) Density of states with respect of the tunneling electron energy. The peak showing T_K appears at the Fermi level. From [47](modified)

1.3.2 Kondo approach

In regular cases, a metal's resistivity decreases with respect to the temperature. Indeed, the electrical resistivity of a metal is dominated by the electron-phonon scattering at room temperature. By lowering the thermal energy, the phonons will be "frozen" and the particles will have lower kinetic energy. Thus, electrons will have a longer diffusion path which results in an increase of the conductivity.

However, in the early 1930's for the first time, Messner et al. followed later by Haas et al. performed a conductance measurements on doped metals with transition atoms where a surprising increase of the resistance is observed at low temperatures, a resistance minima at non-zero temperature was observed as highlighted in Figure 1.3(a).[48, 49] For more than 30 years, scientists had no explanation for such a behavior of these materials. In 1964, Jun Kondo proposed the first quantitative approach to this observation where he conducted a development at the second order of the perturbation theory applied to the Hamiltonian of the system.[50]

His findings led to the observation of the existence of a resistance minima at a non-zero

¹The reader is referred to [43] for the analytical details.

temperature so-called Kondo temperature and noted T_K .

The presence of a magnetic impurity in the material led Kondo to assume that the dopant acts as a diffusion center of the conduction electrons, which are responsible for the presence of the material's conductance. He developed a Hamiltonian of the system as:[43]

$$H = H_{conduction} + H_{exchange} \quad (1.24)$$

The Hamiltonian as proposed by Kondo describes the scattering of the conduction electrons of the metal by the magnetic impurity. As a result, the general transport properties of the material expresses the material conductivity as :

$$\rho = \rho_0 + A.T^5 + BJ.log(T/C), \quad (1.25)$$

where A, B, and C are constants proper to the system.

The conductance expression in 1.25 combines both high and low temperature conductance behavior. At high temperatures, the term containing T^5 dominates the global conductivity thanks to the phonon scattering while the logarithmic term dominates the low temperature behavior of the system, see Figure 1.3(b-c).

This approach is no more valid below a certain temperature which is the same as T_K . [43, 50] Therefore, 1.25 is only in good agreement with experiment when a strong coupling is present and lead to $T \gg T_K$, it can also be extended to the neighbourhood of T_K . However it does not explain the conductivity behavior when $T \rightarrow 0$ at anti-ferromagnetic coupling ($J < 0$) as the resistivity diverges. This non-physical result became then known as the *Kondo problem*.

It is in 1975 where Kenneth G. Wilson gave a solution to the problem using the theory of numerical renormalization group (NRG) for a single spin impurity $S = 1/2$ including the Anderson approach (see next subsection). He found that below T_K a spin flip scattering occurs in the majority of the collision events at the impurity which leads to a complete screening of the magnetic center by the conduction electrons at $T \rightarrow 0$.

1.3.3 Anderson model

Few years before the Kondo formalism, in 1961, P. W. Anderson described the maintain of magnetic properties in transition metal impurities when embedded into a metal.[51] Since

the Coulomb interaction is weakly screened on a local basis at the atomic scale, the unfilled orbitals are suppressed at integer fillings, and the total angular momentum is defined by the orbital filling according to Hund's rule.

In Anderson's model, the development was limited to only one degenerate d -level which is filled by one or two electrons. At the singly occupied level d^1 , the magnetic moment lies below the Fermi level ε_F at energy ε . In the case where a second electron is added, it must populate the same orbital as the first electron, and thus obtains an opposite spin because of the Pauli principle. Adding a second electron will therefore increase the energy by a Coulomb repulsion U . The doubly occupied orbital d^2 must therefore lie above ε_F to ensure an unpaired spin and retain the magnetic moment of the impurity.

Later on, in 1966, a link between the Anderson model of magnetic impurity and the Kondo approach for the magnetic diffusion was made thanks to J. R. Schrieffer and P. A. Wolff.[52] They introduced a canonical transformation in the limit of small $s-d$ hybridization to generate an effective Kondo Hamiltonian for low energies. In this picture, the magnetic impurity in the Anderson model is equivalent to the scattering process described by Kondo, plus, an exchange coupling J between the impurity spin and these electrons must be responsible for the perturbation.

Therefore, the Hamiltonian of this system must be written separated in three as:

$$H = H_{conduction} + H_{impurity} + H_{coupling}, \quad (1.26)$$

where

$$H_{conduction} = \sum_{\vec{k}\sigma} \varepsilon_{\vec{k}} \cdot a_{\vec{k}\sigma}^\dagger \cdot a_{\vec{k}\sigma}, \quad (1.27)$$

represents the Hamiltonian of conduction electrons of energy ε at wave vector \vec{k} and a spin σ describing the non interacting particles in an ideal gas, this term does not take into account the presence of the impurity. $a_{\vec{k}\sigma}^\dagger$ ($a_{\vec{k}\sigma}$) is the operator that generates (destroys) a conduction electron with a wave vector \vec{k} and a spin σ .

The second term,

$$H_{impurity} = \sum_{\sigma} \varepsilon^d \cdot C_{\sigma}^\dagger \cdot C_{\sigma} + U_{n_d \uparrow n_d \downarrow}, \quad (1.28)$$

represents the unperturbed energy of a d -state of the magnetic impurity. ε^d is the energy of one-electron located at the d -orbital. C_{σ}^\dagger (C_{σ}) represent the creation (destruction) operator for a spin σ . This notation accounts for a singly occupied d -orbital level positioned below the Fermi level (ε_F). A second electron of opposite spin would occupy the same level as the Pauli repulsion principle allows it, however a Coulomb repulsive interaction U is added

to the system. Therefore, the second electron of opposite spin can only occupy states at $\epsilon^d + U$ creating a net magnetic moment of the impurity as long as this level remains above ϵ_F . Although local charge fluctuations on the d -level are impossible due to the low temperature regime, a virtual exchange between the d -electrons and the conduction electrons may occur, leading to a spin-flip process.

This equation remains valid of d - states electrons, however, it can be easily generalized to a more realistic models describing $3d$ - and $4f$ -electrons where more than one orbital is considered. The generalized Hamiltonian of such systems can be expressed as following:[53]

$$H_{impurity}^{generalized} = \sum_{\sigma} \epsilon^i \cdot C_{\sigma}^{\dagger} \cdot C_{\sigma} + \sum_{klmn}^{\sigma\sigma'} U_{klmn} C_{k\sigma}^{\dagger} C_{l\sigma'}^{\dagger} C_{m\sigma'} C_{n\sigma}, \quad (1.29)$$

where the variable i represents the considered d - or f -shell and U_{klmn} the direct and exchange Coulomb matrix elements.

The last term of the right hand side of 1.26 represents the transition process between the conduction electrons and the magnetic impurity. It is derived from the simple Heisenberg expression $H_{coupling} = J \cdot \vec{S} \cdot s$, its formal expression is as follows:

$$H_{coupling} = \frac{J}{2N} \sum_{kk'} \left[(a_{k'\uparrow}^{\dagger} a_{k\uparrow} - a_{k'\downarrow}^{\dagger} a_{k\downarrow}) S_z + (a_{k'\uparrow}^{\dagger} a_{k\downarrow} S^- - a_{k'\downarrow}^{\dagger} a_{k\uparrow} S^+) \right], \quad (1.30)$$

where J represents the amplitude of the exchange interaction which is antiferromagnetic ($J < 0$) in order to create a diffusion process and N the number of impurity atoms. s is the spin density operator of the conduction electrons and S denotes the spin operator with the z -component S_z and S_{\pm} the raising and lowering operators of S .

$H_{coupling}$ term describes therefore both the spin-conserving process through the S_z expression and the spin-flip scattering process through S_{\pm} . S_+ (S_-) will change the spin of the magnetic impurity from down to up (or *vice-versa*) while $a_{k'\uparrow}^{\dagger} a_{k\downarrow}$ will flip the spin of the conduction electron from down to up (or *vice-versa*).

The exchange coupling J is derived from the Schrieffer-Wolff transformation where it is expressed by terms of hybridization matrix element $V_{\vec{k}}$ as:[53]

$$J_{\vec{k}\vec{k}'} = -V_{\vec{k}}^* V_{\vec{k}'} \left(\frac{1}{\epsilon_{\vec{k}} - (\epsilon^d + U)} + \frac{1}{\epsilon_{\vec{k}'} - (\epsilon^d + U)} - \frac{1}{\epsilon_{\vec{k}} - \epsilon^d} - \frac{1}{\epsilon_{\vec{k}'} - \epsilon^d} \right), \quad (1.31)$$

where \vec{k} and \vec{k}' represent the wave vectors of the initial and final state respectively.

For a constant hybridization at the d -shell (which is applicable for a closed system with no external contribution), $V_{\vec{k}}^* V_{\vec{k}'} = |V_{\vec{k}}|^2 = V^2$, the conduction band energies $\epsilon_{\vec{k}}$ which are close to the Fermi level can also be neglected. Therefore 1.31 becomes:

$$J_{\vec{k}\vec{k}'} \equiv J = -\frac{2V^2.U}{\epsilon^d(\epsilon^d + U)} \quad (1.32)$$

When applying the perturbation theory at the many-body system in the Hamiltonian of 1.26, the minimum resistance is found at the Kondo temperature T_K . It is found to be dependent on the exchange coupling J and the density of states of the host metal electrons $g(\epsilon)$ through the following relation:

$$T_K \approx \frac{\epsilon_F}{k_B} . e^{-1/(|J|.g(\epsilon))}, \quad (1.33)$$

where k_B represents the Boltzmann constant. It is interesting to see that the Kondo temperature is increased along with the coupling exchange and/or the density of states of the conduction electrons.

1.3.4 Fano resonance

Anderson model presented above describes the system of one magnetic atom embedded in a bulk. The resulting Kondo effect is therefore influenced by the surrounding environment of the impurity. When the conductance of these impurities is measured by a scanning tunneling spectroscopy, different behavior is observed since the environment is modified by the presence of a second electrode (tip).

In a tunneling regime where electron is transferred from tip (surface) to surface (tip), two channels for the tunneling electrons are possible², either the electron is transferred through the Kondo resonance close to ϵ_F with a probability T_1 , or the exchange may occur directly between the tip and the metal substrate without involving the impurity with a probability T_2 . In both cases, the spin information is conserved and no spin-flip process occurs. Therefore, an interference in the incident electronic wave-function between the two systems may occur.[54, 55]

The Fano resonance theory was originally developed to describe the electron-atom resonant scattering.[54] One particularity of the Fano resonance is that the resonant channel have a phase shift that depends on the energy of the incoming electrons which varies between $-\frac{\pi}{2}$ and $\frac{\pi}{2}$. The non-resonant channel has in contrary, its phase-shift energy independent from

²For the theory of tunneling currents refer to Chapter 2

the incoming electron energy. Thus, the resonance amplitude of the system is only dependent on the incoming electrons represented by their initial states.

The total Hamiltonian of the system can then be re-written by adding a term

$$\sum_{\sigma} \varepsilon_{ip} (C_{\sigma}^{\dagger} C_{\sigma} + \hat{M}[T_1; T_2])$$

to 1.26. Here, ε_F is the tip state energy. $\hat{M}[T_1; T_2]$ represents the matrix elements of the tunneling procedures through the two channels which can be simplified to represent a transition operator \mathbf{M} between the initial and final state, $|\Phi_i\rangle$ and $|\Phi_f\rangle$ respectively. The total tunneling probability can then be described as $|\langle\Psi|\mathbf{M}|\Phi_i\rangle|^2$ where $|\Psi\rangle$ represents the total state of the system.

In his approach, Fano considered the problem as a scattered electrons by an unperturbed continuum bath which is represented by $|v\rangle$. Therefore he found that the ratio between the total transition probability and the probability of transition to the metal follows a simple function as:[54]

$$\frac{|\langle\Psi|\mathbf{M}|\Phi_i\rangle|^2}{|\langle v|\mathbf{M}|\Phi_i\rangle|^2} = \frac{(q + \tilde{\varepsilon})^2}{1 + \tilde{\varepsilon}^2}, \quad (1.34)$$

where the normalized energy $\tilde{\varepsilon}$ is calculated from the Kondo resonance energy ε_K and the resonant peak width at half maximum Γ as :

$$\tilde{\varepsilon} = \frac{\varepsilon - \varepsilon_K}{\hbar\Gamma/2}, \quad (1.35)$$

which therefore gives a quantitative contribution of the electrons tunneling into the Kondo state, close to ε_F .

The factor q in 1.34 is called the asymmetry parameter which plays a critical role in the shape of the plotted Fano equation. It is defined as:

$$q^2 = \frac{1}{\pi\Gamma/2} \cdot \frac{|\langle\Lambda|\mathbf{M}|\Phi_i\rangle|^2}{|\langle v|\mathbf{M}|\Phi_i\rangle|^2}, \quad (1.36)$$

where $|\Lambda\rangle$ represent the discrete states of the system.

Although this factor is hardly predictable theoretically, it can be however determined by considering it as a variable in a Fano plot from the experimental Kondo resonance investigations.

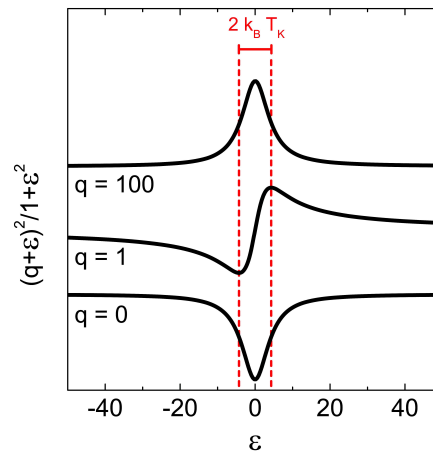


Fig. 1.4 Simulated Fano equation 1.34 for q -factor=0,1,100. From ref [55]

The role of the q factor lays mainly in the determination of the tunneling channel at the resonant electron transfer. For tunneling electrons through the Kondo resonance, the numerator of 1.36 is dominant, which implies $q \gg 1$ which results in a symmetric Breit-Wigner peak shape for the resonance.[56] On the other hand, when the denominator of 1.36 is dominant (*i.e.* $q \ll 1$) the tunneling occurs through the bulk continuum states, its resonance becomes a symmetric dip-like shaped. Intermediate states of q create an asymmetric shape as presented in Figure 1.4.

1.3.5 π -Kondo resonance

The Kondo effect as explained above is induced by the interaction between a magnetic impurity and the conduction electrons of the bulk. However, in 2004, the first purely organic molecule was reported to show a Kondo resonance when adsorbed on a substrate[57]. Multiple other organic molecules were reported with a similar property after that.[47, 58–60] To explain this observation, one needs to go back to the definitions in the above models. When embedded into a bulk metal, the magnetic impurity and the conduction electrons form the many-body system where a conduction electron may pair up with the impurity spin. However, because of the Pauli principle, these two spins are shifted with a coulomb energy. At low temperatures, this conduction electron may develop a polarization at the magnetic impurity, thus quenching the magnetic moment, this process serves as a screening of the impurity unpaired spin leading to a scattering of the conduction electrons (Kondo resonance).

In the case of purely organic molecules, the atoms are not supposed to carry a magnetic moment. However, when exposed to a free electron bath, this molecule is able to be charged by means of electron transfer from the electron sea. After adsorption of such a molecule on a metal substrate for example, the organic molecule is found to possess a spin $1/2$ ground state due to the localization of the unpaired electron in the lowest unoccupied orbital. A Kondo resonance in organic molecules is therefore only possible if a charge reorganization at the molecule occurs.

One interesting result of such a resonance is that the π -orbitals of the molecule are extended. Therefore, the presence of a Kondo resonance may be also delocalized on the molecule. This has to be contrasted with the magnetic impurity resonance where the Kondo is perfectly localized at the magnetic impurity.

Therefore, growing a film would lead to a spatially extended Kondo resonance on the molecular layer. Some works highlighted this behavior, for example Fernandez-Torrente et al. have shown a Kondo resonance on a full monolayer of TCNQ molecules adsorbed on a Au (111) substrate. A charging of the molecule to TCNQ^- is mainly possible because of a high decoupling of the molecular film from the underlying substrate.[59] In contrast, R. Frisenda et al. reported a slightly different Kondo resonance on a PTM-radical where they observed an insensitive resonance toward the modification of the host-environment. It indicates a fully intrinsic Kondo resonance at the radical without a need of charge transfer from the substrate. This is made possible because of the presence of an unpaired electron at the radical center.[60]

1.4 Summary

In this chapter, a brief theoretical overview to the single molecular magnetism was introduced. The possibility for single molecular magnet to proceed a spin flip below the blockade temperature T_B through quantum tunneling was explained.

In a second part, the ligand-field theory was introduced in order to understand the effect of ligands in molecular complexes. It was found that both the ligand nature and the molecular symmetry play a prominent role in the orbital modification of the magnetic ion. Its application to lanthanide ions highlighted a non negligible contributions of the Zeeman effect and the hyperfine interaction.

Finally, the Kondo effect was presented by two complementary approaches to charac-

terize the nature of the zero bias peak (ZBP). A Kondo effect describes the screening of conduction electrons by a localized magnetic moment at an impurity site. The interaction between the free electrons and the impurity magnetic moment is of anti-ferromagnetic type, which leads to a resonant peak of differential conductance at the Fermi level. As a result, a minimum resistance is observed at a non-zero temperature noted T_K .

To approach the Kondo problem, the liquid Fermi theory was recalled, the Anderson model was used to complete Kondo's approach to the electron screening and finally the Fano resonance was introduced in order to fit the experimental observations of this Kondo peak.

Another type of Kondo resonance was also briefly mentioned, there exists a possibility for a purely organic molecule to depict a magnetic resonance, leading to the detection of a Kondo peak.

Although the Kondo resonance can be measured by various techniques, the scanning tunneling spectroscopy remains to-date the best tool sensitive enough to detect the singly occupied orbitals below the Fermi-energy as well as the nearest empty state. For the experimental work of this thesis, a scanning tunneling microscope was used to investigate various molecules. Its principle and characteristics are presented in the next chapter.

REFERENCES

- [1] Lapo Bogani and Wolfgang Wernsdorfer. Molecular spintronics using single-molecule magnets. *Nature materials*, 7(3):179–186, 2008.
- [2] Richard A. Layfield. Organometallic single-molecule magnets. *Organometallics*, 33(5):1084–1099, 2014.
- [3] S. A. Wolf, D. D. Awschalom, R. A. Buhrman, J. M. Daughton, S. von Molnár, M. L. Roukes, A. Y. Chtchelkanova, and D. M. Treger. Spintronics: a spin-based electronics vision for the future. *Science (New York, N.Y.)*, 294(5546):1488–1495, 2001.
- [4] S. J. Blundell and F. L. Pratt. Organic and molecular magnets. *Journal of Physics: Condensed Matter*, 16(24):R771–R828, 2004.
- [5] Kunio Awaga, Tadashi Sugano, and Minoru Kinoshita. ESR evidence for the ferro- and antiferro-magnetic intermolecular interaction in pure and dilute mixed crystals of galvinoxyl. *Chemical Physics Letters*, 128(5-6):587–590, 1986.
- [6] Jeremy M. Rawson and Fernando Palacio. Magnetic properties of thiazyl radicals. In Jaume Veciana, D. Arçon, M. Deumal, K. Inoue, M. Kinoshita, J. J. Novoa, F. Palacio, K. Prassides, J. M. Rawson, and C. Rovira, editors, *p-Electron Magnetism*, volume 100 of *Structure and Bonding*, pages 93–128. Springer Berlin Heidelberg, Berlin, Heidelberg, 2001.
- [7] B. Narymbetov, A. Omerzu, V. V. Kabanov, M. Tokumoto, H. Kobayashi, and D. Mihailovic. Origin of ferromagnetic exchange interactions in a fullerene-organic compound. *Nature*, 407(6806):883–885, 2000.
- [8] Daniel N. Woodruff, Richard E. P. Winpenny, and Richard A. Layfield. Lanthanide single-molecule magnets. *Chemical reviews*, 113(7):5110–5148, 2013.

- [9] Cristiano Benelli and D. Gatteschi. *Introduction to molecular magnetism: From transition metals to lanthanides / Cristiano Benelli and Dante Gatteschi*.
- [10] Jinkui Tang and Peng Zhang. *Lanthanide single molecule magnets*. Springer, Heidelberg, 2015.
- [11] Richard A. Layfield and Muralee Murugesu. *Lanthanides and actinides in molecular magnetism*.
- [12] Shutaro Osa, Takafumi Kido, Naohide Matsumoto, Nazzareno Re, Andrzej Pochaba, and Jerzy Mrozinski. A tetranuclear 3d-4f single molecule magnet: $[\text{Cu}^{\text{II}}\text{LTb}^{\text{III}}(\text{hfac})_2]_2$. *Journal of the American Chemical Society*, 126(2):420–421, 2004.
- [13] T. Lis. Preparation, structure, and magnetic properties of a dodecanuclear mixed-valence manganese carboxylate. *Acta Crystallographica Section B Structural Crystallography and Crystal Chemistry*, 36(9):2042–2046, 1980.
- [14] R. Sessoli, D. Gatteschi, A. Caneschi, and M. A. Novak. Magnetic bistability in a metal-ion cluster. *Nature*, 365(6442):141–143, 1993.
- [15] Louis Néel. Théorie du trainage magnétique des ferromagnétiques au grains fin avec applications aux terres cuites. *Ann. Géophys.*, 5:99–136, 1949.
- [16] Svante Arrhenius. *Über die Reaktionsgeschwindigkeit bei der Inversion von Rohrzucker durch Säuren*. Wilhelm Engelmann, Leipzig, 1889.
- [17] Guillaume Rogez, Bertrand Donnio, Emmanuel Terazzi, Jean-Louis Gallani, Jean-Paul Kappler, Jean-Pierre Bucher, and Marc Drillon. The quest for nanoscale magnets: The example of $[\text{Mn}_{12}]$ single molecule magnets. *Advanced materials (Deerfield Beach, Fla.)*, 21(43):4323–4333, 2009.
- [18] W. Wernsdorfer, M. Murugesu, and G. Christou. Resonant tunneling in truly axial symmetry Mn_{12} single-molecule magnets: sharp crossover between thermally assisted and pure quantum tunneling. *Physical review letters*, 96(5):057208, 2006.
- [19] Eliseo Ruiz, Jordi Cirera, Joan Cano, Santiago Alvarez, Claudia Loose, and Jens Kortus. Can large magnetic anisotropy and high spin really coexist? *Chem. Commun.*, (1):52–54, 2008.
- [20] Oliver Waldmann. A criterion for the anisotropy barrier in single-molecule magnets. *Inorganic chemistry*, 46(24):10035–10037, 2007.

- [21] C. A. Dartora, G. G. Cabrerat, and K. Z. Nobrega. The spin dynamics of molecular magnets beyond kubo's linear response theory. *Brazilian Journal of Physics*, 39(3):587–591, 2009.
- [22] W. Wernsdorfer, S. Bhaduri, C. Boskovic, G. Christou, and D. N. Hendrickson. Spin-parity dependent tunneling of magnetization in single-molecule magnets. *Physical Review B*, 65(18), 2002.
- [23] Johannes Stark. *Beobachtungen über den Effekt des elektrischen Feldes auf Spektrallinien*, volume XLVII, 1913 of *Sitzungsberichte der königlich preussischen Akademie der wissenschaften*. [S.D.], [S.1.], 1913.
- [24] J. Stark. Beobachtungen über den effekt des elektrischen feldes auf spektrallinien. i. quereffekt. *Annalen der Physik*, 348(7):965–982, 1914.
- [25] Hans Albrecht Bethe. *Splitting of terms in crystals: Complete Engl. transl.* Consultants Bureau, New York, 1958, [1958].
- [26] J. H. van Vleck. Theory of the variations in paramagnetic anisotropy among different salts of the iron group. *Physical Review*, 41(2):208–215, 1932.
- [27] K. W. H. Stevens. Matrix elements and operator equivalents connected with the magnetic properties of rare earth ions. *Proceedings of the Physical Society. Section A*, 65(3):209–215, 1952.
- [28] Lorenzo Sorace, Cristiano Benelli, and Dante Gatteschi. Lanthanides in molecular magnetism: old tools in a new field. *Chemical Society reviews*, 40(6):3092–3104, 2011.
- [29] Jinkui Tang and Peng Zhang. *Lanthanide Single Molecule Magnets*. Springer Berlin Heidelberg, Berlin, Heidelberg, 2015.
- [30] Anna-maria Kiss. *Multipolar ordering in f-electron systems*. PhD thesis, 2004.
- [31] E. Wigner. Einige folgerungen aus der schrodingerschen theorie fur die termstrukturen. *Z. Physik (Zeitschrift fur Physik)*, 43(9-10):624–652, 1927.
- [32] Carl Eckart. The application of group theory to the quantum dynamics of monatomic systems. *Reviews of Modern Physics*, 2(3):305–380, 1930.

- [33] J. Dreiser. Molecular lanthanide single-ion magnets: from bulk to submonolayers. *Journal of physics. Condensed matter : an Institute of Physics journal*, 27(18):183203, 2015.
- [34] Hong Jiang, Ricardo I. Gomez-Abal, Patrick Rinke, and Matthias Scheffler. Localized and itinerant states in lanthanide oxides united by GW @ LDA+U. *Physical review letters*, 102(12):126403, 2009.
- [35] Naoto Ishikawa, Miki Sugita, and Wolfgang Wernsdorfer. Quantum tunneling of magnetization in lanthanide single-molecule magnets: bis(phthalocyaninato)terbium and bis(phthalocyaninato)dysprosium anions. *Angewandte Chemie (International ed. in English)*, 44(19):2931–2935, 2005.
- [36] Naoto Ishikawa, Miki Sugita, and Wolfgang Wernsdorfer. Nuclear spin driven quantum tunneling of magnetization in a new lanthanide single-molecule magnet: bis(phthalocyaninato)holmium anion. *Journal of the American Chemical Society*, 127(11):3650–3651, 2005.
- [37] Albert Messiah. *Quantum mechanics*. Dover Publications, Mineola N.Y., 1999.
- [38] P. a. M. Dirac. On the Theory of Quantum Mechanics. *Proceedings of the Royal Society of London A: Mathematical, Physical and Engineering Sciences*, 112(762):661–677, October 1926.
- [39] Alberto Zannoni. On the Quantization of the Monoatomic Ideal Gas. *arXiv:cond-mat/9912229*, December 1999. arXiv: cond-mat/9912229.
- [40] N. H. March, W. H. Young, and S. Sampanthar. *The many-body problem in quantum mechanics*. Dover and London : Constable [distributor], New York, 1995.
- [41] Lev Davidovitch Landau. The theory of a fermi liquid. *Sov. Phys. JETP*, 3:920–925, 1957.
- [42] Lev Davidovitch Landau. Oscillations in a fermi liquid. *Sov. Phys. JETP*, 5:101–108, 1957.
- [43] A. C. Hewson. *The Kondo problem to heavy fermions*, volume 2 of *Cambridge studies in magnetism*. Cambridge University Press, Cambridge, [new ed.] edition, 1997, 1993.
- [44] Gordon Baym and Christopher Pethick. *Landau Fermi-Liquid Theory*. Wiley-VCH Verlag GmbH, Weinheim, Germany, 1991.

- [45] L. D. Landau, E. M. Lifshits, and L. P. Pitaevski. *Statistical physics*, volume v. 5, 9 of *Course of theoretical physics*. Butterworth-Heinemann, c1980, Oxford [England], 3rd ed., rev. and enl edition.
- [46] Hugo Abdiel Vieyra Villegas. *Resistivity and Thermal Conductivity Measurements on Heavy-Fermion Superconductors in Rotating Magnetic Fields*. PhD thesis, Technische Universität Dresden, 2012.
- [47] Gavin David Scott and Douglas Natelson. Kondo resonances in molecular devices. *ACS nano*, 4(7):3560–3579, 2010.
- [48] W. Meissner and B. Voigt. Messungen mit hilfe von flüssigem helium xi widerstand der reinen metalle in tiefen temperaturen. *Annalen der Physik*, 399(8):892–936, 1930.
- [49] W. J. de Haas and J. de Boer. The electrical resistance of platinum at low temperatures. *Physica*, 1(7-12):609–616, 1934.
- [50] J. Kondo. Resistance minimum in dilute magnetic alloys. *Progress of Theoretical Physics*, 32(1):37–49, 1964.
- [51] P. W. Anderson. Localized magnetic states in metals. *Physical Review*, 124(1):41–53, 1961.
- [52] J. R. Schrieffer and P. A. Wolff. Relation between the anderson and kondo hamiltonians. *Physical Review*, 149(2):491–492, 1966.
- [53] Frithjof B. Anders. *Correlated electrons: The Kondo Effect. Chapter 11*, volume Bd. 2 of *Schriften des Forschungszentrums Jülich. Reihe Modeling and Simulation*. Forschungszentrum Jülich, Zentralbibliothek, Verlag, Jülich, 2012.
- [54] U. Fano. Effects of configuration interaction on intensities and phase shifts. *Physical Review*, 124(6):1866–1878, 1961.
- [55] Deung-Jang Choi. *Kondo effect and detection of a spin-polarized current in a quantum point contact*. PhD thesis, Université de Strasbourg, 2012.
- [56] G. Breit and E. Wigner. Capture of slow neutrons. *Physical Review*, 49(7):519–531, 1936.
- [57] Lam H. Yu and Douglas Natelson. The kondo effect in C₆₀ single-molecule transistors. *Nano Letters*, 4(1):79–83, 2004.

-
- [58] Edgar A. Osorio, Kevin O'Neill, Maarten Wegewijs, Nicolai Stuhr-Hansen, Jens Paaske, Thomas Bjørnholm, and van der Zant, Herre S J. Electronic excitations of a single molecule contacted in a three-terminal configuration. *Nano letters*, 7(11):3336–3342, 2007.
- [59] I. Fernández-Torrente, K. J. Franke, and J. I. Pascual. Vibrational kondo effect in pure organic charge-transfer assemblies. *Physical review letters*, 101(21):217203, 2008.
- [60] Riccardo Frisenda, Rocco Gaudenzi, Carlos Franco, Marta Mas-Torrent, Concepció Rovira, Jaume Veciana, Isaac Alcon, Stefan T. Bromley, Enrique Burzurí, and van der Zant, Herre S J. Kondo effect in a neutral and stable all organic radical single molecule break junction. *Nano letters*, 15(5):3109–3114, 2015.

SCANNING TUNNELING MICROSCOPE

The development and control of the smallest electronic device replacing macroscopic components such as transistors, diodes, etc... is one of the major challenges in nanotechnology today. Moore's law predicts that we should reach the nanoscale for transistors within the next decade.[1] Even though multiple molecular transistors were already developed [2–4] it is not possible yet to extrapolate these finding to larger scales. The race to find the best molecule with such properties is therefore still open, many types of nanoobjects are daily investigated and reported to the scientific community.

Advanced techniques are necessary in order to perform precise measurements leading to the comprehension and characterization of new molecules, these techniques should combine stability and high measurement precision. In 1981, the first tunnelling microscope was invented by Nobel prize winners Gerd Karl Binnig and Heinrich Rohrer at IBM laboratories [5]. Since then, it was developed to include facilities such as cooling system, external magnetic field or photon excitation to be used in various domains ranging from physics to biology.

In this chapter the principles of tunnelling microscopy and spectroscopy as well as the experimental setup used to perform the measurements are presented. Besides, various options of the microscope such as topography, dI/dV spectroscopy, scanning modes, contact, tip forming, manipulation will be described in the following discussion.

2.1 Tunnelling microscopy

The tunnelling effect is a well known quantum effect that describes the partial transmission through a potential barrier of a quantum particle. In a classical approach a particle with a certain kinetic energy is described by a collision process with a potential barrier, it will be reflected to the opposite direction following the elastic/inelastic collision law. However, due to the wave-particle duality in quantum mechanics, the wave function of the particle is used to describe its properties instead of a physical particle (sphere). By resolving Schrodinger's equation it is found that there is a non negligible probability to cross the potential barrier and tunnel to the other side of the barrier.

Consider a particle travelling towards the direction of the potential well. Its state is assumed fully defined and represented by a plane wave function to simplify the calculation (this assumption is not abusive considering the large distances taken into account). This simple problem is represented in a basic scheme in Figure 2.1, three states are studied representing the tunneling process between two electrodes with and without an adsorbed molecule.

Each region's Hamiltonian is written as: $H = -\frac{\hbar^2}{2m_e} \frac{\partial^2}{\partial r^2} + V$, where H represents the Hamiltonian of the system, V the potential at region II (Figure 2.1(b)) with a value $V \neq 0$ inside the barrier and null elsewhere. \hbar and m_e represent the reduced Planck constant and the electron mass respectively.

Assuming that $\Psi(r,t)$ represents the eigenfunction of one electron, it becomes possible to study its evolution from one electrode to another through the vacuum barrier when a bias voltage V is applied. Resolving Schrödinger's equation in every region of the system $H|\Psi_i(x,t)\rangle = E_i|\Psi_i(x,t)\rangle$ where i denotes the region number show that there is a transmitted part of the wave to the right side of the barrier. Therefore, the particle q has *tunnelled* from region I to region III . In scanning tunneling microscopy this property is used to scan conductive objects without touching them by tunneling electrons between a tip and a substrate through the vacuum barrier.

The principle of scanning tunneling microscopy (STM) is to approach two electrodes close enough to each others (few angstroms) to get electrons transferred respecting the Pauli exclusion principle. This means that electrons can only be transferred from one electrode's occupied state (sample or tip) to an unoccupied state of the other electrode (tip or sample).

Two different metals have two different Fermi levels. Thus, when they are brought close to each other, electrons from the highest energy electrode will be transferred to the lowest one in order to align both Fermi levels of the metals at the junction area. Thus, to avoid

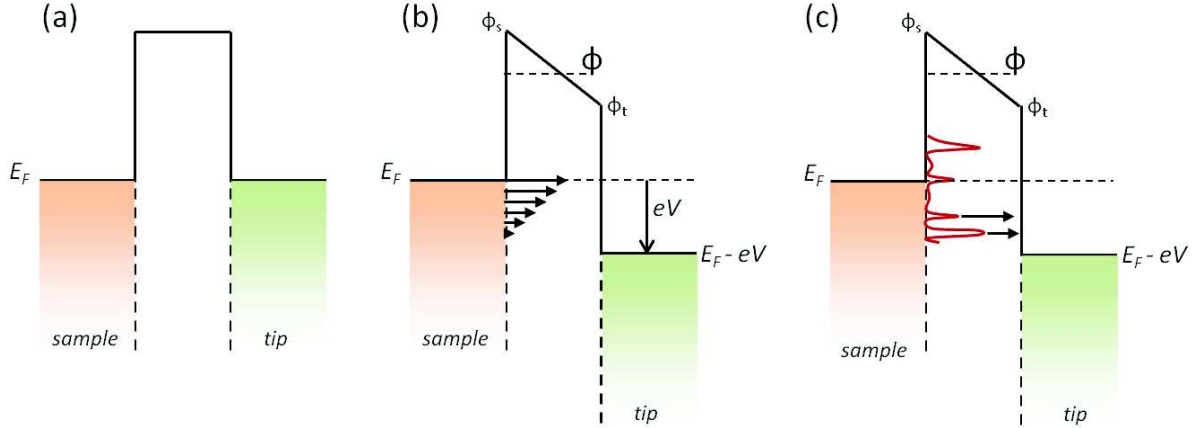


Fig. 2.1 Schematics of a barrier potential with (a) no potential applied (b) applied potential eV between metallic sample and tip (c) applied potential eV between metallic tip and a molecule deposited on substrate.

equilibrium and obtain a continuous flow of tunneling electrons, a bias is applied between tip and sample. This way energy levels (including Fermi level) are shifted from one side to a lower (or higher) level than the other. Electrons in this case are free to tunnel from the occupied states of the higher energy electrode to the empty states of the lower energy electrode.

In case of molecules, electrons are no longer in a conduction band but bounded into molecular discrete states or orbitals, see Figure 2.1(c).

According to Fermi's Golden rule, the density of the tunneling current flow for each electrode through the barrier is expressed as [6] :

$$\text{tip to sample: } J_{t \rightarrow s} = \frac{2\pi e}{\hbar} \int \|T_{ts}\|^2 \rho_t(E - eV) \rho_s(E) f_t(E - eV) [1 - f_s(E)] dE, \quad (2.1)$$

$$\text{sample to tip: } J_{s \rightarrow t} = \frac{2\pi e}{\hbar} \int \|T_{st}\|^2 \rho_t(E - eV) \rho_s(E) f_s(E) [1 - f_t(E - eV)] dE, \quad (2.2)$$

where $f_{s,t}(E)$ denotes the Fermi-Dirac distribution at energy E [7, 8] and $\rho_{s,t}$ represents the density of states of either sample or tip. $T_{s \leftrightarrow t}$ is the matrix element of the perturbation potential between sample and tip.

The net density current is therefore:

$$J = |J_{t \rightarrow s} - J_{s \rightarrow t}| = \frac{2\pi e}{\hbar} \int \|T\|^2 \rho_t(E - eV) \rho_s(E) [f_s(E) - f_t(E - eV)] dE. \quad (2.3)$$

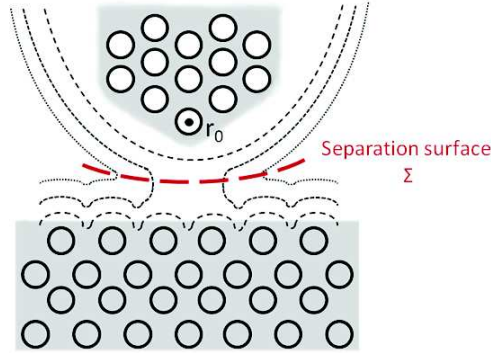


Fig. 2.2 Scheme of tip and sample when tunneling occurs. Red dashed line represents the separation surface Σ and r_0 the reference position of the apex representing the tip.

For low temperatures (close to $T=0$) Fermi-Dirac distribution is a step function which is equal to 1 within the region $[E_F, E_F + eV]$ and null outside $(]-\infty, E_F[\cup]E_F + eV, +\infty[)$. Equation 2.3 is then simplified to:

$$J_{T=0} = \frac{2\pi e}{\hbar} \int_{E_f}^{E_f+eV} \|T\|^2 \rho_t(E - eV) \rho_s(E) dE. \quad (2.4)$$

The matrix element T is the crucial factor in this equation, it is more precisely a transmission matrix which involves the wave function correlation between the two electrodes through the vacuum barrier.

The presence of the tip near the surface states induces a sample wave function distortion falsifying any isolated study of the electrodes. Using a modified Bardeen's formula where the tip potential is neglected in the surface region and *vice-versa*, the matrix element is evaluated as a surface integral on the separation area as Σ between the two electrodes, $\|T\|$ is expressed as [9]:

$$T_{ts} = -\frac{\hbar^2}{2m_e} \int_{\Sigma} (\Psi_t^* \nabla \Psi_s - \Psi_s \nabla \Psi_t^*) \cdot dS, \quad (2.5)$$

where Σ is the surface separating the tip from sample regions (roughly in the middle), dS is the surface element and $\Psi_{s,t}$ are the corrected wave functions of the sample and tip respectively. Besides, tip's wave function satisfies the Schrödinger's equation in the vacuum:

$$(\nabla^2 - \kappa^2) \Psi_t(r) = 0, \quad (2.6)$$

where $\kappa^2 = \frac{2m_e U}{\hbar^2}$ is the decay constant determined by the total potential U . It has to be

noticed that U is shape dependent which technically implies that the tip shape is of importance in an analytical investigation of the tunneling properties.

One must know both electrodes wave functions in order to solve equation 2.4. However, since tip's shape is impossible to determine, a tip model has to be assumed.

The wave functions have an exponential decay expression which lead to safely consider only the outermost tip atom's localized orbitals. In the present model, the tip apex is considered as the closest atom to the substrate centred at r_0 . The Green function related to the Schrodinger's equation of an s-orbital tip wave function under a homogeneous pot well at $|r - r_0|$ is of the following form:

$$\Psi_t^{s-orbital} = \frac{4\pi A}{\kappa} G(r - r_0),$$

$$\text{with: } G(r - r_0) = \frac{e^{-\kappa|r-r_0|}}{4\pi |r - r_0|}, \quad (2.7)$$

where A is a constant determined from the tip wave function expansion as components of the spherical harmonics Y_l^m [10, 11], r_0 is the position of the center of the outermost atom of the tip apex and r the distance between the tip and the separation surface Σ .

Therefore the matrix element applied to the s wave-function is of the following form:

$$T_{ts}^{s-orbital} = \frac{2\pi A \hbar^2}{\kappa m_e} \int_{\Sigma} [G(r - r_0) \nabla \Psi_s - \Psi_s \nabla G(r - r_0)] \cdot dS. \quad (2.8)$$

By using Green theorem this equation can be rewritten into a volume-like integral over Ω_{tip} which represent the occupied space of the s wave-function of the tip (namely the tip side of Σ).

$$T_{ts}^{s-orbital} = -\frac{2\pi A \hbar^2}{\kappa m_e} \int_{\Omega_{tip}} [G(r - r_0) \nabla^2 \Psi_s - \Psi_s \nabla^2 G(r - r_0)] d\tau, \quad (2.9)$$

where Ω_{tip} is the volume of the wave function surrounding the tip and $d\tau$ the volume element. Since both Schrödinger equation $(\nabla^2 - \kappa^2)\Psi_t = 0$ and its equivalent Green function $(\nabla^2 - \kappa^2)G(r - r_0) = -\delta(r - r_0)$ have to be satisfied, equation 2.9 is simplified to:

$$T_{ts}^{s-orbital} = \frac{2\pi A \hbar^2}{\kappa m_e} \Psi_s^{s-orbital}(r_0). \quad (2.10)$$

This equation is the solution of the matrix element T_{ts} applied to only s wave-function of the tip.

Tersoff and Hamann [12, 13] obtained similar result using another definition of s-wave or-

Table 2.1 Tunneling matrix element operators: list of tip states taken into account and its corresponding operator applied to the s-state matrix element at r_0 in order to obtain the matrix element of the desired state.

Tip orbital	$\Psi_s^{x-orbital} (\times \Psi_s^{s-orbital}(r_0))$
s	1
p_x	$\frac{\partial}{\partial x}$
p_y	$\frac{\partial}{\partial y}$
p_z	$\frac{\partial}{\partial z}$
d_{xz}	$\frac{\partial^2}{\partial x \partial z}$
d_{xy}	$\frac{\partial^2}{\partial x \partial y}$
d_{yz}	$\frac{\partial^2}{\partial y \partial z}$
$d_{x^2-y^2}$	$\frac{\partial^2}{\partial x^2} - \frac{\partial^2}{\partial y^2}$
$d_{z^2-\frac{1}{3}r^2}$	$\frac{\partial^2}{\partial z^2} - 1/3 \kappa^2$

bital. They did not represent it as an s-wave component of an atom-like orbital but as a macroscopic spherical potential well. However, this result is only valid for s-states tips. Since materials used experimentally as tips contain other orbitals than s such as $p_x, p_y, p_z, d_{xz}, d_{xy}, d_{yz}, d_{z^2}$ and $d_{x^2-y^2}$, all of them need to be considered in the analytical development. Moreover, z-components are more likely leading to an important enhancement of the corrugation amplitude compared to x and y components.

One might be tempted to state that the whole procedure should be repeated for every orbital, but thanks to Chen et al. this tedious process is not necessary, they demonstrated that matrix elements of other components than s-orbitals can be deduced by taking the derivative with respect to the desired component on the equation 2.10. This procedure is known as the *derivative rule* [14] and gives a direct dependence of the matrix element to the s-wave function.

In a general case, equation 2.10 is transformed to:

$$T_{ts}^{x-orbital} = \frac{2\pi A \hbar^2}{\kappa m_e} \Psi_s^{x-orbital}(r_0), \quad (2.11)$$

where x defines s, p or d orbital of the tip apex. It is important to note that there is no longer an explicit contribution of the tip wave function in the developed form of the matrix elements. These $\Psi_s^{x-orbital}$ wave functions are listed in Table 2.1 with respect to the desired tip state as obtained by Chen et al.

Table 2.2 Table of common workfunctions used in scanning tunneling microscopy as tips. [20]

Element	$\Phi(\text{eV})$
Ag	4.5
Au	5.4
Cu	4.9
Ir	5.4
W	4.8

Therefore solving Schrödinger's equation leads to access to the wavefunction of the tunneling electrons:

$$-\frac{\hbar^2}{2m_e} \frac{\partial^2}{\partial z^2} \Psi_s + U \Psi_s = E \Psi_s. \quad (2.12)$$

Considering Ψ to be a planar wave of the form $\Psi_s = B.e^{i\Phi(z)}$ where $\Phi(z)$ is the space decay operator and B a constant defined by the boundary conditions, equation 2.12 becomes:

$$i \frac{\partial^2 \Phi}{\partial z^2} - \left(\frac{\partial \Phi}{\partial z} \right)^2 - \frac{2m_e}{\hbar^2} (U - E) = 0. \quad (2.13)$$

The WKB approximation states that the potential vary very slowly within the tip-sample distance (z -axis), therefore $\frac{\partial^2 \Phi}{\partial z^2} \rightarrow 0$ simplifying equation 2.13 to the following [15–19]

$$\begin{aligned} \frac{\partial \Phi}{\partial z} &= \pm i \sqrt{\frac{2m_e}{\hbar^2} (U - E)}, \\ \implies \Phi &= \pm iz \sqrt{\frac{2m_e}{\hbar^2} (U - E)} + B, \end{aligned} \quad (2.14)$$

where B represent an integration constant.

In case of trapezoidal potential barrier (which is commonly used for a tip potential representation) U is expressed as $U = \frac{\phi_s + \phi_t}{2} + \frac{eV}{2}$ where V is the applied potential and $\phi_{s,t}$ are the work functions of substrate and tip respectively. Common metals work function used for STM are listed in table 2.2.

When inserted into the plane wave equation $\Psi_s(z)$ it gives:

$$\Psi_s(z) = e^B . e^{-z \sqrt{\frac{2m_e}{\hbar^2} \left(\frac{\phi_s + \phi_t}{2} + \frac{eV}{2} - E \right)}}, \quad (2.15)$$

and since:

$$T = \frac{2\pi A \hbar^2}{\kappa m_e} e^B \Psi_s^{\text{s-orbital}} = \frac{2\pi \hbar^2 C}{\kappa m_e} e^{-z \sqrt{\frac{2m_e}{\hbar^2} \left(\frac{\phi_s + \phi_t}{2} + \frac{eV}{2} - E \right)}}, \quad (2.16)$$

current density equation 2.4 for an s-wave tip will be expressed as:

$$J_{T=0} = \frac{4\pi^2 \hbar C}{\kappa m_e} \int_{E_f}^{E_F + eV} e^{-2z \sqrt{\frac{2m_e}{\hbar^2} \left(\frac{\phi_s + \phi_t}{2} + \frac{eV}{2} - E \right)}} \rho_t(E - eV) \rho_s(E) dE, \quad (2.17)$$

where C is a simplified constant.

The use of the derivative rule led to express the current density for the d_{z^2} -wave which is the common orbital for experimental tips such as tungsten. An increase of the corrugation amplitude allows to get up to atomic resolution.

2.2 Scanning tunneling spectroscopy (STS)

dJ/dV spectroscopy

The current density in equation 2.4 is not only dependent on the tunneling probability expressed by the tunneling matrix elements but also on the the density of states (DOS) of both, tip and sample. The derivative of J with respect to applied voltage V , dJ/dV gives a direct access to the local density of states ρ of both electrodes. The resulting equation is therefore:

$$\begin{aligned} \frac{dJ}{dV}(z, V) &= \frac{2\pi e}{\hbar} \frac{d}{dV} \left[\int_{E_F}^{E_F + eV} \|T\|^2 \rho_t(E - eV) \rho_s(E) . dE \right] \\ &= \frac{2\pi e}{\hbar} \left[\int_{E_F}^{E_F + eV} \frac{d\|T\|^2}{dV} . \rho_t(E - eV) . \rho_s(E) . dE \right. \\ &\quad + \int_{E_F}^{E_F + eV} \|T\|^2 . \frac{d\rho_t(E - eV)}{dV} . \rho_s(E) . dE \\ &\quad \left. + \int_{E_F}^{E_F + eV} \|T\|^2 . \rho_t(E - eV) . \frac{d\rho_s(E)}{dV} . dE \right]. \end{aligned} \quad (2.18)$$

First and second terms of equation 2.18 are to be neglected in basic WKB approximation. Indeed, the transmission matrix is assumed to vary very slowly within the experimental tunneling range (few eV), also, a negligible tip density variation is expected around the Fermi energy.[13, 21] Therefore, the LDOS equation links the current to only sample (substrate or

molecule) density of states and becomes:

$$\begin{aligned} \frac{dJ}{dV}(z, V) &\simeq \frac{2\pi e}{\hbar} \int_{E_F}^{E_F+eV} \|T\|^2 \cdot \rho_t(E - eV) \cdot \frac{d\rho_s(E)}{dV} \cdot dE \\ &\simeq \frac{2\pi e}{\hbar} \|T\|^2 \rho_t(E_F) \rho_s(E_F + eV). \end{aligned} \quad (2.19)$$

Thus accessing the substrate density of states is straightforward using equation 2.19. Usually, the variation is in the range of $\pm 2eV$ below and above the Fermi energy. This bias voltage can also be increased up to $3eV$ however the molecular orbitals will be, in this case, highly affected by the high voltage. Furthermore the tip can get direct access to surface electrons because of the metal close work function compared to the applied bias which may falsify the investigations.

Experimentally this procedure is used to access molecular orbital's energy position, by applying the right bias the tunneling occurs through the molecular orbitals (MOs), these orbitals can either be filled, in which case they are designated as occupied orbitals where the closest to Fermi level is referred to as the highest occupied molecular orbital (HOMO). Orbitals which are not filled with electrons are accessible with a positive bias voltage, the closest to Fermi level is known as LUMO for lowest unoccupied molecular orbital. All following orbitals use the common notation HOMO- n and LUMO+ n where n refer to the orbital position (1,2..).

Surface states

Scanning tunneling spectroscopy (STS) gives also access to the metallic substrate 2D electron gas. In contrary to a bulk periodicity, the electronic structure near the surface is modified by the symmetry breaking.

At the vicinity of the vacuum-metal interface propagated electrons in the metal become reflected at the surface and the wave-functions are generated at the interface. These waves decay exponentially in both, vacuum and bulk directions.[22] These waves constitute the so called *surface states* where electrons are "trapped" in a two dimensional plane formed by the surface.

Because of different dangling bonds, surface states cannot be treated as Bloch-states, electrons should therefore be treated as a 2D-electron gas where Shockley surfaces states lie in the projected band gap following the $\gamma - L$ direction.[23] Furthermore interface electrons

will have different effective mass compared to free electrons.[22, 24]

Energy upon which the surface states occurs is dependent on the phase shift of the wave at the interface region where Bohr-like quantization condition is satisfied [22, 25]

$$\Phi(E) = \Phi_R(E) + \Phi_B(E) = 2n\pi,$$

where E is the Shockley surface states energy and $\Phi_{R,B}$ represent the phase shift of reflected and bulk waves respectively.

STS of noble metals have been extensively studied by angle resolved photoelectron spectroscopy (ARPES) and STM. [24, 26–29] Au (111) and Ag (111) ARPES measurements are presented in Figure 2.3 (a) and (b) respectively. Their corresponding STS measurements are presented in 2.3(c) where the surface-state energy position is indicated with vertical lines. The differential conductance shows, as expected, the Shockley surface states at -450meV and -70meV for Au (111) and Ag (111) respectively.

2.3 Instrument and experimental approach

Research work presented in this thesis investigates single nano-objects such as molecules or atoms adsorbed on various substrates. To this end, a scanning tunneling microscope is used in a perfectly clean environment to perform contamination free and reproducible measurements. This condition is satisfied by using an ultra-high vacuum and low temperature. A low temperature condition is also used to stabilize the nano-objects sensitive to thermal diffusion. *In-situ* preparation of various components is mandatory to keep the system as clean as possible.

2.3.1 STM instrument

The microscope is a home designed Createc® instrument composed of four chambers: Preparation chamber, STM chamber, Load Lock and evaporation chamber as presented in Figure 2.4(a). The preparation chamber equipped with a sputtering gun and an annealing wire in order to prepare *in-situ* the tip and the sample, it is kept at a base pressure of 10^{-10} mbar. The STM chamber is dedicated to the sensitive measurements where the microscope head is kept at low temperature by means of two LN_2 and LHe cryostats, this chamber is kept at 10^{-11} mbar. The load-lock chamber is dedicated to the sample and tip introduction from atmospheric area to avoid any vacuum breaking in the main chambers. At last, evaporation chamber is used only to perform a contamination free molecular evaporation on

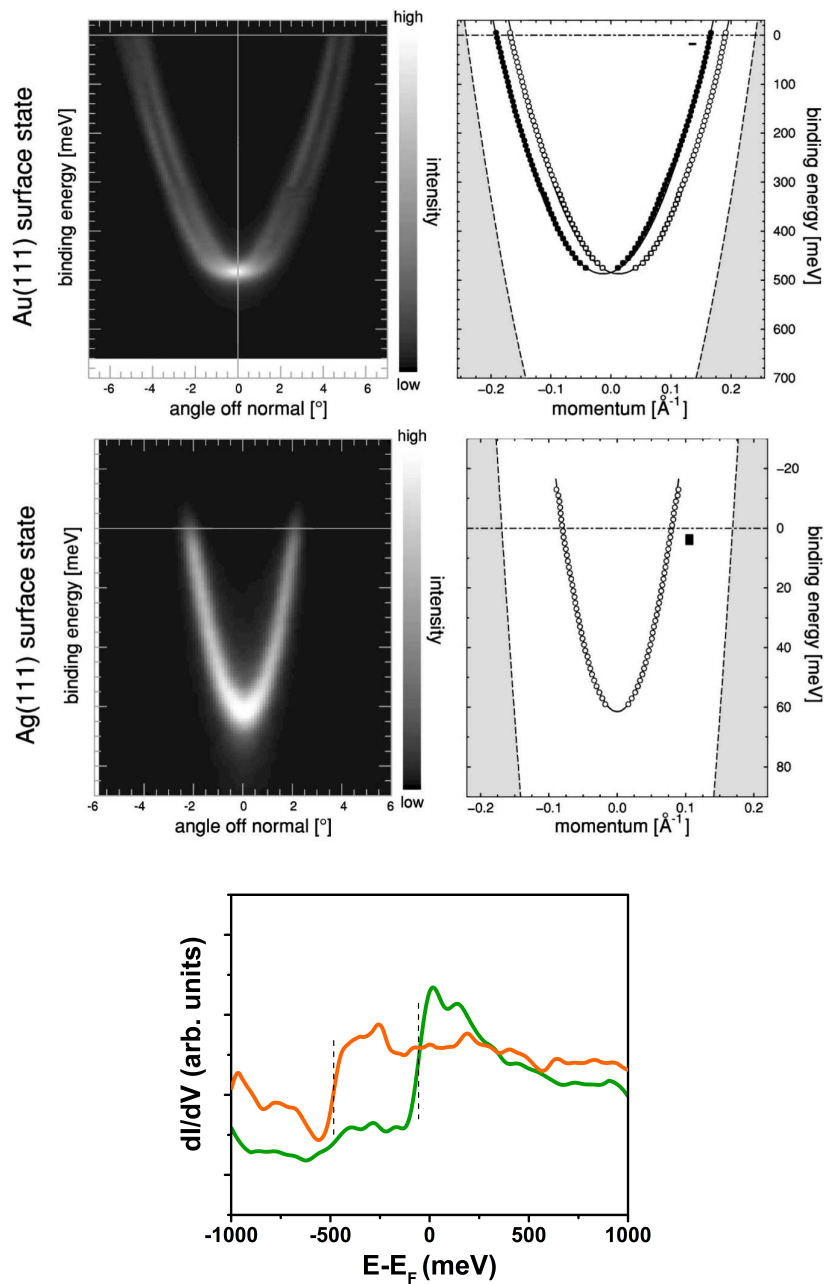


Fig. 2.3 Shockley surface states and parabolic dispersion obtained by ARPES on Au (111) (top) and Ag (111) (middle) near $\bar{\Gamma}$, obtained from ref. [27]. Low noise differential conductance obtained by STM is presented in bottom, it was recorded on Au (111) (orange) and Ag (111) (green).

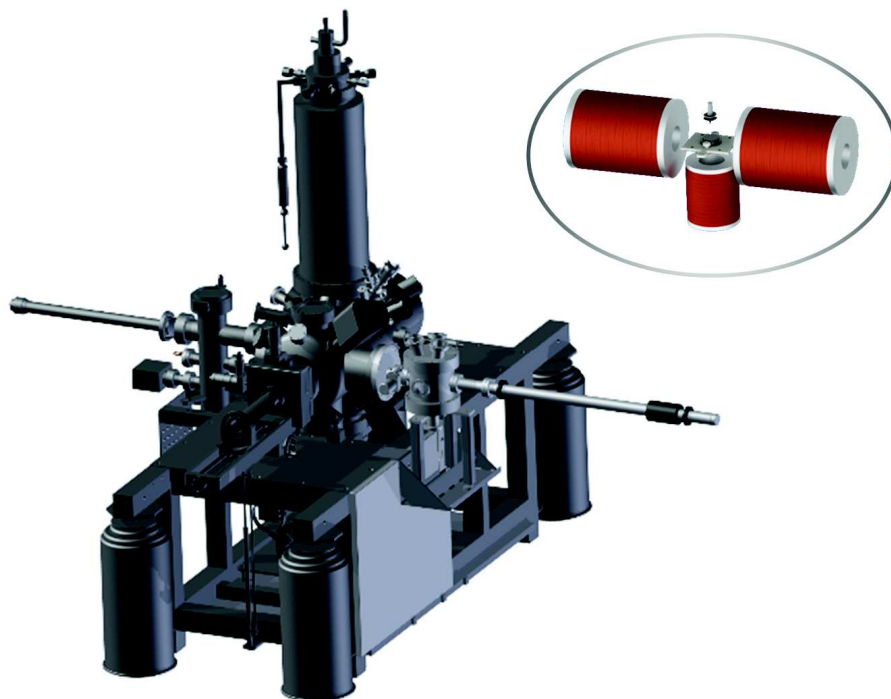


Fig. 2.4 Perspective view of the scanning tunnelling microscope including dampers and the various related chambers. The enlarged image shows the STM head containing the three magnetic coils and the measurement tools (tip and sample).

substrates, this supplementary chamber is kept at 10^{-10} mbar when not in use and has its own pumping system during the evaporation process.

Three magnetic coils are also connected to the STM-head in order to produce two magnetic vector fields, one along Z-direction (up to 0.7 Tesla) and two others along X-direction (up to 1 Tesla) as presented in Figure 2.4(b). The coils are wound by a wire composed of 54 superconducting (SC) NbTi fibres in a copper medium with a Cu:SC ratio of 1.3:1.

In order to ensure a noise free system, the apparatus is fully supported by four Newport® active vibration isolation dampers that can adsorb a full range of vibrations with 98% of noise removal below 10 Hz.

2.3.2 Ultra high vacuum

Ultra high vacuum (UHV) is mandatory to keep the inner environment of the apparatus as clean as possible in order to perform clean and reproducible measurements. For that, four step vacuum approaches are required to reach the working environment of $p \propto 10^{-11}$ mbar:

- Primary pump: A dry pump is highly recommended for a clean vacuum. Primary pumps reaches easily 10^{-3} mbar.
- Turbo pump: Reduces pressure to 10^{-9} mbar.
- Ionic pump: Together with titanium sublimation, decreases the pressure to 10^{-11} mbar
- Cryogenic pump: LN_2 (at 77 K) and LHe (at 4 K), allows a pressure of 10^{-12} mbar

Once the working vacuum level reached, preparation and sensitive scanning processes become possible with very low risk of contamination.

2.3.3 Tip and sample preparation

Tip preparation

Multiple techniques to prepare an STM tip are available. However, for this research, only chemical etching procedure was used. Tips used for this research are made from a tungsten (W) wire of 0.25 mm diameter thick and prepared by chemical etching in a solution of NaOH at (10%). Once introduced into the preparation chamber a smooth Ne^+ bombardment followed by an electron bombardment of 10 mA for less than 5 minutes are performed in order to clean the tip from any contamination caused by the etching process. Tip is therefore introduced into STM head to perform manual indentation and bias pulses on a pristine crystal. This process is repeated until stable and contamination-free apex is obtained. A spectroscopy acquisition reproducibility together with a good scan resolution (atomic resolution) are indicators of a good apex.

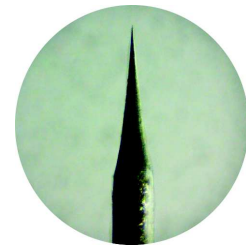


Fig. 2.5 Tungsten tip prepared by chemical etching in 10% NaOH solution.

Substrate preparation

Crystals used for upcoming investigations are Cu (100), Cu (111), Au (111) and Ag (111). The only required preparation for crystals is multi cycles of Ne^+ bombardment and *in situ* annealing process. Extended contamination free terraces under STM investigation were indication of success.

Once prepared, the crystal is re-transferred into the evaporation chamber where molecular and/or atomic deposition is performed at suitable conditions.

2.3.4 Deposition techniques

Molecular deposition

Before the evaporation, desired molecules were first degassed *in-vacuo* at 30K below sublimation temperature for at least 24 h to avoid any impurity that may appear during the evaporation. Once the evaporation chamber vacuum stabilized, molecules were evaporated from an alumina crucible wound by a tantalum wire heated up by means of Joule effect and controlled by a thermocouple. The duration of deposition time was obviously chosen depending on the desired quantity on the substrate.

The molecules were either provided by collaborators at the Karlsruher Institute Für Technology¹ or commercially provided from *Alfa Aesar* ensuring a high purity.

Atom evaporation

Three techniques are used for the atomic deposition, the first one was performed using a standard evaporator for Fe or Co atom deposition on substrates. The second technique was done using a crucible which was gradually heated up to the evaporation temperature. Once obtained, the sample was revealed to the crucible's cross-section. Last technique uses a tungsten/tantalum wire wounded by a wire of the desired specie of evaporation atom. This filament was then fed by a current in order to heat the wounding metal under Joule effect. Standard evaporators were also used to grow cobalt-islands on pristine Cu (111) crystal. Large nano-islands of 15 nm width are obtained with a low contamination rate when the vacuum conditions are satisfied.

2.4 Experimental approach

In scanning tunneling microscopy, a highly stable setup is necessary to acquire high resolution data. Under good conditions, it offers a good topography images, highly resolved point spectroscopy, and low noise conductance mapping. Furthermore, by manipulating the tip position and tunneling parameters, an STM is able to excite atoms or molecules, inject electrons and perform manipulation to create any desired geometry.

¹Pr. Ruben Mario and Dr. Klyatskaya Svetlana; Institute of Nanotechnology, Karlsruhe Institute of Technology (KIT), D-76344 Eggenstein-Leopoldshaffen, Germany.

Topography

When tip-sample distance is short enough to allow tunneling of electrons, a scan of the surface becomes possible when varying the xy-position of the tip. By applying a bias voltage, electrons are transferred and a current is recorded, it is then converted into a height information which can be used to create a 3D reconstruction of the scanned area. Experimentally, typical currents are in the range of 1 pA to $10\text{ }\mu\text{A}$ for a distance of $3\text{ }\text{\AA}$ to $10\text{ }\text{\AA}$.

Topography images gives information about the molecular shape and dimensions, however since this technique uses the current intensity, direct analysis of dimension is not accurate, therefore one speaks about apparent dimensions instead. In fact, two scanning modes can be used to acquire a 3D reconstructed area:

Constant current mode

This mode keeps the tunneling current at a constant value during the all the scanning process, the real distance z separating tip from substrate varies to ensure the constant current. For this purpose, a feedback loop (FB-loop) is necessary to control the vertical displacement of the tip. The FB-loop applies a certain bias voltage to the piezoelectric crystal holding the tip. Therefore, any detected variation of the tunneling current will induce a variation of the tip vertical position.

Constant current mode is a safe scanning mode as it prevent from any tip-sample contact which may seriously alter the sample properties or the tip purity. However, this mode generates vibrations due to the perpetual Z -direction adjustments by the FB making it therefore inappropriate for very sensitive measurements.

Constant height mode

This mode ensures a more stable imaging compared to previous one as it keeps the vertical tip position at a constant value independently from any external variation. This mode offers a very sensitive and noise-free results as the feed back loop is turned off. However, its major weakness is the important risk of tip-sample contact in case of non-flat area. This risk increases when the adsorbed molecules have an important vertical extension such as terbium double-decker molecules (TbPc_2). Furthermore, any thermal drift induces a vertical displacement of the tip, increasing therefore the risk of physical contact.

Figure 2.6 shows both, constant current and constant height mode topography imaging of a terbium double-decker molecule capped with a cerium atom². Both modes are used in

²this molecules is investigated more in detail in Chapter 5

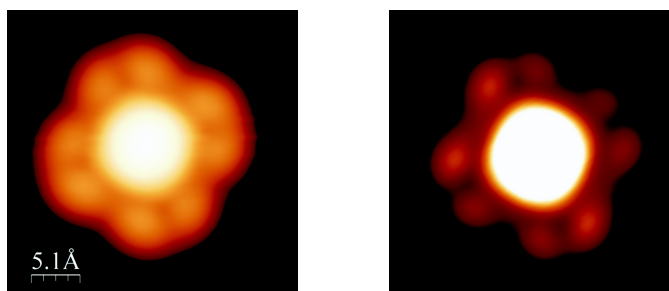


Fig. 2.6 Topography images of a terbium double decker capped with a cerium atom at (a) constant current mode and (b) constant height mode.

the present thesis report in order to ensure safe and sensitive measurements.

Point spectroscopy

As mentioned in section 2.2, by ramping the bias voltage between the tip and a desired point, informations concerning its molecular orbitals may be investigated. It will information about various molecular properties such as energy gap, chemical composition, bounding type or exchange energy. During a dI/dV spectroscopy acquisition, the FB-loop needs to be opened (no variation of the tip-sample distance).

During the acquisition of a dI/dV spectroscopy, the signal can be drown out by a noise at large band gaps. This noise is made to appear at a certain reference frequency of small amplitude falsifying the results. In order to annihilate this non-desired contribution, a so-called *Lock-in detection device* is used. Contrary to analytical derivation of $I(V)$, the lock-in amplifies signal and gives a precise and well resolved conductance value by applying a sinusoidal variation of the bias voltage during the tunnelling spectroscopy.

A Lock-In amplifier operates generally at a mean reference frequency of the signal to measure (usually few hundreds of hertz). The signal is amplified and applied to a phase-sensitive detector operating also at that same frequency. The output signal includes then the value representing the amplitude of the signal of interest as well as noise and interference created by AC components.

By applying a controlled low-pass filter, that undesirable signal is eliminated and the dI/dV signal becomes noise-free. In the present work both, an internal and external lock-in amplifiers were used.

Scanning tunnelling spectroscopy is sensitive to two main variables: thermal variation and lock-in modulation voltage, they both induce a broadening of the spectral resolution:

ΔE_T and ΔE_M respectively. [30, 31]

Thermal broadening originates from the temperature dependency on the Fermi-Dirac distribution and can be expressed as: $\Delta E_T = 3.5 k_B T$. Since all measurements presented here were done under liquid helium temperature (4.5 K) ΔE_T is of the order of 1.4 meV.

On the other hand, modulation voltage broadening is introduced by the Lock-in itself as $\Delta E_M = 2.44 V_{rms}$ with V_{rms} is the root mean square of the modulation voltage. Its value can be manually set as desired to ensure a high resolution and low noise. V_{rms} in this work was chosen between 1 mV and 20 mV.

Therefore the lowest total energy broadening in experiments is

$$\Delta E = \sqrt{\Delta E_T^2 + \Delta E_M^2} = 2.45 \text{ mV} .$$

Ensuring a very stable STS involves noise checking by measuring the fraction of the average signal-value over noise-amplitude $\frac{S}{N}$ ratio which should remain very low (less than 10%). Care should be taken while adjusting the Lock-in parameters as they differ when the environment (tip or molecule) changes.

Conductance mapping

Beside the locally acquired spectroscopy on a desired point of space, it is possible to collect conductance data all over an area, this technique is known as conductance mapping (or dI/dV map). In contrary to the dI/dV spectroscopy the data is no longer recorded over a wide range of bias voltage but a single value of conductance is recorded at each pixel of the image with a voltage V_0 as $\frac{dI}{dV} |_{V=V_0}$. This signal is later converted into an image through a corresponding software. This method provides information on the spacial distribution of molecular density of states. This technique can be used either by a constant current mode or the constant height mode to achieve a better resolution.

Figure 2.7 shows a copper phthalocyanine (CuPc) molecule adsorbed on Ag (100) substrate, topography image depicts the usual four-folded leaf-like behaviour of a metal phthalocyanine. When dI/dV mapping is recorded at HOMO (-280 meV) and LUMO ($+480 \text{ meV}$) positions the image depicts a different spatial distribution corresponding to its orbital distribution.

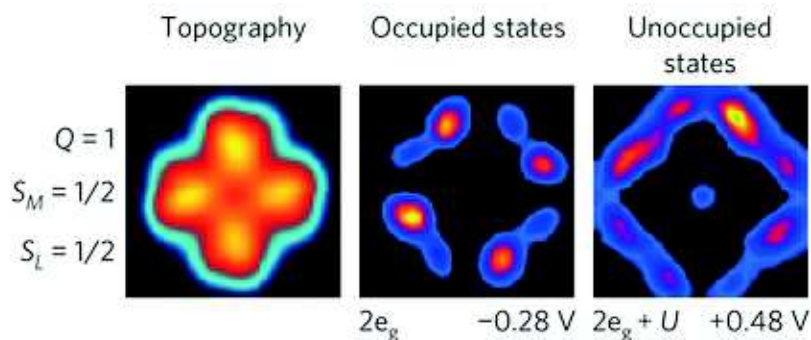


Fig. 2.7 Topography and dI/dV mapping recorded on CuPc molecule adsorbed on Ag (100) substrate. Conductance mapping are recorded at HOMO and LUMO positions i.e. -280meV and $+480\text{meV}$ respectively. From ref. [32]

Hints for good spectroscopy

Better STS comes with better tips!

In order to avoid miscellaneous problems due to a contaminated tip or a non-stable molecule, it is highly recommended to take care during the tip preparation process for STS measurements. A *spectroscopy tip* is not always the same as a topography tip. One has to treat the tip by indentation or pulsing as much as necessary in order to get reproducible spectroscopy over a bare metallic substrate. Checking STS over the substrate within $-2V$ to $+2V$ should be featureless except for the presence of surface states.

Tip treatment processes are various: forced indentation, tip-crystal contact, high voltage pulse (10 V) or scanning with high tunneling parameters. Scanning a clean substrate at a high bias voltage ($7 - 10V$) and high speed seem to be very efficient, specially if the bias polarity is changed during the scan process.

2.5 Summary

In this chapter, the theoretical approach to the quantum tunneling and its application in scanning tunneling microscopy were briefly introduced. Both, the topography and spectroscopy approaches of the STM were introduced in the vicinity of the tunneling process.

A short section details the apparatus used for the present work, where it describes the chambers and tools used for a complete stable work conditions. Various techniques used for the sample preparation as well as the tip conditioning were also presented.

REFERENCES

- [1] G.E. Moore. Cramming More Components Onto Integrated Circuits. *Proceedings of the IEEE*, 86(1):82–85, January 1998.
- [2] Hongkun Park, Jiwoong Park, Andrew K. L. Lim, Erik H. Anderson, A. Paul Alivisatos, and Paul L. McEuen. Nanomechanical oscillations in a single-C₆₀ transistor. *Nature*, 407(6800):57–60, September 2000.
- [3] Mickael L. Perrin, Enrique Burzurí, and Herre S. J. van der Zant. Single-molecule transistors. *Chemical Society Reviews*, 44(4):902–919, February 2015.
- [4] Arieh Aviram and Mark A. Ratner. Molecular rectifiers. *Chemical Physics Letters*, 29(2):277–283, November 1974.
- [5] G. Binnig, H. Rohrer, Ch Gerber, and E. Weibel. Tunneling through a controllable vacuum gap. *Applied Physics Letters*, 40(2):178–180, January 1982.
- [6] Joel A. Appelbaum and W. F. Brinkman. Theory of Many-Body Effects in Tunneling. *Physical Review*, 186(2):464–470, October 1969.
- [7] P. a. M. Dirac. On the Theory of Quantum Mechanics. *Proceedings of the Royal Society of London A: Mathematical, Physical and Engineering Sciences*, 112(762):661–677, October 1926.
- [8] Alberto Zannoni. On the Quantization of the Monoatomic Ideal Gas. *arXiv:cond-mat/9912229*, December 1999. arXiv: cond-mat/9912229.
- [9] J. Bardeen. Tunnelling from a Many-Particle Point of View. *Physical Review Letters*, 6(2):57–59, January 1961.
- [10] Philip McCord Morse and Herman Feshbach. *Methods of Theoretical Physics, Part I*. McGraw-Hill Science/Engineering/Math, Boston, Mass, June 1953.

-
- [11] George B. Arfken and Hans J. Weber. *Mathematical Methods for Physicists, Seventh Edition: A Comprehensive Guide*. Academic Press, Amsterdam ; Boston, 7th edition, January 2012.
- [12] J. Tersoff and D. R. Hamann. Theory and Application for the Scanning Tunneling Microscope. *Physical Review Letters*, 50(25):1998–2001, June 1983.
- [13] J. Tersoff and D. R. Hamann. Theory of the scanning tunneling microscope. *Physical Review B*, 31(2):805–813, January 1985.
- [14] C. Julian Chen. Tunneling matrix elements in three-dimensional space: The derivative rule and the sum rule. *Physical Review B*, 42(14):8841–8857, November 1990.
- [15] Arthur Schlissel. The initial development of the WKB solutions of linear second order ordinary differential equations and their use in the connection problem. *Historia Mathematica*, 4(2):183–204, May 1977.
- [16] Eugen Merzbacher. *Quantum Mechanics*. Wiley, New York, 3 edition edition, December 1997.
- [17] Gregor Wentzel. Eine Verallgemeinerung der Quantenbedingungen für die Zwecke der Wellenmechanik. *Zeitschrift für Physik*, 38:518–529, June 1926.
- [18] H. A. Kramers. Wellenmechanik und halbzahlige Quantisierung. *Zeitschrift für Physik*, 39(10-11):828–840, October 1926.
- [19] L. Brillouin. La mécanique ondulatoire de Schrödinger; une méthode générale de résolution par approximations successives, 1926.
- [20] Herbert B. Michaelson. The work function of the elements and its periodicity. *Journal of Applied Physics*, 48(11):4729–4733, November 1977.
- [21] Vladimir A. Ukraintsev. Data evaluation technique for electron-tunneling spectroscopy. *Physical Review B*, 53(16):11176–11185, April 1996.
- [22] Benjamin Heinrich. Tunneling spectroscopy of nanoscale objects: from metallic islands to single atoms and molecules, Thesis, June 2010.
- [23] William Shockley. On the Surface States Associated with a Periodic Potential. *Physical Review*, 56(4):317–323, August 1939.
- [24] S. D. Kevan. Evidence for a New Broadening Mechanism in Angle-Resolved Photoemission from Cu(111). *Physical Review Letters*, 50(7):526–529, February 1983.

-
- [25] N. V. Smith. Phase analysis of image states and surface states associated with nearly-free-electron band gaps. *Physical Review B*, 32(6):3549–3555, September 1985.
- [26] K. Giesen, F. Hage, F. J. Himpsel, H. J. Riess, and W. Steinmann. Two-photon photoemission via image-potential states. *Physical Review Letters*, 55(3):300–303, July 1985.
- [27] F. Reinert, G. Nicolay, S. Schmidt, D. Ehm, and S. Hüfner. Direct measurements of the L-gap surface states on the (111) face of noble metals by photoelectron spectroscopy. *Physical Review B*, 63(11):115415, March 2001.
- [28] M. F. Crommie, C. P. Lutz, and D. M. Eigler. Imaging standing waves in a two-dimensional electron gas. *Nature*, 363(6429):524–527, June 1993.
- [29] L. Bürgi, L. Petersen, H. Brune, and K. Kern. Noble metal surface states: deviations from parabolic dispersion. *Surface Science*, 447(1–3):L157–L161, February 2000.
- [30] L. J. Lauhon and W. Ho. Effects of temperature and other experimental variables on single molecule vibrational spectroscopy with the scanning tunneling microscope. *Review of Scientific Instruments*, 72(1):216–223, January 2001.
- [31] J. Klein, A. Léger, M. Belin, D. Défourneau, and M. J. L. Sangster. Inelastic-Electron-Tunneling Spectroscopy of Metal-Insulator-Metal Junctions. *Physical Review B*, 7(6):2336–2348, March 1973.
- [32] Cornelius Krull, Roberto Robles, Aitor Mugarza, and Pietro Gambardella. Site- and orbital-dependent charge donation and spin manipulation in electron-doped metal phthalocyanines. *Nature Materials*, 12(4):337–343, April 2013.

ISOLATED TBPC₂ MOLECULES ON SURFACES

The race towards the best molecular magnets with the ability to store information for relatively long relaxation times has reached a point where many promising candidates are studied in a wide range of different domains using a wide variety of techniques.[1–3] Most research focus on metal-organic molecules where electronic properties are structure dependent.[2–4] These promising compounds are mostly based on metal ions with anisotropic electronic properties, either transition metals or lanthanides are investigated because of their large magnetic remanence [5, 6] and promising structural varieties in bulks and self-assembled layers formation. In single molecule magnets (SMMs), anisotropy arises from the metal ions as a preferred orientation without any external influence such as magnetic field or thermal excitation which usually induces a global magnetization of the formed bulk or layer.[7]

As far as single molecules are concerned, a wide range of spin detection techniques have been developed using scanning tunneling microscopy (STM) and spin polarized STM (SP-STM) including scanning tunneling spectroscopy (STS) [8–11], inelastic electron tunneling spectroscopy (IETS) [12, 13] or through Kondo resonance detection [14–17]. Indeed, Kondo resonance of a magnetic molecule results from the diffusion of surrounding spins by the magnetic “impurity” and is reported in STS by a peak of width Γ positioned at the Fermi level (zero bias).

3.1 A brief overview

In 2003, Ishikawa et al. reported on a novel compound based on two phthalocyanines sandwiching a terbium atom behaving as a SMM with only one metal ion. This achievement

highlighted the use of lanthanide based organo-metallic complexes in the field of single molecule magnets.[18] These complexes show much larger anisotropy barriers and prominent hysteresis than previously reported polynuclear complexes based on transition metals [18–27]. A whole new branch of SMM field has then emerged.

Further investigations led to development of SMMs based on only one transition metal such as Fe II [28–31], Fe III [32] and Co II [33, 34] atoms that show a large anisotropy under specific conditions. Indeed, a magnetic exhibition on these complexes appears only if an external static magnetic field is applied. Furthermore, only the first row transition metals lead to a large anisotropy signature. [28, 29] Gomez-Coca and co-workers succeeded in predicting the magnetic anisotropy of these first-row transition metal based mono-nuclear complexes using the extended-Hückel approach to correlate first excited energy to magnetic anisotropy [35].

The later approach as well as more simplified models are generally accurate for transition metals to explain the anisotropy origin. Nevertheless it will lead to a huge misinterpretation when applied to lanthanides because of the presence of f-electrons in their valence shell. Large magnetic moments and strong anisotropies in lanthanides originate from a strong spin-orbit coupling. Rinehart and Long suggested that contrary to transition metals, the total momentum in Ln atoms is not only originating from electronic spins but also from a degeneracy of f-orbitals leading to an unquenched orbital moments m_j . [36]

The spin-orbit coupling in f-orbitals of Ln based organo-metallic complexes remains stronger than the ligand field contribution to the interaction. However, Rinehart and Long showed that the ligand field interacts with the spin orbit J ground state, and generates a magnetic anisotropy barrier between opposite spins. In other words, by carefully choosing the molecule geometry and electronic configuration of the ligands, we may change its magnetic anisotropy. They reported that some lanthanides have a prolate (axially elongated) f-electron charge cloud namely Pm(III), Sm(III), Er(III), Tm(III) and Yb(III) while some others have oblate distribution (equatorially elongated) namely Ce(III), Pr(III), Nd(III), Tb(III), Dy(III) and Ho(III) as presented in Figure 3.1(a).¹

To maximize the anisotropy signal, a careful selection of ligand-metal system is needed to access electronic density distribution in a direction parallel to the shape elongation (parallel to z -direction for prolate elements and parallel to xy -plane for oblate elements). Ishikawa et al. [37, 38] dressed a table listing ground state multiplet J splitting for different

¹Gd(III) and Lu(III) have an isotropic distribution and thus show a spherical shape. Eu(III) however shows no quadrupole moment because its total moment $J=0$.

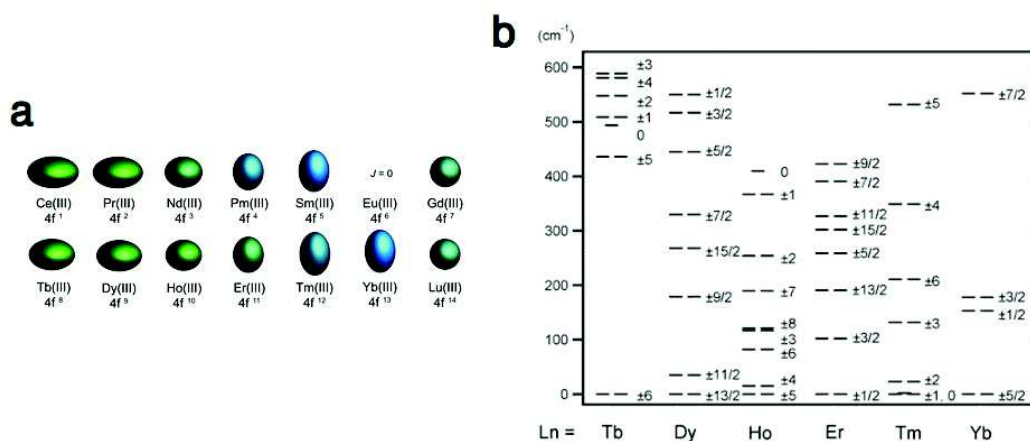


Fig. 3.1 a) Quadrupole approximations of the 4f-shell electron distribution for the Ln(III) atoms. Ce(III), Pr(III), Nd(III), Tb(III), Dy(III) and Ho(III) show an oblate distribution while Pm(III), Sm(III), Er(III), Tm(III) and Yb(III) show a prolate distribution. Eu is not depicted due to its $J=0$ ground state. Gd(III) and Lu(III) show a perfect spherical distribution. From ref. [36]. b) Substates energy diagram of the ground multiplets for various lanthanide based $[\text{LnPc}_2]^-$. The largest gap between ground state and first excited state is found for Tb atom with 440 cm^{-1} followed by Dy with 260 cm^{-1} . [37, 38]

lanthanides complexed in an LnPc_2 molecule (see Figure 3.1(b)). A detailed analysis of these states reveals that the $m_j = \pm 6$ of the Tb(III) is separated by 440 cm^{-1} from the first excited state of $m_j = \pm 5$. In this configuration, terbium shows the highest anisotropy among all the lanthanides. The second largest gap is found for Dy(III) with 260 cm^{-1} separating the ground state $\pm 13/2$ from the first excited state $\pm 15/2$. These two elements are the only ones showing a slow magnetization relaxation, while other elements have either smaller J_z compared to Tb and Dy or smaller gap to the first excited state making them very sensitive to external perturbations.[39–44] Accordingly, TbPc_2 appears to be the most interesting complex to study.

In the case of terbium lanthanide, the atom carries a nuclear spin of $I=3/2$ leading to four nuclear sub-states $|m_I\rangle = \pm 3/2, \pm 1/2$. This spin should be considered in the total Hamiltonian describing any system carrying a Tb^{3+} , this contribution is a quadrupole interaction which is expressed as:

$$H_{\text{Quad}} = P_q(I_z^2 + 1/3(I(I+1))), \quad (3.1)$$

where P_q is the quadrupole constant experimentally measured and found equal to 14.4 mK in a TbPc_2 . [45] This term has to be included along with 1.14 into the total Hamiltonian of a molecular system 1.10.

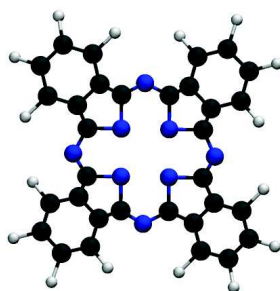


Fig. 3.2 Model of an amine deprotonated phthalocyanine molecule. Four isoindole fragments are coordinated to each other by four nitrogen atoms. Its chemical formula is C₃₂N₈H₁₆. Color code: Blue= Nitrogen; Black= Carbon; White= Hydrogen.

In this chapter measurements performed on TbPc₂ molecules on various surfaces (Cu (111), Cu (100), Ag (111), Au (111) and Cobalt islands grown on copper substrate) will be presented. These investigations led us to analyze several orientations of the molecules on the various substrates thus gathering information on the molecule-substrate interactions. STS measurements have been performed to show the electronic properties of the complex and the effect of the substrate on them. Spatial distribution of the molecular orbitals will also be reported through dI/dV mapping. Finally, molecular island formation by means of atomic manipulation will be demonstrated step-by-step to introduce the next chapter dedicated to molecular domains.

3.2 Addressing terbium double-decker molecules on surfaces

Phthalocyanines H₂Pc are the precursors of the most studied organo-metallic complexes in molecular spintronic. H₂Pc is a simple planar macrocycle molecule carrying two hydrogens in its center; it consists in four isoindole rings coordinated to each other through four nitrogen atoms forming a stable aromatic molecule as shown in Figure 3.2. By substituting the two protons, the new Pc⁻² behaves as a donor and thus accepts to carry a metal ion in its center. Usually a transition metals like Cu⁺², Ni⁺², Zn⁺², Mn⁺², Co⁺² or Fe⁺² are inserted in order to create a coordinated MPc (M= transition metal), leading to a D_{4h} symmetry order. CuPc was the first molecule investigated under STM in 1987 by Gimzewski et al. [46]. It is known that these transition metals are more stable in an oxidation state of +II which thus can strongly bind to a dehydrogenated phthalocyanine. The case where the central atom is replaced by a lanthanide metal leads to another type of coordination where the simple aspect of donor-acceptor is no longer sufficient to describe the coordination.

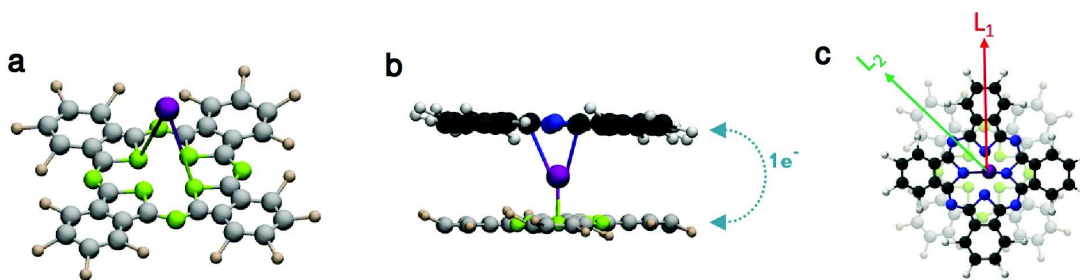


Fig. 3.3 a) TbPc molecule with an out of plane terbium atom. b) Side view of a terbium double-decker molecule (TbPc_2), the terbium atom which is positively charged by +3 creates a covalent bonding with the two deprotonated donor phthalocyanines, they are both charged negatively by -2. c) Top view of a TbPc_2 molecule. L_1 and L_2 denote respectively one of the symmetry axis of the upper and lower phthalocyanine. Different colors were used for the two ligands to have a better visualization. The chemical structure is $\text{TbC}_{64}\text{N}_{16}\text{H}_{32}$. Color code: Purple = Terbium; black/gray = Carbon; blue/green = Nitrogen; white/brown = Hydrogen.

When coordinated to a deprotonated phthalocyanine, the new lanthanide single-decker complex becomes positively charged (LnPc^+). Distance between two opposite pyrrole nitrogens is of 292 pm. As the atomic radius of lanthanides is more important than that of transition metals (225 pm for Tb compared to 152 pm for cobalt which corresponds to a increase of 48%), coordination of the metal is in an out of plane fashion as represented in Figure 3.3.

The LnPc^+ structure has been observed with several lanthanide ions, either after direct evaporation of synthesized mono-phthalocyaninato lanthanide molecules or by “accident” after a fragmentation of a double-decker complex during evaporation because of high sublimation energy. TbPc^+ and DyPc^+ for example have been reported on Au (111) or Pb (111) substrate [40, 47, 48] while LuPc^+ was seen on Ag (111).[49] In the first case, it has been reported that TbPc^+ or DyPc^+ structures adopt a face down position where the ion is directly in contact with the substrate, while in the second case, it is the ligand (Pc) that is in contact with the substrate leading to a tunneling current increase above the ion in STM topography.

The LnPc^+ structure is not stable as the lanthanide is not sufficiently coordinated. Furthermore the positively charged system acts as an acceptor, therefore adding a second deprotonated phthalocyanine (Pc^{-2}) is possible and leads to a more stable complex (see Figure 3.3(b) and 3.3(c)). This new structure noted $[\text{LnPc}_2]^-$ is commonly named double-decker in reference to double deck planes used during the first world war. The TbPc_2 molecule

consists in a central ion (Tb) coordinated to two phthalocyanines (Pc) on each side of the elongation axis of the anisotropy of the terbium, the ion is therefore sandwiched between two ligands as shown in Figure 3.3(b). In this structure, the Ln(III) is coordinated to eight pyrrole nitrogens (four N from each ligand).

Lanthanide double decker complexes have been reported to exist in several oxidation states with different stability orders $[\text{LnPc}_2]^n$ (where $n = -3^2, -2, -1, 0, +1, +2$).^[38, 50–55] However, among all these oxidation states, $n = 0$ and -1 states have been reported to be the most stable for the majority of lanthanides.^[51] In the case of terbium in $[(\text{Pc})\text{Tb}^{\text{III}}(\text{Pc})]^n$, both experimental and theoretical reports are in favor of $n = -1$ as the most stable state.^[38]

The neutral terbium electronic structure is $[\text{Xe}]4f^9 6s^2$. When the atom is coordinated to two -2 donor ligands, it loses three electrons in order to get a filled f-shell. When the lanthanide is at its most stable oxidation state of $+3$ (Ln(III)), its electronic structure becomes $[\text{Xe}]4f^8$. Therefore one of the four electrons of the ligands is distributed to the ion's f-shell, while two others are filling the s-shell. This leaves one excess electron since both phthalocyanines have four supplementary electrons and only three of them are shared with the ion. This supplementary electron is distributed among both ligands as represented in Figure 3.3(b). In terms of orbitals geometrical distribution, lanthanides find their ionic radius decreasing when their atomic number increases. Furthermore the 4f-orbital is located close to the nucleus which makes them hardly accessible in electronic transport experiments. However, recently, S. Fahrenndorf et al. reported a successful STS measurement where they were able to identify and follow the 4f-orbital (close to the Fermi energy) of the NdPc₂ molecule on Cu (100) substrate. Furthermore, Nd atoms are lower in atomic number compared to other commonly used lanthanides in double-deckers. The spatial extension of their 4f-orbital is slightly higher than for other Ln atoms. These properties lead to easier access to the 4f-orbital.^[56]

As mentioned earlier, the large spin-orbit coupling together with an appropriate choice of ligands for the terbium leads to a large anisotropy between the fundamental state and the first excited state. According to Figure 3.1(b) the largest gap (50 meV) is found for the Tb^{+3} . Since presented experimental measurements were done at 4.7 K, only the fundamental state for the ion ($|J|=|L|+|S|=6$) is considered for discussion and interpretation according to Hund's rule for more than half shell filled. ^[57–59]

²See reference ^[50] for the $[(\text{Pc})\text{Ln}^{\text{III}}(\text{Pc})]^{-3}$ oxidation state where it was reported to be very stable during the cyclic voltammetry compared with the $[(\text{Pc})\text{Ln}(\text{acac})_2]^{-3}$ complex

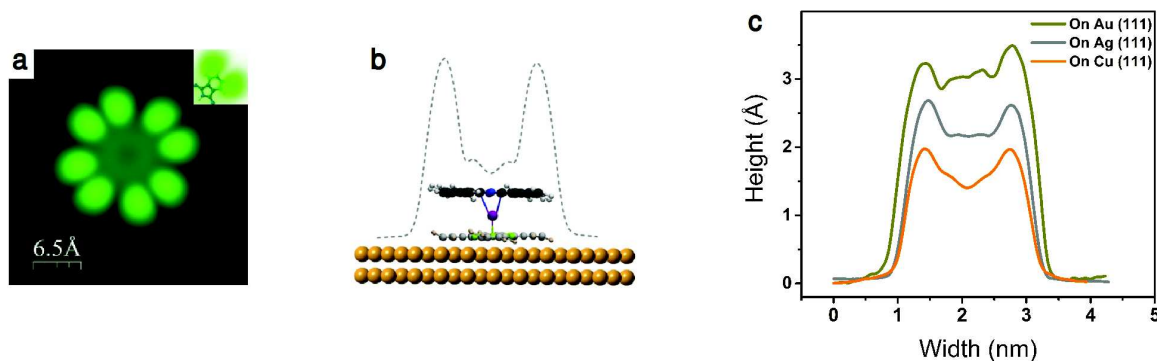


Fig. 3.4 a) Constant current topography image of TbPc₂ adsorbed on a Ag (111) substrate. Four pairs of lobes (making an eight-lobed shape) are visible where each pair belongs to one phenyl (as seen on the inset model of a pyrrole). b) side view of a molecule adsorbed on a (111) plane crystal, the dashed line represent the profile through two opposite lobes. c) Height analysis of the double-decker on various substrates, the difference of height is due to different interaction of the upper ligand with the substrate. Tunneling parameters: $I = 14$ pA and $V = -500$ mV.

The steric repulsion between the two ligands in TbPc₂ complex, leads to a skew angle as represented in Figure 3.3(c), the measured angle is found to be around 45° in the bulk as well as in a the gas phase both, experimentally and theoretically [38, 51, 60–63], whereas Katoh et al. measured an angle of 41.4° on TbPc₂-bulk using X-ray diffraction analysis.[63] However, upon adsorption on a bare surface the orientation of the bottom ligand remains hard to know since the contrast of the upper ligand dominates the STM contrast of the TbPc₂ molecule. Combining present results with previous measurements will help to get more insight into these complexes.

When deposited on substrates, terbium double decker molecules appear as eight lobed structures in the constant current STM topography images of Figure 3.4(a). Each pair of lobes belongs to a single phenyl ring as shown in the phthalocyanine model in the inset. While similar features have been previously reported on occupied state STM images of isolated CuPc and FePc molecules [64–66], decoupling of the upper ligand from the substrate leads to the apparition of eight-lobe features independently from tunneling parameters in the double deckers.

3.3 Height analysis

On different substrates, the molecule shows different heights. First because of the coupling generated by the substrate where the molecule tends to approach the surface as the reactivity increases. Second due to drastic change in the charge transfer between the bottom ligand and the surface resulting in a higher real-space extension of the electronic distribution of the upper ligand (which is contributing to the electron tunneling) when the molecule is close to the substrate. Simple MPc molecules such as CuPc or CoPc have a height between 0.1 nm and 0.15 nm [66]. Under similar tunneling conditions (see caption of Figure 3.4) the TbPc₂ molecules show heights of 3.2 Å, 2.5 Å, 2 Å and 1.8 Å for Au (111), Ag (111), Cu (111) and Co-island respectively. These differences are represented with different colors in Figure 3.4(b). Notice that the geometrical evaluation leads to a molecular height of about 4 Å in the vertical direction. The distance between the bottom-ligand and the substrate plays a major role in the evaluation of the apparent height as between 1.9 Å and 3 Å for Cu and Au respectively are obtained from DFT calculations.

Interestingly, a conductivity drop at the center of the cycle molecule is visible on Cu (111). It is assumed to arise from the higher interaction between the terbium atom and the copper crystal as no conductance is expected in the center of the bottom Pc⁻². [67] Therefore, the substrate also has an effect on the electronic behaviour of the central ion when the Tb-Cu (111) distance is close to 3.4 Å.

Electronic interaction between the substrate and the molecule is summarized through the molecule-interface distance. The binding energy in the case of Co-nanoisland is more pronounced than in Cu (111) followed by Ag (111) and Au (111). Rojas and co-workers have seen a significant increase of the molecule-substrate distance when a H₂TPP molecule is adsorbed on Ag (111) compared to Cu (111). In the latter, the distance between molecule and substrate is $d_{H_2TPP/Cu(111)} = 3.04$ Å, while in the former $d_{H_2TPP/Ag(111)} = 7.02$ Å. This is a 130% increase, as measured from the separation between the pyrrole nitrogens of the molecule and the first atomic layer of the substrate. [68]

Multiple factors are responsible for the vertical displacement of the molecule. Beside the substrate reactivity (or more specifically the work function), the number of atoms underneath the molecule is a major variable since the atomic radius of Au, Ag, Cu and Co atoms are very different. Therefore, the smaller the atomic radius, the higher the number of adsorbate atoms interacting with the molecule.

In Table 3.1 a comparison of calculated and measured TbPc₂ heights are presented along

Table 3.1 TbPc₂ experimental and calculated heights on different substrates (referred to in the first column). d_{ls} denotes the bottom ligand-substrate distance calculated from the center of the closest atom of the first substrate layer to the center of the closest pyrrole nitrogen. Fifth column shows the work function of each substrate in eV.[69, 70]

Metal	Exp. height ($\pm 0,1$ Å)	Calc. height (Å)	Calc. d_{ls} (Å)	Work function (eV)
Au (111)	3.2	5,9	2.9	5,4
Ag (111)	2.5	5,4	2.5	4.5
Cu (111)	2.0	4,6	1.7	4.9
Co-island	1.8	-	-	5

with the upper ligand-substrate distance (d_{ls}). Substrate work function and number of atoms below the molecules are also presented. The area taken underneath the molecule is 3.1 nm^2 , it corresponds to the area measured from the electronic distribution visible through topographic image (Figure 3.4(a)), and therefore not only the bottom phthalocyanine is considered but also the upper one along with molecular orbital extension which also contributes to molecule-substrate interactions.

3.4 Adsorption sites and orientations

Three substrates are presented in this section, Au (111), Cu (111) and Cu (100). Ag (111) and cobalt-islands were not appropriate for the direct identification of TbPc₂ adsorption configuration. In order to determine the adsorption site of the double-deckers on the crystal, simultaneous imaging of double and mono decker molecules (TbPc₂ and either TbPc⁺ or Pc⁻²) on the concerned substrates were recorded. Mono-deckers are obtained after sublimation of TbPc₂ powder by means of crucible evaporator as presented in section 2.3.4. Elevated temperatures necessary to evaporate the double-deckers together with substrate nature lead to an appreciable percentage of fragmentation of the molecule into single phthalocyanine (Pc) or mono-decker (TbPc).[71] This fragmentation is common in LnPc₂ molecules and has already been reported on various substrates.[48, 49, 56, 63]

Substrates were prepared as described in section 2.3.3, atomic resolution images were obtained on some crystals and dI/dV spectroscopy was performed in order to ensure a tip stability and measurements reproducibility. For the site identification, we refer to our own data obtained from the atomically resolved images or to previous investigations on simple phthalocyanine when atomic resolution cannot be recorded. Extrapolation by rotation of the upper ligand by 45° as explained in section 3.2 informs us of the bottom Pc orientation.

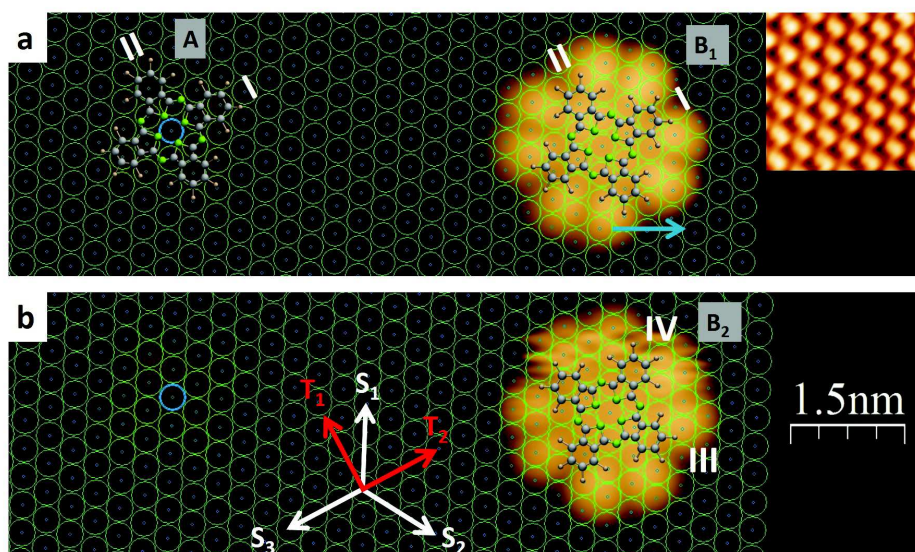


Fig. 3.5 Constant current image of a single Pc⁻² labelled A and a terbium double-decker (B₁ and B₂). Atomic resolution of Au (111) substrate is shown in the inset (top right). a) Shows molecules A and B₁ above which a model of the phthalocyanine molecule is superposed (real configuration for A and bottom ligand for B₁ determined by considering an azimuthal angle of 45° from the upper visible ligand). b) Shows the same molecules after a manual rotation of molecule B₁ along the blue arrow shown in a) the double-decker with new orientation is labelled B₂. Au (111) lattice is superposed on both a) and b) to determine the position site of the bottom ligand of the TbPc₂ and its rotation on the substrate. S₁, S₂ and S₃ represent the three symmetry axes of the (111) surface, an angle of 120° separate them. T₁ and T₂ denote the two direction axes of the single phthalocyanine. T₂ is commensurate with S₃, T₁ makes an angle of 30° with respect to S₁ and S₂. I, II, III and IV represent the real space axes of the bottom ligand.

3.4.1 Gold (111) substrate

It is hardly possible to obtain isolated double-deckers due to long mean free path of the molecules on low reactivity metals such as Au (111) compared to Cu (111) for example. An attempt to deposit TbPc₂ molecules on NaCl layer at 10 K failed, proving that the terbium double-deckers do not stick on insulating layers. Lower temperatures may be needed in order to adsorb the molecules on salt. Atomic manipulation was performed on Au (111) in order to extract single molecule from a domain toward a free area³. Figure 3.5 shows two STM images of a single Pc (A) and two terbium double-deckers (B₁ and B₂) on Au (111). The TbPc₂ molecule was dragged out of a domain by atomic manipulation. The double-decker molecule in 3.5(b) labelled B₂ makes an angle of 30° with respect to the molecule

³Next chapter is dedicated to the domain formation and their properties.

labelled B_1 in Figure 3.5(a). This orientation was generated by pulling one of the lobes along the $[11\bar{2}]$ direction as represented by the blue arrow in Figure 3.5(b).

As observed previously, single phthalocyanines show cross like features corresponding to the molecular geometry of the phthalocyanine. Considering the atomically resolved image shown in the top right inset of Figure 3.5(a) a positioning on a top site for the single decker molecule is observed.

On Figure 3.5 we superimposed the Au (111) lattice structure along with a phthalocyanine model following the atomic resolution topography to show the adsorption site and the directions. The Pc model of molecules B_1 and B_2 represent the bottom ligand which is hybridized to the Au (111) surface as anticipated from the upper ligand visible in the topography image by considering a 45° rotation along its azimuthal axis. Three white axes S_1 , S_2 and S_3 in Figure 3.5(b), separated by an angle of 120° show the close packed high symmetry directions of Au (111) surface. T_1 and T_2 show the two orthogonal directions of two adjacent pyrroles of the phthalocyanine molecule also labelled I and II respectively in A.

We notice in Figure 3.5(a) that for molecule A two opposite pyrroles along the axis labelled I and represented by T_2 direction are aligned following one of the three crystallographic directions which is labelled S_3 . The other pyrroles are aligned along axis II represented by T_1 direction, they do not coincide with any of the other substrate directions (S_1 or S_2). Axis II makes an angle of 30° with respect to S_1 and S_2 .

By extrapolation of the surface lattice towards the double-decker, we observe that the exact same adsorption site and orientation as molecule A occurs for the bottom Pc of the molecule labelled B_1 . The center of both phthalocyanines of A and B_1 is positioned on top of a gold atom. Two opposite pyrroles are adsorbed along axis I while the two others are adsorbed along axis II. The molecular model of the phthalocyanine and the bottom ligand for B_1 clarify this observation.

Indeed, when molecule B_1 is rotated by an angle of 30° (by means of atomic manipulation as shown with the blue arrow of Figure 3.5(b), an adsorption site switch occurs between the four pyrroles. Thus the two opposite pyrroles that were initially adsorbed along axis I, are now adsorbed following axis IV Figure 3.5(b). The axis labelled III goes along with the S_2 direction while IV makes an angle of 90° with respect to S_2 and an angle of 30° with respect to S_1 and S_3 . Molecules B_1 and B_2 can therefore be considered as symmetrically equivalent. Therefore, for the Au (111) substrate, the adsorption site for $TbPc_2$ molecule is a top site, with two pyrroles adsorbed along one of the compact high symmetry direction of the surface lattice, the two other pyrroles lying along an in-plane perpendicular direction. Both, initial adsorption site and after manipulation support the deduction that 45° separates the two ligands.

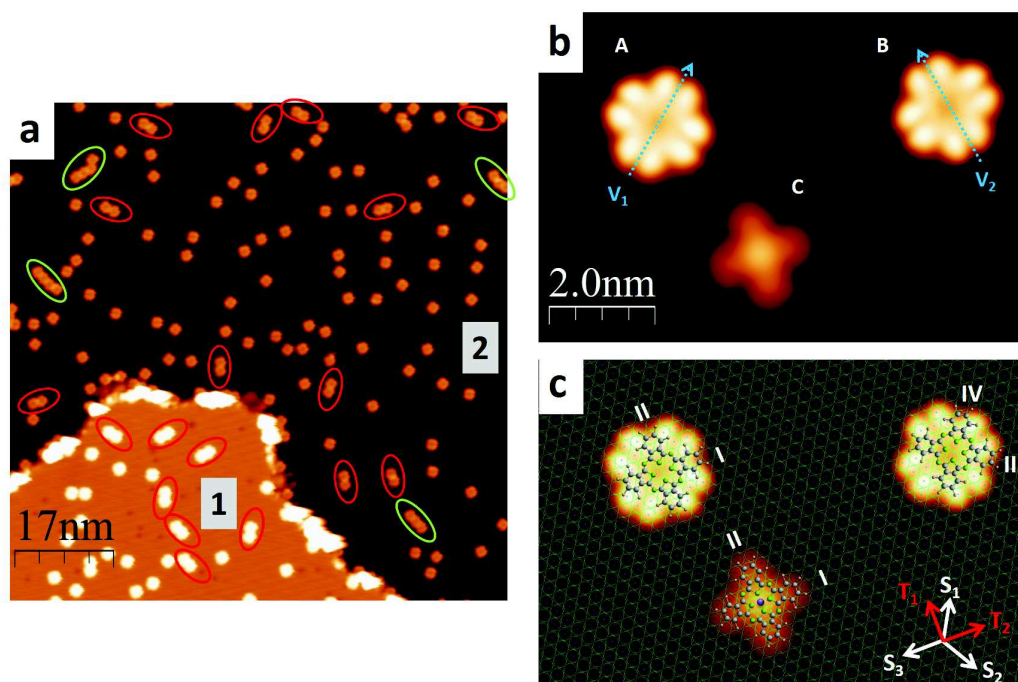


Fig. 3.6 Constant current topography images of Cu (111) substrate after deposition of TbPc₂. a) Large topography image taken at $V = -400$ mV and $I = 0.6$ nA tunneling conditions, two Cu (111) layers are visible. 1 and 2 represent the highest and lowest layer respectively. Protrusions seen on both levels correspond to double-deckers molecules. The red and green ellipses surround dimmers and trimers/tetramers respectively. b) Closer view of an area showing two TbPc₂ molecules (A and B), two orientations are visible through the vectors V_1 and V_2 representing the upper phthalocyanine directions. A single TbPc labelled C is also observed. c) Is the same topography image as b) with Cu (111) model superposed to show the site occupancy and orientation directions. b) and c) were taken at $I = 0.2$ nA and $V = -350$ mV

3.4.2 Copper (111) substrate

On more reactive substrates, as in the case of Cu (111) the molecules are more scattered over the surface because of the small diffusion path at room temperature generated by high molecule-substrate attractive interactions. The distribution of TbPc₂ on Cu (111) is not influenced by repulsive interaction between the molecules as small islands (dimers, trimers...) are found in the STM topography of Figure 3.6(a), see red and green ellipses. This is an indication of a low mean free path of the double-deckers on the Cu (111) substrate. Nevertheless, the presence of islands translates the existence of an intermolecular interaction. The distance measured between two molecules in a dimer is $1.7 \text{ nm} \pm 0.1 \text{ nm}$ which is by 0.2 nm larger than the geometrical size of a single phthalocyanine.

Figure 3.6(a) shows a large area topography image of the Cu (111) substrate with two atomic terraces labelled 1 and 2 after deposition of TbPc₂ molecules under relatively small flux (to avoid the formation of islands and domains). The bright protrusions in Figure 3.6(a) correspond to TbPc₂ molecules. An accumulation of molecules at the step edges of the higher atomic layer 1 is also confirmed.

Isolated double-deckers adopt their adsorption site and orientation by only taking into account the molecule-substrate interaction. Indeed, shortest distance (center to center) measured between two non-interacting molecules adsorbed on Cu (111) substrate is equal to $2.7 \text{ nm} \pm 0.2 \text{ nm}$. This is a major result that informs about the minimum distance upon which the molecule-molecule interaction overcomes the molecule-substrate interaction.

Figure 3.6(b) shows two TbPc₂ molecules labelled A and B, these two molecules have different orientation as indicated by V_1 and V_2 vectors (these two vectors indicate the directions of one of the two symmetry axis of the four-fold symmetric phthalocyanine). Along with an important amount of double-deckers on Cu (111), a few single deckers are also found. Such MPc (labelled C) molecules are identified thanks to their well known four lobed shape and lower height compared to the double-decker. One can expect M to be either a terbium atom, resulting from the decomposition of the double-decker as $\text{TbPc}_2 \rightarrow \text{TbPc}^+ + \text{Pc}^{-2}$ or a metal ion provided by the substrate itself since Pc^{-2} is able to extract one atom from the surface atomic layer to coordinate a Cu^{+2} as previously reported [72, 73]. However the latter possibility is less likely because of the profile height of the molecule which is found higher than what is observed in regular CuPc.[46] Furthermore, an atomic manipulation of the MPc did not show any impurity underneath the initial position of the phthalocyanine, leading to conclude that only a terbium atom can play the role of the coordinated metal in the MPc molecule.

The orientation difference between molecules A and B is measured through the angle created by the two vectors V_1 and V_2 , this angle is found to be $\alpha = 60^\circ \pm 1^\circ$. Interestingly it has the same value as the angle obtained between two symmetry axes of a hexagonal structure.

The analysis of various topographies with multiple molecular adsorptions revealed three main orientations of TbPc₂ molecules on Cu (111) orientations differing from each other by an angle of 120° . Considering a skew angle of 45° between molecular ligands, this observation remains correct for the bottom phthalocyanine joining therefore the close packed high symmetry directions S_1 , S_2 and S_3 corresponding to [110], [101] and [011] directions respectively. Deng et al. have recently confirmed this observation by imaging using an STM a terbium double decker at 45 K highlighting the three S orientations. [74]

B. Heinrich investigated CoPc molecules on a Cu (111) substrate; he imaged the topmost Cu atoms by means of atomic manipulation by co-depositing Co atoms and CoPc molecules. Dragging around a Co atom with the STM tip led him to image the atomic layer of the substrate.[75] By extrapolating the indirectly resolved atomic structure of the crystal layer, he found that the metal atom in a CoPc molecule adopts a bridge site position on the copper substrate (see Figure 3.7). This result confirms other observations of adsorbed MPC molecules on Cu (111). [76–78].

The orientation of the metal-phthalocyanine is deduced from Heinrich's observations. As two opposite phenyls lay on bridge site along one of the three high symmetry directions of the crystal (horizontally in Figure 3.7), the two other phenyls are adsorbed on hollow sites following a direction which makes an angle of 30° with respect to one of the crystal symmetry axes (vertical axis in Figure 3.7).

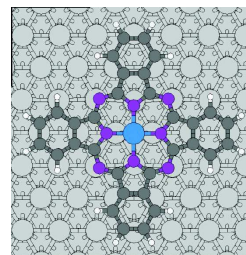


Fig. 3.7 *CoPc (model) adsorbed on Cu (111) substrate, the Co atom is positioned on a bridge site. Two phenyls are sitting on a hollow site, while the two others lay on a bridge site. [75]*

It is therefore legitimate to assume that the same positioning occurs in the present situation. Figure 3.6(c) shows the same topography image as Figure 3.5(b) upon which is superposed a surface lattice model. Phthalocyanine models are also superposed to show the orientation of the molecule, in the cases of molecules A and B, the phthalocyanine model refers to the bottom ligand. It was oriented by 45° according to the direct measurement performed on the upper ligand. The TbPc model of molecule labelled C shows the exact orientation and position of the mono-decker.

From Figure 3.6(c) we observe the same position and orientation for the bottom ligand of molecules A and C. T₁ and T₂ directions denote the two axes of the four-folded mono-decker. In both molecules, T₂ is collinear with S₃ direction. Axis II makes an angle of 30° with respect to both, S₁ and S₂. Molecule B shows a second possibility of orientation where axis III and IV (previously I and II) in B are rotated clockwise by 30° with respect to molecules A and C. Therefore the pyrroles along axis IV lay on the S₁ high symmetry direction of the substrate while the axis III creates an angle of 30° with respect to the other directions (S₂ and S₃).

Both molecules have the same occupancy site according to the extrapolation of the sur-

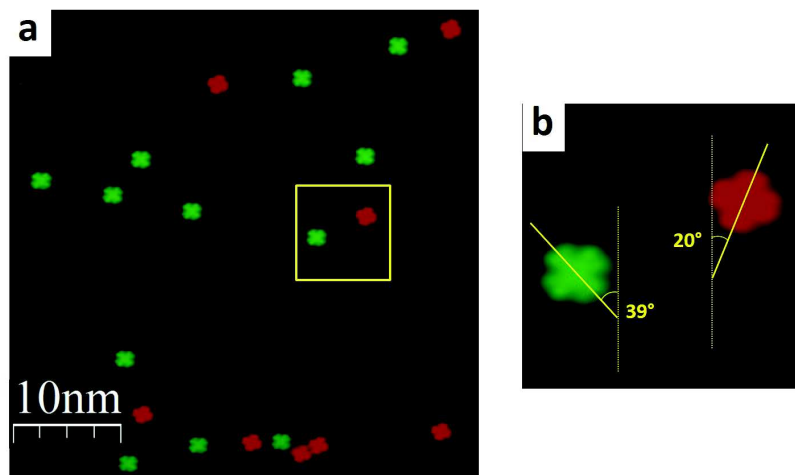


Fig. 3.8 Constant current topography image of Cu (100) substrate after small amount deposition of TbPc₂ molecules. Only two orientations are observed, they are colored in red and green respectively. b) Shows a zoom onto the square area in (a), the configuration difference is measured by means of angle evaluation. Red molecules show an angle of $59^\circ \pm 1^\circ$ with respect to green molecules. Image was treated using fast Fourier transform (FFT) in order to clearly differentiate the two molecular orientations.

face layer in Figure 3.6(b). Their orientation is not different since in both cases the two opposite phenyls occupy a bridge site, while the two others occupy a hollow site. Therefore, we assume that these two molecules are similar in terms of site occupancy and ligand position.

A special case may occur when the molecule occupies a so-called metastable state. In this situation the central ion resides above an atom of the surface layer instead of sitting on a hollow site as seen before [75]. Vitali et al. found a rotational angle of 45° between two isolated TbPc₂ on Cu (111) substrate [62]. In their experiment, the molecules were deposited using a novel technique called “dry-imprint”, a brush was used to drop molecules on the substrate while the whole system was kept at 4 K. One can deduce that one of the terbium double-decker in the latter case occupies the metastable state generating an angle of 45° with respect to a molecule adsorbed at a top site on the same substrate. This configuration has been found by calculation to be by 0.3 eV higher in energy than the bridge site adsorption.[75] During the whole process from evaporation to surface imaging, this energy was not reached; therefore it is hardly possible that our molecules occupy a “top” site.

3.4.3 Copper (100) substrate

Double-decker molecules adsorbed with coverage of 5% Cu (100) are shown in the constant current topography image in Figure 12(a). The substrate-molecule interaction is found to be stronger on Cu (100) compared to Cu (111) as the shortest distance between two non-interacting molecules is found to be equal to $2.0 \text{ nm} \pm 0.2 \text{ nm}$. Contrary to previous cases where three orientations were found on Au (111) and Cu (111), only two orientations were found on copper (100) surface. These two orientations are illustrated with different colors (red and green) in Figure 12(a). A zoom into the area of Figure 12(b) allows analyzing both configurations.

The Cu (100) substrate has a four-fold symmetry. The two orientations differ by an angle of $59^\circ \pm 2^\circ$ in fair agreement with the observation of Liu et al. where an angle of 56° separates two orientations of H₂Pc molecules on Cu (100).[79] In the present situation, as in the (111) direction of the same substrate, the center of the phthalocyanine resides above a copper atom (top site). For simple H₂Pc, a chiral-like topography is observed for both orientations due to the different electron transfer from the substrate through the legs (report to Figure 12 in Appendix). This asymmetry is not apparent when the molecule is a double-decker, mainly because the upper ligand is not in direct contact with the substrate and therefore cannot be influenced by its symmetry.

3.5 Tunneling spectroscopy above single molecules

In order to get further insight into the electronic distribution of terbium double-decker molecules, multiple spatially resolved spectroscopies (STS) have been recorded. The STM tip is positioned on a well contrasted TbPc₂ molecule and the feedback loop is opened in order to eliminate tip-molecule fluctuations during measurement (as described in section 2.2). Then the voltage bias is ramped from negative to positive values to collect averaged conductance. Scanning tunneling spectroscopy is the most convenient technique to access molecular density of states. In the present case, distinct differential dI/dV spectroscopies were recorded on a single isolated TbPc₂ molecule.

On Cu (111)

Figure 3.9 presents a differential conductance investigations performed on a TbPc₂ molecule adsorbed on a Cu (111) substrate. The overall spectral shape shows two major peaks (see Figure 3.9(a) when dI/dV is ramped from -2 eV to + 2 eV on the molecular center. These

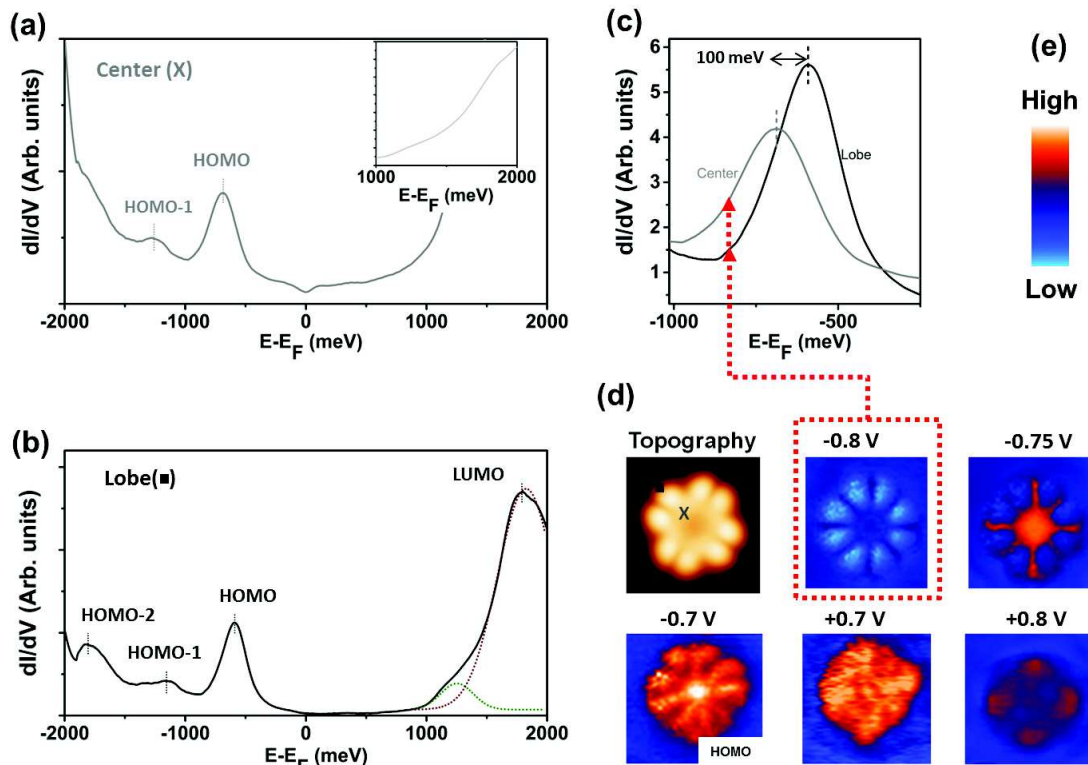


Fig. 3.9 Differential conductance spectrum (dI/dV) within a range of -2 eV to $+2$ eV of a $TbPc_2$ molecule adsorbed on a Cu (111) surface. STS was recorded when the tip was placed above the center (a) and on a lobe (b) as presented in constant current topography image in (d). Two peaks defined as HOMO and HOMO-1 are visible in both locations. On lobe (b) a third HOMO-2 peak appears at -1.8 eV. Two Gaussians (dotted green and red lines) positioned at 1.2 eV and 1.8 eV are superimposed to identify their possible overlapping leading to the apparition of the LUMO. (c) comparative view of the HOMO as recorded on the two positions showing a 100 meV shift. Besides, a conductance amplitude variation is observed. Feedback loop was opened at $I = 0.2$ nA and $V = -0.4$ eV. (d) constant current differential conductance maps of isolated $TbPc_2$ adsorbed on Cu (111) substrate. Positive bias shows a uniform distribution all over the upper ligand. On the negative side, the distribution goes from a delocalized distribution over the upper ligand with a high conductance on the terbium atom at -600 meV to a localized distribution above the metal atom (-700 meV) to reach a conductance inversion at -800 meV where the lobes are less conductive than the rest of the molecule.

two peaks are positioned in the occupied states at -700 meV and -1250 meV, they are defined as HOMO and HOMO-1 respectively. The first resonant peak (HOMO) is consistent with previous reports where it was observed at -1.1 eV on Ir (111) and at -900 meV on cobalt layer grown on Ir (111).[80, 81]

A significant increase of conductance is observed at the edge of the positive bias values without reaching a local maximum (as shown in the inset of Figure 3.9(a). Accordingly, further bias voltage was not recorded as it would change the molecular electronic properties and result in a falsified interpretation. Therefore, no LUMO was observed at the center on Cu (111) translating a high molecule-substrate interaction.

When the tip is moved towards one lobe⁴ (Figure 3.9(b)) dI/dV spectroscopy shows a shifted HOMO by 100 meV towards the Fermi level as highlighted in Figure 3.9(c). This shift denotes that a different contribution from the substrate appears at the lobe compared to the center where fewer electrons are exchanged between upper ligand phenyl rings and the substrate. Moreover, 34% conductance increase is observed for the HOMO in the lobe compared to the center. This increase of amplitude indicates that the upper phthalocyanine mainly participates to the HOMO due to less effective substrate interaction on this ligand.

Interestingly, the gap separating HOMO-1 and HOMO remains stable ($\Delta E \approx 570$ meV) when the tip is moved from center to lobe. It indicates that both orbitals have the same origin which is not affected by the tip displacement over the upper ligand. Since the bottom half of the molecule (TbPc) is strongly coupled to the substrate, an orbital modification on the bottom side is expected between the terbium and the bottom ligand. Therefore, since the upper ligand is further from the crystal, its orbital delocalization is expected to lead to a constant HOMO-1–HOMO gap all over the upper phthalocyanine.

The previously observed conductance increase at the edge of +2 eV on the center (3.9(a)) is now located as a resonant peak at +1.8 V and is ascribed as the LUMO (Figure 3.9(b)). This peak has been reported at +1.5 V and +1.8 eV when the molecule is adsorbed on Ir (111) or Co layer respectively.[80, 81] Besides, a shoulder appears at the rising stage of the LUMO peak, this shoulder can be considered as a Gaussian peak participating to the total LUMO observed by STS. It is indicated as two dotted lines drawn in Figure 3.9(b) representing a potential overlapping of two orbitals separated by 500 meV. It is worth to note that Cu (100) substrate shows exactly the same orbital energy features as Cu (111) meaning that copper crystal symmetry does not affect the molecular electronic structure.

⁴Note that all eight lobes depict the same spectroscopy signature and are therefore assumed similar to each other.

By investigating the dI/dV mapping, substantial information about spatial distribution of the electronic states and their conductance contribution is obtained. Constant current dI/dV mapping performed (as described in section 2.4) on an isolated $TbPc_2$. When adsorbed on Cu (111) substrate is depicted in 3.9(d) showing various conductance contrasts within a small energy range (-0.8 eV to +0.8 eV). For instance, the mapping at the HOMO energy as observed in dI/dV spectroscopy (Figure 3.9(c)) shows a localization of this peak at the central region of the molecule, and a delocalization on the upper phenyls. Furthermore at higher energy (-750 meV) a bright node appears above the metal atom (terbium) with no conductance contribution from the upper phthalocyanine. This suggests that the HOMO evolves from the upper ligand phenyl rings toward localization at the central region.

Interestingly, when mapping the conductance at -800 meV, all lobes appear with a lower conductance compared to the rest of the molecule (Figure 3.9(d)). This spectral inversion is explained by the difference in conductance amplitude as observed in Figure 3.9(c). Indeed the dI/dV amplitude is more pronounced on the center compared to the lobe location as highlighted with vertical dotted line (red) in Figure 3.9(d) translating into a lower conductance over the eight lobes in STS mapping.

On the other hand, when the bias voltage is turned to positive values, the molecule periphery is highlighted as well as the central area, uniformizing therefore the electronic distribution over the upper phthalocyanine. A cross-like shape appears with a bright spot on its center following the four pyrrole directions.

These results are consistent with previously reported measurements of $TbPc_2/Cu$ (111)[62] where Vitali et al. observed a uniform distribution at +800 meV from dI/dV spectroscopy corresponding to the actual LUMO. Nevertheless, their results slightly differ because of different STM/STS investigation parameters.

On Ag (111)

On a lower reactive substrate which is Ag (111), the dI/dV conductance of an isolated $TbPc_2$ molecule depicts one HOMO peak positioned at ≈ -570 meV on lobe and ≈ -600 meV on the central region, see Figure 3.10(a). These values are in lower energy compared to the ones obtained on copper. This displacement is consistent with the expected variation of the adsorbate reactivity. Indeed, by lowering the substrate reactivity, the molecular orbitals shift toward Fermi level. For instance, a non resolved shoulder like appears at the positive bias voltage, this conductance increase is expected to host a LUMO peak. The highest conductance value is positioned at ≈ -330 meV leading to a possible HOMO-LUMO gap of 950

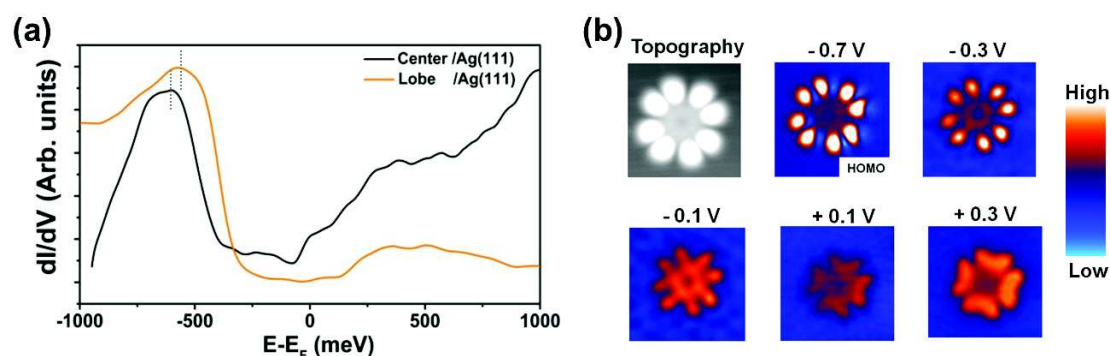


Fig. 3.10 a) dI/dV spectroscopy performed at both, center and lobe of an isolated TbPc₂ molecule adsorbed on Ag (111) substrate. b) constant height differential conductance performed on the same molecule. Voltage bias are indicated on each image. Eight lobes are clearly visible at negative polarity while a boomerang shape is obtained at positive bias. Tunneling parameters were set at $I = 0.7$ nA and $V = 0.4$ V before feedback loop opening.

meV⁵.

Interestingly, a noticeable drop of conductance is observed at -200 meV when the STS is recorded on the center. This feature is similar to the Ag (111) surface states as reported in Figure 2.3. It represents the presence of substrate contribution at the central area (on terbium) as it disappears above the phenyl rings.

Constant current conductance mapping were recorded on TbPc₂ as it was adsorbed on Ag (111) substrate (Figure 3.10(b)). Interestingly, the overall shape of the electronic distribution on the molecule has similar form for a given polarity.

For instance, the eight lobes defining the upper ligand are well-resolved in negative bias voltage as they depict a saturated conductance compared to the rest of the molecule. Investigation of the occupied states shows a well distributed conductance over the upper ligand at low energies (-0.1 eV), while it increases to saturation at the lobes when the energy reaches -0.7 eV. It indicates localization among the occupied orbitals at the phenyls represented by the eight lobes. Interestingly, the central part depicts a dark spot at all negative energies indicating that a low orbital extension originates from the terbium atom.

On the other hand, when the STS mapping investigate the unoccupied states (positive bias voltage), only four elongated “boomerang-like” lobes are observed, see Figure 3.10(b). Two of adjacent phenyls are connected to each other through outer nitrogen atoms. Besides, the conductivity is enhanced on these rings at high positive biases and tends to be reduced

⁵This value is approximative since no well-defined peak is observed for the LUMO on Ag (111), it is however assumed to be close to the one found on Au (111) because they both rise in a similar energy region.

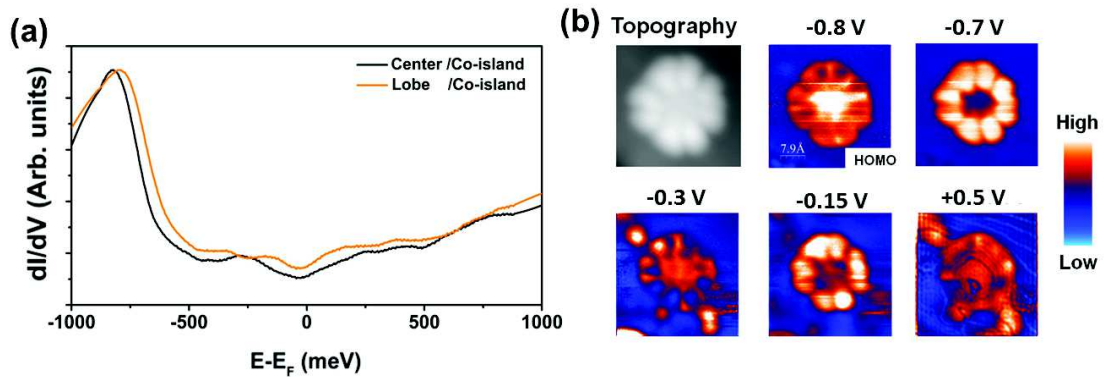


Fig. 3.11 a) dI/dV spectroscopy recorded on a $TbPc_2$ molecule adsorbed on a Co-island grown on a Cu (111) substrate. b) constant current conductance of the same molecule. (b) show a dI/dV mapping at the mentioned voltages. Feedback loop was opened at $I=90$ pA and $V=-0.8$ V

toward a more uniformly distributed conductivity over the upper ligand when the bias is reduced to +100 meV.

On Co-islands

Figure 3.11 shows a dI/dV point spectroscopy and differential conductance mapping of $TbPc_2$ molecule adsorbed on a Co-island. Cobalt nano-islands were grown following the same procedure as described in section 2.3.4. Large islands (≈ 15 nm width) were found on large crystal step-free area (more than 100 nm²). Due to its strong reactivity, cobalt islands are easily contaminated, therefore short exposition to molecular evaporation and fast transfer are necessary. However, even with these cautions, the islands do not have flat-area as most protrusions that are visible in topography image in Figure 14(a) (Appendix) originate from double-decker fragmentation.

The overall spectra shows only one peak at negative bias assigned to a HOMO peak at -800 meV ± 10 meV on both, molecular center and lobe, see Figure 3.11(a). The non variation of this peak among the position indicates a high distribution of the HOMO at the upper ligand including its empty center. This results from a high hybridization of the molecule with the substrate. Indeed, cobalt islands are expected to have the highest reactivity among all studied substrates leading to a higher molecule-substrate interaction. Schwobel et al. [81] investigated similar molecule on a cobalt layer grown on Ir (111) substrate, they observed the HOMO peak at -900 meV.

Figure 3.11(b) shows the spatial orbital extension as seen in the corresponding spectroscopy in Figure 3.11(a). As observed in both, point spectroscopy and STS mapping the HOMO seems to originate from the lobes to become more localized at the center (above the terbium atom) when the bias voltage is increased to vanish afterwards. At -300 meV the orbital distribution is evenly spread at the central area where considerable conductance is measured (see corresponding conductance mapping in Figure 3.11(b)). Furthermore, for -150 meV the upper ligand is again the only contributor for the electronic distribution for the occupied states.

When mapping is performed above E_F , unoccupied states show a relatively uniform distribution all over the molecule as seen in Figure 3.11(b) at +500 meV. This result is predicted by the low variation in the dI/dV spectra at positive energies in Figure 3.11(a).

Summary of substrate effect on molecular orbitals

Accordingly, the conductance on the terbium double decker molecule is altered by the substrate reactivity. Indeed, even though the overall shape of the spectra on all the substrates is similar within -1 eV to +1 eV, decreasing the substrate reactivity from Co-island to Au (111) substrate lead to a HOMO shift toward Fermi level (See Figure 13 in Appendix). It implies that related energy shifts (with respect to E_F) are driven by chemical potentials adjustments to equilibrium at the interface. For vacant states, only gold and silver showed a contribution (non-resolved) testifying that LUMOs are highly affected by the substrate nature upon adsorption.

Furthermore, the molecular screening increases on more reactive substrates such as Co-island or Cu (111) compared to other substrates. This is reflected by a large HOMO-LUMO gap on the former crystals while reduced in the latter ones. Indeed, measured gap value is 800 meV, 950 meV⁶, 2.4 eV and 2.6 eV for Au (111), Ag (111), Cu (111) and Co-islands⁷ respectively. A similar effect is observed when the HOMO-LUMO gap was measured on fullerene molecules as it was found varying by 1.1 eV between Au (110) and Cu (111).[82]

3.6 Kondo resonance appearance on Au (111) surface

By measuring the local density of states above the eight lobes of the terbium double-decker molecule adsorbed on a Au (111) surface, a strong resonance located at the Fermi level

⁶This value is approximative since no well-defined peak is observed for the LUMO on Ag (111), it is however assumed to be close to the one found on Au (111) because they both rise in a similar energy region.

⁷See Figure 14(c) in appendix.

region (zero bias peak, ZBP) is clearly observed. The following measurements were performed on many different isolated molecules at various adsorption sites. Thus the ZBP was proved to be independent on any adsorption site or orientation of the molecule on the substrate.

This resonance vanishes when the tip is shifted away from a lobe and is absent when STS measurements are taken on the bare Au (111) substrate or at the central area of the molecule. Measurements of this peak height versus tip-sample distance have shown its dependency to the vertical displacement and the resonance is more pronounced with high tunneling current. Besides it tends to be reduced to noise level when reducing the tunneling current, as presented in Figure 3.12(e) within a range of 2 Å to 4.7 Å. The resonance has a Lorentzian shape as fitted (in red) in the same image, while the peak apex remains at the same energy position ($5.2 \text{ meV} \pm 0.1 \text{ meV}$) for all measurements where a ZBP appears. For a tip-sample distance Δz higher than 3.7 Å, the ZBP could hardly be observed. Therefore, appropriate tunneling conditions were used to keep Δz below this value. The tip sample distance was stabilized on a free area of Au (111) to avoid any miscellaneous contribution of the molecule or its environment. Appearance of the ZBP peak is similar to previously reported Kondo peaks obtained on magnetic mono-decker and double-decker complexes.[17, 63, 83–85]

Figure 3.12(d) presents the analysis of two high resolved tunneling conductance dI/dV spectroscopies recorded above one lobe within a short energy range of a single isolated molecule TbPc_2/Au (111) marked as I and on a second layer molecule $\text{TbPc}_2/\text{TbPc}_2/\text{Au}$ (111) marked as II. The obtained Kondo resonance on a lobe of a single TbPc_2 molecule is fitted by a Fano function in Figure 3.12(d) (marked as I) with the following Fano parameters: $q=3.93$, $\Gamma=9.56 \text{ mV}$ and $E_0=5.23 \text{ meV}$ (because of the Coulomb repulsion), yielding to a Kondo temperature $T_k=38 \text{ K} \pm 1 \text{ K}$. Nevertheless, it is quite far from temperatures observed on mono-decker molecules as FePc , CoPc or TbPc which were found at higher temperatures.[63, 84, 86] In these systems, the Kondo resonance is produced through 2D surface electron scattering by the magnetic atom, while herein, the magnetic ion is not directly responsible for the Kondo presence. Accordingly, the terbium still plays an important role since no Kondo resonance was found on lobes for the other LnPc_2 complexes. A reduced Kondo temperature along with a high value of Fano parameter q (compared to other systems) indicates smaller ligand hybridization (upper ligand in the present case) to the substrate and high coupling between the tip and the magnetic impurity in accordance with our previous observations.

Besides, atomic manipulation led us to conclude that ZBP appearance is not site dependent

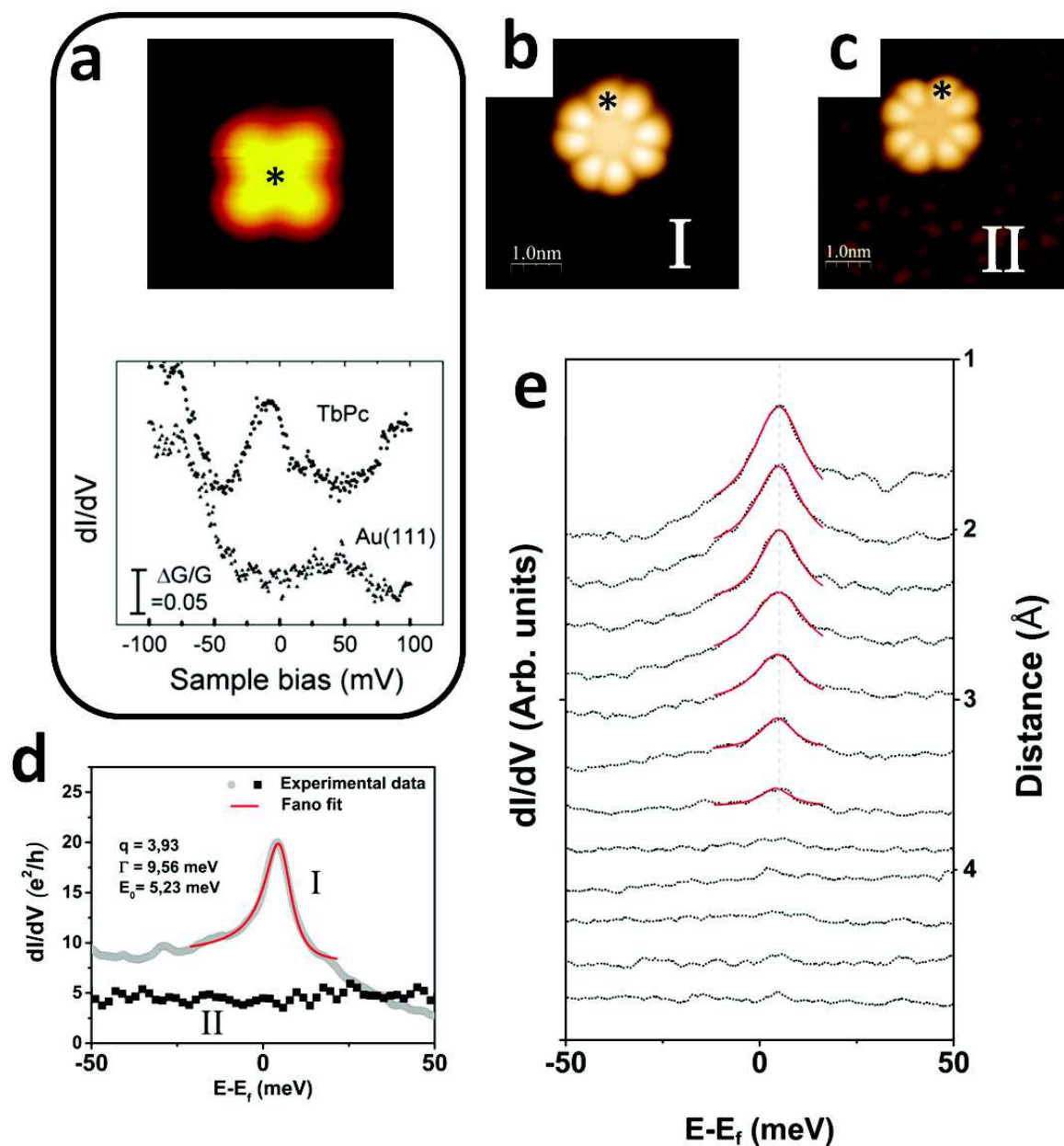


Fig. 3.12 a) Topography image and dI/dV spectroscopy of a TbPc monomer obtained by Katoh et al.[63] showing the presence of a Kondo peak at the terbium position. STS on Au (111) is also recorded for calibration. b) and c) depict a topography image of isolated TbPc₂ molecule at the first layer (I) and a second layer (II) respectively. d) shows a dI/dV spectroscopy obtained at the indicated positions by a star in b) and c). A Kondo resonance is apparent in (I) but not in (II). ZBP peak is fitted with a Fano equation revealing the indicated parameters. e) shows the variation of the Kondo resonance with respect to tip-sample distance.

as it was seen on FePc molecules [84]. It also does not depend on the bottom ligand orientation with respect to crystal directions of Au (111).

As previously mentioned in section 3.2, the electronic configuration of a Tb^{+3} is $[\text{Xe}]4f^8$ and both ligands provide three electrons (to the ion) due to their mutual deprotonation. Therefore two spin systems coexist and may lead to a Kondo resonance. One spin system involves the magnetic atom, at low temperatures and because of a non-negligible hybridization of the terbium and the substrate, the delocalized 2D conduction electrons become polarized in order to balance the total magnetic moment of the impurity and a spin screening occurs between the surface 2D electrons and the terbium.

The second spin system involves the excedentary spin delocalized over the upper ligand and originated from deprotonation of one site of the ligand. In a terbium double-decker molecule, a degenerated spin 1/2 is distributed on both phthalocyanines when the molecule is in a gas phase. When adsorbed on a substrate, the delocalization of this electron is only situated on the upper phthalocyanine, thus filling its open pi-shell. Under tunneling conditions this degenerated 1/2 spin may scatter the 2D surface electrons leading to ZBP apparition at Fermi energy.

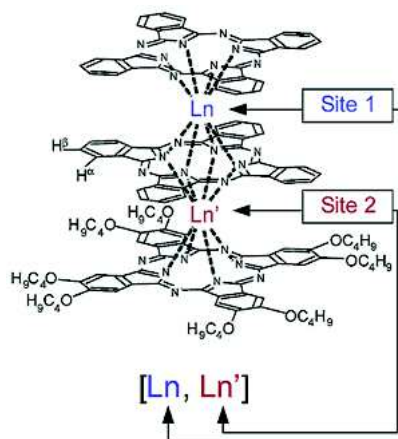
In order to determine which one of these two spin systems is responsible for the Kondo resonance, a discussion will proceed as follows: first a very short overview of previous measurements that contribute to the understanding of this resonance source will be given, then analysis of the results will be made in order to perform a comparison and ascertain the zero bias peak (ZBP) origin.

In 2009, Katoh et al.[63] measured the Kondo peak resonance on a terbium mono-decker TbPc which was obtained after sublimation and fragmentation under high temperature energy. When the tip was positioned above the terbium atom, ZBP was detected and attributed to Kondo resonance. The full width at half maximum (Γ) was determined by fitting the Kondo peak as a Fano resonance with $\Gamma = 22$ mV and a Fano parameter $q = 4.5$.

The corresponding temperature was evaluated to $T_K \approx 250$ K, see Figure 3.12(a). This temperature is comparable to those recorded on other MPc molecules like CoPc (208 K) [86] and FePc (360 K) [84]. Kondo resonance is strictly located on the metal atom and vanishes when the tip is moved away.

N. Ishikawa et al. examined terbium di-nuclear triple-decker complexes by means of superconducting quantum interference device (SQUID).[87] The triple deckers are composed

Fig. 3.13 Molecular model of the PcLnPcLn'Pc* where Ln and Ln' denote two lanthanides. Site 1 and site 2 denote the furthest and closest ion to the substrate respectively. Two different lanthanides were used in order to determine $\Delta X_m T$. From ref. [87]



of two trivalent terbium atoms (Tb⁺³) and three di-anionic Pc ligands (Pc,Ln,Pc,Ln',Pc*)⁸ as presented in Figure 3.13. Under STS measurements no Kondo peak could be observed for this system and a non-negligible f-f interaction between the two terbium atoms was observed. This is surprising considering that f-electrons are located near the nucleus.

Susceptibility measurements led them to ascertain ferromagnetic coupling between the two lanthanides below 50 K. The origin of this interaction was explained by means of the ligand field theory (section 1.2), different lanthanides being compared in the Ln₂Pc₃ system. A large anisotropy is found in the z-direction when Ln=Tb leading to substantial energy exchange value $\Delta X_m T$. In a second communication [88], by measuring the susceptibility, it was proven that in a Tb₂Pc₃ complex two ions relax independently even though they are coupled to each other. Furthermore, when adsorbed on a magnetic layer such as Ni, Tb₂Pc₃ depicts reduced remanance of the upper terbium, thus translating a negligible interaction with the substrate compared to the closer ion to the magnetic substrate.[89] Accordingly, the Tb₂Pc₃ molecule behaves as a SMM and the f-f coupling between the two lanthanides with low relaxation of the upper terbium makes the magnetic behavior of the Tb to act as a SMM independently from the bottom metal or the substrate.

Comparison with an isolated double-decker molecule on a second layer supports assumptions concerning the Kondo peak origin. Figure 3.12(a) presents a constant current topography image of an isolated TbPc₂ molecule on a second molecular layer (marked II in the image). It is well known that for organic and organometallic complexes the first molecular layer acts as a decoupling layer for the second monolayer. Furthermore, the increased distance of the second layer molecule leads to total decoupling from the substrate. When the

⁸Pc* = dianion of 2,3,9,10,16,17,23,24-octabutoxyphthalocyanine (bottom ligand)

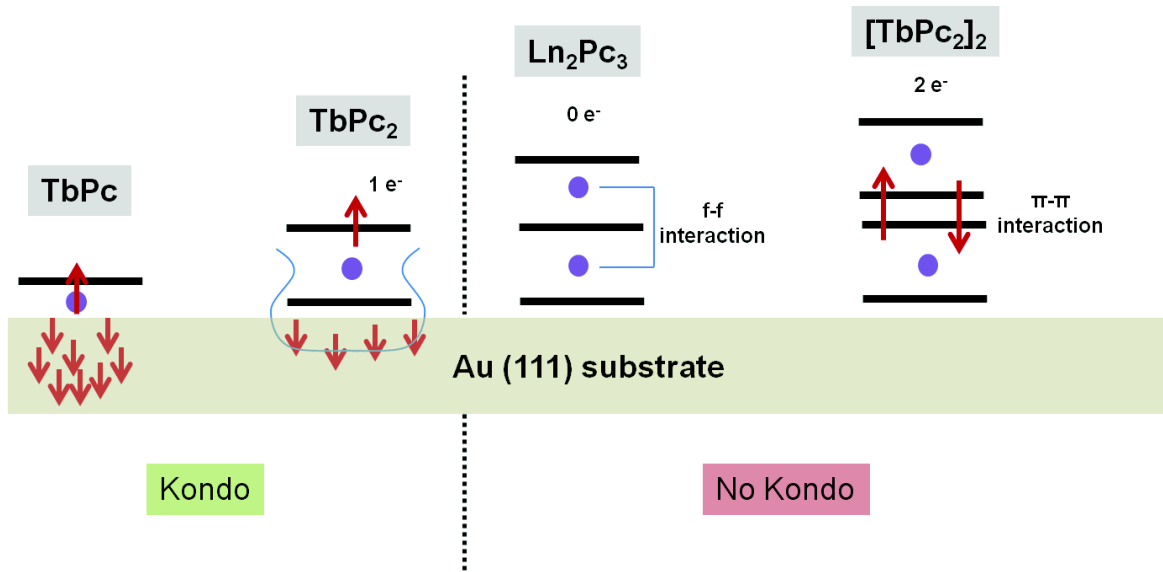


Fig. 3.14 Basic schematics of TbPc, TbPc₂, Tb₂Pc₃ and (TbPc₂)₂ on a Au (111) substrate. The two first representations show the scattering produced by the terbium and the delocalized electron of the π -shell respectively resulting in a Kondo resonance. The third and fourth systems do not show a ZBP. In a Tb₂Pc₃ system a f-f interaction between the two ions couples them ferromagnetically, the total charge is null in contrary to the second representation. The upper ion relaxes independently from to bottom one even if a strong coupling exists between them. The (TbPc₂)₂ case show the pairing of two electrons in the adsorption region originating from a π - π interaction.

dI/dV is recorded on a lobe of the second layer molecule, no ZBP is observed. This absence of resonance is suggested to be due to the bottom ligand of the second layer molecule which is adsorbed on the top of the upper ligand of a first monolayer molecule through a $\pi - \pi$ interaction (Figure 3.14). Therefore, second layer molecule excess electron will relocate at the interface of the two molecules to be paired to the first monolayer's excess electron, thus quenching the spin 1/2 system of the ligand.

Figure 3.14 summarizes the different states of appearance of Kondo peak on various systems. From left to right: the mono-decker, double decker, triple decker and two molecules stacking through a pi-pi interaction. Obtained results for single TbPc₂ and TbPc₂ in a second layer confirm the idea that the degenerated spin 1/2 is responsible for the Kondo resonance. Indeed, the ZBP appears when one electron is unpaired and delocalized above the upper ligand. However, it disappears when two TbPc₂ molecules are π -stacking leading to an electron pairing at the interface. Besides, the Kondo obtained on a mono-decker is assumed to be of a different origin than the one obtained on a double decker as it is only found on the

metal atom.

From topography investigations it was observed that molecules adsorbed on Co-islands and Cu (111) are significantly closer to the substrate compared to ones adsorbed on less reactive crystals such as Ag (111) or Au (111). This is in agreement with higher hybridization for the two first substrates, mainly due to the proximity between the bottom ligand and the crystal thus generating an increased charge transfer between them. Interestingly STS measurements performed at the Fermi level on molecules adsorbed on other substrates than Au (111) did not show any ZBP feature indicating thus that the Kondo effect is highly dependent on the substrate nature. This substrate dependence is due to stronger hybridization of the d states for the most reactive crystals highlighting the unique characteristic of single molecule-metallic bulk coupling.

3.7 Summary and conclusions

In this chapter was demonstrated that the topography imaging of a terbium double decker molecule depicts eight distinguishable lobes, they correspond to the electronic distribution of the upper ligand as two lobes per phenyl ring. Indeed, calculation on isolated phthalocyanine molecule shows similar distribution thus confirming the decoupling of the upper ligand with respect to the substrate.

The height analysis of the structure highlights an important dependency of the apparent dimensions of the molecule with respect to the substrate nature. Furthermore, the adsorption site and orientation depend on both crystallographic structure and atomic nature of the substrate.

The spectroscopic investigations on single TbPc₂ molecules depict a conductance variation with respect to the substrate reactivity thus, confirming the strong impact of the crystal on the molecular orbitals. Both dI/dV point spectroscopy and mapping were performed in order to follow the substrate effect on the molecular electronic and orbital distribution. The overall shape of the spectra remains similar within -1 eV to +1 eV but a shift in energy of the orbitals towards Fermi level is observed when the substrate reactivity is decreased (From Co-islands to Au (111)), this testifies that the chemical potentials adjust to equilibrium at the interface with respect to the substrate nature. The HOMO-LUMO gap is found to be increased when the molecule-substrate interaction is higher which reflects an increased molecular screening on highly reactive substrates such as Co-island and Cu (111) compared to Au (111) and Ag (111).

When the molecule is adsorbed on a Au (111) substrate, it shows a zero bias peak attributed to a Kondo peak with a temperature of $T = 38 \text{ K} \pm 1 \text{ K}$. This resonance is observed only above the lobes of the molecule, when the tip is shifted away from the lobe, the resonant peak vanishes. This result is in opposite observation compared to a single TbPc molecule where the Kondo peak is located at the metallic center of the molecule. This difference strongly suggests that the magnetic element responsible for the electron scattering in a TbPc₂ molecule is the unpaired spin delocalized at both ligands while on TbPc molecule, it is generated by the terbium atom due to the presence of both d- and f-states close to the substrate electrons.

Therefore, the presence of Terbium in a TbPc₂ molecule does not seem to be responsible for the apparition of the ZBP on the lobes. Yet it remains necessary for the observation of such a behavior as no Kondo resonance is reported for other LnPc₂ complexes under similar conditions.

Interestingly, only the adsorption on Au (111) substrate lead to the apparition of this peak indicating that a different molecule-substrate hybridization occurs and affect the electronic properties of the molecule. In order to observe a delocalized π -electron (responsible for the appearance of the Kondo resonance) over a TbPc₂ molecule it is necessary to have a high decoupling of the molecule from the crystal. This property is possible thanks to the weak adsorption of Au (111) compared to other substrates.

REFERENCES

- [1] M. Urdampilleta, S. Klyatskaya, J.-P. Cleuziou, M. Ruben, and W. Wernsdorfer. Supramolecular spin valves. *Nature Materials*, 10(7):502–506, July 2011.
- [2] S. A. Wolf, D. D. Awschalom, R. A. Buhrman, J. M. Daughton, S. von Molnár, M. L. Roukes, A. Y. Chtchelkanova, and D. M. Treger. Spintronics: A Spin-Based Electronics Vision for the Future. *Science*, 294(5546):1488–1495, November 2001.
- [3] David D. Awschalom and Michael E. Flatté. Challenges for semiconductor spintronics. *Nature Physics*, 3(3):153–159, March 2007.
- [4] Willi Auwärter, David Écija, Florian Klappenberger, and Johannes V. Barth. Porphyrins at interfaces. *Nature Chemistry*, 7(2):105–120, February 2015.
- [5] Tommie W. Kelley, Paul F. Baude, Chris Gerlach, David E. Ender, Dawn Muyres, Michael A. Haase, Dennis E. Vogel, and Steven D. Theiss. Recent Progress in Organic Electronics: Materials, Devices, and Processes. *Chemistry of Materials*, 16(23):4413–4422, November 2004.
- [6] V. Dediu, M. Murgia, F. C. Matalotta, C. Taliani, and S. Barbanera. Room temperature spin polarized injection in organic semiconductor. *Solid State Communications*, 122(3–4):181–184, April 2002.
- [7] Wolfgang Kaim. Vital volumes. Molecular magnetism. By Olivier Kahn, VCH, Weinheim 1993, XVI, 380 pp., hardcover, DM 154.00, ISBN 3-527-89566-3. *Advanced Materials*, 6(10):807–808, October 1994.
- [8] R. Wiesendanger, H.-J. Güntherodt, G. Güntherodt, R. J. Gambino, and R. Ruf. Observation of vacuum tunneling of spin-polarized electrons with the scanning tunneling microscope. *Physical Review Letters*, 65(2):247–250, July 1990.

- [9] Roland Wiesendanger. Spin mapping at the nanoscale and atomic scale. *Reviews of Modern Physics*, 81(4):1495–1550, November 2009.
- [10] A. Wachowiak, J. Wiebe, M. Bode, O. Pietzsch, M. Morgenstern, and R. Wiesendanger. Direct Observation of Internal Spin Structure of Magnetic Vortex Cores. *Science*, 298(5593):577–580, October 2002.
- [11] C. Iacovita, M. V. Rastei, B. W. Heinrich, T. Brumme, J. Kortus, L. Limot, and J. P. Bucher. Visualizing the Spin of Individual Cobalt-Phthalocyanine Molecules. *Physical Review Letters*, 101(11):116602, September 2008.
- [12] A. J. Heinrich, J. A. Gupta, C. P. Lutz, and D. M. Eigler. Single-Atom Spin-Flip Spectroscopy. *Science*, 306(5695):466–469, October 2004.
- [13] Noriyuki Tsukahara, Ken-ichi Noto, Michiaki Ohara, Susumu Shiraki, Noriaki Takagi, Yasutaka Takata, Jun Miyawaki, Munetaka Taguchi, Ashish Chainani, Shik Shin, and Maki Kawai. Adsorption-Induced Switching of Magnetic Anisotropy in a Single Iron(II) Phthalocyanine Molecule on an Oxidized Cu(110) Surface. *Physical Review Letters*, 102(16):167203, April 2009.
- [14] P. Wahl, L. Diekhöner, G. Wittich, L. Vitali, M. A. Schneider, and K. Kern. Kondo Effect of Molecular Complexes at Surfaces: Ligand Control of the Local Spin Coupling. *Physical Review Letters*, 95(16):166601, October 2005.
- [15] Aitor Mugarza, Cornelius Krull, Roberto Robles, Sebastian Stepanow, Gustavo Ceballos, and Pietro Gambardella. Spin coupling and relaxation inside molecule–metal contacts. *Nature Communications*, 2:490, October 2011.
- [16] Ying-Shuang Fu, Qi-Kun Xue, and Roland Wiesendanger. Spin-Resolved Splitting of Kondo Resonances in the Presence of RKKY-Type Coupling. *Physical Review Letters*, 108(8):087203, February 2012.
- [17] Tadahiro Komeda, Hironari Isshiki, Jie Liu, Keiichi Katoh, Minoru Shirakata, Brian K. Breedlove, and Masahiro Yamashita. Variation of Kondo Peak Observed in the Assembly of Heteroleptic 2,3-Naphthalocyaninato Phthalocyaninato Tb(III) Double-Decker Complex on Au(111). *ACS Nano*, 7(2):1092–1099, February 2013.
- [18] Naoto Ishikawa, Miki Sugita, Tadahiko Ishikawa, Shin-ya Koshihara, and Youkoh Kaizu. Lanthanide Double-Decker Complexes Functioning as Magnets at the Single-Molecular Level. *Journal of the American Chemical Society*, 125(29):8694–8695, July 2003.

- [19] Cristiano Benelli, Andrea Caneschi, Dante Gatteschi, and Roberta Sessoli. Magnetic ordering in a molecular material containing dysprosium(III) and a nitronyl nitroxide. *Advanced Materials*, 4(7-8):504–505, July 1992.
- [20] Roberta Sessoli, Hui Lien Tsai, Ann R. Schake, Sheyi Wang, John B. Vincent, Kirsten Folting, Dante Gatteschi, George Christou, and David N. Hendrickson. High-spin molecules: $[\text{Mn}_{12}\text{O}_{12}(\text{O}_2\text{Cr})_{16}(\text{H}_2\text{O})_4]$. *Journal of the American Chemical Society*, 115(5):1804–1816, March 1993.
- [21] R. Sessoli, D. Gatteschi, A. Caneschi, and M. A. Novak. Magnetic bistability in a metal-ion cluster. *Nature*, 365(6442):141–143, September 1993.
- [22] Hilary J. Eppley, Hui-Lien Tsai, Nadine de Vries, Kirsten Folting, George Christou, and David N. Hendrickson. High-Spin Molecules: Unusual Magnetic Susceptibility Relaxation Effects in $[\text{Mn}_{12}\text{O}_{12}(\text{O}_2\text{CEt})_{16}(\text{H}_2\text{O})_3]$ ($S = 9$) and the One-Electron Reduction Product $((\text{PPh})_4)[\text{Mn}_{12}\text{O}_{12}(\text{O}_2\text{CEt})_{16}(\text{H}_2\text{O})_4]$ ($S = 19/2$). *Journal of the American Chemical Society*, 117(1):301–317, January 1995.
- [23] Jonathan R. Friedman, M. P. Sarachik, J. Tejada, and R. Ziolo. Macroscopic Measurement of Resonant Magnetization Tunneling in High-Spin Molecules. *Physical Review Letters*, 76(20):3830–3833, May 1996.
- [24] George Christou, Dante Gatteschi, David N. Hendrickson, and Roberta Sessoli. Single-Molecule Magnets. *MRS Bulletin*, 25(11):66–71, November 2000.
- [25] Sheila M. J. Aubin, Michael W. Wemple, David M. Adams, Hui-Lien Tsai, George Christou, and David N. Hendrickson. Distorted $\text{Mn}^{\text{IV}}\text{Mn}^{\text{III}}_3$ Cubane Complexes as Single-Molecule Magnets. *Journal of the American Chemical Society*, 118(33):7746–7754, January 1996.
- [26] Hanspeter Andres, Reto Basler, Hans-Ulrich Güdel, Guillem Aromí, George Christou, Herma Büttner, and Benoit Rufflé. Inelastic Neutron Scattering and Magnetic Susceptibilities of the Single-Molecule Magnets $[\text{Mn}_4\text{O}_3\text{X}(\text{OAc})_3(\text{dbm})_3]$ ($\text{X} = \text{Br}, \text{Cl}, \text{OAc}, \text{and F}$): Variation of the Anisotropy along the Series. *Journal of the American Chemical Society*, 122(50):12469–12477, December 2000.
- [27] Richard A. Layfield. Organometallic Single-Molecule Magnets. *Organometallics*, 33(5):1084–1099, March 2014.

- [28] Danna E. Freedman, W. Hill Harman, T. David Harris, Gary J. Long, Christopher J. Chang, and Jeffrey R. Long. Slow Magnetic Relaxation in a High-Spin Iron(II) Complex. *Journal of the American Chemical Society*, 132(4):1224–1225, February 2010.
- [29] W. Hill Harman, T. David Harris, Danna E. Freedman, Henry Fong, Alicia Chang, Jeffrey D. Rinehart, Andrew Ozarowski, Moulay T. Sougrati, Fernande Grandjean, Gary J. Long, Jeffrey R. Long, and Christopher J. Chang. Slow Magnetic Relaxation in a Family of Trigonal Pyramidal Iron(II) Pyrrolide Complexes. *Journal of the American Chemical Society*, 132(51):18115–18126, December 2010.
- [30] Po-Heng Lin, Nathan C. Smythe, Serge I. Gorelsky, Steven Maguire, Neil J. Henson, Ilia Korobkov, Brian L. Scott, John C. Gordon, R. Tom Baker, and Muralee Murugesu. Importance of Out-of-State Spin–Orbit Coupling for Slow Magnetic Relaxation in Mononuclear Fe(II) Complexes. *Journal of the American Chemical Society*, 133(40):15806–15809, October 2011.
- [31] Joseph M. Zadrozny, Mihail Atanasov, Aimee M. Bryan, Chun-Yi Lin, Brian D. Rekken, Philip P. Power, Frank Neese, and Jeffrey R. Long. Slow magnetization dynamics in a series of two-coordinate iron(II) complexes. *Chemical Science*, 4(1):125–138, November 2012.
- [32] Susanne Mossin, Ba L. Tran, Debashis Adhikari, Maren Pink, Frank W. Heinemann, Jörg Sutter, Robert K. Szilagy, Karsten Meyer, and Daniel J. Mindiola. A Mononuclear Fe(III) Single Molecule Magnet with a $3/2 \leftrightarrow 5/2$ Spin Crossover. *Journal of the American Chemical Society*, 134(33):13651–13661, August 2012.
- [33] Joseph M. Zadrozny and Jeffrey R. Long. Slow Magnetic Relaxation at Zero Field in the Tetrahedral Complex $[\text{Co}(\text{SPh})_4]^{2-}$. *Journal of the American Chemical Society*, 133(51):20732–20734, December 2011.
- [34] Titel Jurca, Ahmed Farghal, Po-Heng Lin, Ilia Korobkov, Muralee Murugesu, and Darrin S. Richeson. Single-Molecule Magnet Behavior with a Single Metal Center Enhanced through Peripheral Ligand Modifications. *Journal of the American Chemical Society*, 133(40):15814–15817, October 2011.
- [35] Silvia Gomez-Coca, Eduard Cremades, Núria Aliaga-Alcalde, and Eliseo Ruiz. Mononuclear Single-Molecule Magnets: Tailoring the Magnetic Anisotropy of First-Row Transition-Metal Complexes. *Journal of the American Chemical Society*, 135(18):7010–7018, May 2013.

- [36] Jeffrey D. Rinehart and Jeffrey R. Long. Exploiting single-ion anisotropy in the design of f-element single-molecule magnets. *Chemical Science*, 2(11):2078–2085, October 2011.
- [37] Naoto Ishikawa, Miki Sugita, Tadahiko Ishikawa, Shin-ya Koshihara, and Youkoh Kaizu. Mononuclear Lanthanide Complexes with a Long Magnetization Relaxation Time at High Temperatures: A New Category of Magnets at the Single-Molecular Level. *The Journal of Physical Chemistry B*, 108(31):11265–11271, August 2004.
- [38] Naoto Ishikawa, Miki Sugita, Tomoko Okubo, Naohiro Tanaka, Tomochika Iino, and Youkoh Kaizu. Determination of Ligand-Field Parameters and f-Electronic Structures of Double-Decker Bis(phthalocyaninato)lanthanide Complexes. *Inorganic Chemistry*, 42(7):2440–2446, April 2003.
- [39] Matteo Mannini, Federico Bertani, Cristina Tudisco, Luigi Malavolti, Lorenzo Poggini, Kasjan Misztal, Daniela Menozzi, Alessandro Motta, Edwige Otero, Philippe Ohresser, Philippe Saintavit, Guglielmo G. Condorelli, Enrico Dalcanale, and Roberta Sessoli. Magnetic behaviour of TbPc₂ single-molecule magnets chemically grafted on silicon surface. *Nature Communications*, 5:4582, August 2014.
- [40] Romain Vincent, Svetlana Klyatskaya, Mario Ruben, Wolfgang Wernsdorfer, and Franck Balestro. Electronic read-out of a single nuclear spin using a molecular spin transistor. *Nature*, 488(7411):357–360, August 2012.
- [41] Luigi Malavolti, Matteo Mannini, Pierre-Emmanuel Car, Giulio Campo, Francesco Pineider, and Roberta Sessoli. Erratic magnetic hysteresis of TbPc₂ molecular nanomagnets. *Journal of Materials Chemistry C*, 1(16):2935–2942, March 2013.
- [42] Peter Robaschik, Michael Fronk, Marius Toader, Svetlana Klyatskaya, Fabian Ganss, Pablo F. Siles, Oliver G. Schmidt, Manfred Albrecht, Michael Hietschold, Mario Ruben, Dietrich R. T. Zahn, and Georgeta Salvan. Tuning the magneto-optical response of TbPc₂ single molecule magnets by the choice of the substrate. *Journal of Materials Chemistry C*, 3(31):8039–8049, July 2015.
- [43] Andrea Candini, Svetlana Klyatskaya, Mario Ruben, Wolfgang Wernsdorfer, and Marco Affronte. Graphene Spintronic Devices with Molecular Nanomagnets. *Nano Letters*, 11(7):2634–2639, July 2011.
- [44] Victoria E. Campbell, H el ene Bolvin, Eric Rivier e, Regis Guillot, Wolfgang Wernsdorfer, and Talal Mallah. Structural and Electronic Dependence of the Single-Molecule-

- Magnet Behavior of Dysprosium(III) Complexes. *Inorganic Chemistry*, 53(5):2598–2605, March 2014.
- [45] Naoto Ishikawa, Miki Sugita, and Wolfgang Wernsdorfer. Quantum Tunneling of Magnetization in Lanthanide Single-Molecule Magnets: Bis(phthalocyaninato)terbium and Bis(phthalocyaninato)dysprosium Anions. *Angewandte Chemie International Edition*, 44(19):2931–2935, May 2005.
- [46] J. K. Gimzewski, E. Stoll, and R. R. Schlittler. Scanning tunneling microscopy of individual molecules of copper phthalocyanine adsorbed on polycrystalline silver surfaces. *Surface Science*, 181(1):267–277, March 1987.
- [47] Yan-Feng Zhang, Hironari Isshiki, Keiichi Katoh, Yusuke Yoshida, Masahiro Yamashita, Hitoshi Miyasaka, Brian K. Breedlove, Takashi Kajiwara, Shinya Takaishi, and Tadahiro Komeda. A Low-Temperature Scanning Tunneling Microscope Investigation of a Nonplanar Dysprosium Phthalocyanine Adsorption on Au(111). *The Journal of Physical Chemistry C*, 113(32):14407–14410, August 2009.
- [48] Yang He, Yajie Zhang, I-Po Hong, Fang Cheng, Xiong Zhou, Qian Shen, Jianlong Li, Yongfeng Wang, Jianzhuang Jiang, and Kai Wu. Low-temperature scanning tunneling microscopy study of double-decker DyPc2 on Pb Surface. *Nanoscale*, 6(18):10779–10783, August 2014.
- [49] Marius Toader, Martin Knupfer, Dietrich R. T. Zahn, and Michael Hietschold. Initial Growth of Lutetium(III) Bis-phthalocyanine on Ag(111) Surface. *Journal of the American Chemical Society*, 133(14):5538–5544, April 2011.
- [50] Akio Iwase, Chokto Harnode, and Yasuo Kameda. Synthesis and electrochemistry of double-decker lanthanoid (III) phthalocyanine complexes. *Journal of Alloys and Compounds*, 192(1):280–283, February 1993.
- [51] Richard Layfield and Muralee Murugesu. *Lanthanides and Actinides in Molecular Magnetism*. Wiley, 2015.
- [52] G. A. Corker. An Explanation of the Electrochromism of Lutetium Diphthalocyanine. *Journal of The Electrochemical Society*, 126(8):1339, 1979.
- [53] M. L’Her, Y. Cozien, and J. Courtot-Coupez. Electrochemical behaviour of lutetium diphthalocyanine in methylene chloride. *Journal of Electroanalytical Chemistry and Interfacial Electrochemistry*, 157(1):183–187, October 1983.

- [54] M. T. Riou and C. Clarisse. The rare earth substitution effect on the electrochemistry of diphthalocyanine films in contact with an acidic aqueous medium. *Journal of Electroanalytical Chemistry and Interfacial Electrochemistry*, 249(1–2):181–190, July 1988.
- [55] Hideo Konami, Masahiro Hatano, Nagao Kobayashi, and Tetsuo Osa. Redox potentials of a series of lanthanide-bisphthalocyanine sandwich complexes. *Chemical Physics Letters*, 165(5):397–400, January 1990.
- [56] Sarah Fahrenndorf, Nicolae Atodiresei, Claire Besson, Vasile Caciuc, Frank Matthes, Stefan Blügel, Paul Kögerler, Daniel E. Bürgler, and Claus M. Schneider. Accessing 4f-states in single-molecule spintronics. *Nature Communications*, 4:2425, September 2013.
- [57] F. Hund. Atomtheoretische Deutung des Magnetismus der seltenen. Erden. *Zeitschrift für Physik*, 33(1):855–859, December 1925.
- [58] Friedrich Hund. *Linienspektren und Periodisches System der Elemente*. Springer Vienna, Vienna, 1927.
- [59] Mark L. Campbell. The correct interpretation of Hund's rule as applied to "uncoupled states" orbital diagrams. *Journal of Chemical Education*, 68(2):134, February 1991.
- [60] Naoto Koike, Hidehiro Uekusa, Yuji Ohashi, Chokto Harnode, Fusao Kitamura, Takeo Ohsaka, and Koichi Tokuda. Relationship between the Skew Angle and Interplanar Distance in Four Bis(phthalocyaninato)lanthanide(III) Tetrabutylammonium Salts ($[\text{NBun}_4][\text{Ln}^{\text{III}}\text{Pc}_2]$; Ln = Nd, Gd, Ho, Lu). *Inorganic Chemistry*, 35(20):5798–5804, January 1996.
- [61] Tadahiro Komeda, Hironari Isshiki, Jie Liu, Yan-Feng Zhang, Nicolás Lorente, Keiichi Katoh, Brian K. Breedlove, and Masahiro Yamashita. Observation and electric current control of a local spin in a single-molecule magnet. *Nature Communications*, 2:217, March 2011.
- [62] Lucia Vitali, Stefano Fabris, Adriano Mosca Conte, Susan Brink, Mario Ruben, Stefano Baroni, and Klaus Kern. Electronic Structure of Surface-supported Bis(phthalocyaninato) terbium(III) Single Molecular Magnets. *Nano Letters*, 8(10):3364–3368, October 2008.
- [63] Keiichi Katoh, Yusuke Yoshida, Masahiro Yamashita, Hitoshi Miyasaka, Brian K. Breedlove, Takashi Kajiwara, Shinya Takaishi, Naoto Ishikawa, Hironari Isshiki,

- Yan Feng Zhang, Tadahiro Komeda, Masakazu Yamagishi, and Jun Takeya. Direct Observation of Lanthanide(III)-Phthalocyanine Molecules on Au(111) by Using Scanning Tunneling Microscopy and Scanning Tunneling Spectroscopy and Thin-Film Field-Effect Transistor Properties of Tb(III)- and Dy(III)-Phthalocyanine Molecules. *Journal of the American Chemical Society*, 131(29):9967–9976, July 2009.
- [64] Cornelius Krull, Roberto Robles, Aitor Mugarza, and Pietro Gambardella. Site- and orbital-dependent charge donation and spin manipulation in electron-doped metal phthalocyanines. *Nature Materials*, 12(4):337–343, April 2013.
- [65] Kezilebieke Shawulienu. *Scanning tunneling microscopy and spectroscopy of metal organic complexes : from single atoms to extended networks*. Strasbourg, January 2014.
- [66] Marcella Iannuzzi, Fabien Tran, Roland Widmer, Thomas Dienel, Kevin Radican, Yun Ding, Jürg Hutter, and Oliver Gröning. Site-selective adsorption of phthalocyanine on h-BN/Rh(111) nanomesh. *Physical Chemistry Chemical Physics*, 16(24):12374–12384, May 2014.
- [67] Alexander Sperl, Jörg Kröger, and Richard Berndt. Controlled Metalation of a Single Adsorbed Phthalocyanine. *Angewandte Chemie International Edition*, 50(23):5294–5297, May 2011.
- [68] Geoffrey Rojas, Scott Simpson, Xumin Chen, Donna A. Kunkel, Justin Nitz, Jie Xiao, Peter A. Dowben, Eva Zurek, and Axel Enders. Surface state engineering of molecule–molecule interactions. *Physical Chemistry Chemical Physics*, 14(14):4971–4976, March 2012.
- [69] J. Hölzl and F. K. Schulte. Work function of metals. In Professor Dr Josef Hölzl, Dr Franz K. Schulte, and Dr Heribert Wagner, editors, *Solid Surface Physics*, number 85 in Springer Tracts in Modern Physics, pages 1–150. Springer Berlin Heidelberg, 1979. DOI: 10.1007/BFb0048919.
- [70] Herbert B. Michaelson. The work function of the elements and its periodicity. *Journal of Applied Physics*, 48(11):4729–4733, November 1977.
- [71] G. Clarisse and M. T. Riou. Synthesis and characterization of some lanthanide phthalocyanines. *Inorganica Chimica Acta*, 130(1):139–144, June 1987.
- [72] Min Chen, Xuefei Feng, Liang Zhang, Huanxin Ju, Qian Xu, Junfa Zhu, J. Michael Gottfried, Kurash Ibrahim, Haijie Qian, and Jiaou Wang. Direct Synthesis of Nickel(II)

- Tetraphenylporphyrin and Its Interaction with a Au(111) Surface: A Comprehensive Study. *The Journal of Physical Chemistry C*, 114(21):9908–9916, June 2010.
- [73] Rubén González-Moreno, Carlos Sánchez-Sánchez, Marta Trelka, Roberto Otero, Albano Cossaro, Alberto Verdini, Luca Floreano, Marta Ruiz-Bermejo, Aran García-Lekue, José Ángel Martín-Gago, and Celia Rogero. Following the Metalation Process of Protoporphyrin IX with Metal Substrate Atoms at Room Temperature. *The Journal of Physical Chemistry C*, 115(14):6849–6854, April 2011.
- [74] Zhitao Deng, Stephan Rauschenbach, Sebastian Stepanow, Svetlana Klyatskaya, Mario Ruben, and Klaus Kern. Self-assembly of bis(phthalocyaninato)terbium on metal surfaces. *Physica Scripta*, 90(9):098003, 2015.
- [75] Benjamin HEINRICH. La spectroscopie tunnel à travers des objets individuels sur une surface magnétique, June 2010.
- [76] B. Amin, S. Nazir, and U. Schwingenschlögl. Molecular distortion and charge transfer effects in ZnPc/Cu(111). *Scientific Reports*, 3, April 2013.
- [77] Ramón Cuadrado, Jorge I. Cerdá, Yongfeng Wang, Ge Xin, Richard Berndt, and Hao Tang. CoPc adsorption on Cu(111): Origin of the C_4 to C_2 symmetry reduction. *The Journal of Chemical Physics*, 133(15):154701, October 2010.
- [78] J. Schaffert, M. C. Cottin, A. Sonntag, C. A. Bobisch, R. Möller, J.-P. Gauyacq, and N. Lorente. Tunneling electron induced rotation of a copper phthalocyanine molecule on Cu(111). *Physical Review B*, 88(7):075410, August 2013.
- [79] Juan Liu, Chao Li, Xiaoqing Liu, Yan Lu, Feifei Xiang, Xuelei Qiao, Yingxiang Cai, Zhongping Wang, Sanqiu Liu, and Li Wang. Positioning and Switching Phthalocyanine Molecules on a Cu(100) Surface at Room Temperature. *ACS Nano*, 8(12):12734–12740, December 2014.
- [80] Ying-Shuang Fu, Jörg Schwöbel, Saw-Wai Hla, Andrew Dilullo, Germar Hoffmann, Svetlana Klyatskaya, Mario Ruben, and Roland Wiesendanger. Reversible Chiral Switching of Bis(phthalocyaninato) Terbium(III) on a Metal Surface. *Nano Letters*, 12(8):3931–3935, August 2012.
- [81] Jörg Schwöbel, Yingshuang Fu, Jens Brede, Andrew Dilullo, Germar Hoffmann, Svetlana Klyatskaya, Mario Ruben, and Roland Wiesendanger. Real-space observation of spin-split molecular orbitals of adsorbed single-molecule magnets. *Nature Communications*, 3:953, July 2012.

- [82] Xinghua Lu, M. Grobis, K. H. Khoo, Steven G. Louie, and M. F. Crommie. Charge transfer and screening in individual C_{60} molecules on metal substrates: A scanning tunneling spectroscopy and theoretical study. *Physical Review B*, 70(11):115418, September 2004.
- [83] Keiichi Katoh, Tadahiro Komeda, and Masahiro Yamashita. Surface morphologies, electronic structures, and Kondo effect of lanthanide(III)-phthalocyanine molecules on Au(111) by using STM, STS and FET properties for next generation devices. *Dalton Transactions*, 39(20):4708–4723, May 2010.
- [84] L. Gao, W. Ji, Y. B. Hu, Z. H. Cheng, Z. T. Deng, Q. Liu, N. Jiang, X. Lin, W. Guo, S. X. Du, W. A. Hofer, X. C. Xie, and H.-J. Gao. Site-Specific Kondo Effect at Ambient Temperatures in Iron-Based Molecules. *Physical Review Letters*, 99(10):106402, September 2007.
- [85] Aidi Zhao, Zhenpeng Hu, Bing Wang, Xudong Xiao, Jinlong Yang, and J. G. Hou. Kondo effect in single cobalt phthalocyanine molecules adsorbed on Au(111) monoatomic steps. *The Journal of Chemical Physics*, 128(23):234705, June 2008.
- [86] Aidi Zhao, Qunxiang Li, Lan Chen, Hongjun Xiang, Weihua Wang, Shuan Pan, Bing Wang, Xudong Xiao, Jinlong Yang, J. G. Hou, and Qingshi Zhu. Controlling the Kondo Effect of an Adsorbed Magnetic Ion Through Its Chemical Bonding. *Science*, 309(5740):1542–1544, September 2005.
- [87] Naoto Ishikawa, Tomochika Iino, and Youkoh Kaizu. Interaction between f-Electronic Systems in Dinuclear Lanthanide Complexes with Phthalocyanines. *Journal of the American Chemical Society*, 124(38):11440–11447, September 2002.
- [88] Naoto Ishikawa, Satoshi Otsuka, and Youkoh Kaizu. The Effect of the f–f Interaction on the Dynamic Magnetism of a Coupled $4f^8$ System in a Dinuclear Terbium Complex with Phthalocyanines. *Angewandte Chemie International Edition*, 44(5):731–733, January 2005.
- [89] Alberto Lodi Rizzini, Cornelius Krull, Aitor Mugarza, Timofey Balashov, Corneliu Nistor, Raoul Piquerel, Svetlana Klyatskaya, Mario Ruben, Polina M. Sheverdyeva, Paolo Moras, Carlo Carbone, Christian Stamm, Piter S. Miedema, Pardeep K. Thakur, Violetta Sessi, Marcio Soares, Flora Yakhou-Harris, Julio C. Cezar, Sebastian Stepanow, and Pietro Gambardella. Coupling of single, double, and triple-decker metal-phthalocyanine complexes to ferromagnetic and antiferromagnetic substrates. *Surface Science*, 630:361–374, December 2014.

TERBIUM DOUBLE-DECKER DOMAINS ON SURFACES

Thin film based organo-metallic electronic devices have attracted much interest during the last decades due to their low cost and applications as large scale flexible devices.[1–4] Ensuring the reproducibility of multifunctional properties in single organo-metallic components is critical when building interfacial layers as the structure of the interface is modified when intermolecular interactions are involved. The substrate nature or molecular geometry at the interface often significantly alter the molecular properties.

As was mentioned in the previous chapter, the neutral TbPc_2 complex contains three spin systems: a central $J=6$ high-spin with an intrinsic anisotropy arising from the central ion, a $S=1/2$ π -radical due to a singly occupied molecular orbital that is delocalized over the two Pc ligands and a nuclear momentum $I=3/2$ arising from the quadrupole interaction. Charge and spin state of the TbPc_2 molecules are altered upon adsorption on surfaces. In particular, it was shown that an adsorption on Au (111) the π -radical localizes in the upper Pc ligand leading to the experimental observation of a Kondo resonance in the dI/dV above the molecule. Katoh et al. observed a Kondo effect on the rafts formed by TbPc_2 molecules on the Au (111) surface.[5, 6] A Kondo resonance was observed only at some lobes of the upper Pc ligand, the ones that lay at crossing points with adjacent molecules. The absence of Kondo effect when the molecule is residing on Cu (111) Ag (111) or Co substrate is rationalized by the fact that the electron in the π -orbital pairs-up with an electron transferred from the substrate due to the much stronger molecule substrate interaction.[7, 8] The molecule then bears a negative charge $[\text{TbPc}_2]^-$.

Despite the work that has been accumulated over the last decade, the effects of the surface and reduced dimensionality on the magnetic properties of SMMs is not well understood. In particular, a drawback of this attractive system lies in the large impact of the

crystalline environment on its magnetic properties.[9] As an example, monolayer islands of TbPc₂ on surfaces show a dramatically reduced blocking temperature compared to the crystalline phase.[10, 11] If these types of molecules are to be used in future spintronic devices, a better understanding of this phenomenon is compulsory. The present chapter aims at studying the different conformations of these SMMs on various surfaces that may provide the key to understanding the strong effect of the structural environment on the magnetic properties. Due to the interaction between molecule-substrate and molecule-molecule, a variety of growth modes of TbPc₂ are expected from the isolated molecule to monolayer islands. The presence of the two Pc ligands promotes face-on adsorption of the molecules on metal surfaces, thus facilitating the investigation of electronic and magnetic properties by high resolution STM/STS. Furthermore, interesting magnetic properties of molecule islands on Au (111) are to be revealed by the STS Kondo analysis at each step of the controlled manipulation of the SMMs with the STM tip.

4.1 Structural and electronic properties of double-deckers

4.1.1 Domain growth on Cu (111) substrate

In all cases the sample was kept at room temperature during the TbPc₂ deposition in order to provide the necessary activation of the diffusion barrier for the domain formation. After deposition, the samples were transferred to the STM where they slowly reach the temperature of T=4.6 K. Figure 4.1(a) shows a high resolution STM topography image after room temperature deposition of TbPc₂ molecules on Cu (111). While domains of molecules are formed, a few isolated molecules are also observed on the surface as well as dimers and trimers. The observed domains have preferential growth directions that do not match the substrate crystallographic direction. Indeed, orientations of 50°, 60° and 70° are spanning the three observed domains. Deng et al. reported an angle of 10° between a the long edge lattice vector and the [1 $\bar{1}$ 0] direction of Cu (111). [12]

The molecular arrangement into domains is a result of intermolecular interaction, any molecule embedded into a given domain has exactly the same orientation as its neighbors. Therefore, based on topographic image of Figure 4.1(c), it is evidenced that TbPc₂ molecules orders in a square lattice pattern with the following parameters: $\vec{a}_1 = \vec{a}_2 \approx 1.33\text{nm} \pm 0.05\text{nm}$ separated by an angle $\alpha \approx 90^\circ$. This four-fold symmetry is confirmed by the analytical 2D-FFT of a molecular domain presented in Figure 4.1. The TbPc₂ monolayer is found to

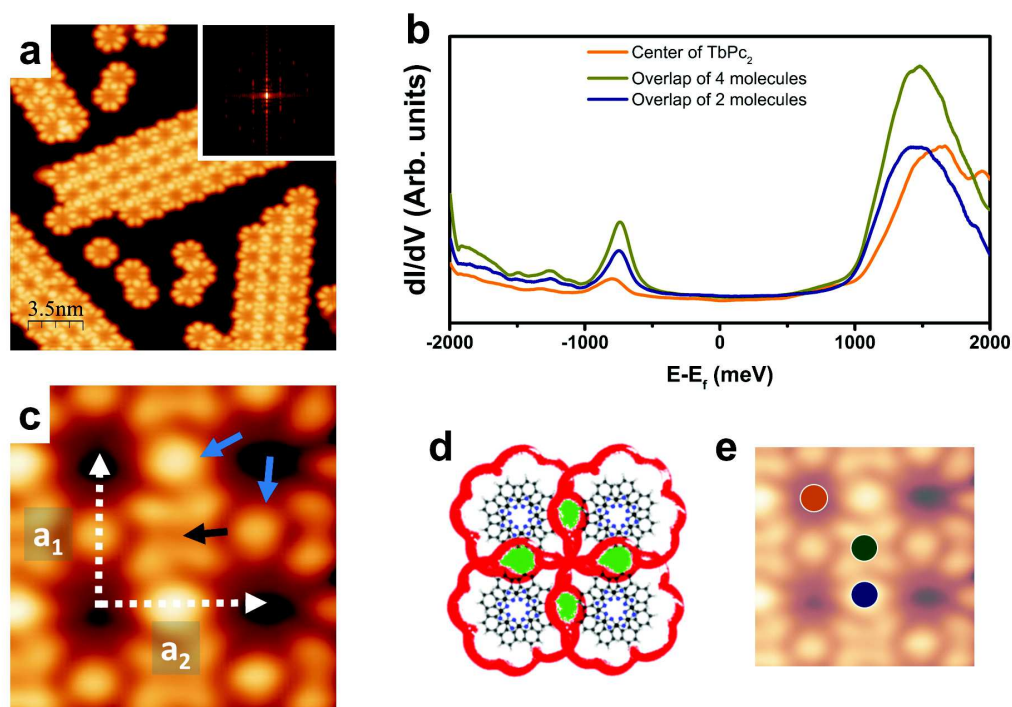


Fig. 4.1 Three TbPc_2 domains on Cu (111) substrate. a) Shows constant current topography image obtained at $I = 0.1$ nA and $V = -1$ V, three main domains are visible along with an isolated molecule, a dimer and a trimer. In inset is presented the 2D-FFT of the domain. b) dI/dV spectroscopy from -2 eV to $+2$ eV on the center, crossing point, and an overlap of two adjacent molecules as indicated in e), two main peaks are observed, defined as HOMO at around -800 meV and LUMO around $+1.5$ eV. c) Image containing four molecules, overlaps between two adjacent molecules are indicated with blue arrows. Cell vectors are represented with \vec{a}_1 and \vec{a}_2 . Black arrow indicates the crossing point where four lobes meet. d) Four molecules as depicted in c) and lateral extension of the electronic distribution (in red). The overlap between two adjacent molecules is shown in green. e) Positions where the tip was stabilized to perform the dI/dV spectroscopy of b).

assemble in a close packed way where both Pc ligands of a double-decker molecule are participating in the intermolecular interaction.

A schematic of the molecules superposed to the topography image of four neighboring molecules is shown in Figure 4.1(d). The red contour shows the lateral extension of the molecular orbitals as visualized by STM from an isolated molecule adsorbed on the same surface. An orbital overlap between two adjacent molecules is clearly observed and highlighted in green in Figure 4.1(d). It is indicated with blue arrows in Figure 4.1(c). These overlapping regions appear brighter in the topography image as more electrons can tunnel simultaneously through two different channels. The area where four molecules meet shows a cross-like form. Later on, this region will be referred to as "crossing point". In this region a negligible molecules overlap is observed, each lobe corresponding to one double-decker molecules.

When the molecule is part of a domain, the molecular configuration due to the substrate nature induces an important electronic evolution. Figure 4.1(b) depicts three dI/dV spectroscopies recorded above three distinct regions of a monolayer (see Figure 4.1(e)). This highly stable system allowed the voltage bias to be ramped from -2 eV to +2 eV under normal tunneling conditions. As a matter of comparison HOMO peaks positions are similar to the one of isolated molecules (see Figure 3.9) above the center. However the shift previously observed when moving the tip from center to lobe of an isolated molecule is absent in a film. Above center and overlapping region of two molecules in a domain show similar energy position. A small shift of 50 meV away from Fermi level is observed when the tip is moved toward the crossing point. Similarly, LUMO peaks are positioned at the same energy at the center and the overlap of two adjacent molecular lobes. The LUMO recorded at the crossing point exhibits same energy displacement towards Fermi level as the HOMO (50 meV). These results indicate that on Cu (111) substrate, an equi-distribution of the molecular orbitals occurs at the TbPc₂ monolayer.

4.1.2 Domain growth on Ag (111) substrate

When evaporating terbium double-deckers on a pristine Ag (111) substrate, topography images show extended and ordered molecular layers as depicted in Figure 4.2(a). The lower diffusion barrier of the Ag (111) substrate compared to Cu (111) leads the TbPc₂ molecule to have a larger diffusion length resulting in the growth of large domain. This is also expected since the molecular assembly is a result of the balance between molecule-substrate

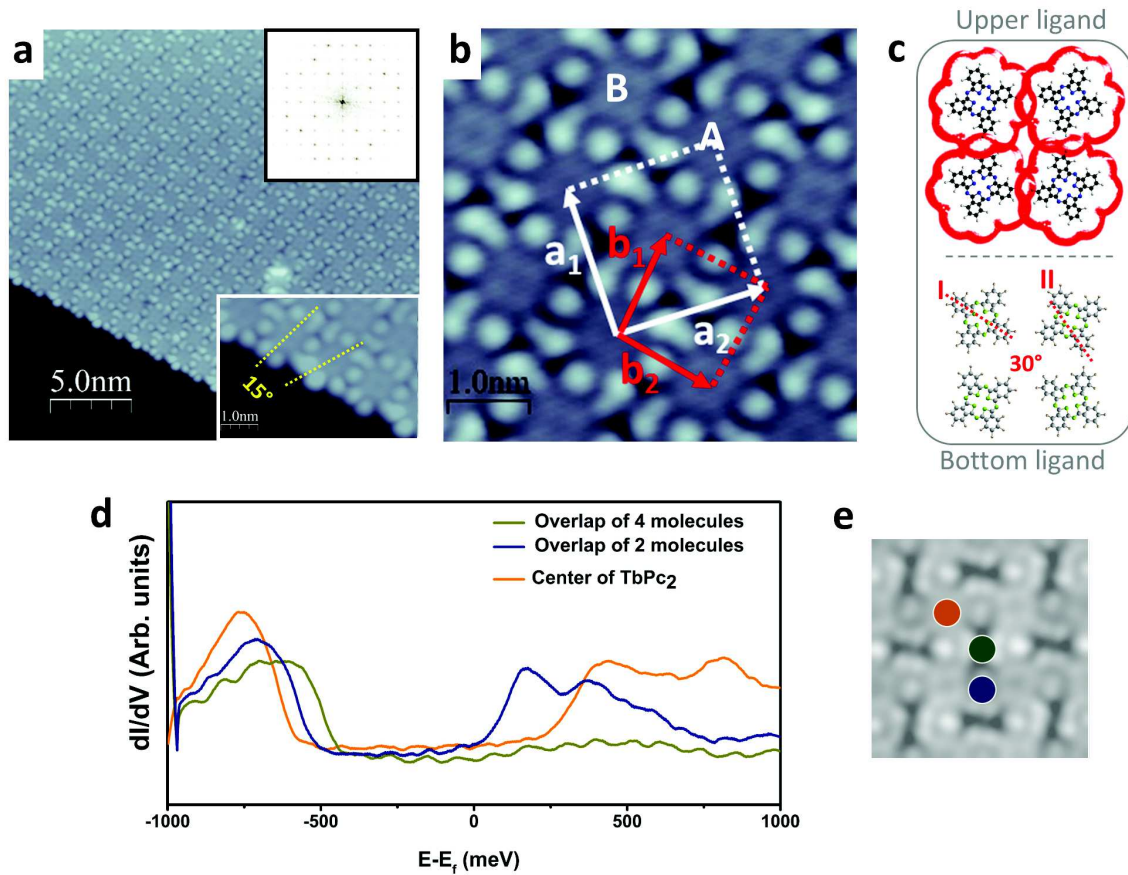


Fig. 4.2 TbPc₂ molecules adsorbed on Ag (111) substrate. a) Constant current topography image obtained at $I=70$ pA and $V= -800$ mV of extended domains shows a well ordered pattern. 2D-FFT of image a) is presented in top right inset. Enlarged image at the edge of an island is shown in the bottom right inset, two molecules labelled A and B in (b) have different orientations and the misorientation between them is found to be 15° as shown by the yellow lines. b) Enlarged image of a domain where the cell parameters are represented as $\vec{a}_1 = \vec{a}_2 = 1.9 \pm 0.1$ nm and $\alpha=90^\circ$. \vec{b}_1 and \vec{b}_2 represent the next neighbor molecules which are of different orientation where $b_1 = b_2 = 1.36 \pm 0.01$ nm. c) representation of both upper and bottom ligand of four molecules in a domain. Electronic extension is modeled for the upper Pc ligand showing the possible overlaps between adjacent molecules. 30° separate the two bottom ligands as represented with two dashed lines I and II. d) dI/dV spectroscopy performed from -1 eV to $+1$ eV above three different location : Center, overlap of two molecules, and crossing point. Peaks observed for the HOMO are positioned at -750 meV, -700 meV and -680 meV. Those observed on the positive side are positioned at $+200$ meV and $+400$ meV. e) Points above which the spectroscopy in (d) was performed.

and molecule-molecule interaction.

The 2D-FFT in inset of Figure 4.2(a) (top right) confirms the square packing of the molecular monolayer on the Ag (111) substrate. However, different orientations seem to emerge as various spots are visible within one given k -range, suggesting that two square lattice packing coexist in the same pattern. Enlarged topography at the edge of a monolayer island is shown in inset of Figure 4.2(a) (bottom right), where two dashed lines (yellow) are drawn on two adjacent molecules at the step edge following the depression between two lobes of two opposite pyrroles. The measured angle between these two lines is found to be $\alpha = 15^\circ$ while it was of $\alpha = 0^\circ$ on the copper substrate. This configuration is alternatively spread to all the molecules of the domain therefore creating two different molecular orientations labelled *A* and *B*. Each *A*-type molecule is surrounded by four next neighbors *B*-type and *vice-versa*. Lattice parameters presented in Figure 4.2(b) depict a unit cell containing two molecules (*A*- and *B*-type) with the following parameters $\vec{a}_1 = \vec{a}_2 \approx 1.9 \pm 0.1 \text{ nm}$ and $\alpha = 91 \pm 1^\circ$. Vectors labelled \vec{b}_1 and \vec{b}_2 represent the next neighboring molecules independently of their type (orientation) where $\vec{b}_1 = \vec{b}_2 \approx 1.36 \pm 0.01 \text{ nm}$ with an angle of $90 \pm 1^\circ$.

As mentioned previously, the influence of the substrate on the upper ligand is relatively small. Therefore, the present study is mostly relevant to the geometrical configuration pertaining to the electronic delocalization over the upper phthalocyanine π -orbital. Contrary to the case of Cu (111), the topography images of TbPc₂ on the Ag (111) substrate are highly dependent on the tunneling bias. As depicted in Figure 4.2(e), the constant current image taken at a lower bias voltage (-100 meV) shows a chiral feature due to a different overlap between adjacent molecular lobes, thus confirming the double periodicity due to two different configurations inside one domain.

In order to highlight this observation, Figure 4.2(c) shows a schematic view of four phthalocyanine molecules superposed in the same position and orientation as the upper ligand of the double-deckers in Figure 4.2(e). Both, the upper and bottom ligands of the four molecules are represented in Figure 4.2(c). The MO extension is represented in red to highlight the overlap between the upper ligands and gather information of the chirality origin in the topography image. The bottom phthalocyanine is determined by considering a skew angle of 45° between the two ligands of the terbium double-decker molecule. Two lines labelled I and II represent one of the two phthalocyanine axes as expected. The measured angle between the two bottom ligands is found to be 30° . It becomes clear that the depression visible at the center of the unit cell is a consequence of the large free area created by the molecular rotation.

As a conclusion the origin of this rotation (rotation of the bottom Pc) is due to the steric repulsion among the phenyl rings of adjacent molecules. Due to prohibited edge-to-edge atomic contact, a homogeneous orientation of the bottom Pc (as observed for Cu (111)) is impossible here. To satisfy both, steric constrain and inter-molecular interactions, only a small change of the next neighbor distance followed by a rotation of 30° is necessary in full agreement with the measured distance between molecules and lattice periodicity. A similar rotation of the bottom Pc-ligands of adjacent molecules has been assumed to explain the domain formation of LuPc₂ molecules on Ag (111).[13]

Compared to Cu (111), the STS measurements performed above the TbPc₂ molecules on the Ag (111) substrate show a more pronounced shift of both, HOMO and LUMO. A shift towards the Fermi energy of the HOMO is observed when moving the tip from the center to crossing point as presented in Figure 4.2(d). On the other hand, the HOMO position is found at -750 meV, -700 meV and -600 meV for the center, the overlap of two adjacent molecules and the crossing point respectively.

On the other hand, LUMO peak showed a shift to lower energies of 230 meV when going from center to a two molecule overlap. Interestingly, this peak disappears on the crossing point. These observations show that substrates nature have a major effect on molecular electronic signature.

4.1.3 Domain growth on Au (111) substrate and Kondo peak appearance

On Au (111) the TbPc₂ grows into numerous domains of various sizes as depicted in Figure 4.3(a). A very high mobility of the molecules is noticed and attributed to weak molecule-substrate interactions. Among the three substrates, Au (111) certainly shows the most complex situation. In particular, appropriate tunneling conditions (low current and bias) are necessary, otherwise the molecules may just be dragged by the tip during the scanning process. Only negative biases gave stable topography and STS maps. From the STM images only half of the molecules show the eight-lobe contrasts observed in isolated molecules, while the other half shows hardly distinguishable contrasts in topography image.

The topography image of Figure 4.3(b) reveals a contrasted checkerboard self-assembly. Bright and dark molecules (marked A and B respectively) corresponding to TbPc₂ molecules

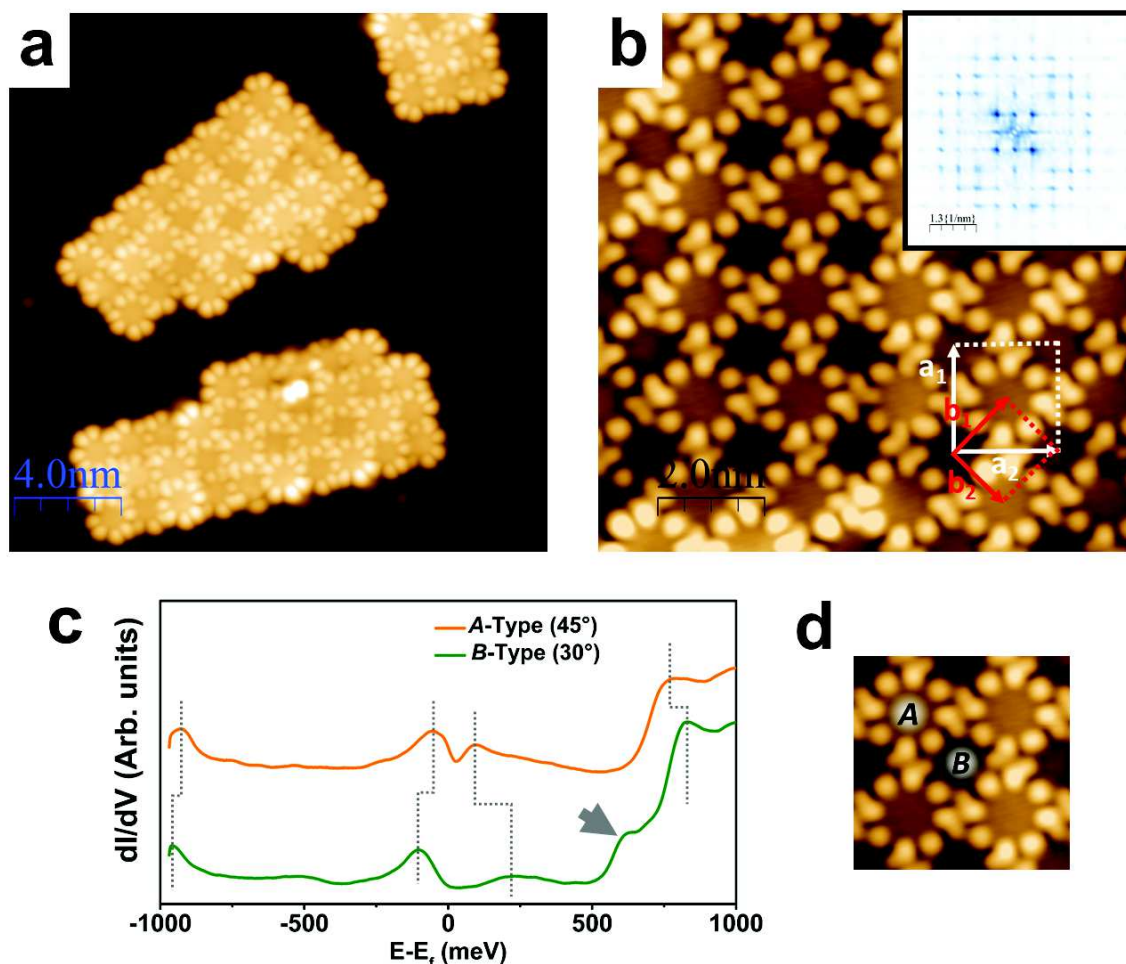


Fig. 4.3 a) and b) represent a constant current topographies of molecules adsorbed on Au (111). Multiple relatively small domains are observed on this crystal and the corresponding 2D-FFT is depicted as inset in top right corner of (b). Two lattice vectors are highlighted. $\vec{a}_{1,2}$ represent the lattice parameters of one molecular type, $\vec{b}_{1,2}$ those of the next neighbors such as: $\vec{a}_1 = \vec{a}_2 = 2\text{nm} \pm 0.2\text{ nm}$ and $\vec{b}_1 = \vec{b}_2 = 1.42 \pm 0.2\text{ nm}$. $\alpha = 90^\circ \pm 1^\circ$ in both lattices. Two topographic contrasts are observed for molecules in a domain. Bright ones labelled A have a skew angle of 45° and dark ones labelled B have a skew angle of 30° . c) dI/dV spectroscopies performed at the center of both A-type (orange) and B-type (green) molecule. Reduced gap is observed on A-type compared to its neighbor. A supplementary LUMO peak is visible for B-type molecule at 620 meV as indicated with an arrow. d) Topography image showing the two molecular types.

in two different states are observed. Unit cell vectors of such compact domain are labelled \vec{a}_1 and \vec{a}_2 with the following lattice parameters: $a_1 = a_2 = 2$ nm and $\alpha = 90^\circ$. The next neighbor molecules are represented by \vec{b}_1 and \vec{b}_2 vectors, where $b_1 = b_2 = 1.42 \pm 0.2$ nm and expected angle between them equal to 90° .

STS spectra recorded at the center of both *A*- and *B*-type molecules show a slight difference as presented in Figure 4.3(d). A HOMO-LUMO gap increase is observed when the molecule rotates by 15° . This gap is measured to be 300 meV above the *B*-type molecule while it was found to be of 150 meV on the *A*-type molecule. Moreover, an additional peak only appearing on *B*-type molecules is observed at +620 meV and defined as a LUMO. The gap reduction observed for *B*-type molecules is due to higher charge transfer between the molecule and the substrate. It reveals a coupling increase between *B*-type double decker and the crystal. Since the relative height of the *B*-type molecule is lower compared to *A*-type, the upper ligand-substrate interaction is increased in accordance with HOMO-LUMO gap reduction. As a result, STS measurements performed above the central area of the molecules may be a help for the identification of *A*- and *B*-type molecules.

The work carried out by T. Komeda et al. to identify the molecular orientation is based on the observation of four hardly distinguishable lobes in *B*-type molecules. In this section more sensitive measurements are presented, based on the observation of molecular orbitals on the inner part of the molecules. A high resolution STM image of a terbium double-decker monolayer on Au (111) is presented in Figure 4.4(a). Both *A*- and *B*-type molecules are distinguishable when tunneling conditions are at the detection limit ($V=5$ meV and $I=10$ pA) revealing the orbital distributions in the central area of both molecular types. Both types of molecular structures are again distributed in a checkerboard fashion inside a domain and are consistent with the calculated HOMO distribution obtained by DFT calculation by Vitali et al.[7]

Figures 4.4(b) and 4.4(c) show enlarged images of both *A*- and *B*-type molecules respectively. The inner molecular orbital distribution are colored in green for better visualization. In order to determine the angle between the two structures, dotted lines are drawn in both images, along the two opposite pyrroles of the upper ligand. The angle between the two lines represents the smallest angle between molecules and is found equal to 15° . This value is in accordance to what has been previously proposed by Komeda et al. [6]

Now that the situation of the upper ligand is clarified, it is necessary to gain more knowl-

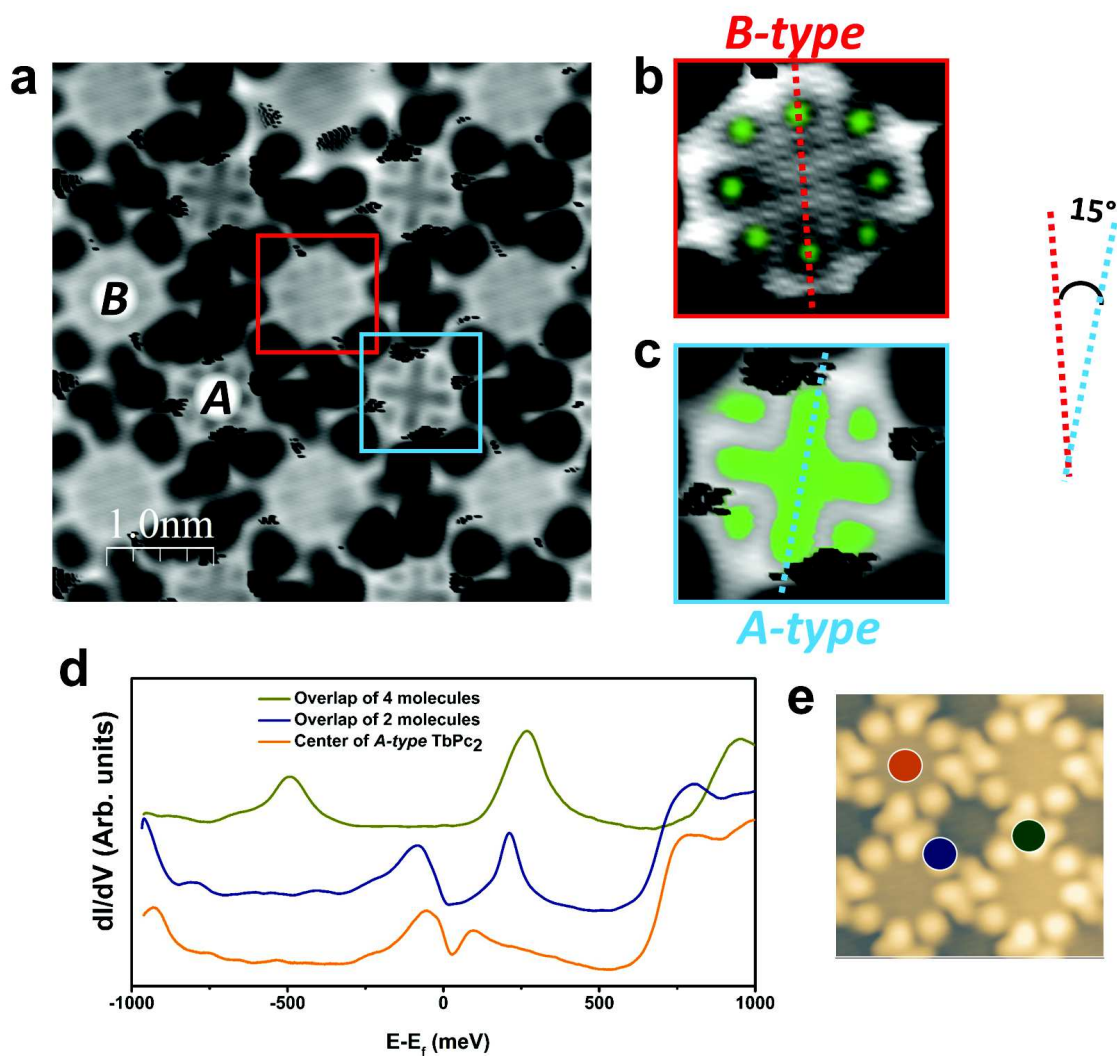


Fig. 4.4 High resolution constant current topography performed at $I = 70$ pA and $V = -50$ mV, under these low tunneling conditions molecules A and B show two different electronic distribution in the central area of the molecule. b) and c) represent a magnified images : *B*-type molecule shows eight distinct spots as colored in green while *A*-type molecules show extended “lobes” leading to a cross-like contrasts in the center. Two lines are drawn on both images to highlight the angle variation between *A*- and *B*-type molecule which is found to be 15° . d) dI/dV spectroscopy performed above the three regions as shown in e). Spectroscopic signatures differ considerably between the three regions indicating a large electronic modification among molecules.

edge about the conformation of the bottom ligands. Komeda et al. reported that by taking into account the orientation observed above and by keeping a 45° azimuthal angle between the two ligands a forbidden structural overlap leading to steric repulsions is found. Therefore the only arrangement possibility of the bottom ligands in order to respect the steric hindrance is the alignment following the same orientation respecting similar adsorption configurations as one monolayer of MPC molecules.[14–16] In this case two configurations of the TbPc_2 can be obtained, one where the azimuthal angle is kept at 45° (*A*-type) as for the isolated molecule, and the other one with an azimuthal angle of 30° (*B*-type) between the two phthalocyanines.

As a consequence of this intrinsic rotation, the apparent height of *B*-type molecules is reduced by 0.3 \AA compared to *A*-type molecules appearing darker in STM topography. The substrate effect is assumed to be similar on the molecule in both types of molecules due to negligible upper ligand-substrate interaction. This height reduction might be induced by an electronic modification since a significant rotation occurred on the molecule. Not surprisingly, the spectroscopy recorded above a monolayer film and an isolated molecule (see Appendix, Figure 15) are different, thus informing on the large influence of molecular neighbors and inter-molecular interactions. Figure 4.4(d) shows dI/dV spectra recorded above the three regions indicated in 4.4(e). The spectra above the center of an *A*-type molecule and above the overlap of two adjacent double-deckers are similar although they exhibit an increase of the HOMO-LUMO gap to 280 meV in the overlapping region of *A*- and *B*-type molecule. More dramatic is the downwards shift of the HOMO above the crossing point (overlap of four molecules), which is now found at -500 meV. An upwards shift of the LUMO to +270 meV above the crossing point is also observed. Finally, a displacement of the LUMO+1 is also noticed from 770 meV for the molecule center to 800 meV for the crossing point. The HOMO-LUMO gap above the crossing point is 760 meV.

Interestingly, when high resolution spectroscopy is performed above the crossing point of four adjacent TbPc_2 molecules, a zero bias peak (ZBP) related to a Kondo effect appears close to the Fermi energy as shown in Figure 4.5. This peak is only present above the crossing point, thus indicating that inter-molecular interactions play a major role in the ZBP appearance. The Kondo origin of the ZBP has been ascertained by Komeda et al. in experiments realized under similar conditions as a function of temperature and external magnetic field. [6] It was found that the width of the ZBP perfectly follows the prediction from Fermi liquid theory leading to $T_K \approx 22 \text{ K}$.

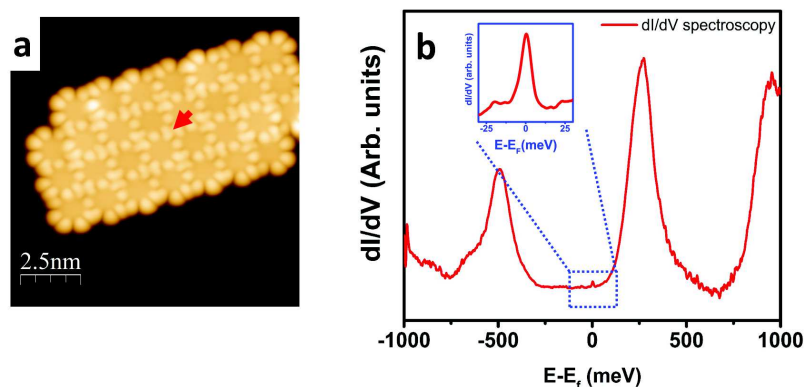


Fig. 4.5 a) Constant current topography image showing a TbPc_2 domain formed on a Au (111) substrate. b) dI/dV spectroscopy performed at the crossing point indicated by a red arrow in a), the inset shows an enhanced spectra at the Fermi region, the Fano fit for this ZBP reveals a Kondo temperature of $T_K \approx 22 \text{ K}$ with the parameters: $q = 3.23$ and $\Gamma = 5.9 \text{ meV}$.

The Kondo resonance observed in monolayer islands exhibits substantial differences compared to the Kondo resonance reported for isolated TbPc_2 molecules on Au (111). While the same molecule is involved, a different mechanism seems to be at work in both cases. Indeed, for isolated molecules T_K was reported to be 38 K, almost twice the temperature observed on the domain. Although the degenerated spin 1/2 is responsible for the Kondo resonance in both cases, this electron has to be in "contact" to a source of spins. In the first case, the substrate produces spins interacting with the delocalized electron of the isolated molecule leading to a ZBP. In the second case, molecules are linked side-by-side and the upper Pc ligands form a 2D-network of delocalized π -electrons. Only the spin properties of the upper ligand are accessible with STM, thus, the excess electron per molecule is probed while interacting with the delocalized electrons of the film. In order to understand the evolution of the Kondo resonance from the single molecule to the molecular film, step-by-step assembling of islands by molecular manipulation with the STM tip was performed.

4.2 Domain construction from isolated molecules

For a detailed understanding of the appearance of the Kondo resonance in a molecular domain, atomic manipulation of single molecules was performed. Molecule-tip interactions are used to laterally manipulate the molecules by means of an attractive potential, similar to the Lennard-Jones potential.[17] Experiments were carried out by the "pulling" procedure. The tip was positioned at 4 Å above the surface, then the feedback loop was opened and

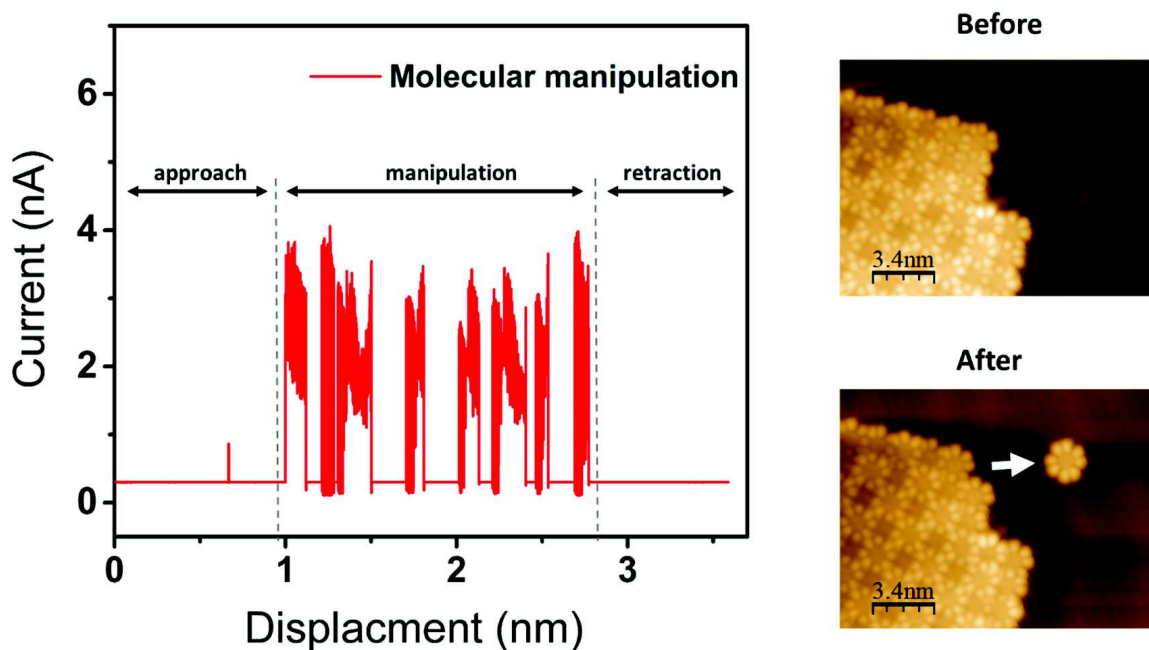


Fig. 4.6 Molecular manipulation, the graph is divided into three phases: approach phase, manipulation process and retraction phase of the tip. An increase in current is observed during manipulation which indicates the step-by-step translation of the molecule during the process. Two constant current topography images recorded at $I = 60$ pA and $V = -0.3$ V show the domain before and after manipulation of one TbPc₂ molecule as indicated by the white arrow.

the tip-sample distance was controlled in order to keep a constant gap-resistance of $R = 250$ M Ω . When the tip is moved at constant height along a predefined path, the molecules move laterally. If the tip path does not pass through the molecular center, a rotational movement occurs along with the translation movement. For the purpose of island construction both, rotation and translation were used to arrange molecules in their best close-packed configuration.

The current variation is recorded with respect to the x - y coordinates, it shows specific signatures corresponding to the manipulation process. An example is depicted in Figure 4.6, where three phases are highlighted. The first phase corresponds to the tip approach from its initial position towards a molecule, the current showing a stable low value. The second phase shows periodic increases in the tunneling current which are interpreted as molecular displacement. Indeed, the molecule moves by steps as the tip is moved from one position to another. The current increases as the molecule moves upwards along the z -axis. This effect is also known as “squeezing mode” where the force-field generated by the tip traps

the molecule which therefore jumps between two electrodes during the lateral manipulation process (see Phase II in Figure 4.6).[18] The third phase corresponds to the tip retraction depicting similar signals as for the approach phase. Therefore, a careful analysis of the current behavior during manipulation provides an easy way to follow the displacement process, therefore saving a precious time. A careful control of the manipulation process allows the creation of dimers, trimers and tetramers which in turn can be manipulated.

Domain creation from single molecules is easily performed by separately manipulating each molecule toward a specific area. Coordination of four molecules succeeded following multiple steps as presented in Figure 4.7. Manipulation was made using a bias voltage $V=0.1$ V and a current $I=4$ nA. We considered the intermolecular interaction to be established when the molecule can no longer be moved under same conditions. From Figure 4.7(b) to Figure 4.7(k) molecular orbitals extensions of the upper phthalocyanine are presented by a red contour. Inside of each contour a model of the upper phthalocyanine is drawn in order to visualize the molecular orientation. In all cases, a minimal distance between molecules larger than the intermolecular contact was found.

During manipulation, the path followed by a molecule may interfere with a second molecule, in such a case, molecules interact and the molecule to be displaced is no longer allowed to move. As a result, the optimal molecule-molecule interaction is considered to be reached. After each manipulation towards the formation of an island, the new structure is investigated by means of dI/dV spectroscopy for the detection of a Kondo signal on the lobes and over the intersection areas.

In a first series of experiments, four single molecules have been extracted from large self-assembled domains. From Figure 4.7(a) to Figure 4.7(e) constant current topography images show the four molecules labelled from 1 to 4. As expected, a Kondo resonance appears when the dI/dV is recorded above all eight lobes of every isolated molecule.

A second type of manipulations is performed on molecule labelled 2 which is moved towards molecule 1 to make them interact through a Van Der Waals forces, thus forming a dimer as depicted in Figure 4.7(f). This dimer shows a center-to-center distance of 1.5 nm close to the distance observed in a self-assembled film (1.44 nm). In contrary to an extended domain, both molecules depict a parallel orientation, thus confirming that confinement is the origin of skew angle modification observed in a film. Spectroscopic measurements performed above the two molecules after manipulation did not show any ZBP, which indicates an absence of a Kondo resonance on the newly formed dimer.

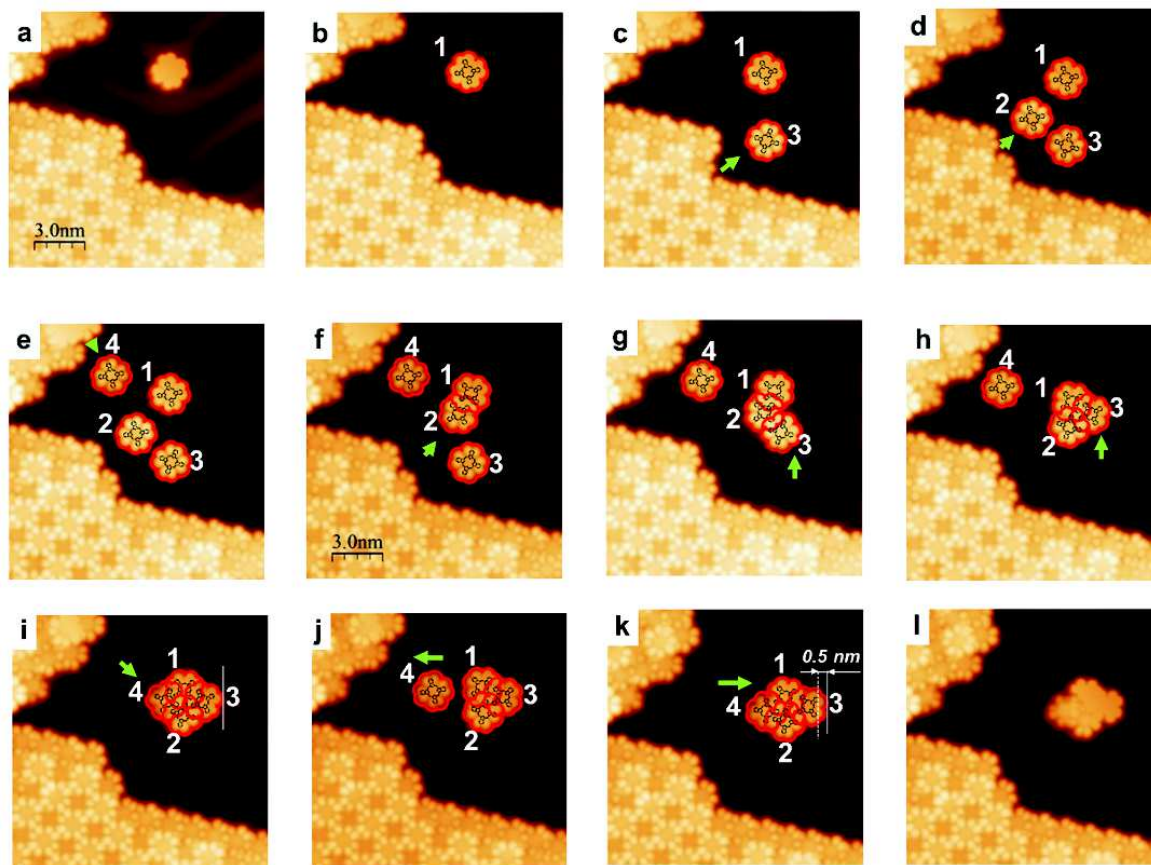


Fig. 4.7 Formation of four molecular islands by using molecular manipulations. Molecules are labelled from 1 to 4. a) One single molecule is used as reference. From b) to k) a model of the upper ligand with its electronic distribution highlighted in red is superposed in order to follow the orientation during manipulation process. From b) to e) molecules 1, 2, 3 and 4 are pulled out of the domains as indicated by the green arrows. f) Molecule 2 is moved to be connected to molecule 1. g) Molecule labelled 3 is added to molecule 2 in order to form a chain like. Similar overlap as between molecule 1 and molecule 2 is observed. h) Shows a second manipulation performed on molecule 3 which creates a trimer with the three molecules interacting among each-others. i) A fourth molecule is inserted symmetrically to molecule 3. j) and k) represent the extraction and insertion with a rotation of molecule 4 in order to optimize the island structure. The whole island is translated by 0.5 nm as depicted in (k). l) Shows the same domain as in k) without the phthalocyanine model. The tunneling parameters for topography were as follows: $I = 70 \text{ pA}$, $V = -0.3 \text{ V}$.

When a third molecule labelled 3 is added to the dimer (Figure 4.7(g)), molecule 2 rotates by 6° to adapt to the presence of both, molecule 1 and 3. Again, no Kondo peak was observed on this molecular chain as expected since locally both molecular intersections concern only two TbPc₂ molecules leading to similar interpretation as for the dimer.

In Figure 4.7(h) molecule number 3 is manipulated so as to form a trimer with symmetric interactions among all three molecules. It is interesting to notice that both, molecules 1 and 2 adapt their orientation by taking into account the steric confinement due to the insertion of molecule 3. Interestingly, this new trimer exhibits a decreased Kondo resonance above the intersection area of the three molecules. This Kondo peak corresponds to a temperature of $T_K = 34$ K and is absent from the center or the external molecular lobes, suggesting that this resonance is created by the interaction of the three molecules.

Next manipulation consisted in the formation of a tetramer as depicted in Figure 4.7(i) where molecule 4 was moved toward the trimer. It is noteworthy that the insertion of the last molecule does not create any geometrical modification (rotation or translation) of the former trimer. It indicates that the structure was already in its equilibrium configuration as a trimer. The tetramer island does not form a square planar geometry which is a result of either an absolute minimum energy configuration or a relative minimum whose origin is the sequential nature of the island formation.

The last experiment consisted in the extraction of molecule 4 from the tetramer and subsequent insertion with a rotation of 25° . The idea was to increase the matching within the formed island in order to increase the interaction between molecules 1 and 4. The resulting island is presented in Figure 4.7(k). Indeed, Figure 4.7(k) demonstrates that pushing on molecule 4 produces the displacement of the entire island without any fragmentation. As a result of the high inter-molecular interaction the whole island was translated by 0.5 nm during this step. This last experiment leads us to conclude that the molecule-molecule interaction overcomes the molecule-substrate interaction, confirming the minor effect of the Au (111) substrate when it comes to double-decker film formation. This result is not intuitive since due to molecular separation there is no chemical bonding between the molecules. As a comparison, Calmettes et al. reported the manipulation of Ad₆HBC¹ dimers and trimers on Ag (111). Although constructed islands can be very robust, they reported island fragmentation in most manipulation processes as well as island rotation when scanning at negative bias.

¹hexa-adamantyl-hexa-benzocoronene

Table 4.1 Summary of the presence and absence of Kondo resonance on various systems (from monomer to film). Temperature and Full Width at Half Maximum (FWHM) are also presented.

	Monomer	Dimer	Trimer	Tetramer	Film
Kondo presence	Yes (Lobes)	No	Yes (Crossing point)	Yes (Crossing point)	Yes (Crossing point)
T_K	37 K	/	34 K	31 K	22 K
FWHM (Γ)	9.56 meV	/	9 meV	8 meV	6 meV

In the following, the newly formed tetramer of TbPc_2 is therefore considered as the most stable structure on Au (111). The occupation area in Figure 4.7(k) is about 12 nm^2 . In both Figure 4.7(i) and Figure 4.7(k), a Kondo resonance is observed when the dI/dV is recorded at the intersection area. This Kondo peak corresponding to $T_K = 31 \text{ K}$ is not present elsewhere on the island suggesting that it comes from the molecular interactions. Table 4.1 summarizes the appearance of Kondo resonances on islands as well as corresponding temperatures and its width.

Isolated monomers show that the delocalized electron over the π -orbital is responsible for spin diffusion leading to a Kondo resonance (see section 3.6). When a dimer is formed, the two upper ligands of both molecules have their molecular orbitals overlapped, see Figure 4.7(f). The two delocalized electrons are therefore paired up, which explains why the Kondo resonance is no longer present on a dimer. However above a trimer, the same reasoning leads to an unpaired electron (the two others being paired up) which gives rise to magnetic impurity. The Kondo temperature reduction compared to the isolated molecule is explained by the additional decoupling of the upper ligand from the substrate.

While application of the above interpretation to tetramer should lead to Kondo peak disappearance, STS measurement clearly showed a ZBP at the crossing point. When inserted into a trimer, the fourth molecule is found to have minor impact on island electronic properties which might explain the small modification of Kondo temperature (reduced by only 3 K). Delocalized electrons in that case would interact with each other to create the magnetic resonance.

It is remarkable to find that the Kondo temperature is decreased when the island size increases. Kondo temperature crucially depends on the availability of electrons ($g(\epsilon)$) for scattering process by the magnetic impurity. On the other hand, T_K is exponentially reduced if the exchange coupling (J) with the magnetic impurity increases, since $T_K \propto$



Fig. 4.8 From left to right, constant current topography of a TbPc_2 film adsorbed on Cu (111), Ag (111) and Au (111) respectively. Each image contains nine molecules where four full molecules are identified at the center. All substrates were represented with a grey-scale to highlight the difference.

$\exp[-1/(g(\epsilon).J)]$. [19, 20] In the present case, a spin network is formed at the upper ligand layer as every TbPc_2 molecule hosts one excess electron delocalized at its upper phthalocyanine. Moreover, a distortion of the upper ligand due to molecular assembly will change the electron density $g(\epsilon)$ provided to the magnetic impurity. Thus embedded molecule in a film will have lower interactions with the surface compared to the ones in smaller islands. By adding molecules to a small island, the position where Kondo resonance is measured is less and less exposed to the substrate 2D electrons thus decreasing $g(\epsilon)$. As a consequence the Kondo temperature drops to a lower value of 22 K when a film is formed.

A similar conclusion has been drawn by Iancu et al. in their investigation of TBrPP-Co on copper. They measured a Kondo temperature decrease from 170 K to 105 K when going from the monomer to the 7-molecules island. [21]

4.3 Molecular densities

Lattice properties on different substrates were reported in Section 4.1 when a molecular film is formed on them, this change is induced by the geometrical modification where different molecular arrangements were observed depending on the substrate.

Figure 4.8 shows topographic image of nine terbium double-decker molecules adsorbed on three different substrates: Au (111), Ag (111) and Cu (111). Interestingly, it is found that the molecular density increases along with an increase of substrate reactivity. The following molecular densities: 0.48 molec/nm^2 , 0.53 molec/nm^2 and 0.58 molec/nm^2 are obtained on gold, silver and copper respectively. These results are summarized in Table 4.2 along with substrate-bottom ligand distance and the distance to next neighbor.

A decrease in surface reactivity towards the molecular layer is normally expected to increase the inter-molecular interaction thus leading to an increased molecular density. Nevertheless, experimental results are not consistent with this simplistic view evidencing the contribution from other mechanisms of inter-molecular interactions.

The three investigated crystals showed different molecular orientations. On Cu (111) the molecules keep their skew angle of 45° between the ligands and all molecules show a parallel adsorption orientation in a monolayer. The inter-molecular distance is therefore measured to be 1.33 nm. On Ag (111) a different confinement is created thanks to 15° rotation of moiety of molecules due to lower substrate reactivity. Therefore empty space is increased between adjacent molecules resulting in an increase of the inter-molecular distance found to be $b=1.36$ nm. On the other hand, the Au(111) substrate generates a situation where half of the molecules in a domain have a skew angle of 30° . This change also alters the electronic properties since different LUMO peaks and HOMO-LUMO gaps are measured on the two molecular types. In addition, molecular interactions are expected to be modified due to the gold substrate. Therefore, the trend for the molecules is to balance between molecule-molecule interactions and molecule-substrate interactions resulting in increased inter-molecular distance of 1.42 nm.

For comparison, densities of MPc are found to vary as well, depending on substrate reactivity. For example, the CoPc film was found to have the following molecular density: 0.80 molec/nm², 0.54 molec/nm² on Au (111) and Ag (111) respectively, and CuPc to have a density of 0.41 molec/nm² on Cu (111) due to close packing in mono-planar structures.[22–24] Although the TbPc₂ molecules interact with neighboring molecules by mean of both, upper- and bottom-ligands the influence of the substrate nature seems to follow the same tendency as for normal MPc on noble metal surfaces.

Table 4.2 Density variation with respect to the investigated substrate. Next neighbors and calculated substrate-bottom ligand distance are also reported.

	Au (111)	Ag (111)	Cu (111)
Next neighbor (nm)	1.44	1.36	1.33
Distance substrate-bottom ligand (Å)	3	2.5	1.9
Density (Molec/nm ²)	0.48±0.02	0.53±0.02	0.58±0.02

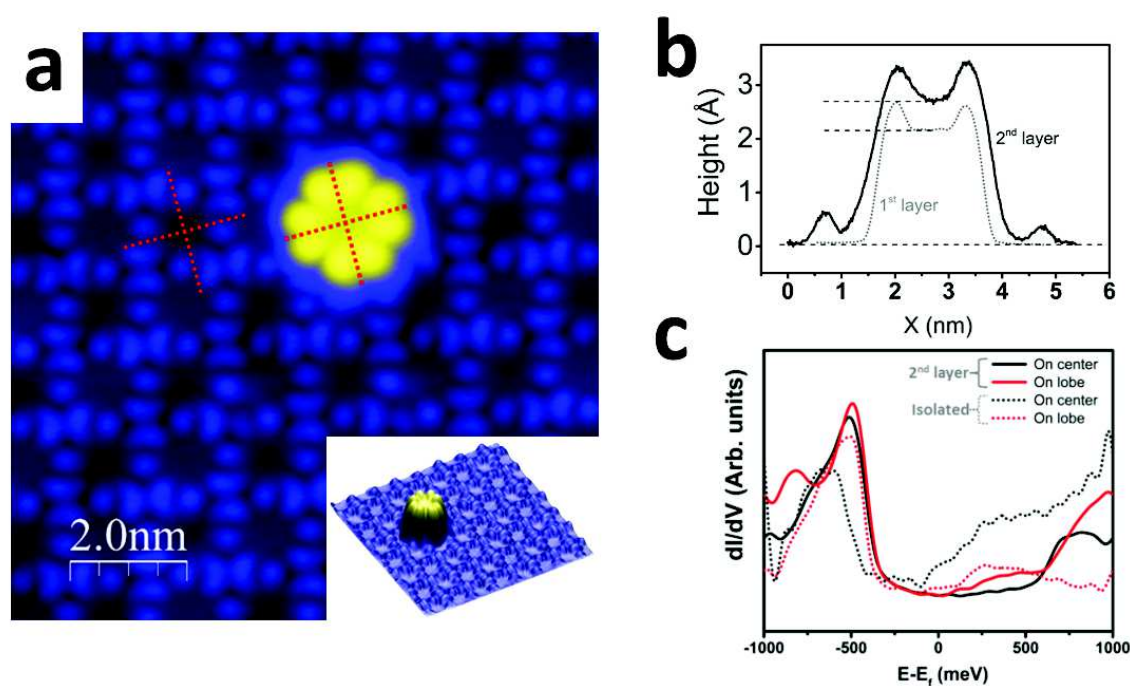


Fig. 4.9 a) Two TbPc₂ layers grown on Ag (111) substrate. a) Topography image where the color-code is different from previous representations in order to enhance the appearance of the second layer. Inset: 3D view of the 2nd layer molecule. b) molecular profile measured along two opposite lobes. 3 Å are measured from the bottom layer to the upper ligand of the second layer, a comparison with the molecular height of the first layer molecule is shown in dotted lines. c) dI/dV spectroscopy recorded at the center and lobe on both, first (isolated) and second layer molecule.

4.4 Second layer molecule

Only a few experiments revealed the adsorption of double decker molecules in second layer as shown in Figure 4.9(a). By assuming that all molecules involved in this system have a skew angle of 45°, it is straightforward that the second layer adsorbs above initial double-decker with a parallel arrangement sharing the same D_{4d} axis. The upper ligand of the lower molecule meets the bottom ligand of the second layer molecule with an angle of 45° resulting in a perfectly parallel $\pi - \pi$ stacking. This result is consistent with previously reported second layer DyPc₂ by He et al. and LuPc₂ by Toader et al. [13, 25]

Second layer molecules also show eight lobes under STM imaging. As expected, due to the first layer decoupling, the second layer TbPc₂ shows an increased height, see the profile of Figure 4.9(b). The height of the second layer molecule is measured to be 3 Å, this value is by 0.5 Å higher compared to isolated molecule directly adsorbed on Ag (111). While

the experiments presented here on TbPc₂ molecules only show eight lobes, He et al. also reported four-lobe features on topographic image of second layer DyPc₂ molecules depending on the voltage bias.

Conductance measurements on both, center and lobes of second layer TbPc₂ molecules, show slight differences compared to the STS recorded on isolated molecule in direct contact with the substrate. Second layer molecules reveal more localized orbitals over the molecule (4.9(c)). As expected, a larger HOMO-LUMO gap is found on the 2nd layer molecule compared to the 1st layer since the molecule is more efficiently decoupled by the 1st layer in the former case. Furthermore it is found that the LUMO peak of the 2nd layer molecule is shifted away from Fermi energy as the substrate effect is reduced due to increased decoupling induced by the first layer.

Interestingly, the previously observed HOMO peak on a lobe of the 1st layer molecule splits in two when investigating the 2nd layer molecule, thus becoming HOMO-1 and HOMO respectively. However, only one large HOMO peak is present when investigating the conductance at the center of a second layer molecule. The HOMO on both, center and lobe of the 2nd layer is positioned at the same energy (-500 meV) while 100 meV separate them when the molecule is in direct contact with Ag (111) crystal (1st layer). This result indicates a relatively uniform distribution of the orbital on the upper ligand of the second layer. On the other hand, the peak splitting when the tip is moved over a lobe is a proof for a HOMO-1 localization on the terbium atom of the second layer.

4.5 Summary and conclusions

In this chapter, islands and monolayers of TbPc₂ molecules were investigated on various substrates where a different assembling process depending on the nature of the substrate has been observed. Interestingly, on Au (111) half of molecules in a monolayer find their skew angle between their Pc ligands reduced by 15° from the initial 45°. These differences are reported to a molecular density variation on substrates, thus, a monolayer adsorbed on Cu (111) is by 20% more compact compared to an adsorption on Au (111). This result does not correspond to expectations since the inter-molecular interactions should increase when the molecule-substrate interactions are reduced. However, the geometrical modification on low reactive substrates may lead to such a density variation thus, a direct comparison between the adsorbates is not relevant.

The Kondo resonance previously observed above the lobes of single TbPc₂ molecule is now located at the crossing points of a domain adsorbed on Au (111), its relative temperature is by half reduced compared to single molecule. In order to understand this localization of the resonance and a temperature reduction, a four molecule island was constructed molecule by molecule to mimic the first stage of a monolayer formation, the ZBP behavior was investigated by STS at each step of the manipulation.

Interestingly the Kondo resonance was found only on monomer, trimer and tetramer islands and was totally absent on a dimer. Furthermore, the related Kondo temperature was found to decrease when the island size increases, result of a reduction of hybridization of the upper ligand with the electron bath provided by the substrate.

The local adsorption site and monolayer arrangement of TbPc₂ molecules on various substrates can be controlled very precisely by STM tip, it opens a reliable technique of mastering the molecular growth. The intermolecular interactions strongly depend on the molecule-molecule distance as well as their adsorbate. Manual construction of molecular islands leads to a possible tuning of the electronic and magnetic properties intrinsic to molecules. By following the intrinsic properties such as Kondo resonance during the island formation, it becomes possible to draw the real space evolution of the π -unpaired electron responsible for the conduction electron scattering.

REFERENCES

- [1] Stephen R. Forrest. The path to ubiquitous and low-cost organic electronic appliances on plastic. *Nature*, 428(6986):911–918, April 2004.
- [2] Michele Muccini. A bright future for organic field-effect transistors. *Nature Materials*, 5(8):605–613, August 2006.
- [3] Norbert Koch. Organic Electronic Devices and Their Functional Interfaces. *ChemPhysChem*, 8(10):1438–1455, July 2007.
- [4] Marko Burghard, Hagen Klauk, and Klaus Kern. Carbon-Based Field-Effect Transistors for Nanoelectronics. *Advanced Materials*, 21(25-26):2586–2600, July 2009.
- [5] Keiichi Katoh, Yusuke Yoshida, Masahiro Yamashita, Hitoshi Miyasaka, Brian K. Breedlove, Takashi Kajiwara, Shinya Takaishi, Naoto Ishikawa, Hironari Isshiki, Yan Feng Zhang, Tadahiro Komeda, Masakazu Yamagishi, and Jun Takeya. Direct Observation of Lanthanide(III)-Phthalocyanine Molecules on Au(111) by Using Scanning Tunneling Microscopy and Scanning Tunneling Spectroscopy and Thin-Film Field-Effect Transistor Properties of Tb(III)- and Dy(III)-Phthalocyanine Molecules. *Journal of the American Chemical Society*, 131(29):9967–9976, July 2009.
- [6] Tadahiro Komeda, Hironari Isshiki, Jie Liu, Yan-Feng Zhang, Nicolás Lorente, Keiichi Katoh, Brian K. Breedlove, and Masahiro Yamashita. Observation and electric current control of a local spin in a single-molecule magnet. *Nature Communications*, 2:217, March 2011.
- [7] Lucia Vitali, Stefano Fabris, Adriano Mosca Conte, Susan Brink, Mario Ruben, Stefano Baroni, and Klaus Kern. Electronic Structure of Surface-supported Bis(phthalocyaninato) terbium(III) Single Molecular Magnets. *Nano Letters*, 8(10):3364–3368, October 2008.

- [8] Jörg Schwöbel, Yingshuang Fu, Jens Brede, Andrew Dilullo, Germar Hoffmann, Svetlana Klyatskaya, Mario Ruben, and Roland Wiesendanger. Real-space observation of spin-split molecular orbitals of adsorbed single-molecule magnets. *Nature Communications*, 3:953, July 2012.
- [9] Luigi Malavolti, Matteo Mannini, Pierre-Emmanuel Car, Giulio Campo, Francesco Pineider, and Roberta Sessoli. Erratic magnetic hysteresis of TbPc₂ molecular nanomagnets. *Journal of Materials Chemistry C*, 1(16):2935–2942, March 2013.
- [10] Ludovica Margheriti, Daniele Chiappe, Matteo Mannini, Pierre-E. Car, Philippe Sainctavit, Marie-Anne Arrio, Francesco Buatier de Mongeot, Julio C. Cezar, Federica M. Piras, Agnese Magnani, Edwige Otero, Andrea Caneschi, and Roberta Sessoli. X-Ray Detected Magnetic Hysteresis of Thermally Evaporated Terbium Double-Decker Oriented Films. *Advanced Materials*, 22(48):5488–5493, December 2010.
- [11] Satoshi Takamatsu, Tadahiko Ishikawa, Shin-ya Koshihara, and Naoto Ishikawa. Significant Increase of the Barrier Energy for Magnetization Reversal of a Single-4f-Ionic Single-Molecule Magnet by a Longitudinal Contraction of the Coordination Space. *Inorganic Chemistry*, 46(18):7250–7252, September 2007.
- [12] Zhitao Deng, Stephan Rauschenbach, Sebastian Stepanow, Svetlana Klyatskaya, Mario Ruben, and Klaus Kern. Self-assembly of bis(phthalocyaninato)terbium on metal surfaces. *Physica Scripta*, 90(9):098003, 2015.
- [13] Marius Toader, Martin Knupfer, Dietrich R. T. Zahn, and Michael Hietschold. Initial Growth of Lutetium(III) Bis-phthalocyanine on Ag(111) Surface. *Journal of the American Chemical Society*, 133(14):5538–5544, April 2011.
- [14] Xing Lu and K. W. Hipps. Scanning Tunneling Microscopy of Metal Phthalocyanines: d^6 and d^8 Cases. *The Journal of Physical Chemistry B*, 101(27):5391–5396, July 1997.
- [15] Xing Lu, K. W. Hipps, X. D. Wang, and Ursula Mazur. Scanning Tunneling Microscopy of Metal Phthalocyanines: d^7 and d^9 Cases. *Journal of the American Chemical Society*, 118(30):7197–7202, January 1996.
- [16] I. Chizhov, G. Scoles, and A. Kahn. The Influence of Steps on the Orientation of Copper Phthalocyanine Monolayers on Au(111). *Langmuir*, 16(9):4358–4361, May 2000.

- [17] J. E. Jones. On the Determination of Molecular Fields. II. From the Equation of State of a Gas. *Proceedings of the Royal Society of London A: Mathematical, Physical and Engineering Sciences*, 106(738):463–477, October 1924.
- [18] D. M. Eigler, C. P. Lutz, and W. E. Rudge. An atomic switch realized with the scanning tunnelling microscope. *Nature*, 352(6336):600–603, August 1991.
- [19] Cyril Alexander Hewson. *The Kondo Problem to Heavy Fermions*. Number 2 in Cambridge Studies in Magnetism.
- [20] Nikolaus Knorr, M. Alexander Schneider, Lars Diekhöner, Peter Wahl, and Klaus Kern. Kondo Effect of Single Co Adatoms on Cu Surfaces. *Physical Review Letters*, 88(9):096804, February 2002.
- [21] Violeta Iancu, Aparna Deshpande, and Saw-Wai Hla. Manipulation of the Kondo Effect via Two-Dimensional Molecular Assembly. *Physical Review Letters*, 97(26):266603, December 2006.
- [22] Z. H. Cheng, L. Gao, Z. T. Deng, N. Jiang, Q. Liu, D. X. Shi, S. X. Du, H. M. Guo, and H.-J. Gao. Adsorption Behavior of Iron Phthalocyanine on Au(111) Surface at Submonolayer Coverage. *The Journal of Physical Chemistry C*, 111(26):9240–9244, July 2007.
- [23] Tomohide Takami, Clarisa Carrizales, and K. W. Hipps. Commensurate ordering of iron phthalocyanine on Ag(111) surface. *Surface Science*, 603(21):3201–3204, November 2009.
- [24] J. Y. Grand, T. Kunstmann, D. Hoffmann, A. Haas, M. Dietsche, J. Seifritz, and R. Möller. Epitaxial growth of copper phthalocyanine monolayers on Ag(111). *Surface Science*, 366(3):403–414, November 1996.
- [25] Yang He, Yajie Zhang, I.-Po Hong, Fang Cheng, Xiong Zhou, Qian Shen, Jianlong Li, Yongfeng Wang, Jianzhuang Jiang, and Kai Wu. Low-temperature scanning tunneling microscopy study of double-decker DyPc₂ on Pb Surface. *Nanoscale*, 6(18):10779–10783, August 2014.

CAPPING A TERBIUM DOUBLE-DECKER WITH A CERIUM ATOM

The discovery of the intricate role of the radical spins in the magnetic interplay of TbPc₂ molecules on Au (111) is one of the main results of the previous chapter. The π -radical also seems to play a key role in recent molecular spin valve experiments which can hardly be explained without assuming a coupling between the Tb nuclear spin and the radical spin through the Tb electronic moment.[1, 2] In view of the potential applications of similar molecules in the quantum information processing [3, 4] it is of prime importance to get further information on the role of the π -radicals in the coupling between two different spin systems i.e. between different metal atoms in SMM.

In a domain, no direct interaction between the f -systems of two adjacent molecules was observed and the Kondo resonance remained exclusively a result of scattering conduction electrons by the unpaired π -electron at the upper ligand. Moreover, to now, no information was given about the role of the second spin system in the magnetic response of the TbPc₂. In this respect, the investigation of multiple-deckers (triple or quadruple) has opened a way to test the coupling between lanthanide moments.[5–10] These elements has to be contrasted with π -stacked Pc based molecules such as CoPc where a direct d-d exchange occurs between the two magnetic centers.[11, 12]

However, another more versatile way consists in depositing the Ln atom on top of a double decker, leading to Ln-Pc-Ln'-Pc. In the case of the TbPc₂ the upper Pc ligand is then sandwiched between the Tb atom and the on-top Ln atom, thus playing a key-role in the coupling of both magnetic moments. It is this second approach that is examined in the present chapter by means of a cerium capping atom. In addition, through atomic manipulation with the STM tip, this approach allows turning on and off the interaction.

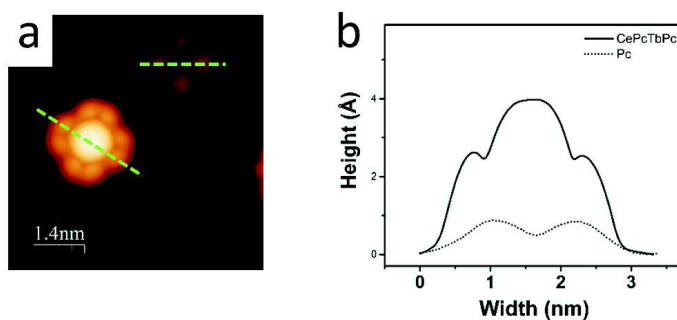


Fig. 5.1 a) constant current topographic image of TbPc_2 molecule and a single phthalocyanine. Higher conductance is measured at the central region (where the cerium resides) denoting an increased apparent height towards the tip. Eight lobes of the upper ligand are still visible surrounding the cerium atom. Four lobes are found as expected for the single phthalocyanine. b) profile line revealing an apparent height of 4 Å of CePcTbPc on Cu (111) substrate along with the apparent height of single phthalocyanine along lines superposed in topography image (a).

5.1 CePcTbPc complexes

TbPc_2 molecules were deposited according to the processes described in previous sections. Prior to the double-deckers capping experiment, a large amount of molecules was deposited such as to create large domains. The sample was first investigated under the STM to ascertain the molecular film growth. For cerium atom deposition, special care was taken to prevent both, contamination and large Ce-atom diffusion. In order to achieve this goal, a special atomic evaporator made of an alumina crucible was designed. A cerium foil cut into small pieces was introduced into the crucible. For atomic evaporation, the crucible was heated up to 1100 K while the sample was kept at liquid helium temperature on the cold stage of the STM chamber. In this process, the sample had to be manually transferred from the cold stage to the STM head causing a warming-up of the sample to an estimated value of ≈ 10 K. After cerium evaporation, the deposit was carefully investigated by STM. As shown Figure 5.1(a), cerium atoms are clearly identified as the bright protrusion that shows up at the center of the capped double-decker molecule.

As expected, the topography image (Figure 5.1(a)) shows an increase of apparent height compared to the un-capped double-decker (Figure 3.3). A cross section analysis reveals that the total height of an isolated CDD molecule adsorbed on Cu (111) surface is about 4 Å. In

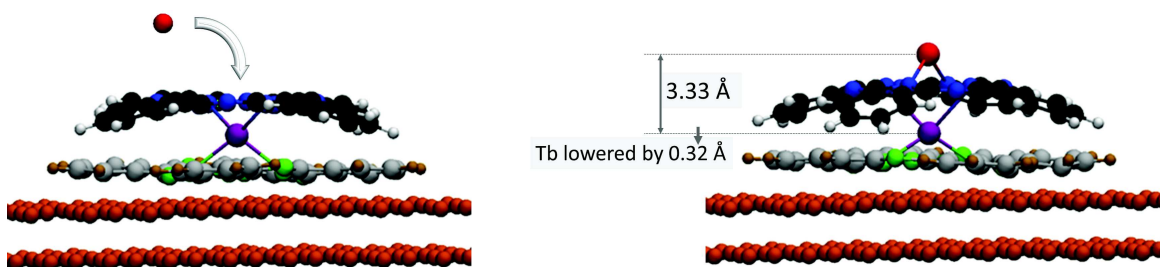


Fig. 5.2 Calculated model of TbPc_2 molecule (left) and CeTbPc_2 molecule (right) adsorbed on a Cu (111) substrate. Terbium position is lowered towards the substrate by 0.32 \AA after cerium coordination with the upper ligand by reducing terbium-upper phthalocyanine interactions. 3.33 \AA separate Ce and Tb, this value is constant when substrate is modified to Au (111) or Ag (111).

Figure 5.1(b) eight lobes of the upper ligand are still apparent after the cerium adsorption but the overall shape of the molecule becomes larger. A distance of 2.2 nm is measured between the two opposite lobes on CDD molecule while 2 nm were measured under similar conditions for an isolated TbPc_2 . As a conclusion, it is found that the spatial electronic distribution of the molecule is increased due to the presence of the cerium atom.

The structures have been grown on the following three substrates: Cu (111), Ag (111) and Au (111). Depending on the crystal nature various molecular TbPc_2 growth modes were obtained (Chapter 4). It is found that cerium atoms adsorb on TbPc_2 by coordinating with the nitrogen atoms from the pyrroles of the upper ligand. As a result, two capped complexes can be found on Au (111) depending on whether the adsorption takes place on the *A*- or *B*-type double-decker molecules. On the other hand, only one configuration is observed on copper and silver substrate (corresponding to *A*-type molecules).

This novel capped double decker (CDD) structure is different from the one of CsPcYPC investigated by Robles et al. [13]. In the later, they demonstrated a change of the electronic and magnetic properties of the YPC_2 double-decker due to the Cs adsorption. The presence of Cs atom produces a spin donation leading to a quenching of the π -electron spin of the upper ligand. As a result, the Kondo peak appearing at a crossing region of the YPC_2 domains disappears when Cs is adsorbed on an *A*-type molecule.[14] On *B*-type molecules, on the contrary, the cesium capping does not affect considerably the magnetic and electronic behavior of the double-decker.

DFT calculations showed that cerium CDD complexes are stable, both lanthanide elements sharing the same magnetic anisotropy axis. Thus D_{4d} symmetry of the double-decker is reduced to a C_{4h} upon presence of the second lanthanide. A single $TbPc_2$ molecule adsorbed on a Cu (111) substrate is shown in Figure 5.2(a) where the bottom ligand exhibits a planar adsorption parallel to the substrate while the upper ligand shows a slightly convex distortion towards the substrate. An angle of 9° is measured on bare $TbPc_2/Cu$ (111) while presence of the cerium atom increases this distortion (Figure 5.2(b)) leading the upper ligand to bend down towards the substrate with an angle of 14.5° . The presence of the cerium atom induces a bond weakening between the terbium and the upper ligand shifting the Tb downwards by 32 pm. The terbium shift is induced by the cerium coordination to four pyrrole nitrogens of the upper phthalocyanine. Therefore, both lanthanides are not evenly spaced with respect to the upper ligand. However, the bottom ligand remains at the same distance of 1.7 Å from the substrate. Furthermore, it is found that the Ce-Tb distance remains constant and equal to 3.33 Å on all substrates. Finally, the skew angle between the upper and the lower phthalocyanines is kept unchanged after capping the terbium double-decker with a cerium.

5.2 Site and substrate dependent STS

As discussed previously, the $TbPc_2$ double-decker molecules show different electronic structures depending on the molecule-substrate interactions. By capping this molecule with a cerium atom, additional changes in the electronic identity are expected: in the newly formed CDD complex, cerium interacts with the upper ligand thus strongly affecting the exchange between the upper ligand and the terbium atom; the global electronic structure of the molecule is then dramatically changed. Isolated molecules deposited on Cu (111) and those forming compact rafts on the same substrate exhibit a different electronic signatures when investigated by STS. Due to different growth modes no isolated molecules can be found on Ag (111) and Au (111), therefore only CDD complexes embedded into a molecular layer will be investigated on those substrates.

STS investigations on cerium CDD molecules on various substrates provides information about the substrate indirect effect on the local density of states at the cerium atom as well as information on the coupling between the two lanthanides. It is found that even though the Ce-Tb interactions remains mainly similar above all the substrates (similar Ce-Tb distance), the 2D substrate electrons play a major role in the exchange between the

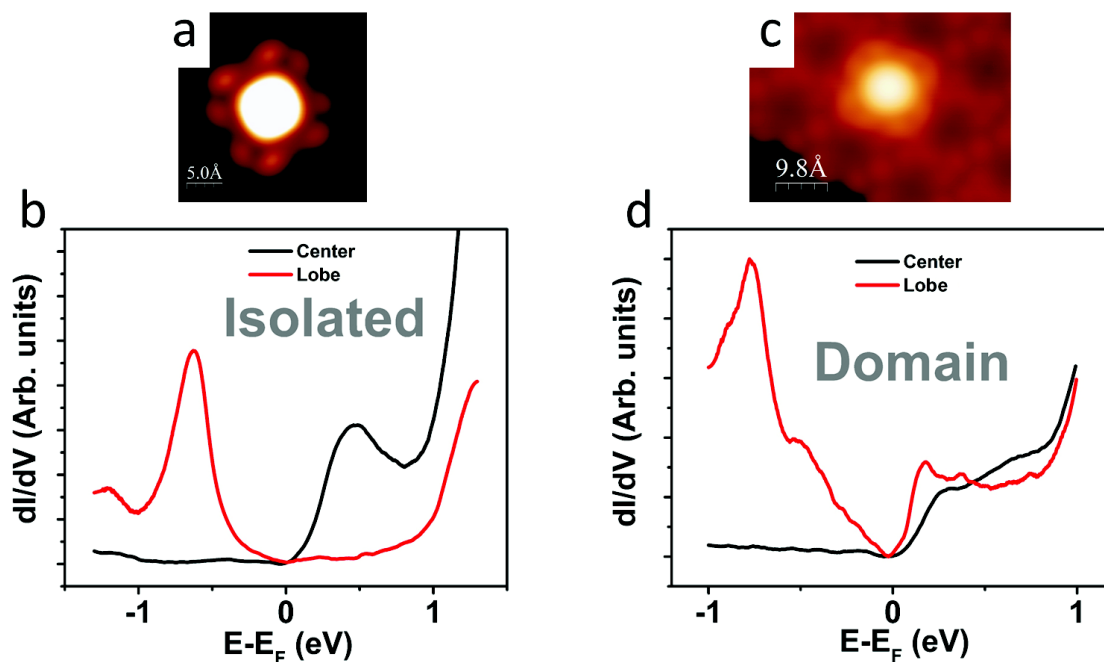


Fig. 5.3 a) and c) depict constant current topography images recorded at $I=80$ pA and $V=+0.3$ V on Cu (111) crystal on both, isolated and domain CDD molecule respectively. The bright protrusion in both images indicate the cerium adsorption site. b) and d) show STS spectra recorded above both center (black) and lobe (red) of both systems as indicated.

lanthanides and sandwiched phthalocyanine.

5.2.1 Ce/TbPc₂/Cu (111)

The STS data presented in Figure 5.3(b) and (d) were recorded above two locations (center and lobes) on both, an isolated CDD and a CDD belonging to a domain; see Figure 5.3(a) and 5.3(c) respectively.

When dI/dV is recorded on the center of an isolated CDD molecule (Figure 5.3(b)) only one pronounced peak corresponding to a LUMO at +450 meV is clearly visible. No HOMO is observed when the STS is taken above the Ce. Therefore, the HOMO-LUMO gap would be higher than 1.45 eV.

On the other hand, STS recorded above a lobe (Figure 5.3(b)) is expected to show similar behavior as the un-capped molecules in Figure 3.9 since the lobe results from an orbital expansion of one phenyl ring, which is not in direct contact with the cerium. Indeed, it is

found that the lobe of an isolated Ce/TbPc₂ molecule on Cu (111) exhibits a dI/dV that looks similar to the one recorded on a lobe of a bare TbPc₂ molecule (Figure 3.9). The STS depicts one major peak at -630 meV that can be ascribed to the HOMO. On the other hand, the LUMO previously observed at the center of an isolated CDD molecule is no longer present on the lobe, indicating that this LUMO is localized exclusively on the Ce atom.

When the STS is performed on the center of a CDD molecule in a domain Figure 5.3(d), the LUMO is found at +300 meV and the overall shape of the spectrum remains similar to that of an isolated molecule. It indicates that the presence of TbPc₂ molecules adjacent to the CDD molecule does not alter the molecular orbitals at the cerium position. The LUMO shift towards Fermi level indicates a larger charge transfer in a domain compared to isolated molecule. Not surprisingly, for molecules in a domain, a significant orbital overlap with cerium is expected with both the underlying and the neighboring TbPc₂ double-deckers.

Contrary to the isolated CDD, the presence of Ce has a relatively strong incidence on the lobe of a CDD embedded in a TbPc₂ domain. In particular a significant Ce contribution to the conductance is measured above overlapping lobes for a positive bias (Figure 5.3(d)). Two peaks are clearly distinguishable on CDD embedded in a TbPc₂ domain at +180 meV and +370 meV ascribed to LUMO and LUMO+1 respectively. A strong HOMO peak is observed on the lobes of both, isolated CDD and the CDD embedded in a domain. The HOMO above a lobe of the CDD inside a domain is shifted downwards by 140 meV revealing a new peak that appears as a shoulder at -530 meV. This peak is assumed to be induced by neighboring TbPc₂ molecules as it does not correspond to any cerium signature.

The spectroscopic difference highlighted in Figure 5.3 may be explained by the structural difference between the two systems. For the isolated CDD it was observed by DFT calculations that the phenyl rings point towards the substrate. A partial molecular-orbital overlap with the substrate may then explain the changes observed in the dI/dV spectroscopy above the lobes. Simultaneously, the dI/dV of the cerium atom is not much affected by the substrate (see Figure 5.3(b)).

On the other hand, the upper ligand of a CDD molecule embedded in a domain deserves particular attention since the inter-molecular interactions between adjacent molecules leads to reducing their interactions with the substrate.[15] As a result, the electronic signature on the lobes of a CDD molecule reflects both, TbPc₂ HOMO (expected for the double-decker) and the cerium contribution at positive bias voltage (Figure 5.3(d)).

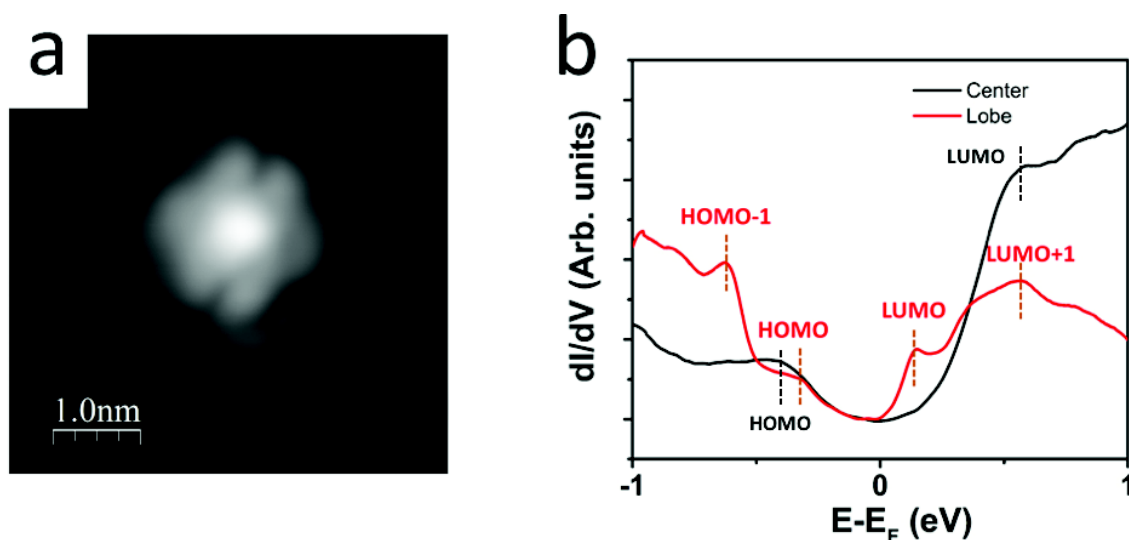


Fig. 5.4 a) Constant current topography image of a CDD molecule on a Ag (111) substrate. The four-fold symmetry is broken as two opposite phenyl rings point towards the tip while the two others remain at original positions. The cerium appear as the bright protrusion in the center of the image. b) dI/dV spectroscopy recorded on the lobe (red) and the center (black) of the CDD. Vertical lines highlight major peak position when STS is recorded above a lobe. Tunneling parameters: $I = 0.1nA$, $V = -0.4V$

5.2.2 Ce/TbPc₂/Ag (111)

As reported in section 4.1.2 TbPc₂ molecules form extended domains on Ag (111) as well and their interaction with the substrate is weaker compared to Cu (111). When the cerium atom is adsorbed on such a layer, a similar coordination with pyrrole nitrogens is observed. However, contrary to the situation observed on the Cu (111) surface, the four-fold symmetry reduces to a two fold symmetry. Figure 5.4(a) shows a constant current topography of CDD molecule in a domain on a Ag (111) surface. Two opposite pairs of lobes corresponding to two phenyl rings are clearly distinguishable while the two other orthogonal phenyls do not as double lobes. This result is an indication that the molecular conformation on Ag(111) (Section 4.1.2) is such that structural modification occurs at the upper ligand. Two opposite phenyls (among the four) bend upwards, appearing as two double lobes while the two others point downwards to the substrate and thus appear as single lobes. Their respective molecular orbital extension are modified as well due to a different interaction with the surrounding molecules.

The STS recorded on a CDD molecule co-adsorbed on a Ag (111) substrate shows small differences compared to the adsorption on Cu (111). When the tip is positioned above a cerium atom the STS only shows two shoulder-like features on both sides of the Fermi level, see Figure 5.4(b). The flattening out of the conductance between -400 meV and -1 eV is interpreted as a multiple peak contributions where the first one is positioned at -410 meV. This peak is ascribed to a HOMO as it is positioned at the same energy as the one observed on isolated CDD molecule on copper (Figure 5.3). At a positive bias voltage of 600 meV a conductance increase attributed to a LUMO peak, similar to the one observed on the copper crystal for isolated and domain CDD, generates a gap-like feature centered at the Fermi level.

When the tip is moved towards a lobe (red curve in Figure 5.4(b)), two peaks at -410 meV and -630 meV are found at negative voltage, the first peak has similar characteristic as the one observed at the center and thus is ascribed to the HOMO. The second peak is however ascribed to a HOMO-1 originating from the upper ligand of the molecule since its conductivity is more pronounced on the lobe compared to the center. For positive values of the bias voltage on a lobe, two peaks are found at +150 meV and +550 meV respectively. The first peak appears at the same position as LUMO observed for TbPc₂ molecules in domain on Ag (111) substrate, it is therefore considered as a LUMO originating from the upper ligand of the double-decker. The second peak is similar to the one observed at the molecular center and is attributed to a LUMO+1 orbital.

5.2.3 Ce/TbPc₂/Au (111)

As previously described in Section 4.1.3, the gold substrate generates two distinct conformations of the TbPc₂ molecules inside the monolayer, the *A*-type molecules with a skew angle of 45° between the bottom and the top ligands and the *B*-type molecules where this angle is 30°. The cerium atom spontaneously adsorb on top of both, *A*- and *B*-type molecules as shown in Figure 5.5.

When the Ce atom is adsorbed on top of a *A*-type molecule, it appears as a bright protrusion surrounded by the eight lobes of the upper phthalocyanine (Figure 5.5(a)). If on the contrary, the Ce atom is capping a *B*-type molecule, it shows a reduced topographic height in the cross section analysis. In addition, the eight lobes are no longer visible since the *B*-type molecule is partially hidden by its next neighbors as explained in section 4.1.3. Nevertheless, four lobes belonging to either one of the four nearest neighbor molecules are

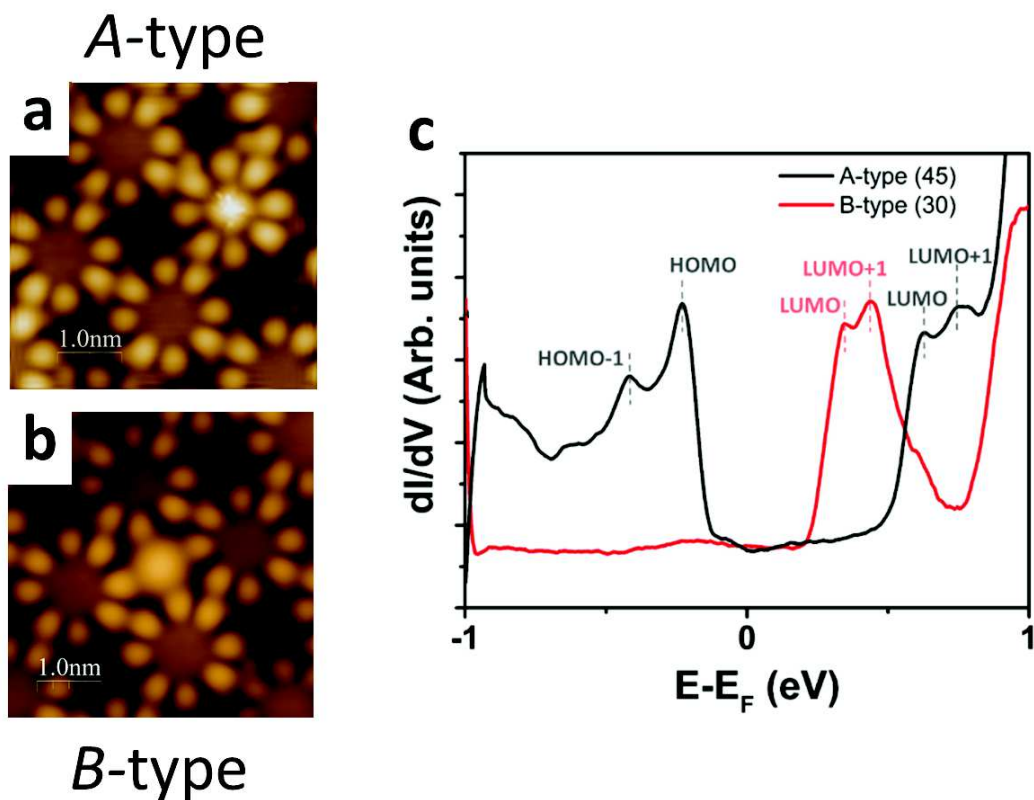


Fig. 5.5 a) and b) Constant current topography images recorded for TbPc₂ on Au (111) substrate with the following tunneling parameters $I=40$ pA and $V=-0.4$ V. Cerium is adsorbed on either A- and B-type molecule and appears as a bright protrusion in both images. On a B-type CDD (b), four lobes of adjacent molecules overlap the orbital extension of the cerium. c) dI/dV recorded above the cerium atom of both molecular types as indicated. Similar STS features are observed in both situations and the LUMO-LUMO+1 gap is conserved on both positions (100 meV \pm 10 meV).

pointing towards the cerium atom making it look like a four branch star in Figure 5.5(b). Therefore, the coordination of the cerium atom to the upper ligand is quite different in *A*-type and *B*-type molecules. As a matter of fact, in these experiments, a great majority of cerium atoms are found to adsorb preferentially on *B*-type molecules. Furthermore, cerium atoms adsorbed on *A*-type molecules can easily be moved by the tip during the scanning process while they remain stable on *B*-type molecule under normal tunneling conditions.

Whether cerium is capping an *A*- or a *B*-type molecule has also a strong incidence on the conductance spectra measured above the Ce atom:

- *A*-type CDD molecules show two well defined negative voltage peaks at -230 meV and -400 meV labelled HOMO and HOMO-1 respectively as shown in Figure 5.5(c) (black). Positive voltage peaks at +630 meV and +750 meV are attributed to LUMO and LUMO+1 respectively. The HOMO-LUMO gap of *A*-type CDD molecule is therefore determined to be of 860 meV.
- *B*-type CDD molecules, on the contrary, exhibit low conductance values at negative bias. Positive bias peaks at +350 and +450 meV are attributed to LUMO and LUMO+1 respectively. Interestingly these two peaks resemble to LUMO and LUMO+1 peaks observed on the *A*-type molecule. In both cases the LUMO-LUMO+1 separation is the same to within ± 10 meV. Significant differences in electronic properties between *A*- and *B*-type CDD molecules are due to different structural environments.

These results demonstrate that small changes in the molecular environment can lead to significant modifications in the transfer integrals and ultimately to an energy shift of the orbitals under consideration. [16–18] On *B*-type CDD molecules, the interaction of cerium with the underlying molecule is weaker because of the presence of four next neighboring molecules. The fact that the LUMO-LUMO+1 gap remains nearly identical (~ 100 meV) denotes similar chemical bonding between the lanthanide and the underlying molecule for both types.[19, 20]

The spectral shift of 280 meV observed between the LUMO of *A*- and *B*-type molecule is induced by a charge transfer between the cerium and the double-decker. This charge transfer cannot be a result of substrate effect since no LUMO broadening is observed [21–23]. This shift refers to an important charge transfer between the cerium and the neighboring molecules, which is confirmed by the gap reduction on *B*-type CDD. Since both systems have common substrate i.e. Au (111), charge screening rises from either:

- Electronic modification due to skew angle reduction (structural modification)

- Interaction with next neighboring molecules in *B*-type
- Both effects at the same time

The charge transfer between the double-decker molecule and the cerium can hardly be obtained from the STS analysis and further investigation by theoretical analysis is needed. Oehzelt et al. [24] developed a new technique where a detailed electrostatic model was implemented to reproduce the alignment between Fermi energy of the electrode and the transport states of an organic molecule. However this technique applies only to organic molecules adsorbed on metal substrates and is limited to light elements containing a small amount of electrons.

On the other hand, by implementing DFT calculation along with STS data Robles et al. gathered information about charge transfer in cesium doped yttrium double-decker. An excess of 0.91 e⁻ is found on the CsYPC₂ molecule. On *A*-type cesium CDD molecules the DOS obtained by DFT showed a HOMO and LUMO shift of 0.2 eV and 0.1 eV respectively toward the Fermi level. Surprisingly, *B*-type molecules did not show any electronic modification when cesium atom is adsorbed on top of them.[13] This may be an indication of a weak charge transfer between the cesium and the underlying *B*-type TbPc₂, the bonding then mainly occurs between the between the ad-atom and its surrounding *A*-type molecules. Therefore answering the question above is not an easy task and needs to be investigated carefully. For the present system it was not possible to carry DFT calculations as such amount of molecules necessitate heavy computational time and resources.

5.2.4 General discussion

After investigating the electronic and structural configuration of CDD complexes adsorbed on various surfaces, it became clear that the substrate nature has a major impact on their electronic properties. The tunneling spectroscopy measured on a cerium atom after adsorption on a monolayer of TbPc₂ depicts important modifications depending on substrate nature. Figure 5.6(a) summarizes the situation for the various orbitals of the CDD molecules on the corresponding substrates. The change in the HOMO and LUMO levels originates from the surrounding geometrical configuration.

When a CDD molecules is adsorbed on a Au (111) substrate, the LUMO level is shifted upwards from Fermi level compared to Cu (111) and Ag (111), meaning that the CDD molecule has less excess electron on Au (111). One explanation is that the LUMO originates

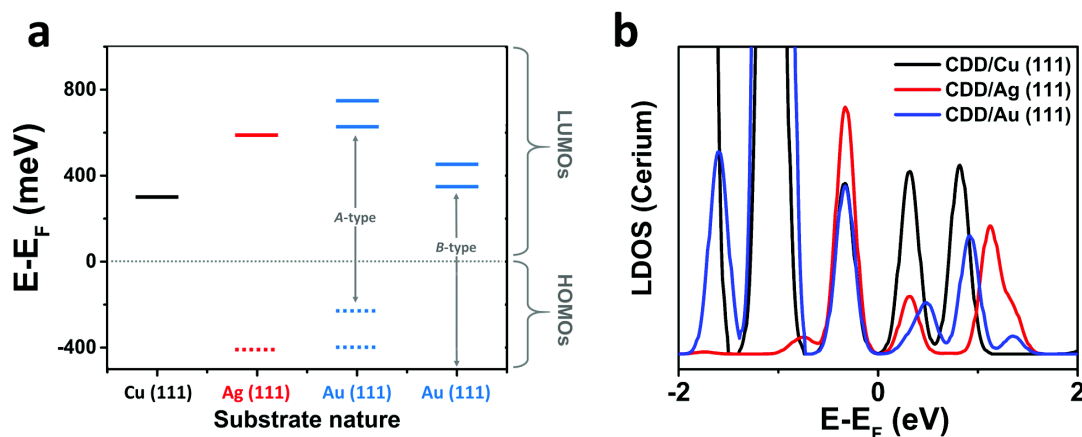


Fig. 5.6 a) Experimental energy position of molecular orbitals of the cerium CDD molecule as recorded experimentally above the cerium position (center). b) Theoretical LDOS as obtained from DFT calculations, the DOS are projected on the cerium which therefore gather information about the spectroscopy above the central area of a CDD molecule. Black, red and blue curves indicate the crystal nature (copper, silver and gold respectively). One observes that all HOMOs are positioned at the same energy (-300 meV) while the LUMO is positioned at +330 meV on copper and silver and at +460 meV on Au (111) substrate. Note that only A-type molecule was used for the calculations.

from the underlying TbPc_2 in this case (see Chapter 4). Actually the molecule-substrate decoupling is more important on Au (111) compared to the two other substrates. After capping with a cerium atom, the excess electron of the underlying molecule becomes likely to interact with the ad-atom which is in accordance with previous STS observations (Figure 5.5). However, this interpretation does not seem to apply for B-type CDD molecule on Au(111) since a much higher gap compared to A-type molecule and a shift of both LUMOs toward the Fermi energy are observed. This difference is probably induced by the structural variation (ligand rotation) and important interaction of the cerium with neighboring molecules as shown in Figure 5.5.

The DFT calculation of the local density of states (LDOS) projected on cerium atom shows that the HOMO peak does not shift as a function of substrate. Therefore, all HOMOs are positioned at -330 meV as shown in Figure 5.6(b). On the contrary, LUMOs remain at +320 meV on Cu (111) and Ag (111) but shift by 160 meV away from Fermi level on Au (111). Even though DFT calculations were performed on isolated CDD molecule adsorbed on three different substrates, the shifts for HOMOs and LUMOs are expected to be coherent with the experimental data, assuming in first approximation that the effect of the

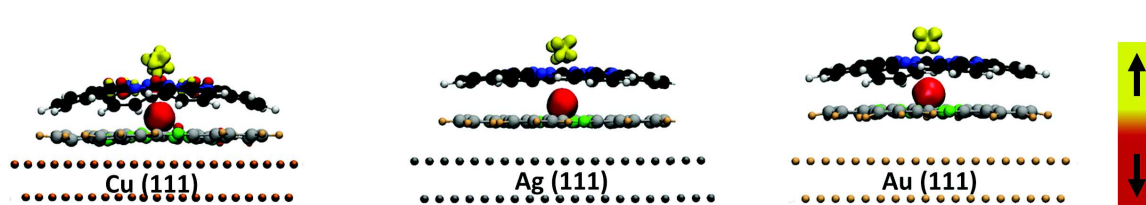


Fig. 5.7 Spin density of the cerium CDD complex. The yellow color indicates spins are up, while the red color indicates spin down contributions with isovalue $0.003 \text{ e}\cdot\text{\AA}^{-3}$. It is remarkable that the spins on both Ce and Tb ions are opposite indicating an antiferromagnetic interaction. Notice also that on Cu (111) the spin distribution is also visible within this isovalue on the next neighbor organic elements (C and N). The spin distribution on the Tb center seems to have multi L-orbital character while the Ce ion has a f-orbital like shape.

TbPc₂ network on the electronic properties of cerium is negligible. The calculation predicts correctly the upwards shift of the LUMO for the A-type CDD on Au (111) compared to Ag (111) and Cu (111) substrates. No change in the HOMO-LUMO gap however is predicted for the CDD on Ag (111) and Cu (111). Due to the contradiction with the experiment and since the calculation is done on isolated molecules, one has to conclude that the substrate is not the main parameter affecting the electronic properties. On the other hand, the charge transfer analysis from DFT calculations reveals that about -1.24 e⁻, -1.18 e⁻ and -1.17 e⁻ are donated by the terbium double decker to the cerium atom on Cu (111), Ag (111) and Au (111) respectively. These values are very close to each other confirming the minor contribution of the substrate to the Tb-Ce interaction. At this point, it becomes clear that the networking associated with the change in monolayer density of molecules on Cu (111), Ag (111) and Au (111) are chiefly responsible for the charge difference between cerium and the molecule, leading to the molecular orbitals shift.

5.3 Magnetic investigation and spin density analysis

The magnetic analysis based on DFT calculations revealed that the total spin of the molecule calculated from the spin up and spin down difference is equal to zero. This indicates the loss of the global SMM property of the molecule upon capping with a cerium atom. However, such assumption is not always valid since a slower relaxation of one atom compared to the other one is indicative of SMM property as shown in bis-terbium phthalocyaninato porphyrininato triple-decker.[25]

A preferential orientation is found on both, terbium and cerium lanthanides as presented in Figure 5.7, they both depict different magnetic direction because of their last orbital occupancy, indicating that unpaired electrons are present in these shells. The two metal atoms exhibit opposite spin value as shown in Figure 5.7 by the yellow (spin up) and red (spin down) colors. This is a clear indication for an anti-ferromagnetic coupling of cerium and terbium atoms independently from the substrate nature. Due to a strong perpendicular anisotropy, only the parallel to easy axis magnetic components of lanthanides are able to interact.

In Figure 5.7, the terbium atom exhibits a spherical spin density reflecting a spin localization of multiple L-orbitals while the cerium shows an opposite spin density localized at the f-orbital. The fact that both, the long distance between the lanthanides (3.33 Å) and the localization of spin density on the f-shell of the cerium atom, implies that the f-f coupling must take place through the Pc organic ligand creating therefore an indirect interaction also called super-exchange interaction. Moreover, shared covalence of cerium with pyrrole nitrogen atoms may create a mechanism accounting for the anti-ferromagnetic exchange mediating the Ce-Tb super-exchange interaction. [26]

A super-exchange interaction arises when one electron of the upper ligand is shared with the f-orbital of the cerium atom while the remaining electron on the π -orbital is shared with the terbium atom resulting in an anti-ferromagnetic state. Furthermore, rare earth elements with unquenched L-orbital momentum usually induce strong super-exchange anisotropy due to a large spin-orbit coupling compared to the crystal field potential.[27]

The spin density of a CDD molecule on Cu (111) shows a spin distribution on the C and N closest to cerium that is opposite to the one of the cerium atom as shown in Figure (5.7(a)). The presence of a magnetic contribution on the non-metallic elements is due to hybridization of d- and f-orbitals of lanthanides with p-orbitals of both pyrrole carbon and nitrogen. However, the absence of this contribution when the CDD is on Au (111) and Ag (111) indicates a substrate contribution to the spin delocalization from the metal ions toward the upper ligand. The exchange energy (J_{ex}) is not evaluated in the present discussion due to the lack of available CPU-time, as both, anti-ferromagnetic and ferromagnetic coupling between the ions have to be investigated. However this energy is expected to be small (< 2 meV) due to the low interaction of the cerium with the double-decker molecule as explained in Section 5.5 of the present chapter, devoted to atomic manipulation. Moreover, J_{ex} is expected to be negative because of the anti-ferromagnetic coupling between the two

metals which is evaluated as follows:

$$J_{ex} = \frac{E_F - E_{AF}}{\langle S_F \rangle - \langle S_{AF} \rangle},$$

where E and S denote the total energy and the spin state of the system, F and AF indexes represent the ferromagnetic and anti-ferromagnetic coupling between the two lanthanides respectively.

The relative stability of the cerium atom on top of the double-decker creates a charge redistribution among all the elements of the CDD, particularly between the cerium and the upper ligand. A calculation of this redistribution when the CDD molecule is adsorbed on Au (111), demonstrates that about 1.1 e⁻ are donated from the upper phthalocyanine toward the cerium atom after coordination. More precisely, by adding the cerium atom to the double-decker molecule, the charge of the upper ligand drops from -1 e⁻ (unpaired) to -0.3 e⁻, suggesting that the excess electron available on the double-decker is now shared with the cerium. This operation, contributes reducing the negative charge of the TbPc₂ molecule and increasing the cerium one.

On the other hand terbium was found with seven unpaired electrons before cerium coordination. After coordination, only six electrons are unpaired thus indicating that one electron is shared with the cerium. However this value (one electron) exceeds by 0.8 e⁻ the calculated charging value of the cerium. This is expected since it was found that the presence of the cerium on the double-decker molecule lowers the terbium position towards the bottom ligand (Figure 5.2(b)) sharing therefore more electrons with the bottom ligand than with the upper one.

In comparison, the Tb₂Pc₃ triple-decker complex has a particular SMM property as reported by Ishikawa et al. A ferromagnetic coupling through f-f intra-molecular interaction is observed in isolated PcLnPcLn'Pc* molecule (see Figure 3.13), where [Ln-Ln']=[Tb-Tb], [Dy-Dy] and [Ho-Ho]. The same molecules adsorbed on a non-magnetic substrate exhibit a similar behavior while an anti-ferromagnetic coupling is observed in Er and Tm systems.[28] In [Tb-Tb] system, the magnetic field generated by a magnetic substrate leads to an anti-ferromagnetic coupling of the bottom terbium of Tb₂Pc₃ molecule with the substrate. The upper Tb however remains unperturbed due to the dipolar field created by the bottom terbium at the position of the upper lanthanide.[27, 29, 30]

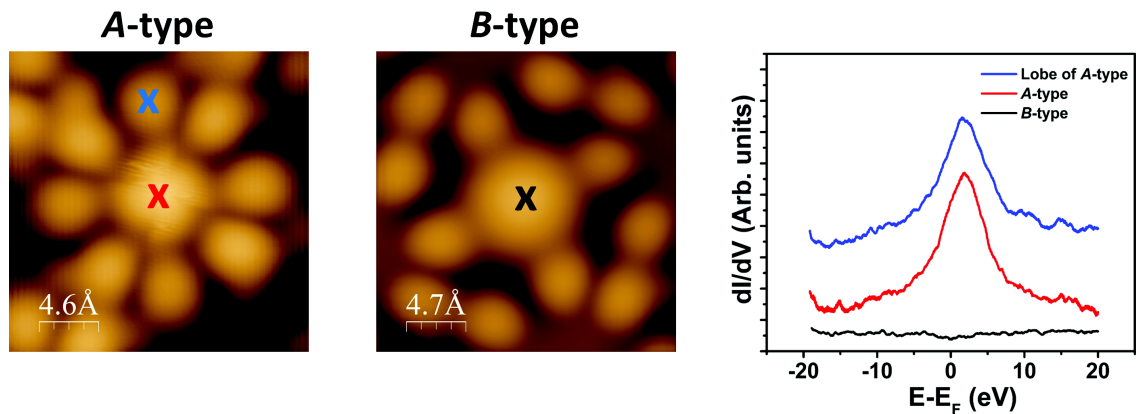


Fig. 5.8 Kondo resonance recorded above a CDD molecule. The tip was positioned above the locations marked by a cross on both, *A*- and *B*-type CDD molecules. The corresponding Kondo resonance ($T_K = 30$ K) is plotted in the right panel, the temperature was obtained after a Fano fit of the peak with the parameters $q = 30$ and $\Gamma = 7.8$ meV. Both Cerium (red) and a lobe (blue) of a *A*-type show a ZBP with similar characteristics while no resonance was observed when the tip was positioned above a *B*-type molecule (black). Tunneling parameters: $I = 40$ pA, $V = -0.4$ V

5.4 Kondo resonance (Magnetic CDD)

As mentioned in section 4.2 devoted to the domain growth and the Kondo resonance, the TbPc₂ monolayer film is made of unpaired spins able to interact among each others. In particular, it was evidenced that every double-decker molecule in a domain contains a spin $\frac{1}{2}$ delocalized on the upper Pc ligand. The cerium coordination to the pyrrole nitrogens of the upper ligand creates an electronic exchange path between the ad-atom and the host TbPc₂ molecule. In addition, the cerium *f*-shell now contains an unpaired $4f^8$ -electron that might lead to a Kondo resonance.

High resolution dI/dV spectroscopy recorded above an *A*-type CDD molecules on Au (111) revealed a resonant peak close to Fermi level as shown in Figure 5.8 (red). This ZBP is interpreted as a Kondo resonance governed by the coupling between the cerium local magnetic moment and the electrons available on the TbPc₂ monolayer. The Kondo temperature is evaluated by measuring the FWHM of the Lorentzian fit of the observed peak leading to $\Gamma = 7.9$ meV and a Kondo temperature of $T_K = 30$ K according to the fermionic liquid theory. Further investigations revealed that this resonance is also present on the eight lobes surrounding the cerium of *A*-type CDD molecule with similar width and amplitude (see Figure 5.8 (blue)). It suggests that the magnetic impurity generates the Kondo reso-

nance which becomes delocalized on all the upper ligand of the CDD molecule.

This magnetic impurity may originate either from the unpaired electron present on the upper-Pc film that becomes delocalized on the cerium position, or from the unpaired f -electron of the cerium. This electron could have its spin information transferred to the upper ligand of the CDD leading to a measurable Kondo peak on the eight lobes surrounding the A -type CDD, see Figure 5.8. The first possibility is less likely because of the different T_K found between a domain TbPc_2 (Figure 4.5) and a CDD molecule. If the Kondo resonance obtained on a domain TbPc_2 and a CDD were of the same origin, the electron density at the magnetic impurity ($g(\epsilon)$) would be similar along with the exchange coupling (J) leading to a similar Kondo temperature $T_K \propto \exp[-1/(g(\epsilon)J)]$. However, T_K on the CDD and the one on the ligand's π -electrons are different by 8 K. As a result, the presence of a more localized magnetic impurity might be the reason for this difference and thus, the unpaired f -electron of cerium turns out to be the only possible candidate for an electron diffusion center.

As mentioned earlier (section 4.1.3), the network formed by the upper ligand of the TbPc_2 molecules on Au (111) contains a 2D-electron sea that is moderately influenced by the substrate. Therefore the 2D-electrons are the ones that are diffused by the cerium atom leading to a resonant peak at the Fermi level. About one electron is donated by the TbPc_2 molecule to populate the f -shell of the adsorbed cerium atom. This electron remains unpaired, therefore its spin constitutes a magnetic impurity capable of diffusing the surrounding excess electrons of the film.

Surprisingly, the spin responsible for the Kondo resonance seem to be quenched at the center of the B -type CDD molecule since no ZBP resonance is observed. Yet, the reason causing the loss of the Kondo resonance on a B -type molecule has to be clarified by calculations. However as mentioned above, the cerium on a B -type CDD, has additional molecular orbital overlap with the surrounding A -type molecules clearly visible on the topography of Figure 5.8. This remark is corroborated in the dI/dV of CDD molecules adsorbed on Au (111) (see Figure 4.3(c)), the first HOMO peak at -230 meV, is only visible on the A -type molecule while it is hardly noticeable on the B -type CDD. Additionally, in the absence of any calculation it is hard to put forward an explanation based on the change in electronic property upon a skew angle reduction. It is however reasonable to consider that this remarkable difference between the two structures is responsible for the occurrence or not of the Kondo resonance.

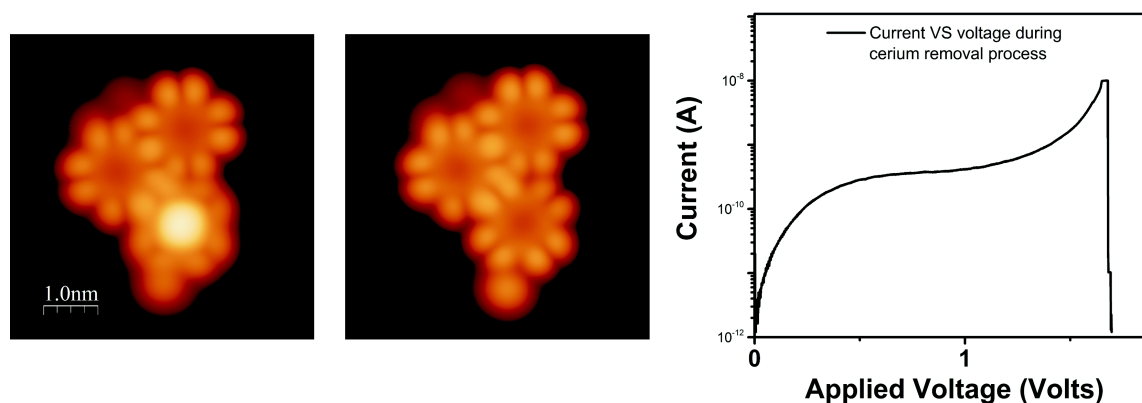


Fig. 5.9 Topography images showing the manipulation process where the cerium atom capping a TbPc₂ molecule on Cu (111) is removed. Left image shows the topography of a trimer with a CDD molecule before the manipulation process. Central image shows the same island after an application of +1.7 V above the cerium location. The corresponding tunneling current versus the applied voltage bias is plotted in the right panel.

5.5 Atomic manipulation

In the present section, a structural modification is induced by means of the tip assisted manipulation of a CDD complex on Cu (111) and Au (111) substrates. As discussed earlier, the upper Pc ligand is sandwiched between a terbium and a cerium atom. Since this ligand can only provide two electrons after de-protonation, only a partial coordination of the cerium to the TbPc₂ is achieved. Due to its small interaction with the underlying TbPc₂ molecule, the cerium ad-atom can easily be manipulated by means of the STM tip with and without pulse excitation. However, the outcome of the manipulation is rather different on Cu (111) and Au (111) confirming the substrate effect on the upper ligand-cerium coordination.

5.5.1 Uncapping the CePcTbPc

By applying a well-defined bias voltage, desorption of the capping-atom from the TbPc₂ takes place. Cerium is transferred from the complex to the tip. This manipulation works on both, isolated and embedded CDD molecules. However, this process is irreversible as applying higher voltage with opposite polarity does not lead to any Ce drop from the tip to the sample. Even worse, under such high voltage, molecule fragmentation was observed.

This result confirms the small interaction force between the lanthanide and the TbPc₂ molecule. Figure 5.9 shows a constant current image of three molecules, one of them is

capped with a cerium atom as indicated by the bright protrusion. After gradual increase of the bias voltage between the tip and the CDD molecule, a remarkable drop of current is observed at +1.7 V.

It is interesting to notice that after removal of the cerium from the TbPc_2 , the topography shows a similar contrast on all the three un-capped molecules suggesting that capping a double-decker is a fully reversible operation. This result is also confirmed by the STS investigation after uncapping, since the dI/dV spectrum is identical to the one of a normal pristine TbPc_2 molecule (see Figure 3.9). It has to be noticed that in this experiment, the new *Ce-tip* does not show any particular contribution in the dI/dV features of the investigated objects.

5.5.2 Hiding cerium (a new way to store information)

When the manipulation is performed on a CDD adsorbed on a Au (111) substrate, the cerium behaves differently compared to a CDD adsorbed on Cu (111). A pulse of +1.5 V of 50 ms duration pushed the cerium under the upper ligand of two adjacent molecules as shown in Figure 5.10. It results in a lifting up of the phenyl rings which appear as two bright pairs of lobes for every phenyl moiety.

Surprisingly, this process is made reversible by applying a pulse of opposite polarity (-3 V) above the original cerium position. It becomes therefore possible to hide, on request, an atom under the upper-ligands network of a film formed on a Au (111) substrate.

When the cerium goes underneath the upper ligand of a neighboring molecules, only the closest phenyls shows an increased height while the other molecules keep their normal in-plane position. Such stability is consistent with the expected strong inter-molecular interactions in a film. The reversible lifting of the upper ligand proves again the robustness of the molecular network achieved mainly by the Tb atom. It is noteworthy that this manipulation is only possible when the cerium atom is capping a *B*-type molecule due to the weak bonding of the cerium atom on top of the *A*-type position.

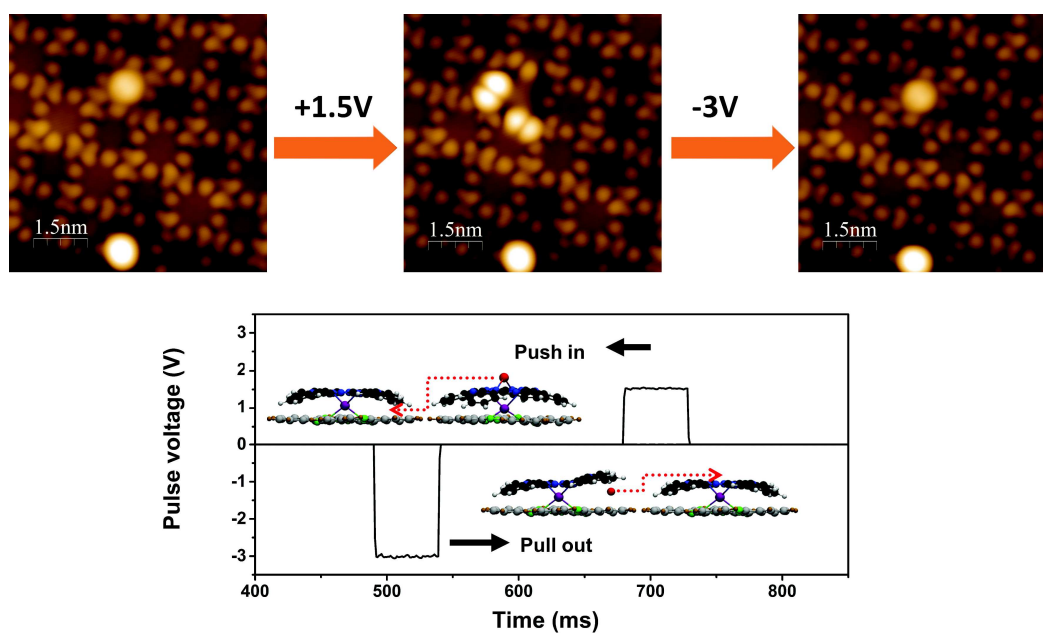


Fig. 5.10 Manipulation process of a cerium atom adsorbed on Au (111) surface. The manipulation consists in pushing down the capping atom under the neighboring TbPc₂ molecules by applying a pulse of +1.5 V during 50 ms above the Ce location. When hidden, the atom lifts up the phenyl ring of the adjacent molecules leading to the appearance of a brighter pairs of lobes on topography. When about -3 V are applied at the same location, the process is reversed.

5.6 Summary and conclusions

Investigations on the electronic transport of capped TbPc₂ molecules with cerium atom were reported in this chapter. The molecular orbitals were investigated in the local basis of the CDD complexes when adsorbed on various substrates. The interaction between the two lanthanides is reported stable and the molecular environment highly dependent on the substrate nature. On the other hand, DFT calculations allowed the determination of the amount of charge transferred from the upper ligand towards the cerium upon capping process. Moreover, it made possible an identification of molecular orbitals and determination of the substrate role in both structural and electronic configuration. Interestingly, independently from the crystal nature, an anti-ferromagnetic coupling between the two lanthanides is found when analyzing the spin density of the CDD molecules.

STS investigations at the Fermi region on these complexes highlighted a Kondo resonance at both, the cerium position and the eight lobes of the host's upper ligand. This resonance is observed only on molecules with a skew angle of 45° adsorbed on Au (111). Contrary to previous case of un-capped molecules where the ZBP was observed on isolated TbPc₂ or in a crossing point of a domain, the Kondo peak on a CDD molecule is expected to originate from the 4*f*–electron of the cerium.

The interaction force between the cerium and its hosting molecule is evaluated by means of atomic manipulation. Interestingly, depending on the substrate nature and molecular domain conformation, a different process is observed under similar manipulating conditions. Indeed, the cerium was removed from an embedded CDD molecule on copper while it remained at the vicinity of the film on Au (111) substrate. Furthermore, this process is reversible which opens a new approach for the information storage.

REFERENCES

- [1] M. Urdampilleta, S. Klyatskaya, J.-P. Cleuziou, M. Ruben, and W. Wernsdorfer. Supramolecular spin valves. *Nature Materials*, 10(7):502–506, July 2011.
- [2] Matias Urdampilleta, Svetlana Klayatskaya, Mario Ruben, and Wolfgang Wernsdorfer. Magnetic Interaction Between a Radical Spin and a Single-Molecule Magnet in a Molecular Spin-Valve. *ACS Nano*, 9(4):4458–4464, April 2015.
- [3] Lapo Bogani and Wolfgang Wernsdorfer. Molecular spintronics using single-molecule magnets. *Nature materials*, 7(3):179–186, 2008.
- [4] Stefano Sanvito. Molecular spintronics. *Chemical Society Reviews*, 40(6):3336–3355, May 2011.
- [5] Naoto Ishikawa, Satoshi Otsuka, and Youkoh Kaizu. The Effect of the f–f Interaction on the Dynamic Magnetism of a Coupled $4f^8$ System in a Dinuclear Terbium Complex with Phthalocyanines. *Angewandte Chemie International Edition*, 44(5):731–733, January 2005.
- [6] Keiichi Katoh, Takashi Kajiwara, Motohiro Nakano, Yasuhiro Nakazawa, Wolfgang Wernsdorfer, Naoto Ishikawa, Brian K. Breedlove, and Masahiro Yamashita. Magnetic Relaxation of Single-Molecule Magnets in an External Magnetic Field: An Ising Dimer of a Terbium(III)–Phthalocyaninate Triple-Decker Complex. *Chemistry – A European Journal*, 17(1):117–122, January 2011.
- [7] Yanli Chen, Wei Su, Ming Bai, Jianzhuang Jiang, Xiyong Li, Yunqi Liu, Lingxuan Wang, and Shuangqing Wang. High Performance Organic Field-Effect Transistors Based on Amphiphilic Tris(phthalocyaninato) Rare Earth Triple-Decker Complexes. *Journal of the American Chemical Society*, 127(45):15700–15701, November 2005.

- [8] Keiichi Katoh, Rina Asano, Akira Miura, Yoji Horii, Takaumi Morita, Brian K. Breedlove, and Masahiro Yamashita. Effect of f–f interactions on quantum tunnelling of the magnetization: mono- and dinuclear Dy(III) phthalocyaninato triple-decker single-molecule magnets with the same octacoordination environment. *Dalton Transactions*, 43(21):7716–7725, May 2014.
- [9] Hailong Wang, Chenxi Liu, Tao Liu, Suyuan Zeng, Wei Cao, Qi Ma, Chunying Duan, Jianmin Dou, and Jianzhuang Jiang. Mixed (phthalocyaninato)(Schiff-base) didysprosium sandwich complexes. Effect of magnetic coupling on the SMM behavior. *Dalton Transactions*, 42(43):15355–15360, October 2013.
- [10] Keiichi Katoh, Yoji Horii, Nobuhiro Yasuda, Wolfgang Wernsdorfer, Koshiro Toriumi, Brian K. Breedlove, and Masahiro Yamashita. Multiple-decker phthalocyaninato dinuclear lanthanoid(III) single-molecule magnets with dual-magnetic relaxation processes. *Dalton Transactions*, 41(44):13582–13600, October 2012.
- [11] Xi Chen, Ying-Shuang Fu, Shuai-Hua Ji, Tong Zhang, Peng Cheng, Xu-Cun Ma, Xiao-Long Zou, Wen-Hui Duan, Jin-Feng Jia, and Qi-Kun Xue. Probing Superexchange Interaction in Molecular Magnets by Spin-Flip Spectroscopy and Microscopy. *Physical Review Letters*, 101(19):197208, November 2008.
- [12] Michele Serri, Wei Wu, Luke R. Fleet, Nicholas M. Harrison, Cyrus F. Hirjibehedin, Christopher W. M. Kay, Andrew J. Fisher, Gabriel Aeppli, and Sandrine Heutz. High-temperature antiferromagnetism in molecular semiconductor thin films and nanostructures. *Nature Communications*, 5:3079, January 2014.
- [13] Roberto Robles, Nicolás Lorente, Hironari Isshiki, Jie Liu, Keiichi Katoh, Brian K. Breedlove, Masahiro Yamashita, and Tadahiro Komeda. Spin Doping of Individual Molecules by Using Single-Atom Manipulation. *Nano Letters*, 12(7):3609–3612, July 2012.
- [14] Tadahiro Komeda, Hironari Isshiki, Jie Liu, Yan-Feng Zhang, Nicolás Lorente, Keiichi Katoh, Brian K. Breedlove, and Masahiro Yamashita. Observation and electric current control of a local spin in a single-molecule magnet. *Nature Communications*, 2:217, March 2011.
- [15] Dimas G. de Oteyza, Iñaki Silanes, Miguel Ruiz-Osés, Esther Barrena, Bryan P. Doyle, Andrés Arnau, Helmut Dosch, Yutaka Wakayama, and J. Enrique Ortega. Balancing Intermolecular and Molecule–Substrate Interactions in Supramolecular Assemblies. *Advanced Functional Materials*, 19(2):259–264, January 2009.

- [16] Veaceslav Coropceanu, Jérôme Cornil, Demetrio A. da Silva Filho, Yoann Olivier, Robert Silbey, and Jean-Luc Brédas. Charge Transport in Organic Semiconductors. *Chemical Reviews*, 107(4):926–952, April 2007.
- [17] Jean-Luc Brédas, David Beljonne, Veaceslav Coropceanu, and Jérôme Cornil. Charge-Transfer and Energy-Transfer Processes in π -Conjugated Oligomers and Polymers: A Molecular Picture. *Chemical Reviews*, 104(11):4971–5004, November 2004.
- [18] J. L. Brédas, J. P. Calbert, D. A. da Silva Filho, and J. Cornil. Organic semiconductors: A theoretical characterization of the basic parameters governing charge transport. *Proceedings of the National Academy of Sciences*, 99(9):5804–5809, April 2002.
- [19] Xinghua Lu, M. Grobis, K. H. Khoo, Steven G. Louie, and M. F. Crommie. Charge transfer and screening in individual C_{60} molecules on metal substrates: A scanning tunneling spectroscopy and theoretical study. *Physical Review B*, 70(11):115418, September 2004.
- [20] W. A. Little. Possibility of Synthesizing an Organic Superconductor. *Physical Review*, 134(6A):A1416–A1424, June 1964.
- [21] Anna Amat and Filippo De Angelis. Challenges in the simulation of dye-sensitized ZnO solar cells: quantum confinement, alignment of energy levels and excited state nature at the dye/semiconductor interface. *Physical Chemistry Chemical Physics*, 14(30):10662–10668, July 2012.
- [22] A. J. Fisher and P. E. Blöchl. Adsorption and scanning-tunneling-microscope imaging of benzene on graphite and MoS_2 . *Physical Review Letters*, 70(21):3263–3266, May 1993.
- [23] Supriyo Datta, Weidong Tian, Seunghun Hong, R. Reifenberger, Jason I. Henderson, and Clifford P. Kubiak. Current-Voltage Characteristics of Self-Assembled Monolayers by Scanning Tunneling Microscopy. *Physical Review Letters*, 79(13):2530–2533, September 1997.
- [24] Martin Oehzelt, Norbert Koch, and Georg Heimel. Organic semiconductor density of states controls the energy level alignment at electrode interfaces. *Nature Communications*, 5:4174, June 2014.
- [25] Shohei Sakaue, Akira Fuyuhiko, Takamitsu Fukuda, and Naoto Ishikawa. Dinuclear single-molecule magnets with porphyrin–phthalocyanine mixed triple-decker ligand

- systems giving SAP and SP coordination polyhedra. *Chemical Communications*, 48(43):5337–5339, May 2012.
- [26] Saranyan Vijayaraghavan, Willi Auwärter, David Ecija, Knud Seufert, Stefano Rusponi, Torsten Houwaart, Philippe Sautet, Marie-Laure Bocquet, Pardeep Thakur, Sebastian Stepanow, Uta Schlickum, Markus Etzkorn, Harald Brune, and Johannes V. Barth. Restoring the Co Magnetic Moments at Interfacial Co-Porphyrin Arrays by Site-Selective Uptake of Iron. *ACS Nano*, 9(4):3605–3616, April 2015.
- [27] A. Lodi Rizzini, C. Krull, T. Balashov, J. J. Kavich, A. Mugarza, P. S. Miedema, P. K. Thakur, V. Sessi, S. Klyatskaya, M. Ruben, S. Stepanow, and P. Gambardella. Coupling Single Molecule Magnets to Ferromagnetic Substrates. *Physical Review Letters*, 107(17):177205, October 2011.
- [28] Naoto Ishikawa, Tomochika Iino, and Youkoh Kaizu. Interaction between f-Electronic Systems in Dinuclear Lanthanide Complexes with Phthalocyanines. *Journal of the American Chemical Society*, 124(38):11440–11447, September 2002.
- [29] Alberto Lodi Rizzini, Cornelius Krull, Aitor Mugarza, Timofey Balashov, Corneliu Nistor, Raoul Piquere, Svetlana Klyatskaya, Mario Ruben, Polina M. Sheverdyaeva, Paolo Moras, Carlo Carbone, Christian Stamm, Piter S. Miedema, Pardeep K. Thakur, Violetta Sessi, Marcio Soares, Flora Yakhou-Harris, Julio C. Cezar, Sebastian Stepanow, and Pietro Gambardella. Coupling of single, double, and triple-decker metal-phthalocyanine complexes to ferromagnetic and antiferromagnetic substrates. *Surface Science*, 630:361–374, December 2014.
- [30] L. Malavolti, L. Poggini, L. Margheriti, D. Chiappe, P. Graziosi, B. Cortigiani, V. Lanzilotto, F. Buatier de Mongeot, P. Ohresser, E. Otero, F. Choueikani, Ph Sainctavit, I. Bergenti, V. A. Dediu, M. Mannini, and R. Sessoli. Magnetism of TbPc₂ SMMs on ferromagnetic electrodes used in organic spintronics. *Chemical Communications*, 49(98):11506–11508, November 2013.

GENESIS OF METAL-PHTHALOCYANINE ON SURFACES

In this chapter, the formation of metal-phthalocyanine on surfaces are reported. The genesis of this structure follows multiple steps in which both, theoretical and experimental results will be discussed. A focus on the electronic properties obtained by DFT will, however, dominate this discussion. The experimental part was mainly carried out by Dr. K. Shawulienu¹ using scanning tunneling microscope.[1, 2] DFT calculations were performed to establish both intermolecular and metal-molecule interactions responsible for the formation of either TCNB layer or Fe(TCNB)₄ complex through an intermediate state. Self-assembling of 1,2,4,5-Tetracyanobenzene (TCNB, C₉N₄H₂) molecules will be discussed as well as its two steps coordination path with Fe atom on a Au (111) surface.

6.1 DFT calculation

All calculations presented in this chapter were performed with Car-Parinello molecular dynamics program (CPMD)[3] using first principle molecular dynamics within the framework of the density functional theory (DFT)[4]. The simulation was implemented with Born-Oppenheimer Molecular Dynamics approach when dynamics were needed.[5]

Valence electrons were explicitly treated and expanded in a plane-wave basis set with 70 Ry energy cut-off. All elements (Fe, C, N and H) were described in terms of norm-conserving Troullier-Martin's pseudo-potentials[6, 7]. Semi-core metal definition was used to account the valence-core interactions. Simulation was complemented with the Becke's & Lee-Yang-

¹Dr. Kezilebieke Shawulienu, AALTO university, PO Box 11000 FI-00076 AALTO, Finland. (Temporary address)

Parr exchange correlation quantum chemistry functional (BLYP)[8, 9]. The Grimme's empirical approach was used to introduce the Van Der Waals dispersion forces[10].

Convergence limits were set at 1.10^{-5} and 2.10^{-4} for orbital and geometry optimization respectively. Preconditioned conjugate gradients (PCG) method was used for the wave functions optimization[11], direct inversion in the iterative subspace (GDIIS) method was also used for the geometry optimization.[12]

Ions temperature was controlled by means of a Nosé-Hoover thermostat with a frequency energy of 200 cm^{-1} . [13, 14]

6.2 From TCNB to Fe-4(TCNB)

6.2.1 1,2,4,5-Tetracyanobenzene

Tetracyano derivatives (TCNE, TCNP, TCNQ and TCNB) were extensively studied by scanning tunneling microscopy on various substrates[1, 2, 15–23], among them the common phthalocyanine derivatives. The 1,2,4,5-Tetracyanobenzene (TCNB, Figure 6.1(a)) has a simple chemical structure which makes it suitable for both monolayer growth and surface science investigations. When part of a monolayer, this molecule adopts an in-plane adsorption configuration through π -stacking with the surface atoms. However, these π electrons weakly interact with the substrate compared to the hydrogen bonding C-N \cdots H-C. In consequence, the formation of coordination bonds with Au (111) substrate atoms as it was seen with TCNQ molecules[24] is prevented leading to a well ordered mono-molecular layer as depicted by topography image in Figure 6.3(a). Au (111) herringbone reconstruction is weakly perturbed by the TCNB monolayer, which is a signature of small interactions between molecules and gold surface. A recent communication reported an interdependence between intermolecular and molecule-surface interactions. Indeed, when the inter-molecular interactions grow stronger, the molecule-substrate gets weaker.[25]. TCNB monolayers self-assembling is stabilized by the H-bond where the N \cdots H distance is found equal to 2.5 \AA which is typical value of intermolecular H bonding. [26, 27]

Figure 6.1(a) shows a visualisation of gas phase relaxed TCNB molecule performed by DFT calculation. Four C \equiv N groups are connected via four benzene carbons creating therefore a D_{2h} group symmetry. Figure 6.1(b) and 6.1(c) depict respectively both highest occupied and lowest unoccupied molecular orbitals (HOMO and LUMO) which were calculated on the gas phase relaxed structure of Figure 6.1(a). Important is to note that none of these orbitals is located on the central C-H elements. These HOMO and LUMO orbitals

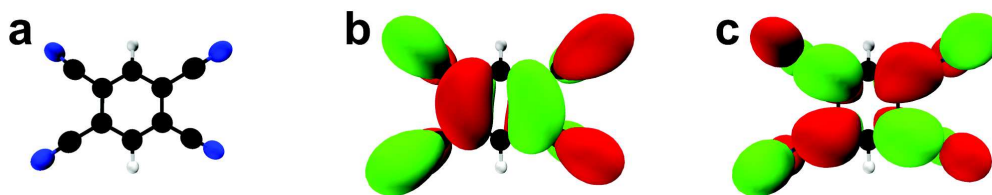


Fig. 6.1 Visualisation of (a)TCNB molecule relaxed by DFT calculation. Molecular orbitals HOMO at -4.78 eV and LUMO at -4.57 eV are represented in (b) and (c) respectively with an isovalue of 0.02 e/Å³. Chemical potential is positioned at -4.77 eV.

are separated by 3.24 eV which correspond to the energy gap which define the necessary energy to transfer one electron from an occupied state (valence band) to an unoccupied state (conduction band). TCNB energy diagram is represented in Figure 6.2. These values are in agreement with UV-vis absorption spectra measurements as previously reported. [28, 29]

Experimentally, TCNB molecules were deposited by evaporation on a pristine Au (111) substrate kept at room temperature. Extended monolayer network was formed when the evaporation rate was large enough as shown in Figure 6.3(a). TCNB self-assembling forms a hexagonal unit cell with the following parameters: $|\vec{a}_1| = |\vec{a}_2| \approx 0.8$ nm, $\alpha \approx 87^\circ$ as indicated in the inset image shown in Figure 6.3(a).

The charge transfer is found to be equal to 0.06 e/molecule which is a clear indication of neutrality of TCNB molecules on gold leading to assume that these film molecules are physisorbed on Au (111) surface. The Au (111) Shockley surface states are shifted upwards by $+87$ meV as expected according to various reports on similar systems[30, 31]. The dI/dV spectrum performed over the center of a TCNB molecule shows a pronounced peak at $+1.8$ eV attributed to the LUMO.

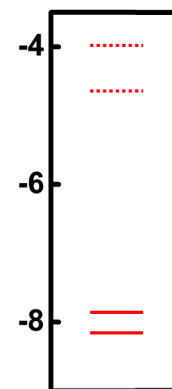


Fig. 6.2 TCNB energy diagram with HOMOs (plain) and LUMOs (dashed). E_F is determined at -7.41 eV.

6.2.2 Dosing TCNB layer with Fe

Surface assisted self assembling has been extensively investigated with a promising results for a controlled polymerization.[32–34] However, its relative steric hindrance induced by the inter-molecular interactions is poorly addressed. In the present work, through a combined evaporation of Fe atoms and TCNB molecules on Au (111), the self-assembling process is investigated by STS at each step towards the formation of the final molecular complex.

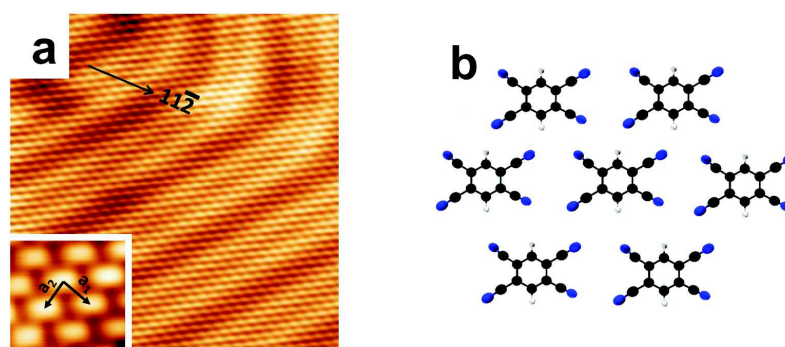


Fig. 6.3 a) topographic image of TCNB monolayer on Au (111) substrate. The herringbone reconstruction is still visible in the main image. The inset image is an enhanced SM topography showing the lattice vectors marked by \vec{a}_1 and \vec{a}_2 such as $|\vec{a}_1| = |\vec{a}_2| \approx 0.8\text{nm}$ and $\alpha \approx 87^\circ$. b) representation of a TCNB monolayer.

Careful evaporation of Fe atoms on pristine TCNB monolayer led to the formation of Fe-4(TCNB) structures on Au (111) surface. For each iron atom, four next neighbouring TCNB molecules will rearrange to accommodate Fe atom presence as shown in Figure 6.4. The layer cell dimensions ($|\vec{a}_1|$, $|\vec{a}_2|$ and α) are left unchanged when the metal is inserted in a unit cell which is composed of one Fe and four TCNB molecules. Only one rotation of 90° is observed on TCNB molecules in order to host the ad-atom taking into account the repulsive C-N \cdots N-C interactions between neighbouring molecules. This new structure has a D_{4h} symmetry with respect to Fe atom. Due to the D_{2h} symmetry of the TCNB molecule, and depending on which C \equiv N groups are pointing towards the Fe atom, a chirality is observed for each Fe-4(TCNB) structure as shown in Figure 6.4(b). For extensive Fe deposition on a TCNB monolayer, domains of this new chiral structure are created inside the primary TCNB network. It has to be noticed that the chirality orientation (clockwise or anti-clockwise) is reported on each neighbouring structures due to the confined Fe-4(TCNB) area driven by the C-N \cdots N-C repulsion and undoped surrounding TCNB molecules. Further in this chapter, this Fe-4(TCNB) structure will be referred to, as the confined structure.

Without an adsorbate, the structure follows an out of plane bending trend due to steric repulsion and obvious reasons of three-dimensional relaxation. In order to avoid such effects result of adsorbate absence, corresponding calculations did not take into account the molecular dynamic process. Thus only simple wave function and geometry optimizations were performed in order to obtain the electronic properties and atomic optimized positions. Electronic density distribution calculation shows that up to an isovalue of $2 \cdot 10^{-2} e \cdot \text{\AA}^{-3}$, a very small overlap between the metal atom and two TCNBs through the C \equiv N group over four is seen (Figure 6.4(a)), while all the neighbour nitrogens are equidistant from Fe (about

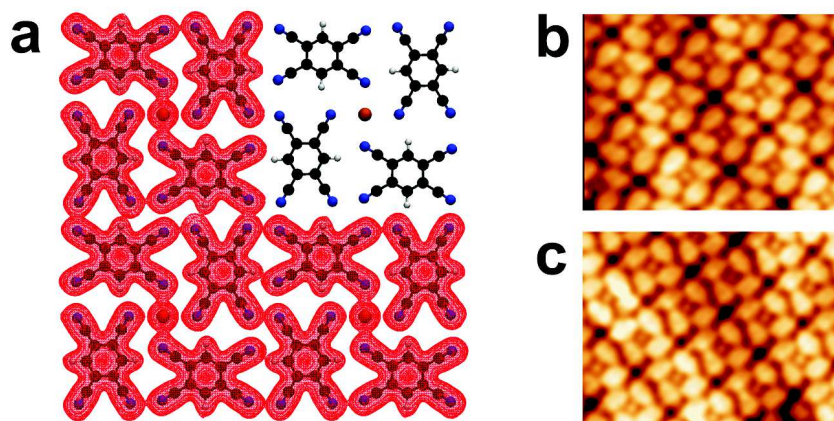


Fig. 6.4 a) anti-clockwise confined structure model, the unit cell is represented in the top right side of the image. Electronic density distribution is shown in red web over three unit cells of Fe-4(TCNB). (b) and (c) show respectively the clockwise and anticlockwise images obtained experimentally by STM.

2.72 Å as shown in table of distances in Appendix 3). This strong binding accounts for the stable interaction between TCNB and Fe which then is expected to be in a +II oxidation state. Face-to-face nitrogen atoms do not show any electronic density overlap as no electronic overlap (red cloud in Figure 6.4(a)) are observed. It translates into a negligible steric repulsion among the TCNB molecular blocks, conferring stability to this pattern.

Concerning hydrogen bonds, each C-H group pointing towards an N site of a neighbouring ligand correspond to a distance of 3.46Å, a C-N...H-C distance of 2.35Å and a bounding angle of $\widehat{C.H.N} = 160^\circ$. These values are close to typical H-bonding reported in literature[35].

dI/dV spectroscopy taken above an embedded Fe atom inside a TCNB domain is similar to the one taken on bare Fe/Au (111)[1] as they both show a localization of the Au (111) Shockley surface state at -500 meV. Furthermore, when the spectroscopy is taken on a TCNB in the Fe-4(TCNB) structure, similar shift of +87 meV as undoped TCNB layer is observed. Knowing that Shockley surface states are very sensitive to interface modifications, these two results indicate the non-coordination between the metal and TCNB molecules, even if the Fe-4(TCNB) is stable on the substrate. Thus it supports the assumption of using our calculations on gas phase mode as the only role of the surface in this case is to provide layers in-plane stability.

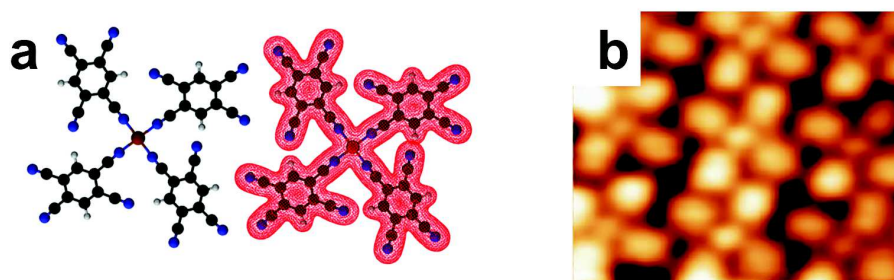


Fig. 6.5 a) $\text{Fe}(\text{TCNB})_4$ monomer (relaxed structure) and its corresponding electronic distribution at the isovalue of $2 \cdot 10^{-2} e/\text{\AA}^3$. b) Topographic image of relaxed structure obtained at $I=0.2$ nA and $V=+1$ V

6.3 Thermally activated $\text{Fe}(\text{TCNB})_4$

When thermally activated², $\text{Fe}-4(\text{TCNB})$ structure relaxes toward a lower local minimum, the four next nitrogens will then coordinate to Fe atom to form a new structure noted $\text{Fe}(\text{TCNB})_4$. This new molecule possesses a higher $\widehat{\text{Fe.N.C}}$ bond angle (180°) compared to the confined structure as depicted in Figure 6.5(a). Interestingly, the unit cell is then occupying more space where the cell parameters are extended to 1.55 ± 0.1 nm compared to the confined structure (1.40 ± 0.1 nm).

Electron density distribution as depicted in red cloud in Figure 6.5 shows a clear electronic exchange between the metal ion and its four ligands. Actually, it appears that the Fe d -orbitals are strongly hybridized with the next nitrogens p -orbitals. In this structure, the formation of a tight Fe-N coordination bound is also observed. In addition Figure 6.5(b) enhances the chirality disappearance upon STM topographic imaging of the structure after thermal activation while it still does exist in the geometrical structure.

6.3.1 Valence and charge properties

From Table 6.1 it is obvious that when evolving from a confined structure to a relaxed phase, the valence remains unchanged for all elements except for Fe. As expected, a change in valence from 0 to 2 is observed in the metal. Indeed, coordination of Fe with four TCNB ligands induces a metal oxidation to form $\text{Fe}(\text{TCNB})_4$ structure, characterized by Fe-N distances [36] (1.86 \AA). Compared to the confined structure where the ligand do not coordinate the Fe atom, the Fe-N distance decreases as expected in the case of coordination complex.

²Thermal activation can either be done by leaving the sample at room temperature for several hours or by controlling the heating up to higher temperatures for a shorter amount of time.

Table 6.1 Mulliken charge distribution and valence of main sites for both confined and relaxed structures. Depicted values are averaged on equivalent atoms. C(1st) and C(2nd) denote the first and second next neighbour carbon atoms to Fe respectively along the Fe-N-C-C chain.

Element	Confined structure		Relaxed structure	
	Mulliken	Valence	Mulliken	Valence
Fe	1.958	0	3.063	2.094
N	-0.095	2.897	-0.379	2.938
C(1 st)	0.158	3.838	0.171	3.790
C(2 nd)	0.064	3.904	0.044	3.858

[22, 23]

Charge distribution analysis gives more insight into the electronic properties of Fe(TCNB)₄, a total charge transfer of $-1|e|$ occurs from the metal atom to the four coordinating organic ligands. This charge becomes delocalized and distributed all over TCNB ligands. Moreover, a comparative analysis confirms this result through the Mulliken charges (see Table 6.1) where about $-0.28|e|$ are donated to each N atom.

Energy diagram of the complex as obtained upon diagonalization of the Kohn-Sham Hamiltonian is shown in Figure 6.6, the HOMO-LUMO gap becomes of 2.4 eV, which is smaller than what is found for the bare TCNB layer (3.23 eV).

DOS were calculated at the end of molecular dynamics relaxation on a gas phase state. As explained earlier, the absence of substrate in this calculation should not affect the results since the interaction with the substrate is weak compared to the coordination binding. Furthermore, it has been experimentally proven that Fe atom slightly lifts up from the surface when it coordinates with the 4 TCNBs[1]. In this calculation, molecular dynamics did not affect significantly the molecular elements out of plane movement and the structure remained mainly planar.

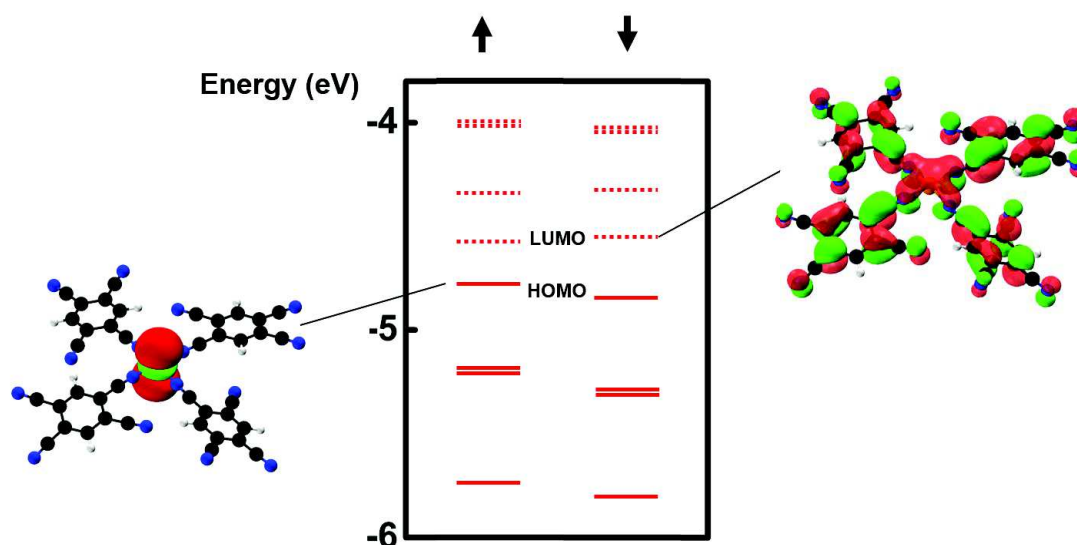


Fig. 6.6 Energy diagram of relaxed structure $\text{Fe}(\text{TCNB})_4$, calculation in this model took into account the spin polarisation because of the presence of the metal ion shown in up and down arrows. HOMO and LUMO projections are represented in left and right side of the diagram respectively. Red color denotes the spin up while green color denotes the spin down.

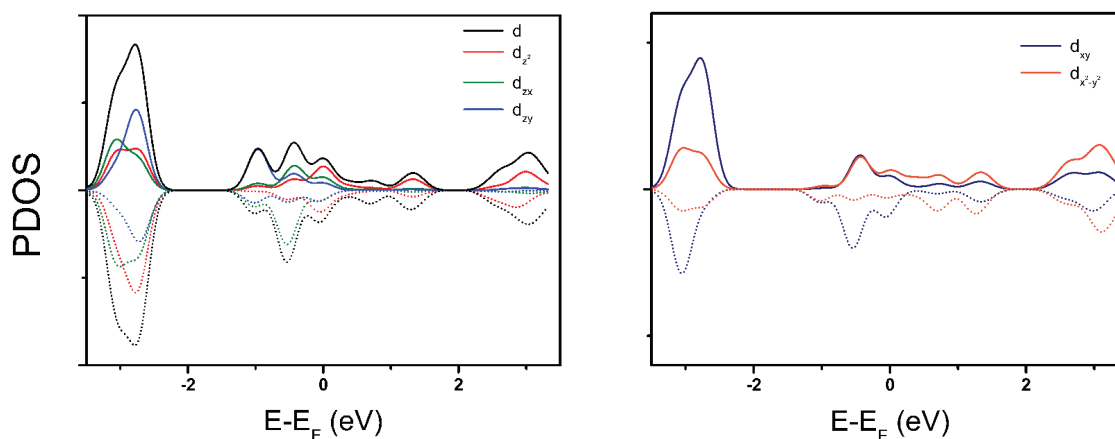


Fig. 6.7 Projected density of states of a relaxed structure. **Left** panel shows the projection on a_{1g} and e_g orbitals that are sensitive to STM measurements along with the total d-states contribution. **Right** panel is the PDOS of t_{1u} orbitals. The straight lines correspond to the upper spins projection while the dotted lines correspond to their bottom spins counter parts. A significant shift between the two spins contributes to the broadening of the total DOS for non spin polarized spectroscopy.

6.3.2 Density of states

When the DOS are projected over both, a_{1g} and e_g orbitals, a set of peaks (absent in the experimental spectra within the same range) will appear. However only the out of plane orbitals are visible using STS measurements, thus partial DOS (PDOS) as projected over a_{1g} and e_g orbitals is presented in Figure 6.7(a). The e_g orbitals are dominant in the HOMO and HOMO-1 orbitals while a_{1g} is dominant in the HOMO-2, LUMO and LUMO+1. Furthermore, a small energy shift between the upper and bottom spins is observed.

In addition, the t_{1u} is presented in Figure 6.7(b) as d_{xy} and $d_{x^2-y^2}$. Their contribution is not negligible in the global DOS, however their in-plane distribution only allow them to contribute to the Fe-N bond. Moreover these orbitals are invisible in experimental STS.

Although the total spin of the system is equal to 0, its spatial distribution, shown in terms of spin density (Figure 6.8) is localized on specific regions of the $Fe(TCNB)_4$. Namely, all the spin-up amplitude is localized on top of Fe, whereas the spin-down amplitude is spread on the ligands. This gives a global antiferromagnetic character to the molecule.

Moreover, the spin-down component repartition on the four ligands is characterized by a well-defined pattern covering half of the TCNB moiety. It adds a chirality character to what can be seen in topographic images. The spin distribution character on top of the Fe center is a d_{z^2} as observed by its geometrical shape (Yellow contribution in Figure 6.8) and confirmed by projecting the Kohn-Sham orbitals onto atomic wave functions. More specifically, the HOMO level is the one contributing mainly to this d_{z^2} orbital; as a consequence, they do not participate to the planar Fe-N-C... bonds and account for the spin sign of the metal.

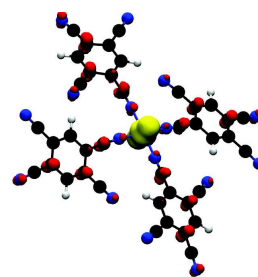


Fig. 6.8 *Spin density distribution of the $Fe(TCNB)_4$ complex with isovalue 0.01 $e/\text{\AA}^3$.*

6.4 On-surface synthesis of FePc by covalent self-assembly

Larger Fe deposition amount on a TCNB monolayer at the rate of 2:1 followed by an annealing up to 450 K leads to the formation of a fully reticulated $Fe-(TCNB)_2$ monolayer as presented in topography image in Figure 6.9(a). These networks have shown similar behavior on Au (111) and Ag (100) substrates indicating that the coordination network is relatively independent of the substrate nature. This confirms the low monolayer-substrate

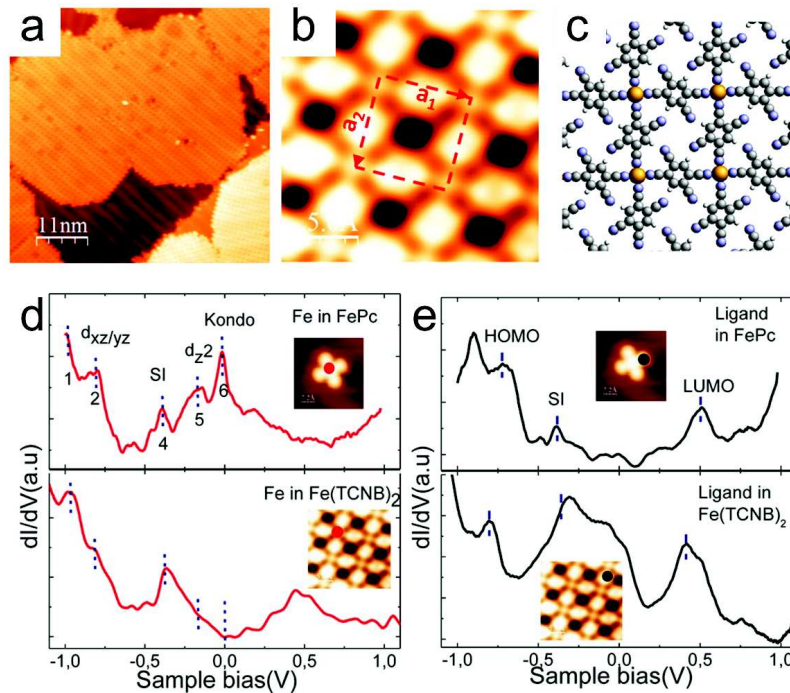


Fig. 6.9 a) STM topography image showing extended network of Fe-(TCNB)₂ on Au (111) substrate. b) depict a larger image where the unit cell vectors $\vec{a}_1 = \vec{a}_2 = 1.15 \pm 0.10 \text{ nm}$ are superimposed with red arrows. Tunneling parameters for a) and b) were $I = 0.2 \text{ nA}$ and $V = -0.9 \text{ V}$. c) Corresponding schematics of the network with a clockwise chirality. d) and e) Comparison of dI/dV spectroscopy taken on the Fe(TCNB)₂ network and FePc molecule on Au (111) surface under similar conditions ($I = 0.2 \text{ nA}$ and $V = -0.7 \text{ V}$). In a) the tip was positioned above the metal ion, in b) the tip was positioned above the ligand or the lobe. Work published in [2]

interactions as previously observed on Fe-(TCNB)₄ (see section 6.3).

The Fe-(TCNB)₂ has a periodic square lattice with the following parameters $\vec{a}_1 = \vec{a}_2 = 1.15 \pm 0.10 \text{ nm}$ and $\alpha = 90^\circ$ as shown in Figure 6.9(b). The estimated Fe-N coordination distance from topography images is of about 1.8 \AA with a $Fe\hat{N}C$ angle of 180° which is similar to the relaxed structure (see Figure 6.5). The TCNB C_2 symmetry lead to two distinct chiralities in a domain, Figure 6.9(c) depict a clockwise Fe-(TCNB)₂ rotation.

In order to obtain a clear sight into the coordinated network, both Fe-(TCNB)₂ and FePc molecules³ were investigated when formed/adsorbed on a Au (111) surface. The metal atom in the Fe-(TCNB)₂ molecule is coordinated to four nitrogens of four distinct TCNB ligands,

³FePc are commercially available and bought from Alfa Aesar.

which is a similar environment as FePc where the metal ion is coordinated to four pyrrole nitrogens of the Pc ligand. Thus the electronic investigations on these two structures should lead to a better understanding of the coordination process of such complexes.

STS measurements performed on both structures at the Fe location are presented in Figure 6.9(d), they reveal several similarities in the conductance signals indicating a similar electronic environment for both systems. They both depict a feature at -790 meV when the tip is positioned above the metal atom which is attributed to the d_π (d_{xz} and d_{yz}) orbitals. Moreover, the induced surface states are reproduced on the two systems at -380 meV leading to conclude that the Fe atom has similar hybridization with the Au (111) electronic s and p surface states.

On the other hand, STS recorded on the ligand (Figure 6.9(e)) depict a HOMO orbital at -760 meV and -720 meV on Fe-(TCNB)₂ network and FePc molecule respectively. A LUMO, on the positive bias voltage, is observed at about +490 meV and +500 meV on Fe-(TCNB)₂ and FePc respectively. The HOMO-LUMO gap is therefore similar in both cases with about 1.2 eV separation energy. All these features are summarized in Table 6.2.

DFT calculations were performed for FePc⁻ and Fe-(TCNB)₂ molecules to rationalize the experimental observations and gather a better understanding of the electronic modifications. FePc⁻ was chosen to get closer to the adsorbed situation of the molecule on a noble metal substrate. The resulting projected density of states (PDOS) are presented in Figure 6.10.

FePc⁻ depicts three d-orbital contributions in the calculated PDOS within -1 to +1 eV. One peak is positioned at the occupied states at -450 meV, it is ascribed to a d_{xy} -orbital. A second peak is observed at the empty states with an energy of +250 meV, it corresponds to a d_π orbitals (d_{xz} and d_{yz}) which are, therefore, positioned slightly below the LUMO observed in STS measurement. A third resonance positioned at the Fermi region corresponds to a d_{z^2} -orbital, this partially or fully filled orbital is close in energy to peak no.5 observed by

Table 6.2 Summary of common peak positions for both FePc and Fe-(TCNB)₂ on Au (111) substrate. Work published in [2].

Peak	no.	FePc (meV)	Fe-(TCNB) ₂ (meV)
d_π	2	-790	-790
HOMO	3	-720	-760
SI	4	-380	-380
d_{z^2}	5	-170	-
Kondo	6	yes	no
LUMO	7	+500	+490

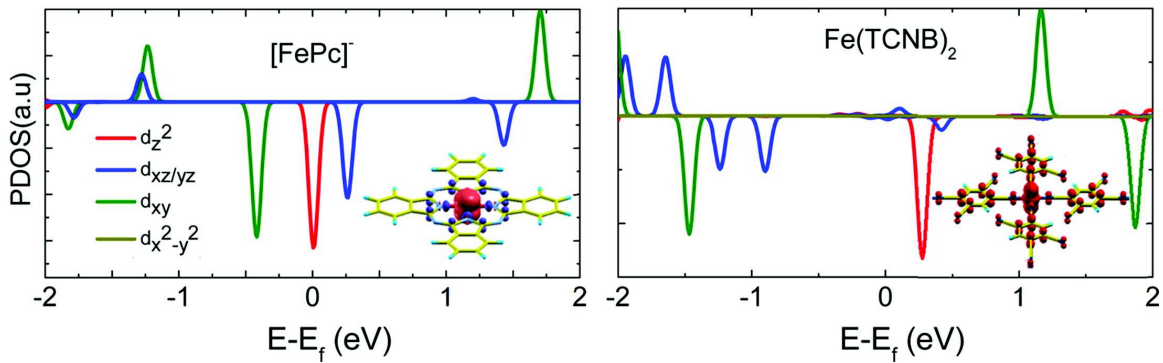


Fig. 6.10 Spin resolved projected density of states of FePc^- (left) and $\text{Fe}-(\text{TCNB})_2$ (right) onto different d-orbitals. The insets show the spin density isosurfaces for an electron density of $0.004e.\text{\AA}^{-3}$. Work published in [2]

STS in Figure 6.9(d).

PDOS of a $\text{Fe}-(\text{TCNB})_2$ gas phase molecule shows that its d_π orbitals situated at -850 meV reproduces well the experimentally observed peak no. 2 (-790 meV). d_{z^2} resonance is, in this case, positioned above the Fermi level indicating an empty orbital contrary to what have been observed on FePc^- . This d_{z^2} -orbital filling difference explains the reason why the Kondo resonance is no more apparent in the $\text{Fe}-(\text{TCNB})_2$ in contrary to FePc^- .

Corresponding spin densities are shown in the insets of Figure 6.10, as expected the total spin $S=1$ in FePc^- is located on the Fe atom with marginal distribution of the opposite spin on the next neighbors nitrogens. In contrary, the $\text{Fe}-(\text{TCNB})_2$ depicts a lower localization at the metal ion ($S=0.68$) as a non negligible part of the spin is spread among the four TCNB ligands.

Higher annealing temperature (up to 550 K for 3 minutes) induces the first stage polymerization by reducing the inter-molecular coordinations. Octacyano- FePc [$\text{FePc}(\text{CN})_8$] units are therefore formed as presented in Figure 6.11 (a-c). The molecular density reduction on this second annealing process, is induced by the originally coordinated to Fe, TCNB desorption from the substrate thus lowering the extension of pre-polymerized $\text{FePc}(\text{CN})_8$ monolayer.

STS investigation on this novel structure (Figure 6.11 (d-e)) reveals a more comparable conductance variation with the FePc in contrast with the $\text{Fe}-(\text{TCNB})_2$. More interestingly, $\text{FePc}(\text{CN})_8$ complex depicts a Kondo resonance as a peak is visible in dI/dV spectroscopy of Figure 6.11(d). This indicates that similar magnetic behavior occurs between FePc and

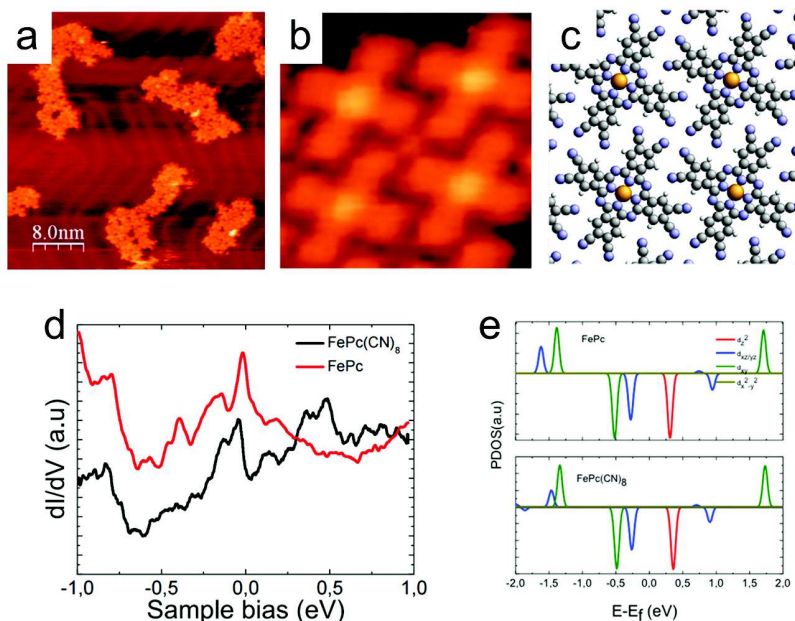


Fig. 6.11 a) and b) STM topography image showing $\text{FePc}(\text{CN})_8$ units after annealing the $\text{Fe}(\text{TCNB})_2$ network up to 550 K obtained at $I = 1.8$ nA and $V = -0.9$ V. These molecules correspond to a pre-phase of polymerization. c) Schematics of four $\text{FePc}(\text{CN})_8$ assembly. Notice the re-orientation of TCNB ligands compared to the network, where the chirality disappears. d) dI/dV spectra recorded above the Fe atom in both, $\text{FePc}(\text{CN})_8$ and FePc molecules (at $I = 0.2$ nA and -0.5 V). e) PDOS of FePc (top) and $\text{FePc}(\text{CN})_8$ (bottom) on d-orbitals. Similar behavior is obtained which indicates a similar electronic environment for the Fe atom in both systems. Work published in [2]

$\text{FePc}(\text{CN})_8$. Indeed, PDOS of both structures reveals the exact same electronic distribution which indicates that the Fe surrounding does not modify its orbital configuration at this level, thus, the magnetic moment and spin state remain similar in both structures.

6.5 Specific calculation parameters

TCNB

Gas phase calculation on single TCNB molecule was performed within an isolated supercell and initial geometry positions were taken from literature.[37] Cell dimensions were intentionally taken large enough in order to neglect any boundary conditions. The structure was relaxed by means of molecular dynamics up to a temperature of 150 K. The purely organic composition of small amount of this molecule allow such low relaxation temperatures.

Furthermore no magnetic effect or spin polarization are expected, thus no local spin density analysis was performed.

Fe-4(TCNB) (confined structure)

The initial structure of Fe-4(TCNB) was generated with the ChemSketch software using a relaxed TCNB molecule as mentioned above. Due to heavy calculation process for the confined structure, a very basic calculation was performed. As shown in the top right of Figure 6.4(a) the unit cell is inserted in an orthorhombic super-cell with boundary conditions and energy cut-off of 80 Ry. $|\vec{a}_1|$, $|\vec{a}_2|$ box vector lengths were adjusted at each calculation step in order to optimize the distances for periodicity. The perpendicular to plane $|\vec{a}_3|$ direction was kept long and unchanged since no boundary conditions should be applied on z-direction. The final convergent box size (which also corresponds to the unit cell) is $16.31*16.31*30 \text{ \AA}^3$.

Fe(TCNB)₄ (relaxed structure)

More developed calculations were performed for the free Fe(TCNB)₄ complex (see Figure 6.4). The structure was placed inside an isolated orthorhombic cell with a fixed size of $30*30*20 \text{ \AA}^3$ without periodic boundaries and an energy cut-off of 80 Ry. An initial heating up to 170 K was performed in order to efficiently relax the molecule, it was then cooled down to 5K to be compared with experimental results obtained at the same temperature.

Fe-(TCNB)₂, FePc and FePc⁻

Calculations performed on Fe-(TCNB)₂, FePc and FePc⁻ were mainly carried out by Dr. Abel Mathieu⁴ using SIESTA package. The wave function of the valence electrons is expanded on a double- ζ plus polarization basis set for each atom.[38, 39] The core electrons are treated within the frozen core approximation in which norm-conserving Troullier-Martins pseudopotentials were used.[6] The exchange-correlation energy is treated within the generalized gradient approximation (GGA) using parametrization proposed by Perdew-Burke- Ernzerhof.[40] In this study, spin polarized calculations are done on molecules in a gas phase configurations with a fixed total spin of S=1 that corresponds to the most stable

⁴Dr. Abel Mathieu, IM2NP, CNRS UMR 7334, Université Aix-Marseille, campus St-Jérôme, case 142, F-13397 Marseille Cedex 20. France

configuration. A k grid ($4*4*1$) was used in the case of $\text{Fe}(\text{TCNB})_2$, and ($1*1*1$) was used for the calculations of isolated FePc molecules.

Electronic properties

Density of states is obtained after calculating Kohn-Sham energies and its corresponding orbitals. Up to thirteen empty states were added, however only five of them succeeded in reaching the desired convergence. Wavefunctions were then projected onto different basis ($s, p_x, p_y, p_z, d_{xy}, \dots$) to calculate each orbital contribution at each Kohn-Sham energy.

6.6 Summary and conclusion

This chapter was devoted to the on-surface genesis of iron phthalocyanine from a simple TCNB molecule. Sequential deposition of TCNB molecules and Fe atoms on Au (111) surface led to the formation of a well ordered and confined Fe-4(TCNB) phase. This complex depicts unusual bond angles that prevent the structure from reaching its most stable state. It is demonstrated that a new ordered $\text{Fe}(\text{TCNB})_4$ monomer is formed upon thermal activation which structure is more relaxed and occupies a larger space compared to the initial state. STS investigations showed a clear signature of metal-organic coordination which is in full agreement with the Mulliken analysis obtained by DFT calculations at every step.

At last, on-surface synthesis of FePc was obtained by annealing the covalent self-assembly of TCNB and Fe at 550 K. The obtained structure was identified by topological and electronic investigations. It showed a d_{z^2} peak and a Kondo resonance under dI/dV spectroscopy which is a clear signature of FePc molecule.

The procedure presented here offers a promising method for the interpretation of dI/dV spectra of similar self-assembled systems. The ability of controlling the covalent bond formation on metal surfaces allows to extend the concept to polymerization of metal-phthalocyanine sheets.

REFERENCES

- [1] Shawulienė Kezilebiekienė, Anis Amokrane, Mauro Boero, Sylvain Clair, Mathieu Abel, and Jean-Pierre Bucher. Steric and electronic selectivity in the synthesis of Fe-1,2,4,5-tetracyanobenzene (TCNB) complexes on Au(111): From topological confinement to bond formation. *Nano Research*, 7(6):888–897, May 2014.
- [2] Shawulienė Kezilebiekienė, Anis Amokrane, Mathieu Abel, and Jean-Pierre Bucher. Hierarchy of Chemical Bonding in the Synthesis of Fe-Phthalocyanine on Metal Surfaces: A Local Spectroscopy Approach. *The Journal of Physical Chemistry Letters*, 5(18):3175–3182, September 2014.
- [3] R. Car and M. Parrinello. Unified Approach for Molecular Dynamics and Density-Functional Theory. *Physical Review Letters*, 55(22):2471–2474, November 1985.
- [4] W. Kohn and L. J. Sham. Self-Consistent Equations Including Exchange and Correlation Effects. *Physical Review*, 140(4A):A1133–A1138, November 1965.
- [5] M. Born and R. Oppenheimer. Zur Quantentheorie der Molekeln. *Annalen der Physik*, 389(20):457–484, January 1927.
- [6] N. Troullier and José Luís Martins. Efficient pseudopotentials for plane-wave calculations. *Physical Review B*, 43(3):1993–2006, January 1991.
- [7] S. Goedecker, M. Teter, and J. Hutter. Separable dual-space Gaussian pseudopotentials. *Physical Review B*, 54(3):1703–1710, July 1996.
- [8] A. D. Becke. Density-functional exchange-energy approximation with correct asymptotic behavior. *Physical Review A*, 38(6):3098–3100, September 1988.
- [9] Chengteh Lee, Weitao Yang, and Robert G. Parr. Development of the Colle-Salvetti correlation-energy formula into a functional of the electron density. *Physical Review B*, 37(2):785–789, January 1988.

- [10] Stefan Grimme. Accurate description of van der Waals complexes by density functional theory including empirical corrections. *Journal of Computational Chemistry*, 25(12):1463–1473, September 2004.
- [11] R. Hestenes Magnus and Eduard Stiefel. Methods of conjugate gradients for solving linear systems. *Journal of Research of the National Bureau of Standards. Research Paper 2379*, 49(6):409–436, December 1952.
- [12] Jr. Dennis, J. Practical Methods of Optimization, Vol. 1: Unconstrained Optimization (R. Fletcher). *SIAM Review*, 24(1):97–98, January 1982.
- [13] Shuichi Nosé. A molecular dynamics method for simulations in the canonical ensemble. *Molecular Physics*, 52(2):255–268, June 1984.
- [14] William G. Hoover. Canonical dynamics: Equilibrium phase-space distributions. *Physical Review A*, 31(3):1695–1697, March 1985.
- [15] Mathieu Abel, Sylvain Clair, Oualid Ourdjini, Mireille Mossoyan, and Louis Porte. Single Layer of Polymeric Fe-Phthalocyanine: An Organometallic Sheet on Metal and Thin Insulating Film. *Journal of the American Chemical Society*, 133(5):1203–1205, February 2011.
- [16] L. Giovanelli, A. Savoyant, M. Abel, F. Maccherozzi, Y. Ksari, M. Koudia, R. Hayn, F. Choueikani, E. Otero, P. Ohresser, J.-M. Themlin, S. S. Dhesi, and S. Clair. Magnetic Coupling and Single-Ion Anisotropy in Surface-Supported Mn-based Metal-Organic Networks. *The Journal of Physical Chemistry C*, 118(22):11738–11744, June 2014. arXiv: 1311.2775.
- [17] Thorsten Deilmann, Peter Krüger, Michael Rohlfing, and Daniel Wegner. Adsorption and STM imaging of tetracyanoethylene on Ag(001): An *ab initio* study. *Physical Review B*, 89(4):045405, January 2014.
- [18] Daniel Wegner, Ryan Yamachika, Xiaowei Zhang, Yayu Wang, Tunna Baruah, Mark R. Pederson, Bart M. Bartlett, Jeffrey R. Long, and Michael F. Crommie. Tuning Molecule-Mediated Spin Coupling in Bottom-Up-Fabricated Vanadium-Tetracyanoethylene Nanostructures. *Physical Review Letters*, 103(8):087205, August 2009.
- [19] Daniel Wegner, Ryan Yamachika, Yayu Wang, Victor W. Brar, Bart M. Bartlett, Jeffrey R. Long, and Michael F. Crommie. Single Molecule Charge Transfer and Bonding

- at an Organic/Inorganic Interface Tetracyanoethylene on Noble Metals. *Nano Letters*, 8(1):131–135, January 2008.
- [20] Manuela Garnica, Daniele Stradi, Sara Barja, Fabian Calleja, Cristina Díaz, Manuel Alcamí, Nazario Martín, Amadeo L. Vázquez de Parga, Fernando Martín, and Rodolfo Miranda. Long-range magnetic order in a purely organic 2d layer adsorbed on epitaxial graphene. *Nature Physics*, 9(6):368–374, June 2013.
- [21] N. Abdurakhmanova, T.-C. Tseng, A. Langner, C. S. Kley, V. Sessi, S. Stepanow, and K. Kern. Superexchange-Mediated Ferromagnetic Coupling in Two-Dimensional Ni-TCNQ Networks on Metal Surfaces. *Physical Review Letters*, 110(2):027202, January 2013.
- [22] Tzu-Chun Tseng, Nasiba Abdurakhmanova, Sebastian Stepanow, and Klaus Kern. Hierarchical Assembly and Reticulation of Two-Dimensional Mn- and Ni-TCNQ_x (x = 1, 2, 4) Coordination Structures on a Metal Surface. *The Journal of Physical Chemistry C*, 115(20):10211–10217, May 2011.
- [23] Nasiba Abdurakhmanova, Andrea Floris, Tzu-Chun Tseng, Alessio Comisso, Sebastian Stepanow, Alessandro De Vita, and Klaus Kern. Stereoselectivity and electrostatics in charge-transfer Mn- and Cs-TCNQ₄ networks on Ag(100). *Nature Communications*, 3:940, July 2012.
- [24] Marisa N. Faraggi, Nan Jiang, Nora Gonzalez-Lakunza, Alexander Langner, Sebastian Stepanow, Klaus Kern, and Andres Arnau. Bonding and Charge Transfer in Metal–Organic Coordination Networks on Au(111) with Strong Acceptor Molecules. *The Journal of Physical Chemistry C*, 116(46):24558–24565, November 2012.
- [25] Dimas G. de Oteyza, Iñaki Silanes, Miguel Ruiz-Osés, Esther Barrena, Bryan P. Doyle, Andrés Arnau, Helmut Dosch, Yutaka Wakayama, and J. Enrique Ortega. Balancing Intermolecular and Molecule–Substrate Interactions in Supramolecular Assemblies. *Advanced Functional Materials*, 19(2):259–264, January 2009.
- [26] Robin Taylor and Olga Kennard. Crystallographic evidence for the existence of CH···O, CH···N and CH···Cl hydrogen bonds. *Journal of the American Chemical Society*, 104(19):5063–5070, September 1982.
- [27] R. Scott Rowland and Robin Taylor. Intermolecular Nonbonded Contact Distances in Organic Crystal Structures: Comparison with Distances Expected from van der Waals Radii. *The Journal of Physical Chemistry*, 100(18):7384–7391, January 1996.

- [28] Hiroshi Ikeda. An Organic Radical Light-Emitting Diode Based on the Fluorescence Emission of a Trimethylenemethane Biradical. *Journal of Photopolymer Science and Technology*, 21(3):327–332, 2008.
- [29] Weigang Zhu, Renhui Zheng, Xiaolong Fu, Hongbing Fu, Qiang Shi, Yonggang Zhen, Huanli Dong, and Wenping Hu. Revealing the Charge-Transfer Interactions in Self-Assembled Organic Cocrystals: Two-Dimensional Photonic Applications. *Angewandte Chemie International Edition*, 54(23):6785–6789, June 2015.
- [30] B. W. Heinrich, L. Limot, M. V. Rastei, C. Iacovita, J. P. Bucher, Duval Mbongo Djimbi, Carlo Massobrio, and Mauro Boero. Dispersion and Localization of Electronic States at a Ferrocene/Cu(111) Interface. *Physical Review Letters*, 107(21):216801, November 2011.
- [31] R. Temirov, S. Soubatch, A. Luican, and F. S. Tautz. Free-electron-like dispersion in an organic monolayer film on a metal substrate. *Nature*, 444(7117):350–353, November 2006.
- [32] Willi Auwärter, David Écija, Florian Klappenberger, and Johannes V. Barth. Porphyrins at interfaces. *Nature Chemistry*, 7(2):105–120, February 2015.
- [33] U. Schlickum, R. Decker, F. Klappenberger, G. Zoppellaro, S. Klyatskaya, M. Ruben, I. Silanes, A. Arnau, K. Kern, H. Brune, and J. V. Barth. MetalOrganic Honeycomb Nanomeshes with Tunable Cavity Size. *Nano Letters*, 7(12):3813–3817, December 2007.
- [34] U. Schlickum, F. Klappenberger, R. Decker, G. Zoppellaro, S. Klyatskaya, M. Ruben, K. Kern, H. Brune, and J. V. Barth. Surface-Confined MetalOrganic Nanostructures from Co-Directed Assembly of Linear Terphenyl-dicarbonitrile Linkers on Ag(111). *The Journal of Physical Chemistry C*, 114(37):15602–15606, September 2010.
- [35] Mauro Boero, Kiyoyuki Terakura, Tamio Ikeshoji, Chee Chin Liew, and Michele Parrinello. Hydrogen Bonding and Dipole Moment of Water at Supercritical Conditions: A First-Principles Molecular Dynamics Study. *Physical Review Letters*, 85(15):3245–3248, October 2000.
- [36] Núria Aliaga-Alcalde, Serena DeBeer George, Bernd Mienert, Eckhard Bill, Karl Wieghardt, and Frank Neese. The Geometric and Electronic Structure of [(cyclam-acetato)Fe(N)]⁺: A Genuine Iron(V) Species with a Ground-State Spin S=1/2. *Angewandte Chemie International Edition*, 44(19):2908–2912, May 2005.

- [37] Marçal Capdevila-Cortada, Joel S. Miller, and Juan J. Novoa. Orientational Preference of Long, Multicenter Bonds in Radical Anion Dimers: A Case Study of π -[TCNB] $_2^{2-}$ and π -[TCNP] $_2^{2-}$. *Chemistry – A European Journal*, 21(17):6420–6432, April 2015.
- [38] J. Tersoff and D. R. Hamann. Theory of the scanning tunneling microscope. *Physical Review B*, 31(2):805–813, January 1985.
- [39] Dik Bouwmeester, Jian-Wei Pan, Klaus Mattle, Manfred Eibl, Harald Weinfurter, and Anton Zeilinger. Experimental quantum teleportation. *Nature*, 390(6660):575–579, December 1997.
- [40] H. Krauter, D. Salart, C. A. Muschik, J. M. Petersen, Heng Shen, T. Fernholz, and E. S. Polzik. Deterministic quantum teleportation between distant atomic objects. *Nature Physics*, 9(7):400–404, July 2013.

GENERAL CONCLUSION

Implementation of nano-objects based on organic materials in electronics allows a large expansion of the molecular spintronics field. Ambitious results lead scientists to believe in a fully functioning quantum computing devices within the next decades. The research presented in this thesis focused on single molecular magnets based on lanthanides. These molecules depict a large high spin ground state and easy axis magnetic anisotropy. Interactions of this structure with other molecules and lanthanides on various substrates have been investigated.

After a brief introduction to the aim and motivations of this work, this thesis presented in a first chapter a short theoretical overview. It aims to introduce to some fundamentals of molecular magnetism, in particular to effects observed experimentally. A very short introduction to the ligand field theory is also given in this chapter in order to explain the magnetism of the terbium double-decker molecule. Also, a detailed background to the Kondo physics, which is a key results in this thesis, is explained by means of Anderson model and Fano resonance.

Second chapter of this thesis gives the first principles of the scanning tunneling microscopy. At first, a detailed theoretical approach to the tunneling effect leading to the detection of tunneling current in STM is given, it is followed by the principles of current detection and tunneling spectroscopy analysis. Then, the STM apparatus is presented with its various experimental approaches and proper working conditions.

In this work, the terbium double-decker molecule was chosen for its ability to show a very large anisotropy barrier and prominent hysteresis. This structure is widely investigated by multiple approaches, however its electronic and magnetic properties still remain obscure and needs further knowledge. Herein, experiments focused on these properties with respect to the molecular environment.

An extensive investigation was carried by a combination of the experimental approach using a scanning tunneling microscopy and a theoretical investigation by means of DFT calculations. The molecule-substrate interactions is a fundamental factor in the molecular scale investigations, in order to satisfy a wide range of interactions, various adsorbates were used.

The following chapters investigate the properties of a single molecule and a molecule embedded in a domain. Single TbPc₂ molecules adapt their adsorption site and orientation following the bottom phthalocyanine's interaction with the substrate. As expected for low reactive substrates like gold or silver, the molecules have a longer diffusion path compared to more reactive substrates (cobalt or copper). Supported by DFT calculations, the substrate-molecule distance increases by 60% when going from Cu (111) to Au (111), this decoupling is transferred to the electronic properties of the molecules as explained in the fourth chapter. On gold substrate, a supplementary electron occupies the π -orbitals of the upper ligand, this electron carries a spin 1/2 which becomes a source of diffusion of conduction electrons. This behavior is observed by a Kondo resonance with a temperature $T_K = 37\text{ K}$ at the eight lobes of the TbPc₂ upper phthalocyanine.

Below a certain inter-molecular distance (which depends on the substrate), the proximity of other molecules will develop a non-covalent interactions between the ligands. These interactions are strongly dependent on the substrate nature as various domain configurations are observed in the fifth chapter of this thesis. Results led to draw an overview of the conformation on Au (111), Ag (111) and Cu (111) substrates. Furthermore, a molecular density variation is induced and an intra-molecular geometrical modification occurs when the film grows on a gold substrate. This is observed by a skew angle reduction between the two molecular ligands from 45° to 30° for moiety of molecules. As consequence, a TbPc₂ monolayer on Au (111) becomes less dense compared to the Cu (111) substrate. This structural modification affects the magnetic properties of the molecules. The Kondo resonance, previously observed on the eight lobes of the un-capped TbPc₂, is now observed only on the crossing points where four molecules in a domain meet. This variation is induced by the inter-molecular interactions, they affect the behavior of the supplementary electron by localizing it in space. Thus for a dimer, no Kondo resonance is observed because of pairing between two supplementary π -electrons while on a larger island, the magnetic resonance progressively locates at the center of the island and appears with a resonance temperature that decreases with respect to the island size. The Kondo temperature drops from 37 K for single molecules to 22 K for a film. This is explained by the fact that less electrons are available for the screening process because of the presence of a decoupling layer formed by

the upper ligands.

In order to get further information of the role of the π -electrons in the coupling between different spin systems in SMM, a cerium atom is placed on the top of the TbPc₂ structure. Investigations on this new complex are summarized in the fifth chapter of this thesis. This second lanthanide bonds covalently to the upper phthalocyanine creating a semi-stable structure. Indeed, only one electron is shared between the atom and the host molecule. Atomic manipulations at the cerium position revealed a very weak interaction as it is possible to remove cerium from a molecule adsorbed on Cu (111) by applying a bias voltage of ≈ 1.7 V. Interestingly, when adsorbed on Au (111) substrate the cerium can be hidden under the first Pc layer of the film when ≈ 1.5 V is applied between the tip and the molecule. This process is found reversible under different conditions opening a new consideration for information storage based only on geometrical configuration.

STS investigations reveals a Kondo resonance at the Fermi region of $T_K = 30$ K, this peak is expected to originate from the $4f$ -electron carried by the cerium atom. Furthermore, it is observed only on a A-type CDD molecule adsorbed on Au (111).

DFT calculations highlight an indirect exchange between the two lanthanides generating an anti-ferromagnetic coupling. This observation is almost totally independent from the substrate nature as similar charge transfer is observed between the terbium and the cerium on all substrates.

Parallel to the main subject, additional work has been carried out on the genesis of FePc molecules from simple TCNB molecules. It was shown in the last chapter of this thesis that by co-depositing TCNB molecules and Fe atoms on a Au (111) surface, it is possible to form a FePc molecule.

First experiments led to the formation of Fe(TCNB)₄ monomers. A non-covalent bounding is obtained after a deposition of Fe atoms with a ratio of 1:4 with a majority of molecules, this state shows two separate STS signatures where every element (TCNB or Fe) depict a spectroscopy as if it was singly adsorbed on the crystal. This indicates that no electronic modification occurred at the atomic/molecular level. After a thermal activation, the iron atom coordinates with the four surrounding molecules through a Fe-N covalent bond. The STS in this case shows a localization of the d_{z^2} -states at the Fe location. DFT calculations support these results and find a charge transfer of $-0.28 |e|$ donated from the metal to the molecule.

When the initial deposition ratio is increased to 1:2 (with a majority of TCNB) followed by an annealing of 450 K, a fully reticulated Fe(TCNB)₂ network is formed. STS inves-

tigations on this new system reveals multiple orbital similarities with the spectroscopy of a FePc molecule indicating a similar electronic environment for both systems. However, a Kondo resonance which is present on FePc is absent in the Fe(TCNB)₂ network because of a different d_{z^2} -orbital filling. Indeed, this orbital is found above the Fermi level on the network while it is filled with one electron in FePc molecules, allowing a conduction electron scattering.

Higher annealing to 550 K of the Fe(TCNB)₂ network led to the formation of Octacyano-FePc molecules which consist of a pre-polymerization stage. The inter-molecular bondings are reduced and the complexes depict a layer of what seems to be isolated monomers. Furthermore, STS investigations reveal in this case a Kondo resonance on the Octacyano-FePc similar to a simple FePc indicating a similar magnetic moment and spin state of the two structures.

Therefore the genesis of the FePc molecule is revealed by self-assembling on surface of Fe atoms and TCNB molecules. This procedure offers a promising method for the interpretation of spectroscopic data of similar self-assembled molecules.

APPENDICES

When H₂Pc molecule is adsorbed on Cu (100) substrate its phenyl rings are asymmetrically adsorbed on the copper layer. In one case, more Cu atoms are underneath the left side of the phenyl while in a second case, they are superior in the right side of the phenyl. See Figure 12.

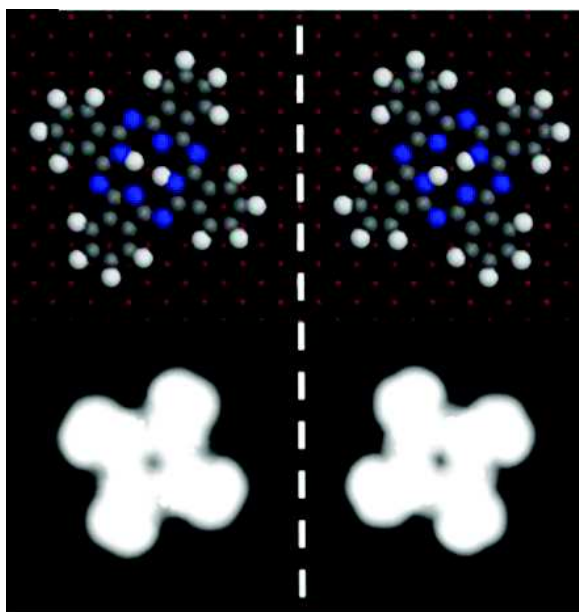


Fig. 12 Model (up) and calculated (bottom) electronic distribution of H₂Pc molecule adsorbed on Cu (100) surface. A clockwise (left) and anticlockwise (right) chirality is observed when simulating a tunneling topography. The model where the phenyl rings are adsorbed with their left part laying on more Cu atoms compared to their right part is represented in the left. The mirror symmetric adsorption is shown in the right part. Juan Liu et al. Positioning and Switching Phthalocyanine Molecules on a Cu(100) Surface at Room Temperature. *ACS Nano*, 8(12):12734–12740 (2014)

The dI/dV spectroscopy recorded above a lobe of TbPc₂ molecule shows some similarities when the substrate nature is modified. Indeed, the global shape remains similar in the negative energies (HOMOs) as only one large peak is observed, see Figure 13. This peak also depicts a shift to higher energies (away for the Fermi energy) which is expected given the modification in the substrate reactivity (Co>Cu>Ag>Au). This is also reported on the LUMO orbitals as only Au (111) and Ag (111) led the appearance of empty states while the other substrates seem to push it away from E_F.

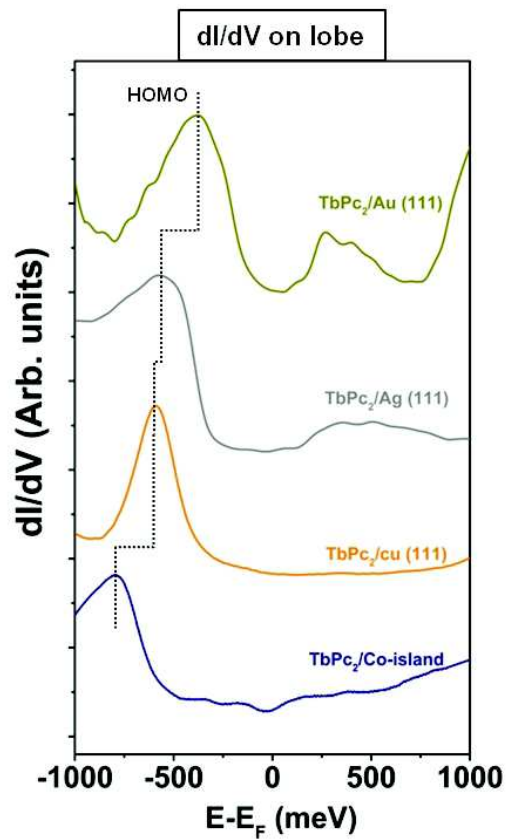


Fig. 13 dI/dV spectroscopies recorded above a lobe of single TbPc₂ molecule adsorbed on four different substrates from bottom to top: Co-island, Cu (111), Ag (111) and Au (111). HOMO position is shifted toward the Fermi level as the substrate reactivity decreases as indicated by vertical line.

When a TbPc_2 molecule adsorbs on Cu (111) substrate filled with Co-islands, the molecule tends to locate preferentially at the islands edge as observed in Figure 14(a). However, when it comes to an adsorption above the island, multiple protrusions are observed they correspond to a fragmentation of the TbPc_2 because of the high reactivity of the copper. A dI/dV spectroscopy shows similar features on all the molecule as shown in Figure 14(c). However, on lobe, the third peak representing the HOMO-2 as well as HOMO-1 is shifted towards the Fermi level. On the other side, the LUMO remains at the same position all over the molecule.

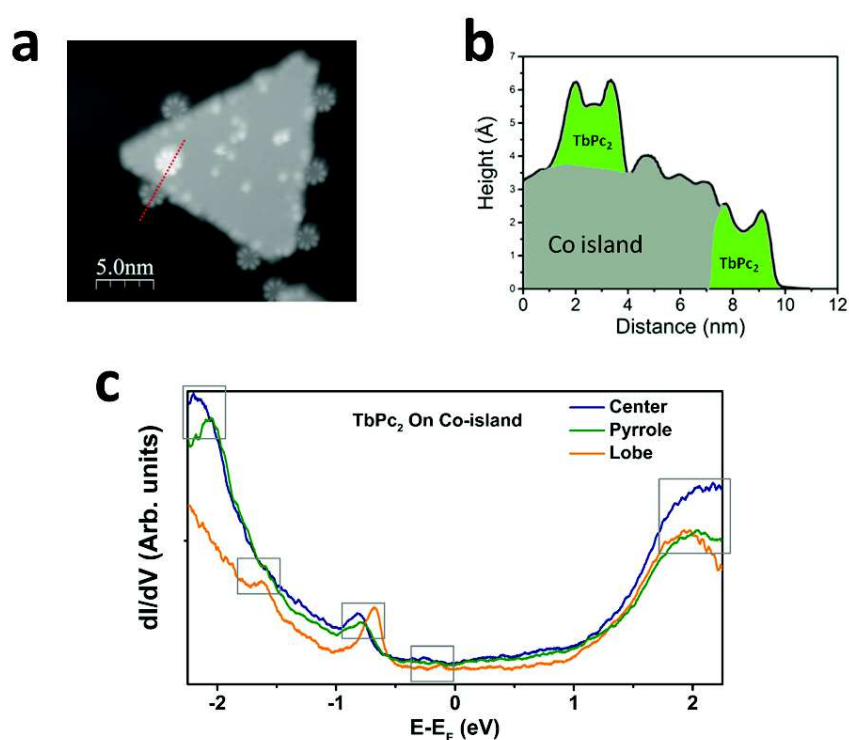


Fig. 14 a) Topographic image of TbPc_2 molecules adsorbed on a cobalt island grown on Cu (111) surface. b) profile analysis of a two TbPc_2 molecules, one is adsorbed on the island while the other is adjacent to the island as presented in dotted lines in topography image. The apparent height of the molecule is of $\approx 2.5 \text{ \AA}$. c) STS spectroscopy recorded above the center, pyrrole and lobe of a double decker molecule adsorbed on a Co-island.

STS spectroscopy recorded above an isolated double-decker molecule on Au (111) substrate shows a different dI/dV spectra compared to the one in a domain as shown in Figure 15. This difference highlights the inter-molecular interaction at the local basis of a single molecule. Furthermore, none of the two molecular types on Au (111) have a similar (or even close) STS shape to the isolated molecule which indicates a total modification of the molecular orbitals of a $TbPc_2$ molecule when it forms a molecular layer.

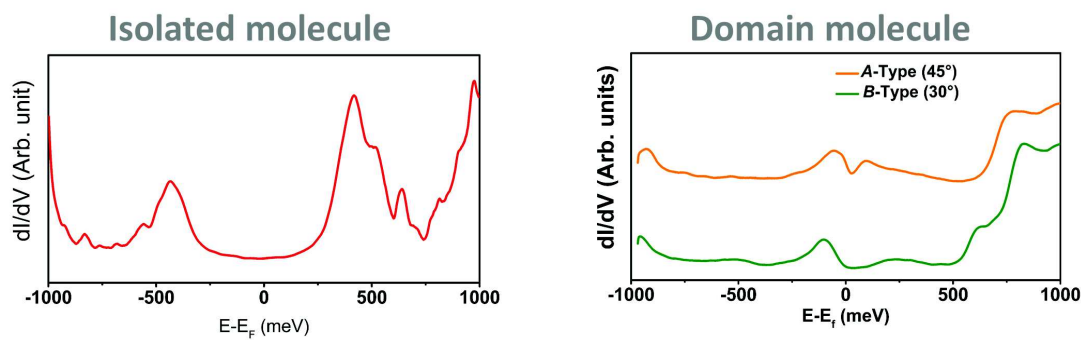


Fig. 15 Comparison between the STS obtained in single $TbPc_2$ molecule (left) and a molecule embedded in a domain (right). Both structures are adsorbed on Au (111) substrate.

When a TbPc₂ molecule on Au (111) (domain) is capped with a cerium atom, the molecular orbitals become modified such as a larger HOMO-LUMO gap is observed in both *A*- and *B*-type molecules. A comparative view of the STS of both molecular types when the molecule is capped or not is presented in Figure 16.

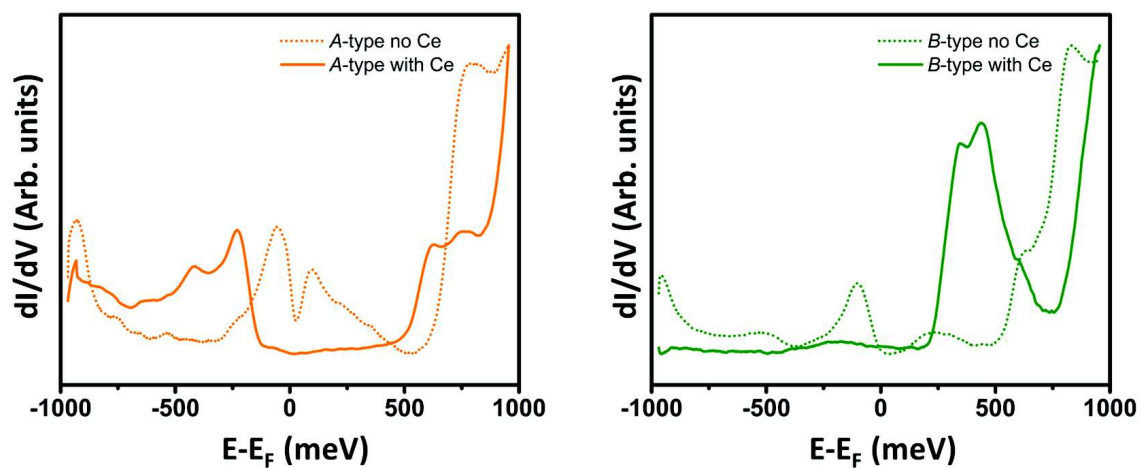


Fig. 16 dI/dV spectroscopy recorded above the center of both TbPc₂ and CDD molecule adsorbed on Au (111) is shown in a comparative way. The two molecular types are shown as indicated in the plots.

Table 3 shows the main atom-atom calculated distances in both relaxed and confined Fe-(TCNB)₄ structures which are in good agreement with experimental measurements. The Mayer bond and the inter-atomic distance variations highlights the modification of the structure before and after thermal activation.

	Confined structure		Relaxed structure	
	Mayer bond	Distance (Å)	Mayer bond	Distance (Å)
Fe-N	-	2.6	0.32 → 0.38	1.86
C-N	2.72	1.16	2.42	1.17
H-N	-	2.3	0.014 → 0.054	2.2 → 2.5

Table 4 presents the orbital position of the relaxed structure (by DFT) and the occupation level for the four highest occupied and the four lowest unoccupied orbitals. Up arrow denotes the spin up distribution while their counter part spin down, are represented by a down arrow.

↓		↑	
energy (eV)	occupation	energy (eV)	occupation
-5.73	1	-5.80	1
-5.20	1	-5.31	1
-5.18	1	-5.29	1
-4.77	1	-4.84	1
-4.57	0	-4.55	0
-4.33	0	-4.32	0
-4.01	0	-4.05	0
-3.99	0	-4.02	0

